UNIVERSIDADE DE LISBOA
FACULDADE DE CIÊNCIAS
DEPARTAMENTO DE CIÊNCIAS DA TERRA E ENERGIA

Unraveling the Evolution of Mineral Deposits in Rainbow Hydrothermal Field Through Micro-Scale Analysis of Sulfide Phases

Bernardo Alexandre Martinho Ferreira

Mestrado em Geologia
Especialização em Geodinâmica e Recursos Geológicos

Dissertação orientada por:
Ágata Alveirinho Dias
Ana Filipa Marques Abraham-James

2025

Acknowledgments

The realization of this work would not have been possible had it not been for the efforts and contributions of a number of entities and individuals, to whom I must thank.

This work was funded by the Macao Science and Technology Development Fund (No. FDCT 043/2014/A1) – project "SeaMin - In-situ trace elemental and isotopic constraints on modern seafloor massive sulfide mineralization" and the Portuguese "Fundação para a Ciência e a Tecnologia" (FCT) I.P./MCTES through national funds (PIDDAC):

UIDB/50019/2020 (https://doi.org/10.54499/UIDB/50019/2020);

UIDP/50019/2020 (https://doi.org/10.54499/UIDP/50019/2020);

LA/P/0068/2020 (https://doi.org/10.54499/LA/P/0068/2020).

I would like to wholeheartedly express my gratitude to my supervisors, Dr. Ágata Alveirinho Dias and Dr. Ana Filipa Marques, for their guidance, support and seemingly unlimited patience which I found between the subtle (and some not so much) corrections and useful tips that proved crucial for the completion of this work. Furthermore, I would like to thank Dr. Ágata Alveirinho Dias for providing me with all the samples, data and all the necessary conditions for the smooth functioning of this thesis.

This project was a culmination of many steps, and to conclude each one, a series of people helped me reach this final goal, as such I would like to express my gratitude to Pedro Costa (ISE, USJ) and Dr. Sofia Rodrigues (FCUL) for their assistance in preparing mounds and polished thin sections, an especially hard task given the materials at hand; to Dr. Pedro Rodrigues (FCUL) for the assistance during electron microprobe analyses; to Dr. Whenhong Qiu for the assistance in the *in-situ* S analyses and finally to Dr. Alvaro Pinto (FCUL), not only for the assistance with petrographic imaging and the microscopy "mini-lectures", but also for all the help and talks over this period in which he acted as a third supervisor.

I would also like to thank all my close friends, that throughout the years have been with me. Amongst them I'd like to mention my best friend, António, thank you for your friendship throughout all these years.

Lastly I´d like to thank my family, Inês, Tio "Toni" and Tia (Ana), thank you for all the love and support you have always given me, and finally, my mom and dad, firstly thank you for encouraging me to pursue this thesis, for helping me throughout these degrees and thank you for everything you have done throughout my whole life, the love and support you've given me, this thesis is as much mine as it is yours, so once again, thank you.

Resumo

Os campos hidrotermais são uma das principais fontes de elementos químicos para os oceanos, com particular relevância no fornecimento de metais (e.g. Ni, Cu, Zn, Fe), metais esses solubilizados em fluidos formados através da interação da água do mar aquecida com as rochas encaixantes em profundidade, criando um fluxo ascendente que emerge através de chaminés hidrotermais.

O presente estudo debruçou-se na investigação da composição mineralógica e geoquímica de chaminés ricas em sulfuretos do Campo Hidrotermal Rainbow (CHR), um sistema hidrotermal ativo e vigoroso alojado em rochas ultramáficas. Localizado a sul do arquipélago do Açores, o CHR desenvolve-se nas proximidades de uma zona de Falha Não-Transformante (FNT), que separa dois segmentos de expansão lenta (segmentos AMAR e AMAR Sul), da Crista Média Atlântica (CMA). O CHR apresenta condições únicas, destacando-se por registar a temperatura mais elevada, o pH mais baixo e a maior cloridicidade entre os sistemas hidrotermais Atlânticos. Estas características são o reflexo de prolongadas interações fluido-rocha, que culminam em fluidos hidrotermais fortemente enriquecidos em metais de transição e outros elementos remobilizados das rochas hospedeiras, evidenciando anomalias positivas face a campos hidrotermais semelhantes em Mn, Fe, Co, Ni, Cu, Zn, Au, Ag, Cd, Cs, Pb, Y.

Foram estudadas 14 amostras de chaminés do CHR, recolhidas diretamente no fundo do mar com o auxílio do submarino *Nautile* (IFREMER) durante a missão oceanográfica SALDANHA (1998).

O objetivo principal deste trabalho consistiu na caracterização da variação composicional das chaminés por forma a relacioná-las com os processos de formação e evolução do sistema hidrotermal, através da análise da distribuição espacial sistemática de elementos traço e da composição isotópica (*in-situ*) do enxofre ($\delta^{34}S$) em diferentes gerações de sulfuretos. O estudo procurou contribuir para a compreensão do sistema hidrotermal submarino do CHR, fornecendo dados complementares de mineralogia e geoquímica integrados em estilos de mineralização propostos em trabalhos anteriores. Este contributo visa aprofundar o conhecimento sobre sistemas hidrotermais submarinos associados a rifts de expansão lenta.

Os métodos aplicados incluíram: análise detalhada dos vídeos e relatórios da missão para contextualização geológica e de amostragem; descrição mineralógica e textural preliminar das amostras para seleção de zonas representativas; preparação de lâminas polidas para observações em microscopia petrográfica; microanálises por sonda electrónica (EPMA); microscopia eletrónica de varrimento com espectroscopia de energia dispersiva (SEM/EDS); análise *in situ* da composição isotópica de enxofre (LA-MC-ICP-MS); e análise geoquímica de rocha total (elementos maiores, menores e terras raras). A integração dos dados à micro- e macro-escala representa um passo importante e permitiu aprofundar o conhecimento sobre a dinâmica complexa dos campos hidrotermais.

Também este estudo permitiu refinar e redefinir a classificação dos estilos de mineralização previamente definidos para os depósitos do CHR, integrando-os nas tipologias já estabelecidas, dominadas pela prevalência em sulfuretos de cobre, esfalerite ou pirrotite, e detalhando as suas associações mineralógicas, sendo elas:

- **Estilo-Cu** (rico em sulfuretos de cobre): Caracterizado pela presença de fases sulfuretadas ricas em Cu, com vários graus de recristalização, variando de isocubanite (com a menor concentração de Cu) até digenite (maior concentração de Cu). As amostras classificadas nesta tipologia revelaram-se, contudo, bastante mais complexas do que as dos restantes estilos de mineralização, permitindo a sua subdivisão em três sub-estilos: Tipo-I - caracterizado pela calcopirite como mineral principal dentro da associação, tendo como minerais secundários outros sulfuretos ricos em Cu; Tipo-II – semelhante ao Tipo-I , contudo, os sulfuretos encontram-se envolvidos so seio de uma matriz de sulfatos (i.e. sulfatos > sulfuretos), com destaque para anidrite; Tipo-III – dominado por isocubanite, tendencialmente instável

(por vezes na forma de SSI - solução sólida intermédia), em processo de evolução/retrabalhamento para calcopirite, sendo a covelite o único sulfureto de Cu adicional presente.

- **Estilo-Sph** (rico em esfalerite) – Definido pela ocorrência de três formas distintas de esfalerite: Esfalerite I que corresponde à forma inalterada desta fase e que constitui o corpo principal das amostras; Esfalerite oxidada, presumivelmente derivada da Esfalerite I, exibindo diferentes graus de oxidação e, Esfalerite II que corresponde à fase tardia associada ao preenchimento do interior de antigos microcanais de circulação de fluidos (circundados por anéis de isocubanite). Sendo que neste caso, a isocubanite constitui um membro importante da associação mineral, uma vez que permite uma clara distinção entre Sph-I e Sph-II.

- Estilo-Po (presença de pirrotite) – Caracterizado pela presença de pirrotite, embora a sua quantidade seja um fator secundário, apresentam associações variadas com as outras fases presentes nos outros estilos.

Cada um destes estilos de mineralização reflete condições físico-químicas distintas de precipitação, permitindo inferir variações na evolução temporal dos fluidos hidrotermais no CHR.

Os valores de $\delta^{34}S$ obtidos variam entre -2,77 ‰ e +3,82 ‰, refletindo a diversidade dos estilos de mineralização e dos minerais presentes. As fazes minerais sulfuretadas correspondentes à mineralização do Estilo-Cu apresentam os valores mais elevados, sendo os valores mais baixos registados nas fases pertencentes ao Estilo-Sph. Existe uma correlação direta entre o tempo de exposição á agua do mar e um aumento dos valores de $\delta^{34}S$, essa correlação dá-se ao longo do tempo, sendo mais notória em chaminés inactivas e mais antigas, onde os sulfuretos são tendencialmente retrabalhados, sofrendo um processo de enriquecimento supergénico associado também ele à interação com a àgua do mar através do qual se formam minerais ricos em Cu, comparativamente à calcopirite que os origina.

Estes resultados sugerem que o tempo de interação com água do mar fria e os processos de enriquecimento supergénico (promovidos pela oxidação resultante da interação com a àgua do mar) subsequentes são fatores chave para a alteração da assinatura isotópica e que neste sentido trabalham de forma complementar na variação de $\delta^{34}S$. Ainda assim, outros factores, nomeadamente, a dinâmica, a temperatura e a composição do fluido podem também contribuir significativamente para o resultado final dos valores de $\delta^{34}S$.

A classificação revista dos estilos de mineralização que categorizam os depósitos da CHR nas já estabelecidas tipologias dominadas pela prevalência em sulfuretos de cobre, esfalerite ou pirrotite (Estilo-Cu, Estilo-Sph e Estilo-Po, respectivamente), e procura aprimorar e afinar os detalhes mineralógicos de cada estilo.

Os resultados obtidos permitiram aferir os estilos de mineralização presentes no CHR e inferir dois mecanismos complementares de evolução dos fluidos hidrotermais: uma evolução pré-deposicional caracterizada por variações na composição primária dos sulfuretos e nos estilos de mineralização associados, cuja diferenciação se dá por alterações à dinâmica, temperatura e composição dos fluidos que culmina na diferenciação nos diferentes estilos de mineralização, e uma evolução pós-deposicional, associada a processos supergénicos e de recristalização mineral, caracterizada pela alteração isotópica do enxofre ($\delta^{34}S$) e transformação progressiva de fases minerais, (e.g. transformação da isocubanite em calcopirite, por sua vez retrabalhada para sulfuretos enriquecidos em Cu por via de um enriquecimento supergénico em amostras correspondentes ao Estilo-Cu).

A integração dos dados mineralógicos, geoquímicos e isotópicos com dados mineralógicos fornece uma visão abrangente da evolução do CHR, enfatizando a sua capacidade de transpor os mecanismos de deposição de metais envolvidos como um análogo moderno para depósitos antigos, que é onde reside a grande importância de compreender estes processos, para além disso, estas comparações também

ajudam a melhor compreender e poderão providenciar de forma geral uma perspetiva diferente sobre os processos que moldam a atividade hidrotermal.

Este trabalho reforça a importância do estudo mineralógico detalhado, integrando petrografia, geoquímica e estudos isotópicos para a compreensão da génese de depósitos sulfuretados ricos em metais em ambientes oceânicos de expansão lenta e propõe um estudo detalhado em que as alterações mineralógicas e composicionais das chaminés sejam um tema de destaque em trabalhos futuros.

Palavras-chave: Campo Hidrotermal Rainbow; Crista Média Atlântica; Chaminés hidrotermais; Sulfuretos; $\delta^{34}S$.

Abstract

Seafloor hydrothermal fields are a key source of metals to the oceans, via interaction of seawater with deep underlying rocks (e.g. Ni, Cu, Zn, Fe). This study focuses on the mineralogical and chemical composition of sulfide-rich chimneys in the Rainbow Hydrothermal Field (RHF), an active and vigorous hydrothermal system hosted in ultramafic rocks located near the Mid-Atlantic Ridge (MAR). The RHF has a set of unique conditions (lowest pH, highest temperature and chlorinity among Atlantic hydrothermal systems). These characteristics reflect prolonged fluid-rock interactions, resulting in fluids heavily enriched in transition metals, while showing positive anomalies in other elements remobilized from the host rocks.

Fourteen chimney samples of the RHF were collected during the SALDANHA oceanographic mission (1998) and were studied using detailed petrography, electron probe microanalysis (EPMA), SEM/EDS, whole-rock geochemistry, and in situ sulfur isotopic analysis (LA-MC-ICP-MS).

The compositional data allowed to redefine the mineralization styles into three main typologies, each with a signature mineral/mineral assemblage: Cu-style (copper sulfides), Sph-style (sphalerite), and Po-style (pyrrhotite), with Cu-style proving to be more complex and thus requiring the subdivision into three different sub-styles. Each of these mineralization styles reflects distinct physicochemical precipitation conditions, allowing usto infer variations and distinguish between pre- and post-deposition processes in the temporal evolution of hydrothermal fluids in the RHF.

The obtained δ34S values range from -2.77 ‰ to +3.82 ‰, reflecting the diversity of mineralization styles and the present minerals, with the highest values associated to the Cu-style and the lowest values belonging to the Sph-style. The obtained values, along with the petrographic and geochemical data also reiterate that both pre-depositional processes driven by changes in fluid dynamics, temperature and composition and post-depositional processes characterized by isotopic alteration and mineral transformation are fundamental factors to the evolution of hydrothermal fields.

Keywords: Rainbow Hydrothermal Field; Mid-Atlantic Ridge; Hydrothermal chimneys; Sulfides; $\delta^{34}S$.

Table of contents

List of Figures, Tables and Equations:

1. Introduction

The first discovery of active seafloor hydrothermal systems dates to 1977, when the submarine hydrothermal activity at Galápagos Rift in the Pacific was explored using a manned deep ocean research submersible Alvin (Corliss et al., 1979). It soon became evident that these systems, where circulating hydrothermal fluids, driven by a heat source associated to magmatic bodies, interact with cold seawater, lead to the precipitation of hydrothermal minerals at or near the seafloor often forming seafloor massive sulfides (SMS). These are considered modern analogues to ancient volcanogenic massive sulfide (VMS) systems and are important sources of base and precious metals such as copper (Cu), zinc (Zn), lead (Pb), gold (Au), and silver (Ag) (Pat Shanks, 2013; Petersen et al., 2018).

Seafloor hydrothermal fields are often found along mid-ocean ridges (MOR) where they are more abundant, followed by volcanic arcs, back-arc spreading centers, and seamounts. The most recent InterRidge database reports a total of 721 vent fields across the world´s oceans, with 666 confirmed or inferred active and 55 inactive (*Vent Fields List All - InterRidge Vents Database Ver. 3.4*, 2020). However, previous studies suggest that this number may underestimate the real extent of hydrothermal venting. For example, Baker et al., 2016, suggested that the number of vents associated with fast and intermediate spreading ridges, could be 3-6 times bigger than previously reported. Additionally, (Beaulieu et al., 2015) estimated that the actual number of vents should come closer to 1305 (95% confidence limits 713– 1853). When this hypothesis was proposed, only 435 fields had been confirmed, suggesting that many undiscovered vents are likely located along slow and ultra-slow spreading ridges, which are notoriously difficult to survey due to the theoretically less significant release of both mass and heat (Beaulieu et al., 2015). Based on these works, of the estimated 1305 hypothesized fields, 1099 should theoretically occur throughout MOR, while 206 would be associated with back-arc spreading centers. More recently Liao et al. (2024) estimated, using geochemical signatures of the seafloor, that the abundance of off-axis inactive hydrothermal fields along MOR, particularly at ultra-slow spreading ridges, may be double of what was previously assumed. The study also suggests that SMS on slow and ultraslow-spreading ridges could be significantly higher than earlier estimates, as previous research did not account for the mineral deposits currently inactive, since detecting and assessing these fields remains an ongoing challenge due to the absence of active venting indicators such as hydrothermal plumes.

Beaulieu et al. (2013) highlights the importance of the *InterRidge Vents Database* as the authoritative source for the locations of hydrothermal vent fields worldwide. The database is open-source and includes detailed information for each vent field, such as unique identifiers, location, water depth, tectonic setting, and literature references (usually to its first publication). Furthermore, it also distinguishes between confirmed (visually observed) or inferred (detected through water column measurements) fields, thus providing an important tool unifying extensive datasets regarding vent fields worldwide. The distribution of known active (red circles for confirmed and yellow for inferred) and inactive (blue circles) hydrothermal fields is illustrated in Figure 1.1.

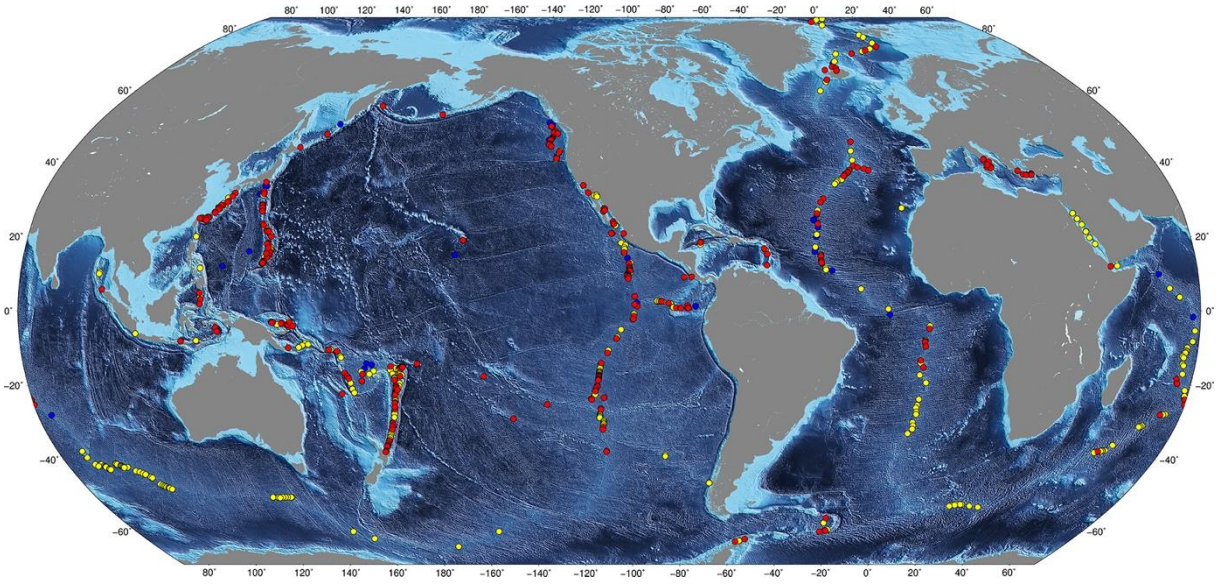

Figure 1.1: Locations of known active vent fields, distinguishing confirmed (red circles) and inferred (yellow circle) and known inactive fields (blue circle). Map from S. Beaulieu & Szafranski, (2020): https://doi.org/10.1594/PANGAEA.917894 , based on InterRidge Global Database of Active Submarine Hydrothermal Vent Fields: https://vents-data.interridge.org/ .

On the northern sector of the Mid-Atlantic Ridge (MAR), both north and south of the Azores archipelago (Portugal), several hydrothermal fields were discovered and explored. The map shown in Figure 1.2 highlights the diversity of hydrothermal fields along the Portuguese seafloor, which includes the area within the Exclusive Economic zone (EEZ) and the proposed extended area of the Continental Shelf Project (CSEP) as presented by Portugal to the United Nations Convention under the Law of the Sea (UNCLOS: https://en.emepc.pt/projeto-pepc).

Portugal´s seafloor includes significant segments of the MAR (Mid Atlantic Ridge) influenced by the Azores mantle plume anomaly. Here the MAR consists of slow-spreading ridge segments separated by non-transform offsets (NTOs) where several hydrothermal fields have been identified displaying diverse hydrothermal regimes, fluid signatures, and mineralization processes (German & Seyfried, 2013). The MAR fields are hosted by different lithologies, including Normal-Mid Ocean Ridge Basalts (N-MORB) and Enriched-Mid Ocean Ridge Basaltic (E-MORB, showing stronger geochemical influence from the Azores mantle). Additionally, some fields are hosted in ultramafic rocks, particularly in zones where hydrothermal circulation is mainly controlled by deep, low-angle detachment faulting associated to NTOs. The geochemical signatures and geotectonic context of these fields suggest potential for the discovery of additional hydrothermal systems within this Portuguese sector of the MAR, representing a valuable opportunity to further understand the relationship of ridge dynamics and hydrothermal processes (Dias et al., 2022).

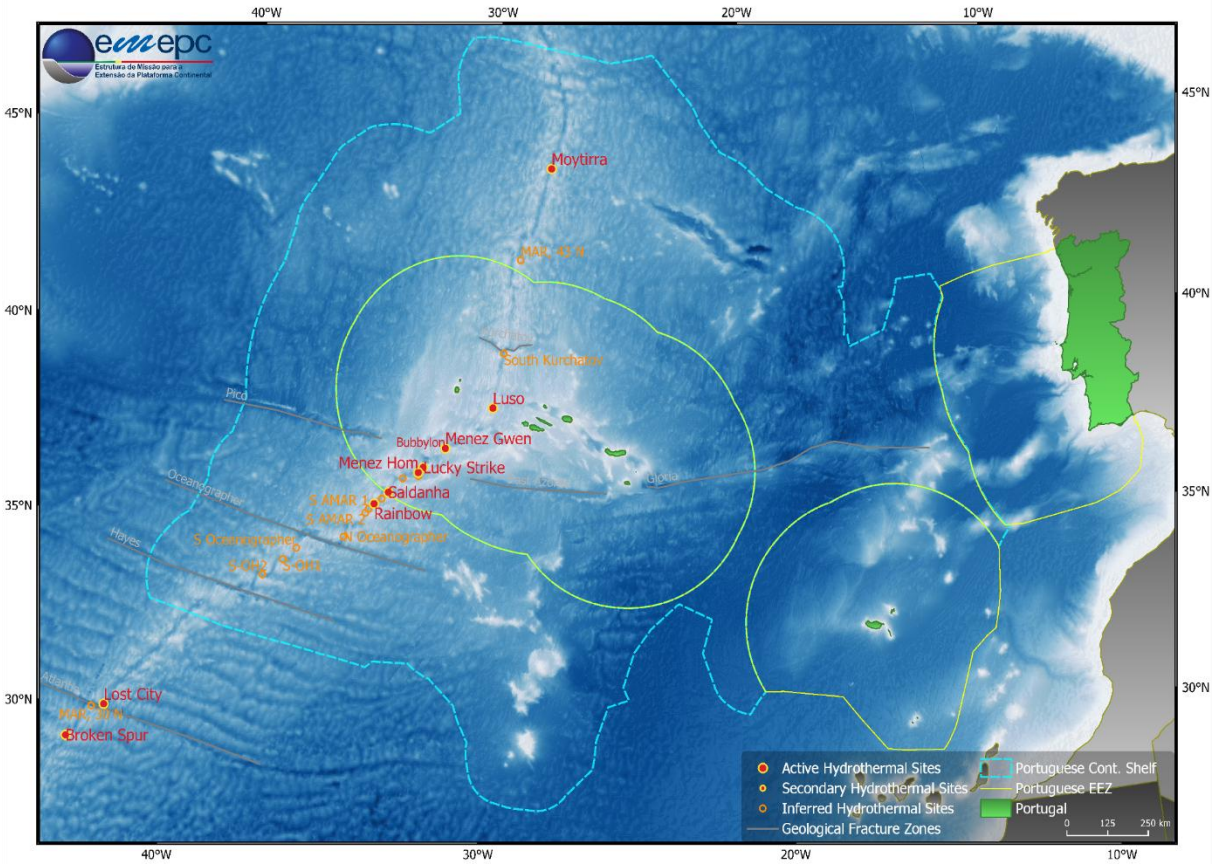

Figure 1.2: Active, secondary and inferred hydrothermal sites inside and near the portuguese continental shelf and EEZ.

1.1 Seafloor Hydrothermal processes and seawater circulation

Seafloor hydrothermal processes occur near tectonic boundaries such as MOR, where the infiltration of cold seawater through the fractured and permeable ocean lithosphere drives mass and heat exchange between the oceanic lithosphere and the surrounding seawater (Jamieson & Gartman, 2020). During hydrothermal circulation, seawater infiltrates structural weaknesses – such as fractures and/or faults - in the oceanic lithosphere, establishing a convective system. Here, the unmodified seawater interacts with the underlying rocks in the presence of a heat source, which enhances the fluid´s reactivity and its capacity to leach and transport chemical elements in solution to the surface (Humphris et al., 1995; Jamieson& Gartman, 2020).

Hydrothermal circulation represents the pathway seawater follows as it percolates the oceanic crust, undergoing significant chemical and physical changes. This process involves three distinct zones: a **recharge zone**, where seawater infiltrates the lithosphere; a **reaction zone**, where the fluids are heated and become chemically reactivity, gaining the ability to exchange elements with the surrounding rocks due to the interaction with a heat source; and the **discharge zones,** where altered sweater (hydrothermal fluids) are expelled back into the ocean (German & Damm, 2003; German & Seyfried, 2013; Humphris & Mccollom, 1998; Tivey, 2007).

Each one of these zones is crucial to the hydrothermal processes that occur and represent the pathway fluids must take to transform cold seawater into hot, enriched hydrothermal fluids.

In the recharge zones, cold seawater sinks into the oceanic crust through fractures and permeable zones, still oxygen-rich. The seawater then interacts with volcanic rocks and simultaneously heats up and loses the oxygen along with potassium and other alkali elements, leading to the formation of iron oxides and

hydroxides still in the upper crust, this process is responsible for making the recharge seawater more acidic and reaching temperatures < 60ºC (German & Seyfried, 2013; Humphris & Mccollom, 1998a; Tivey, 2007).

In the reaction zone, the seawater enters in contact with the heat source that is driving the hydrothermal circulation system and thus reaches higher temperatures (> 400ºC) at higher depths (i.e. higher pressure), which further promotes the leaching of metals and other elements from the underlying rocks, leading to the formation of hydrothermal fluids rich in metals such as Fe, Cu and Zn (that may react with S from seawater sulfates to form sulfides), or other elements that will contribute to the precipitation of alteration minerals (including chlorite, sodium-rich feldspar, amphibole, epidote, and quartz); all able to precipitate and accumulate prior to reaching the ocean floor (German & Seyfried, 2013; Humphris & Mccollom, 1998a). In cases where the host rocks are ultramafic, serpentinization may occur with the seawater reacting with olivine and pyroxene to form serpentine-group minerals, magnetite and releasing hydrogen and methane in what is generally an exothermic reaction that furthermore feeds into the hydrothermal budget (e.g., German & Seyfried, 2013).

The final zone is the discharge zone, where the now modified seawater returns to the seafloor due to its increased buoyancy. As these fluids rise, they rapidly cool when mixing with seawater. This sharp decrease in P and T triggers the precipitation of minerals, forming altered mineral assemblages, that may be rich in silica, chlorite and sulfides, in the fluid's pathways as well as within the hydrothermal vents and chimneys at the surface, often interlinked with sulfate and/or carbonate assemblages rich in Fe-Cu-Zn (German & Seyfried, 2013; Humphris & Mccollom, 1998a)

Other processes may occur enhancing the mineralization potential. The process of fluid phase separation, that occurs in hydrothermal systems, plays a crucial role in the fluids' composition. One of the primary mechanisms that triggers phase separation is change in temperature and pressure as the fluid ascends through the oceanic crust. leading to the separation of the original fluid into two distinct phases, liquid and vapor. The liquid phase may become enriched in transition metals, such as Fe, Zn, Cu, Ag, while volatile components such as CO2, H2S and CH4 concentrate in the vapor phase (Foustoukos & Seyfried, 2007).

These processes are highly influential to the overall chemical budget of the ocean floor, with global influence on both temperature and compositional balance of the oceans and a more local influence on the geology and biology aspects of the influenced areas (German & Seyfried, 2013; Humphris & Mccollom, 1998a; Tivey, 2007). An example to the extent of this influence is presented in Seyfried et al. (2015), which suggests that low to moderate-temperatures hydrothermal systems at slow-spreading ridges hosted in ultramafic contexts (e.g. the Lost City hydrothermal system) experience an approximate 30% reduction in silica content as fluids cool from 200°C to 150°C, which is attributed to the precipitation of silica minerals, highlighting the role of ultramafic rock alteration in contact with seawater. Furthermore, it also justifies the diminished presence of Si at high temperatures, the high metal content of these fluids, and their low pH, providing a direct correlation to the higher temperatures (that tend to decrease during the ascend) attained from the host rock, thus providing evidence as to how host-rocks may influence the entire circulation process (Seyefried et al., 1991).

1.2 Physical and chemical properties (T, Eh, pH, chemistry)

Hydrothermal fluids composition and behavior are strongly influenced by temperature, pressure, and interactions with the underlying rock (whether it be the host-rock or the substrate upon which it deposits) and given that high-temperature systems (>300°C) are typically characterized by acidic conditions (i.e. low pH), these conditions serve as the catalyst to enhance and promote the leaching of metals along with

other dissolved components, that are later transported with the fluids to the surface, as observed in experimental studies of peridotite-seawater interaction (Seyfried Jr & Dibble Jr, 1980). Additionally, the redox state (Eh) is buffered by mineral assemblages such as magnetite and sulfides, leading to reduced fluid conditions conducive to the precipitation of sulfide minerals (Campbell et al., 1988; Seyfried Jr & Dibble Jr, 1980).

Overall, these hydrothermal fluids show a significant enrichment in transition metals such as Fe, Mn, and Zn (Seyfried Jr & Dibble Jr, 1980), if in presence of direct magmatic influence, volatiles such as CO_2, SO_2, and H_2S may further modify fluid chemistry, often increasing acidity and promoting metal mobilization (Campbell et al., 1988; Klinkhammer et al., 1994).

1.3 Fluids generated in Mafic vs Ultramafic Settings

The compositional difference between mafic and ultramafic host rocks exerts control on the composition of hydrothermal fluids. Ultramafic systems, often exposed along slow-spreading ridges through tectonic activity, are subjected to serpentinization processes, which gain effectiveness at 200 to 300ºC, largely above the temperatures at which olivine hydrolysis can start to occur (McCollom et al., 2016; Seyfried Jr & Dibble Jr, 1980). This process leads to and enrichment in Fe, H_2, and CH_4 accompanied by increased fluid. In contrast, hydrothermal fluids circulating through mafic rocks may be enriched Si and light rare earth elements (LREE) (with Ce as an exception due to the Ce anomaly in the seawater resulting from the oxidation of Ce^{3+} and subsequent precipitation as Ce^{4+}), due to dissolution of minerals such as plagioclase and pyroxene (Klinkhammer et al., 1994). The mafic systems will suffer oxidation processes at a greater degree, with magma as the main driver in the process, furthermore, this process will lead to an enrichment in different metals as elements such as Ni and Cr are no longer as predominant as they would be in systems where there would be interaction with ultramafic rocks (Klinkhammer et al., 1994; Seyfried Jr & Dibble Jr, 1980).

1.4 End-Member fluid, boiling point, phase separation and magmatic degassing

The chemical composition of hydrothermal fluids may also be influenced by additional processes such as: phase separation, boiling, and magmatic degassing. Phase separation (the creation of two distinct phases from a single homogeneous mixture), is often achieved by reaching the critical pressure-temperature point (which varies amongst different elements), and results in the partitioning of volatiles (e.g. CO_2 or H_2S) into gas-rich phases and the metals in a brine phase (Klinkhammer et al., 1994).

With the boiling point corresponding to the temperature at which the pressure surrounding a liquid becomes equal to its vapor pressure, thus making the reaction possible, with chemical/structural factors also influencing said temperatures. These factors will be influenced by solid solutions (e.g. $(Mg,Fe)_2SiO_4$ [$Mg^{2+} \leftrightarrow Fe^{2+}$] and respective end-members), as they alter the predetermined conditions that must be met which in turn fluctuates the effectiveness of said processes.

Finally, magmatic degassing introduces volatile components such as SO_2, which increase fluid acidity and enhance the leaching capability of metals from the host-rocks by the liquid (Campbell et al., 1988). In ultramafic systems due to the high temperatures, phase separation will occur at a greater rate, with the serpentinization process crucially contributing to insert water into the system and therefore increase the likelihood of further chemical changes. These processes are crucial in defining the fluid's geochemistry, impacting therefore the overall conditions of the deposits, more specifically their composition and element proportions (Klinkhammer et al., 1994; Seyfried Jr & Dibble Jr, 1980).

1.5 Hydrothermal venting and deposits

1.5.1 Type of venting

The type of venting observed in seafloor hydrothermal fields relates directly to the composition and temperature of the fluids expelled from the discharge zones of the hydrothermal convective circulation. Other factors also influence the nature of venting, namely the extent and nature of structural pathways that enable fluid flow.

In broad, general terms, hydrothermal fluid flow can either be focused or diffuse.

Focused fluid flow: Typically resembles "smokers" and form hydrothermal chimneys when high-temperature fluids mix with seawater at the seafloor, causing minerals to precipitate and form chimney-like structures that grow directly above the vent orifice. As these fluids reach the surface, they may continue to be focused, discharging either through a chimney, or follow more tortuous pathways to emerge as a diffuse flow. High-temperature fluids are highly reactive and carry metals that precipitate readily as (dark-colored) sulfides, giving name to black-smokers (Humphris & Mccollom, 1998). Conversely, lower-temperature fluids have a reduced capacity for subsurface leaching, therefore carrying different and less temperature dependent elements in solution, often enriched in barium (Ba), calcium (Ca) and silicon (Si), venting as clear (white)-smokers and precipitating sulfate an/or carbonates into edifices-like venting structures.

Diffuse fluid flow: Occurs when hydrothermal fluids rise from depth and mix with cold seawater at the subsurface before exiting the seafloor through a network of diffuse multiple channels often within hydrothermal sediment mounds or volcaniclastic deposits. Lower-temperature and diffuse venting may be associated to nearby black smokers, though they may also occur independently. This diffuse venting is a common occurrence throughout the vent's lifecycle, either at the margins of existing high-temperature upflow areas (i.e. smokers) or when the venting process is in a transitional state – either in the early stages of development or as the venting system weakens and nears cessation. In addition to its diffuse nature, these flow patterns are often characterized by translucent fluid that may appear as a shimmering haze in the water column. (e.g., Á. Dias, 2009).

The differentiation process is further demonstrated in Figure 1.3, in which diffuse zones are contrasted with the pathways leading to the formation of elemental richer smokers, highlighting the temperature differences associated with the different types of venting.

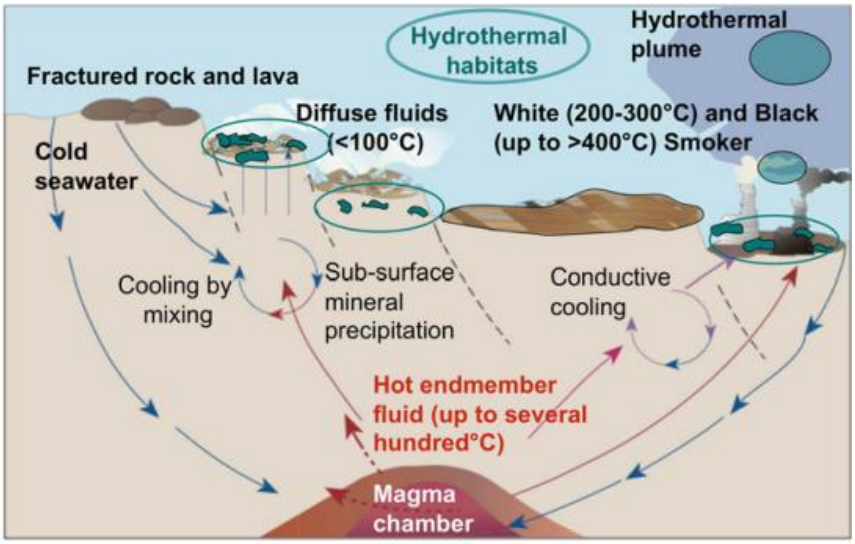

Figure 1.3: Simplified sketch showing the evolution of hydrothermal fluids in a geologically active site (Koschinsky, 2016) in which diffuse zones, where the fluids cool due to interaction with cold seawater, are highlighted in contrast to the more focused, higher temperature smoker's pathways.

1.5.2 Deposits

The process that leads to the precipitation and genesis of mineral deposits on the seafloor is influenced by various factors, including the temperature and composition of the hydrothermal fluids, as well as the geological and chemical environment of the vent sites (German & Seyfried, 2013). Mineral accumulations can be divided into several types, those being:

- **Black smokers:** Chimney-like structures characterized by high-temperature flow of dark, metal-rich hydrothermal fluids, reaching up to 300-400ºC. They are typically black due to the immediate precipitation of sulfide minerals in suspension (Humphris & Mccollom, 1998a).
- **White smokers:** Chimney-like structures venting clear fluids. These vents, with lower temperatures usually only a few tens of degrees above ambient, exhibit reduced reactivity, resulting in the leaching of fewer elements into the solution. These elements are typically barium, calcium, and silicon, leading to the formation of clear-colored structures (Á. Dias, 2009).
- **Flanges** (also referred as "inverted cones" or "inverted bells")**:** Horizontal and concave structures that form around the base of hydrothermal chimneys. They are created when hot fluids rise from below and become trapped in a concave structure above, forming an inverted reflective surface due to the difference in densities between the hot, lower-density fluid and the surrounding cold, denser seawater (Woods & Delancey, 1992).
- **"Beehive diffuser":** Structures located on the top of a more focused flow chimneys releasing lower-temperature fluids, forming a shape that resembles a beehive. These structures consist of a bulbous shape with multiple small openings or "diffusers" through which hydrothermal fluids are expelled (Mottl et al., 1994).
- **Mounds:** mound-like accumulations of large and dense mineral deposits formed around hydrothermal vents. They are often composed of collapsed hydrothermal structures as well as minerals deposited by diffuse venting through the mound.
- **Metalliferous Sediments** (also referred to as metal-rich hydrothermal sediments)**:** metal-rich pelagic deposits typically found in areas surrounding primary hydrothermal vent zones. These sediments usually form layered deposits as a result of the accumulation of metal-rich particles that settle out of hydrothermal plumes. Additionally, the collapse of venting structures through sulfide mass wasting and debris flow, as well as the contribution of local diffuse hydrothermal flow, can also contribute to the formation of metalliferous sediment (Á. S. Dias et al., 2008, 2011).
- **Stockwork:** complex networks of sulfide-rich veins and fractures formed beneath the seafloor, typically at the apex of the reaction zone and below the venting area. These deposits form from hydrothermal fluids percolating through host rock, precipitating minerals within cracks and fissures. They contribute significantly to the metal content in hydrothermal systems and offer insights into subsurface hydrothermal fluid flow and mineral deposition conditions (Marques et al., 2006; Murton et al., 2019).

2. Geological setting and mineralization

Hydrothermal fields can occur in a variety of geological settings, which often determine the type of mineralization and associated deposits. These settings are predominantly found in tectonically active regions, where magmatic activity is the principal driver of hydrothermal fluid circulation, and include MOR, volcanic arcs and back-arc basins, with the most notorious setting for hydrothermal fields and hydrothermal activity being MOR. In these settings, as described above, cold seawater interacts with the heat generated underneath the ridge axis and is propelled to the surface after leaching the underlying rocks. This process generates venting, and both the chemistry and quantity of expelled fluids draw a direct correlation to spreading rates, which vary from ultra-slow to fast spreading (Hannington et al., 2005).

Non-transform offsets (NTOs) are regions that cross the Mid Ocean Ridge (MOR) and where the ridge is offset without a significant transform movement. This sort of setting is often seen in slow to ultra-slow spreading ridges. Oceanic core complexes (OCC) also associate to slow and ultra-slow MOR and are the result of low angle detachment faults that expose deep crust and mantle rocks. Both these processes create a geothermal imbalance that may lead to hydrothermal activity, with NTO generating a tectonic environment favorable to the formation of OCC (Canales et al., 2017).

Also important, are mantle plumes or hot spots. These are regions where deep sourced magma upwelling from the mantle reaches the oceanic crust, leading to increased volcanic (and hydrothermal) activity. Whether through heat, mass transfer, or both, hydrothermal activity may occur in these regions (Hannington et al., 2005). An example is the Luso Hydrothermal Field, whose influence comes from the Azores hot spot.

In contrast to MOR hydrothermal activity, Arc/Back-Arc settings are associated with subduction zones and the partial melting of the mantle into the crust. This occurs due to the heating of oceanic seawater subducted along with the tectonic plate, as well as fluids ascending from the dehydration of the subducted plate over time. These processes collectively prompt hydrothermal activity (Whitney et al., 2013).

Finally, hydrothermal activity may also occur as a consequence of tectonic activity, where movement and the subsequent energy generated may initiate or enhance hydrothermal processes (Hannington et al., 2005).

In all these settings, whatever the geological setting may be, the underlying constant is water/hydrothermal fluids, which these processes enhance via the energy and dynamics they provide, that in turn, allows for the mineralization process to occur.

2.1 Slow-spreading ridges

The spreading ridge rate is a key factor influencing the morphological, magmatic and hydrothermal processes occurring at MORs. Slow-spreading (20–55 mm/yr) and ultraslow-spreading ridges (<20 mm/yr) exhibit additional hydrothermal settings comparing to fast spreading ridges (>80 mm/yr) due to their distinct tectonic and magmatic characteristics. At slower spreading ridges, tectonic processes facilitate the development of oceanic core complexes (OCC) through the movement of detachment faults, leading the exposure of ultramafic rocks. These settings often host hydrothermal activity, with systems ranging from mafic- to ultramafic-hosted environments, exhibiting distinct rock and fluid compositions (Fontaine et al., 2008; Krasnov et al., 1995; Zhao et al., 2024).

Along with magmatic dominant hydrothermal activities, typically located at ridge segments, hydrothermal fields discovered in slow-spreading ridges can be also influenced by a mixture of

ultramafic and gabbroic lithologies, with the serpentinized peridotite outcrops serving as an indicator of these environments (Cannat, 1993). Then, unlike fast-spreading ridges, which are predominantly characterized by volcanic activity along the segment centers, slow-spreading ridges can be associated with both magmatic and amagmatic bodies. Theses environments may coexist (particularly along NTO) where hydrothermal fields are often influenced by deep-seated heat sources commonly associated with volcanic occurrences (Dick et al., 2003). These large hot bodies promote a low fluid/rock (f/r) ratio, through which hydrothermal fluids gain their high mineral enrichment.

These magmatic and amagmatic bodies display, in Rainbow's and similar areas, a strong correlation to heat anomalies such as the Azores hot spot, that can produce heat and promote the formation of such bodies (Dick et al., 2003). The understanding of processes occurring underneath these slow-spreading ridges is also crucial for their overall understanding.

Due to the aforementioned conditions, these slow-spreading regimes will, more often than not, promote serpentinization processes, which are also found to be particularly ineffective processes at lower temperatures ("Olivine hydrolysis rate data, however, indicate ineffective conversion to serpentine at temperatures equivalent to Lost City vent fluids (40–75°C)"; Allen & Seyfried, 2004), whilst remaining increasingly effective at higher temperatures where serpentinization and thus, olivine hydrolysis can occur (e.g. Rainbow; Allen & Seyfried, 2004). This serpentinization process is also responsible for the increment in Fe, CH4 and H2 contents into the vent's composition and to the hydrothermal fluids (Allen & Seyfried, 2004; Gràcia et al., 2000), with those also being large indicators of a magmatic heat source given the vent field's high heat flux (~0.5 GW) and fluid volume flux (~450L/s) (Canales et al., 2017; Dunn et al., 2017).

The first discovered ultramafic-hosted hydrothermal system (only considering their direct discovery and not just the detection of its plume) was Logatchev, located at 14°45'N on the MAR (Bogdanov et al., 1995) Since then, multiple active and inactive ultramafic-hosted hydrothermal sites have been identified along other slow and ultra-slow spreading ridges. On the MAR the most relevant sites identified to date include Menez Hom (37°90'N; Fouquet et al., 1994), Saldanha (36°34'N; Á. S. Dias & Barriga, 2006), Lost City (30°;(Kelley et al., 2001), Ashadze and Krasnov (12°58'N and l6º38'N, respectively; Cherkashov et al., 2008a; Fouquet et al., 2008), and Nibelungen (8.3°S; (Melchert et al., 2008).

2.2 Rainbow Hydrothermal Field

The initial detection of hydrothermal activity around the Rainbow Hydrothermal Field was attained through geochemical anomalies in the water column, attributed to hydrothermal plumes suggesting potential hydrothermal activity on the seafloor. This anomaly was detected 10-15km east of a NTO, in 1994, and was the first evidence of hydrothermal activity pointing towards the Rainbow Hydrothermal field (German et al., 1996). These plumes were incredibly rich in metals, with concentration surpassing those of the Trans-Atlantic Geotraverse (TAG) vent-field, which had previously recorded the highest metal concentration in the MAR (German et al., 1996). The metal-rich plumes would be a strong indicator and directly correlate with the high metal concentration in the fluids later retrieved in-situ (i.e., at the vent site).

The discovery Rainbow hydrothermal field came a year later, in 1997, during the FLORES cruise as part of the MAST III AMORES Project (Barriga et al., 1997; Fouquet et al., 1998). The field is located on a "dome-shaped massif" at 36°13.80'N, 33°54.12'W, approximately 400 km southwest of the Azores triple junction, associated with a non-transformant fault offsetting of the MAR, more precisely within a second-order discontinuity on the western flank of a nonvolcanic ridge situated on an offset between AMAR and the South AMAR (Douville et al., 2002). The massif itself consists of three different

ultramafic-hosted sites: Rainbow field (active, high temperature), Clamstone and Ghost City fields (both inactive), located 1 km E and 2 km NE of the Rainbow field, respectively (Andreani et al., 2014). Figure 2.1 provides a conceptual profile view of the Rainbow field and its location within the MAR, while also providing a schematic view of how the three fields are arranged, while also depicting a likely explanation for the fluid's circulation at the site.

For simplification it is worth noting that when mentioning the Rainbow, unless stated otherwise, it refers to the active Rainbow Hydrothermal Field and not the Rainbow Massif.

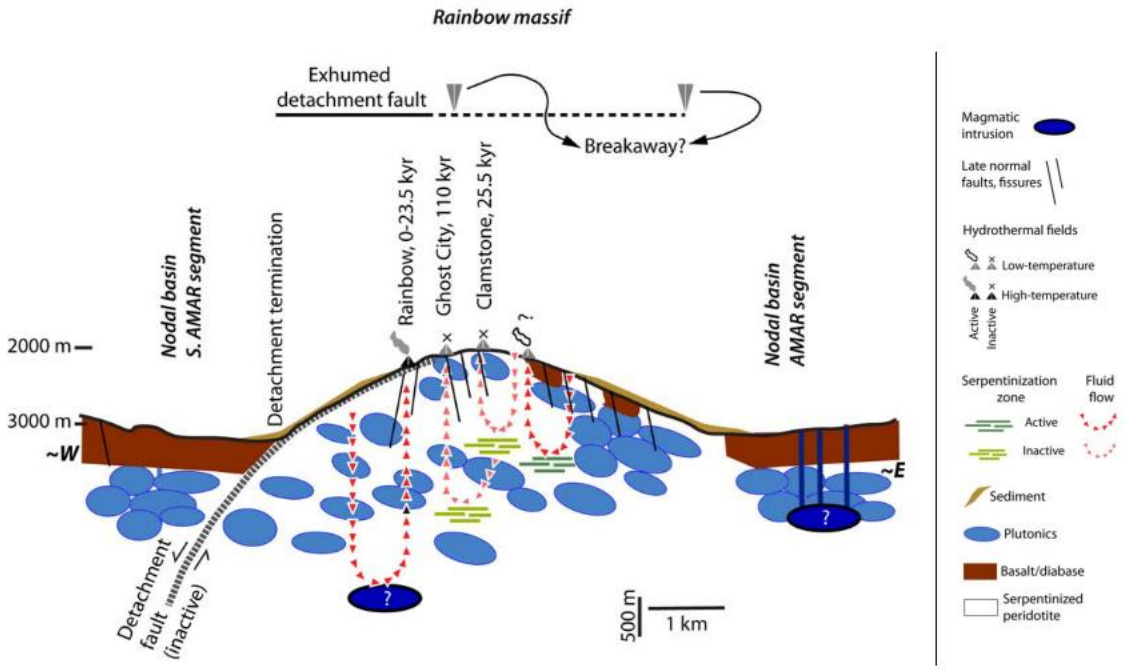

Figure 2.1: Schematic drawing of an E-W cross section of the Rainbow massif summarizing Andreani et al., (2014) along with the proposed interpretation of the structural and hydrothermal observations in the Rainbow massif.

The active field has an extent of ~200-250 x 100 m and is hosted in gabbros and serpentinized peridotites. The depth of the field ranges from the minimum of 2270m to a maximum of 2320m, with 13 registered groups of black smokers on the *InterRidge Database*, most of them showing strong hydrothermal activity (Andreani et al., 2014; Douville et al., 2002; *Rainbow - InterRidge Vents Database Ver. 3.4*, 2020). Figure 7.1(B), later shown in chapter 7.1 provides further clarification of the disposition of some of these groups of black smokers, sampled during the Flores cruise.

At 350-365º C and with a pH of 2.8, the fluids emanating from the Rainbow chimneys have not only the highest temperature measured in the MAR, but also the lowest pH (Douville et al., 2002). These unique fluids have also the highest chloride concentration (750 mM; Douville et al., 2002) and high base metal contents that suggest a more mafic contribution to the ultramafic system, later confirmed by isotopic evidence by Marques et al., (2006) . The same work also advances with the interpretation of the mineral system at depth by sampling the partially exposed stockwork of the Rainbow system, which consisted of mineralized serpentinites, thus providing a relative timeline to the sulfide mineralization events.

Canales et al. (2017) and Konn et al. (2021) later corroborate this view with their seismic data, which infers the presence of a large quantity of magmatic sills, located between 2 and 10 km of depth below the Rainbow massif, explaining the system's high temperatures, that would be unlikely by serpentinization processes alone, as advanced by Marques et al. (2006, 2007) after Lowell & Rona

(2002)'s calculations. Canales et al. (2017) also specifies that the magmatic source has been altered by its interaction with seawater, as concluded after the velocity analysis of seismic waves P-waves crossing the ultramafic heat source.

Thus, it seems that there are two main heat sources at Rainbow: the first being the serpentinization of underlying ultramafic rocks, an exothermic process, and the second being the intruded mafic bodies compatible with magmatic sills.

In summary, at Rainbow, serpentinization has occurred under a low-temperature (<270°C) retrograde regime, later overprinted by a higher temperature sulfide mineralization event fueled by a magmatic heat source (Marques et al., 2006, 2007) following a sequence listed below:

- At <270°C, the temperature at which low temperature retrograde serpentinization occurs, we cannot justify fluids emanating at ~360ºC.
- The sulfide mineralization event occurs after the main low temperature serpentinization event (since it overprints it), which implies separate events for the serpentinization and mineralization.
- The metals leached and later exhumated at the Rainbow chimneys have no correlation with those expected with a purely low temperature retrograde serpentinization event.

An additional point is brought up by Koschinsky (2016), stating that, in order to leach large quantities of Fe and Cu and maintain them in solution, the system must provide not only high temperatures but also high acidity (both conditions present in Rainbow).

In concordance with fields with similar settings, in relation to high temperature and low pH (e.g. Logatchev and Ashadze), the Rainbow fluids show a positive anomaly for Mn, Fe, Co, Ni, Cu, Zn, Au, Ag, Cd, Cs, Pb, Y, and rare earth elements (REE), having the highest recorded trace metals and REE recorded in the MAR. Emphasis can be done on LREE, particularly Eu, as well as transition metals such as Fe, Mn and Cu, that reflect a low pH in-situ, and that combined with the high chlorinity and host rock composition (ultramafic rocks) promote this enrichment (Allen & Seyfried, 2003; Andreani et al., 2014; Douville et al., 2002).

Table 2.1 presents a brief summary of crucial Rainbow characteristics that can be used to single out some of the most important and unique aspects of the Rainbow field.

Table 2.1: Brief summary of the most notable aspects that characterize the Rainbow Hydrothermal Field.

Location	36°13.8′N–33°54.15′W (~550 km south from the Azorean Islands)
Depth (m)	2,270 to 2,320 meters
Area	~200 × 100 m
Main Hydrothermal fluid characteristics	Max T = 365ºC; 2.8 pH; high chlorinity (750 mmol/kg); low silica content (6.9 mmol/kg); high concentrations of hydrogen (H_2: 16 mmol/kg), methane (CH_4: 2.5 mmol/kg), and carbon monoxide (CO: 5 μmol/kg) [significantly higher than other fields along the MAR]. Low H_2S levels (1.20 mmol/kg) compared to basalt-hosted hydrothermal systems, but high H_2 (H_2 > 40% of total gas volume), serpentinization-driven hydrogen production and extensive fluid-rock interactions during the alteration of ultramafic lithologies.
Main geological settings	Located on the MAR at the center of a right-stepping a NTO, between AMAR and S-AMAR ridge segments within an OCC. Hosted by an ultramafic dome composed primarily of serpentinized peridotite, gabbros and mid-ocean ridge basalt.

Vents characteristics	The dominant type of venting consists of black smoker chimneys (at least 10 up to 365°C; metal-rich, primarily Fe, Cu, and Zn, reaching up to 30 meters high). However, white smoker chimneys (less than 250°C; poor in metals, but rich in SiO_2, $CaSO_4$, and Ba) are also present, along with diffuse venting (50–200°C), where hydrothermal fluids slowly seep through cracks in the seafloor. Some areas, apparently with extinct chimneys, characterized by a red ochre color and highly oxidized deposits, are also present. Chimneys are often marked and/or named during research missions some relevant markers close to the chimneys studied in this study include PP28, PP35, PP36, PP37, PP39, PP4 and F5. The chimneys are mostly black smokers, however, there are also white smokers, diffuse venting and inactive chimney zones.
Year and how it was Discovered	1994 - initially identified through seawater anomalies using Conductivity-Temperature-Depth (CTD) analyses (HEAT cruise; (German et al., 1996). 1997 - Submersible Nautile (FLORES cruise; Barriga et al., 1997; Fouquet et al., 1998).
InterRidge Reference	https://vents-data.interridge.org/ventfield/rainbow

Types of edifices in the Rainbow Hydrothermal Field early works (e.g. Bortnikov et al. (2002)) described the four different typologies of hydrothermal edifices found, which were confirmed upon seeing the "SALDANHA" mission footage with aid of the mission reports.

The first type consists of small Fe hydroxides slopes (20-30 cm high), thought to be the resulting alteration of previously sulfide minerals, and deemed ubiquitous in the region.

The second type is described as a set of sole relic vents forming rows between 10 and 15m disposed from east to west, with the highest ranging from 20cm to 2m.

The third type exhibits a significant increase in hydrothermal activity, forming edifices that can reach up to 20m in height, resembling gothic cathedrals, characterized by disproportionately narrow bases (5 to 10m in diameter), formed mainly by chimneys grown and stacked on top of each other.

The fourth and final type seems to be a continuation of the third type´s process. Here, as vents grow longer (up to 40m), they become more unstable and start collapsing (as clearly seen in the dive videos). This collapse widens the base, forming a brecciated basement, on the top and sides of which new vents can form and develop into larger chimneys.

2.3 Similar hydrothermal fields along the MORs

Combining a slow-spreading regime in a hydrothermal field with an ultramafic rock host, results in a field whose conditions swerve away from the basalt hosted standard. As previously mentioned, in section 2.1 (Slow-spreading ridges), the combination of spreading rate and tectonic setting with host rock favors high rock to water ratio (r/w) implying a longer residence period for the fluids, thus making them richer in leached elements and consequentially of greater economic interest.

Comparing the Rainbow with similar fields is an important step. For this comparison, two ultramafic-hosted hydrothermal fields that have been more extensively study in the recent years will be considered: Logatchev at the MAR (slow-spreading ridge) and Tianzuo at Southwest Indian Ridge (SWIR; ultra slow-spreading ridge).

Logatchev is an active ultramafic-hosted hydrothermal system located at 14º45' N, 44°58′W on the MAR, at a depth ranging from 2925 to 3050m. It consists of 5 hydrothermal fields (Logatchev 1 through 5; (Fouquet et al., 2010; *Vent Fields List All - InterRidge Vents Database Ver. 3.4*, 2020)). Although similar to the Rainbow field, Logatchev shows slightly less extreme values in temperature, pH and a lower chlorinity as well as trace elements concentration. These differences are attributed to factors such as, (a) a smaller degree of phase separation at Logatchev, (b) a lesser degree of fluid-ultramafic rock interaction, which in turn, promotes a lower effective ultramafic rock/water ratio, resulting in a weaker ultramafic influence when compared to the Rainbow (Douville et al., 2002; Vent Fields List All - InterRidge Vents Database Ver. 3.4, 2020).

However, both fields show similar mineral assemblage. The most common sulfide minerals in Logatchev samples are pyrrhotite, isocubanite, chalcopyrite and sphalerite (Fouquet et al., 2010).

The Tianzuo field, located at 27°57′ S, 63°32′ E in the SWIR (SouthWest Indian Ridge, a plate boundary between the African and Antarctic plates), is an inactive ultramafic-hosted hydrothermal system, at a depth of 3650m. It has similar geological setting to the Rainbow Hydrothermal field, sitting on top of a dome shaped structure, controlled by a deep-rooted detachment fault. The sulfide mineral assemblage is often subdivided in early high-temperature associations (consisting of isocubanite, pyrrhotine and sphalerite) and late low-temperature associations (comprised of pyrite and covellite; Ding et al., 2021; Tao et al., 2023).

A large table of whole rock geochemistry is presented in **Appendix IV.II**. The greatest takeaway from the data provided in said table is the variance of each element, especially Cu, Fe, Zn and S, which may help further identify trends that can be used to correlate the samples to a mineralization style and to each other. A table with only the Cu, Fe and Zn is also present in Table 2.2 in which these elements are shown in percentage to highlight the overall similarities between the three fields, with the main difference shown being the lack of Zn in the TVG21 samples, and an higher overall Cu content in the analyzed Logatchev samples, furthermore, Rainbow samples show a broader distribution of the elements, which is an indicative of a more even distribution of the minerals.

Table 2.2: Comparison of three major elements in the Rainbow, Logatchev and Tianzuo hydrothermal fields

	Cu	Fe	Zn	reference
Mean Logatchev	41%	45%	14%	Fouquet et al, (2010)
Rainbow (others)	22%	51%	27%	Fouquet et al, (2010)
Average TVG21 samples	13%	87%	0%	Cao et al, (2021)

3. Mineralization styles

The mineralization typology of the Rainbow samples was first described by Bortnikov et al. (2002), who identified three different mineralization styles. These observations are independent to the studied samples and may offer a useful framework for distinguishing and categorizing the samples into three primary, easily distinguishable, groups. Previous works, such as Haymon (1983), also described general concepts regarding the development of a typical black smoker in terms of mineralogy and texture. However, since these are general models, they lack the specific details that arise from Rainbow's unique characteristics.

The three mineralization styles, after Bortnikov et al. (2002) are described as follows:

Copper style: Consists of chimneys that display concentrically zoned fabric and consist of three main layers. The first layer is composed of isocubanite grains with a radial orientation in relation to the center, where the fluid passes through. The second layer is mainly composed of chalcopyrite which is losing Fe and turning into bornite, covellite, and chalcocite (the latter bearing small grains of chalcopyrite, pyrite, and marcasite). This alteration is stronger near cracks that form, also radially, from the outside of the vent inwards and can carry mineral aggregates of such as bornite, chalcopyrite, millerite, pentlandite, and magnetite. A third layer may occur consisting of an association between chalcopyrite and sphalerite or in the case of the copper-anhydrite substyle, anhydrite covering the exterior of the vent.

Pyrrhotite style: This style is characterized by pyrrhotite covering from 10 up to 100% of the samples, with significant variation associated mineral content. Euhedral isocubanite-chalcopyrite aggregates and colloform sphalerite-isocubanite-chalcopyrite are found within pyrrhotite aggregates, in essence, this mineralization style is simply characterized by the presence of Pyrrhotite.

Sphalerite style: This style is nearly composed of monometallic aggregates of sphalerite, which occurs in reniform and dendritic forms with high porosity. Smaller quantities of isocubanite are found in the interior, as well as marcasite near the exterior zones. The exterior of the vents is covered in Fe-hydroxides (which may also be found simultaneously with Fe-oxides within the vents in some cases).

4. Sulfur Isotopes as Geochemical Tracers of Mineralizing Processes

Sulfur, with an atomic weight of 32.06, is the 14th most common element in the Earth's crust. It is found in several different environments, and its presence can be traced through the isotopic composition of the several mineral phases, particularly sulfide minerals (Canfield, 2001; Seal, 2006).

Differences in mineral textures and composition can often highlight system and/or environment differences even within the same minerals. However, slight changes might not be always easily detected, in such cases, sulfur isotopes can help to expose gradual system evolution, undetected otherwise, thus contributing to characterization of the system's evolution.

These variations, caused by fractionation that is sensitive to temperature and oxidation-reduction states are crucial to understand the seafloor hydrothermal systems, revealing fluid sources, pathways, conditions, and various geological processes, including mineral deposits formation, hydrothermal fluids evolution, and biomineralization (Seal, 2006).

Of the five different natural occurring S isotopes ^{32}S, ^{33}S, ^{34}S, ^{35}S, and ^{36}S, all but ^{35}S are stable, and as such only those are considered in stable isotope geochemistry, with their respective abundances of 95.02 %, 0.760 %, 4.22 %, and 0.0136% (VCDT - Vienna Canyon Diablo Troilite, used as a standard in the measurement of sulfur isotopes). In sulfide minerals, the isotope ratio used is $^{34}S/^{32}S$ (the two most common species of sulfur), which is referred as $\delta^{34}S$ and can be calculated as follows (Canfield, 2001):

Equation 4.1: sulfur isotopic composition of a sample against the reference values (VCDT) in ‰ (Canfield, 2001).

$$\delta 34S = \left(\frac{\left(\left(\frac{34S}{32S}\right)\text{sample} - \left(\frac{34S}{32S}\right)\text{reference}\right)}{(34S/32S)reference}\right) \times 1000$$

The ratio of $^{34}S/^{32}S$ is a sensitive indicator for the S sources.

4.1 Sulfur sources (reservoirs):

Seawater: Sulfur occurs as sulfate in seawater with $\delta^{34}S$ values of about +21‰ (Rees et al., 1978). The incorporation of seawater sulfate-derived sulfur, reduced without isotope fractionation, can increase $\delta^{34}S$ values. However, theoretical modeling shows that mixing of hydrothermal fluids with seawater at the seafloor cannot generate $\delta^{34}S$ values of sulfide mineral heavier than +4.5‰ (Janecky, 1988).

MOR igneous rocks: Sulfur associated with igneous rocks derived from the mantle is isotopically similar to that of meteorites, with $\delta^{34}S$ values close to 0‰. The $\delta^{34}S$ value of mid-ocean ridge basalt (MORB) varies within a narrow range of $+0.1 \pm 0.5$‰ (Sakai et al., 1984).

- **Fast Spreading Ridges:** Examples include the EPR 9°–10°N (Rouxel et al., 2008) EPR 21°N (Woodruff & Shanks, 1988), Galapagos Rift (Knott et al., 1995), etc.
- **Slow Spreading Ridges:** Examples include Snake Pit (Kase et al., 1990), Trans-Atlantic Geotraverse (TAG; (Herzig et al., 1998)), Logatchev, Broken Spur and Rainbow (Lein et al., 2001) etc..
- **Ultra-Slow Spreading Ridges:** Examples include Yuhuang (Liao et al., 2018), Duanqiao, Dragon Horn, etc.

Magmatic Degassing: Magmatic sulfur derived from magmatic degassing can have $\delta^{34}S$ values lower than 0‰, as seen in sulfides from the Hine Hina field in the Lau basin (Herzig et al., 1998) or at the

Seven Sisters in the Arctic Mid-Ocean Ridge (Marques et al., 2020). Magmatic degassing and/or bacterial activity can also cause the $\delta^{34}S$ values of sulfides to be lower than 0‰. During fluid–rock interaction, oceanic basement rocks undergo oxidation and reduction processes, leading to variations in sulfur speciation, concentrations, and isotopic compositions.

Mantle Peridotites: Depleted mantle peridotites, resulting from 15–20% melting, generally contain 60–120 ppm total sulfur and have $\delta^{34}S$ values of +0.1 ± 0.5 (Alt & Anderson, 1989; Sakai et al., 1984).

Serpentinized peridotites: Formed when mantle peridotite undergoes serpentinization, a process involving the hydration and transformation of ultramafic rocks. The $\delta^{34}S$ values can vary depending on the extent of interaction with seawater sulfate and the degree of serpentinization. Typically, these values may show some enrichment due to interaction with seawater. High sulfide-sulfur contents, require high fluid fluxes and water–rock ratios. The H2S-rich hydrothermal fluids produced during the hydrothermal alteration of gabbroic rocks at high temperatures (300–400°C) can subsequently react with serpentinites at lower temperatures (~300°C) and precipitate Ni-rich sulfides under reducing conditions, with $\delta^{34}S$ values between 4‰ and 13‰ (Alt & Shanks, 2003).

Biogenic signatures: $\delta^{34}S$ values can be significantly negative, sometimes as low as -30‰, particularly in areas with substantial microbial activity (Canfield, 2001). Variations in $\delta^{34}S$ values are caused by two processes: reduction of sulfate to sulfide by anaerobic bacteria, which increases the $\delta^{34}S$ of the residual sulfate, and various exchange reactions that concentrate $\delta^{34}S$ in the compound with the highest oxidation state of sulfur. Sulfur associated with sedimentary processes generally reflects the composition of biogenic sulfide produced by bacterial reduction of marine sulfate and has negative $\delta^{34}S$ values. Microbial sulfate reduction occurs at low temperatures (up to 110°C) and is typically associated with a large sulfur isotope fractionation of 20‰ to 70‰ (Brunner & Bernasconi, 2005; Goldhaber & Kaplan, 1980).

Igneous Rocks from Island Arcs and Back-Arcs: Island arc magma has higher $\delta^{34}S$ values of up to +21‰ due to the presence of a subduction-related seawater sulfate component in the sub arc mantle source. The $\delta^{34}S$ values of back-arc magma lie between those of MORB and island arc rocks (Alt et al., 1993).

4.2 Rainbow Hydrothermal field and comparable MAR fields case

Previous studies based on the bulk S isotopic composition of separate sulfide phases (not *in situ*) at Rainbow have shown that the $\delta^{34}S$‰ is consistently higher in chalcopyrite compared to sphalerite (Figure 4.1.) Lein et al., (2001). It also shows an interesting correlation between the age of the vents and the observed $\delta^{34}S$‰ values, with the lowest value found in active vents, increasing as the vent gets older (Lein et al., 2001). This suggests that significant environmental changes occurred from the initial formation of the chimneys to their aging, highlighting the evolution of $\delta^{34}S$ ‰, which generally increases in chalcopyrite and sphalerite in older, inactive samples. A summary view of these values is shown in Figure 4.1.

Rainbow black smokers' chimneys typically emanate fluids that not only have high temperatures (between 350º and 365º C), but most importantly, high acidity (with a pH of 2.8). When these fluids contact directly with large volume of cold and unmodified seawater (around 2ºC; pH of 7.8 ; Seward et al., 2014; Toffolo et al., 2020), an instability occurs, leading to shifts in $\delta^{34}S$‰ values towards those of seawater sulfates, whose $\delta^{34}S$‰ values can reach upwards of 21‰, even though sulfides never get to reach said values (Alt & Shanks, 1998; Dubinina et al., 2020). In this situation, the resulting interaction values may lie between the two, depending on the ratio of the interaction.

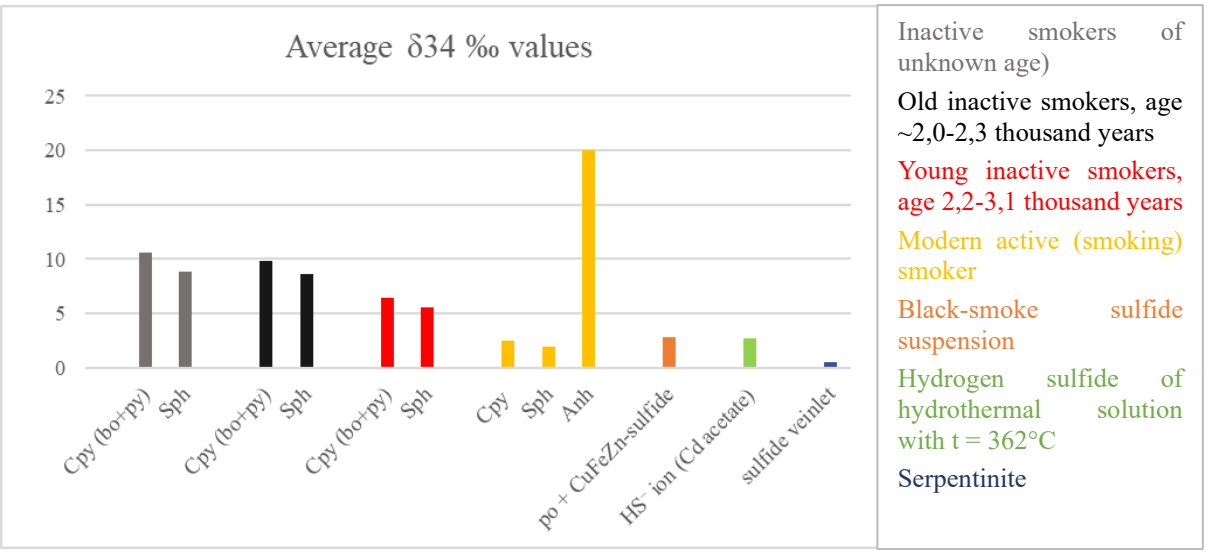

Figure 4.1: Summary of the average bulk δ34 ‰ values of Rainbow sulfide deposits, after Lein et al., (2001).

Another reason lies in the fractioning of sulfur isotopes by sulfate reducing bacteria, which preferentially metabolize ^{32}S, rather than ^{34}S, implying an increase of $\delta^{34}S$ in sulfate minerals over time compared to sulfide minerals, which should have similar values upon their formation. This is further emphasized when considering that seafloor vent sulfides have lower $\Delta^{33}S$ values than biogenic sulfides, which, once again further reinforces how little their contribution towards hydrothermal sulfides is (German & Seyfried, 2013; Seal, 2006).

As such, isotope studies in sulfur (especially in the case of $\delta^{34}S$) reveal themselves as particularly important not only to portray the evolution of the hydrothermal system through different mineral assemblies but also within the same mineral species.

Later works in the Rainbow show the values for $\delta^{34}S$ in sulfides varying between +2.1 to +8.4 ‰, with later sulfides showing relative enrichments when compared to the earlier sulfides (Dubinina et al., Later works in the Rainbow show narrower values for $\delta^{34}S$ in sulfides, varying between +2.1 to +8.4 ‰, with later sulfides showing relative enrichments when compared to the earlier sulfides (Dubinina et al., 2020).

Table 4.1 shows the average $\delta^{34}S$ values of early compared to late sulfide minerals in three different fields of the MAR, with similar characteristics in the case of Logatchev (more precisely, Logatchev-1) and the Rainbow (both active fields with high temperature, low acidity, on slow spreading ridge and ultramafic host-rocks), and Krasnov (inactive field on slow spreading ridge with basaltic host and one of the largest hydrothermal deposit on the MAR [17.4Mt]) (Cherkashov et al., 2008; Fouquet et al., 2008). This table highlights the increasing $\delta^{34}S$ values, seemingly increasing at a predictable rate of roughly +2 ‰ in late sulfides, with the higher values present in the Krasnov field likely as a result of the field's inactivity, which leads to an overall increase in $\delta^{34}S$.

Table 4.1: Average of bulk $\delta^{34}S$ compositional values of early compared to late sulfide minerals in three different fields of the MAR. Adapted from (Dubinina et al., 2020).

Field	Early sulfides			Late sulfides		
	$\delta^{34}S$	±1σ	n	$\delta^{34}S$	±1σ	n
Krasnov	7,7	0,4	7	9,7	0,2	3
Logatchev	4,4	0,3	11	5,5	0,3	12
Rainbow	3,9	1,1	19	5,5	1,2	23

Dubinina et al. (2020) shows that the $\delta^{34}S$ values for early sulfides is 1-2 ‰ lower than for late sulfides, not only for the hydrothermal fields, but also for on-land deposits, thus attributing the variation in $\delta^{34}S$ solely to the fluid evolution: "This suggests that neither composition, nor texture of the minerals are controlling factor during sulfide precipitation from hydrothermal solutions. Independence of sulfur isotope composition on mineralogy and pronounced relation of the $\delta^{34}S$ values to paragenetic sequence assume that the sulfur isotope composition of sulfide minerals is determined only by sulfur isotope characteristics of hydrothermal fluid, which regularly evolve over time".

5. Objectives

This study aims to advance the understanding of the Rainbow hydrothermal field, focusing on the composition and evolution of its chimneys 's and contribute to the overall knowledge of seafloor hydrothermal systems. For this, hydrothermal chimney samples collected from this field were studied as they can provide crucial insights into the origin of the hydrothermal fluids and the dynamics of hydrothermal circulation within systems such as the Rainbow.

Although the Rainbow hydrothermal field has been extensively studied, significant knowledge gaps persist, particularly regarding the evolution of the fluids during chimney formation and the mechanisms driving chimney development. Conventional bulk geochemical analyses are commonly employed to investigate evolutionary processes; however, these methods homogenize fine-scale geochemical signatures and thus do not reflect the mineralogical zoning of the chimney, limiting our understanding of the reaction-transport processes within the walls. Additionally, prior research often considers Rainbow samples as homogeneous entities, focusing on general categories (e.g., chimney, SMS, stockwork, serpentinite), without addressing the specific types of chimneys or their detailed mineralogical composition.

To fill these gaps, and to fully understand the processes governing the chimneys formation and the fluid evolution, this study categorized sample and conducted detailed micro-scale (*in situ)* analyses to investigate the composition and relations of the mineral phases that were deposited by the fluids. This approach provides a solid foundation for interpreting the processes underlying chimney formation and fluid evolution.

This research addresses the following key questions:

- How does the hydrothermal fluid evolve (both over time and distance), and what role does temperature play in transport processes?

- How do chimneys develop over time, including the effect of fluids evolution and interaction with seawater.

6. Methodologies

6.1 Sampling methods and seafloor observations

The Saldanha oceanographic mission occurred in July 1998 with a total of ten dives that took place along the MAR, between the Rainbow and Menez Gwen hydrothermal sites using the manned submersible *Nautile* (IFREMER) on board of the research vessel (RV) *Nadir*. During these dives, various seafloor samples, vent fluids and basement rocks were recovered, as well as and many hours of video images, recorded with the aid of the *Nautile's* cameras. Out of the ten dives, three took place in the Rainbow field (Dives 3, 4 and 5). The chimney samples and video images obtained from these dives were used for this dissertation.

Each sample was referenced with a coding system which includes the mission's name abbreviation (SAL), followed by the respective dive number (XX) and the order (YY) in which they were retrieved (e.g., SAL-XX-YY). Additional descriptors were occasionally appended in the sample name in cases where the same sample shows distinct features. The samples selected for this work are present in Table 6.1.

Table 6.1: Dive number and respective sample references.

Dive Number	Sample Names
Dive 3	SAL-03-03, SAL-03-04, SAL-03-06, SAL-03-08
Dive 4	SAL-04-02
Dive 5	SAL-05-01, SAL-05-03, SAL-05-04, SAL-05-05

Although unable to participate in the oceanographic mission in person, field observation was conducted using video recordings of the dives where the samples were collected, as well as through access to mission reports. This approach provided a comprehensive geological context for the sampling sites. Detailed annotations were made to enhance the understanding of the sample context and description, offering a clear perspective of how the samples were retrieved, and the specific arrangement of the vents and associated geological features.

Although the Saldanha cruise was a multidisciplinary research mission, the observations in this study focused specifically on the site and the areas directly related to the collected samples. Dive observations are summarized in Chapter 7.1, "Characterization and location of the samples".

6.2 Petrographic characterization

For mineralogical and textural examinations, polished sections of selected sample zones were prepared after the samples were dried and consolidated by impregnation with an epoxy resin. Observations were conducted using a Leica DM2700 petrographic microscope under reflected light conditions. Additionally, a Leitz ORTHOPLAN microscope was used in conjunction with a Leica FLEXCAM C1 camera working with LAS-X software to capture the samples under reflected light.

6.3 Bulk geochemistry

For the analysis of bulk geochemical compositions, samples were dried, crushed, and powdered at the Institute of Science and Environment, University of Saint Joseph (ISE, USJ). Major and trace element concentrations, including Rare Earth Elements (REE), were determined at Activation Laboratories, Ltd. (Canada) using the geochemical analytical package 4E–Research.

Major oxides content (SiO_2, Al_2O_3, MnO, MgO, CaO, Na_2O, K_2O, TiO_2, P_2O_5, Fe_2O_3(T) and Fe_2O_3) and some elements such as Ba, Sr, V, Zr were determined through Fusion Inductively Coupled Plasma (FUS-ICP), Total Digestion-Inductively Coupled Plasma (TD-ICP; Cd, Ni, Pb, S)

Trace elements were measured by Instrumental Neutron Activation Analysis (INAA; Au, As, Br, Co, Cr, Hg, Sb, Sc, Se), Multiple Instrumental Neutron Activation Analysis / Thermal Ionization Mass Spectrometry (MULT INAA / TD-ICP; Ag, Zn), Fusion Mass Spectrometry (FUS-MS; Ga, Ge, In, Mo, Sn, U), inductively coupled plasma–mass spectrometry (ICP-MS) and by instrumental neutron activation analysis (INAA). The titration method was employed to determine FeO and obtain the reduced from of Fe (Fe^{2+}), based on the reaction between Fe^{2+} and EDTA (Ethylenediaminetetraacetic acid) and Fusion Sodium Peroxide (FUS-Na2O2) method to determine Cu and Zn concentrations. FUS-MS was also used to determine the Rare Earth Elements (REE; La, Ce, Pr, Nd, Sm, Eu, Gd, Tb, Dy, Ho, Er, Tl, Tm, Yb, Lu) concentrations.

In-house standards and several certified reference materials from the Certified Reference Materials (GBW), Exploration Reference Materials (GXR), Noble-metals-bearing Copper-nickel matte (PTM), USGS Geochemical Reference Material (DNC, SCD, NOD, W-2, DTS, SY, BIR, SGR), OREAS certified reference materials (CRM, MP), Geological Survey of Japan (JGB), and South African Reference materials (SARM) were used. Errors associated with accuracy were ≤4% for major elements and better than 9% for REEs and the most widely used incompatible elements. Duplicate measurements of samples indicated that errors associated with reproducibility were generally lower than 5% for both major and trace elements. Information about detection limits is provided in the Appendix. For detailed information regarding analytical and control procedures, refer to Actlabs (www.actlabs.com).

6.4 Electron probe microanalysis (EPMA)

Chemical compositions of selected minerals phases were conducted on carbon-coated polished thin sections and mounds using a JEOL SUPERPROBETM microprobe, model JXA-8200, equipped with four wavelength-dispersive spectrometers (WDS) at the Instituto Dom Luiz, Faculdade de Ciências da Universidade de Lisboa (IDL-FCUL). Measurements were made with a 20s acquisition time for the peaks and 5s for the background, using an accelerating voltage of 15 kV and a beam current of 25 nA, and an electron beam diameter of 5 μm. The analyses were calibrated using the composition of in-house standard materials, with reproducibility errors being lower than 2% and ordinarily around 1%. A range of natural and synthetic minerals was used as standards, such as sphalerite (S, Zn) and chalcopyrite (Cu, Fe). The standard analytical data was determined based on a series of standardized values for each element, these standards are presented in **Appendix. II.I**.

6.5 Scanning electron microscopy and energy dispersive spectroscopy (SEM/EDS)

Trace elemental analyses and mapping were performed on selected samples to achieve high-resolution imaging with detailed elemental composition and distribution across the chimney walls. Analyses were conducted at the HERCULES laboratory, from the University of Évora. A Hitachi S-3700N (Hitachi

High Technologies, Berlin, Germany) Scanning Electron Microscope coupled with a Bruker XFlash-5010 (Bruker Corp, Billerica, Mass. USA) Silicon Drift Defector (SDD) Energy Dispersive X-ray Spectrometer was used to perform the micro-analysis of the samples. The analysis was carried out under variable pressure, operated with an accelerating voltage of 20 kV and a chamber pressure of 40 Pa. The spectra for the chemical analysis were plotted on an energy scale of 0-20 keV with a spectral resolution of 129 eV at Mn Kα. Data were obtained in the form of elemental distribution maps, point and multipoint analysis processed with Esprit 1.9 software. The SEM images were captured in backscattered (BSE) mode.

6.6 *In-situ* LA–MC–ICP–MS Sulfur (S) isotopic analysis

In-situ sulfur isotopic composition of selected sulfide phases, such as chalcopyrite, isocubanite, sphalerite, bornite and covellite, was determined using laser ablation multiple collector – inductively coupled plasma – mass spectrometry (LA-MC-ICP-MS) on well-characterized polished sections at the at the Institute of Geochemistry, Chinese Academy of Sciences, Guangdong (IGCAS).Coupled with the RESOlution-155 ArF 193-nm excimer laser ablation system, this setup is optimized for direct (*in-situ*) analysis of solid samples, allowing direct sampling by ablating the surface of the minerals. The ablated material is then carried by a gas stream into the MC-ICP-MS, where the ions are analyzed. The instrument was operated in pseudo-medium resolution mode (Millet et al., 2012) to resolve polyatomic interferences from ^{16}O–^{16}O for ^{32}S and ^{16}O–^{18}O for ^{34}S, adjusting the source slit to medium (0.05 mm) in conjunction with using the alpha slit. Sulfide was ablated in a mixture of helium (200 ml/min) and nitrogen (3 ml/min) atmosphere using the following parameters: 20 s baseline time, 40 s ablation time, 40s wash time, 40-60 μm spot size, 5 Hz repetition rate and 2.5 J/cm^2 energy density. Data acquisition followed standard protocols, ensuring high precision and accuracy in isotopic measurements. The use of a pseudo-medium resolution mode allowed for effective separation of polyatomic interferences, crucial for accurate sulfur isotopic analysis. The results were validated through repeated measurements and calibration with known standards, ensuring the reliability of the isotopic data obtained.

All analyses followed standard sample bracketing procedures with the calibrator of a pressed powder tablet (GBW07270) for sphalerite and natural chalcopyrite material (IGSD) for chalcopyrite. The standard deviation for GBW07270 and IGSD were ± 0.16‰ and ± 0.18‰ (2 SD), respectively. The technical specifications of the LA-MC-ICP-MS system used as GIGCA are described in Table 6.2.

Table 6.2: Technical specifications of the LA-MC-ICP-MS (Laser Ablation Multiple Collector - Inductively Coupled Plasma - Mass Spectrometry) system at GIGCA.

LA-MC-ICP-MS at IGCAS		
MC-ICP-MS	**Nu plasma III**	
Forward power	1400	W
Carrier gas (Ar)	0.85	l min^{-1}
Integration time	0.4	s per cycle
Faraday cup configuration	H6–^{34}S; Ax–^{33}S; L5–^{32}S	
Mass resolution	Medium resolution	
Laser ablation	**Resolution-LR-S155**	
Wavelength	193	nm
Pulse length	5–10	ns
Energy density on the sample	2	J cm^{-2}
Pulse frequency	5	Hz
Spot size	60	μm
Carrier gas (He)	200	ml min^{-1}

All of the data was reported relative to $(^{34}S/^{32}S)_{\text{V-CDT}}$ (Vienna Canyon Diablo Troilite standard). The measured $^{34}S/^{32}S$ ratios were convenient to convert as a per mil (‰) variation relative VCDT:

Equation 6.1: sulfur isotopic composition of a sample against the reference values (VCDT) in ‰ (Canfield, 2001).

$$\delta 34S = \left(\frac{\left(\left(\frac{34S}{32S}\right)\text{sample} - \left(\frac{34S}{32S}\right)\text{reference}\right)}{(34S/32S)reference}\right) \times 1000$$

Where:

- $(^{34}S/^{32}S)$ sample is the $^{34}S/^{32}S$ ratio of obtained in the sample
- $(^{34}S/^{32}S)$ reference is the $^{34}S/^{32}S$ ratio for the V-CDT standard = 0.0441626.

δ value indicates how much the sample deviates in terms of sulfur isotopic composition from the standard.

6.7 Statistical analysis

Descriptive statistics was used to measure the average values, dispersion and variation and correlation between the elements in the different samples and in different zones identified in the chimney's walls. The Pearson's correlation coefficient was used to analyze the relationships between variables and Principal Component Analysis (PCA) was conducted to analyze the relationship between the variables and evaluate the factors affecting hydrochemical components. In PCA, the Principal Components (PCs) are expressed as the eigenvectors of the sample covariance matrix and sorted in decreasing order. The elements used were Cu, Fe, Zn, S, Ba, Ca, Pb, Cd, Ag, As, Sb, Ni, Co, Se, Mo, In, Sn, Mn, Sr, U, Ge, Bi, Hg, Tl, Ga, Au and V, with a second dataset corresponding of REE. The enrichment characteristics of elements were described by the histograms of PC eigenvalues, PC biplots, and scatterplots of spot data.

Two approaches were used to analyze the chemical composition of the samples, correlation coefficient matrixes for each of the samples as well as each mineralization style, complemented by Principal Component Analysis (PCA) for both major + minor elements and REE. These multivariate statistical techniques were used to identify patterns and relationships among the samples based on their bulk geochemical compositions, in which the correlation coefficient matrixes provided clarity as to the relation between each element in each sample, while the PCA provided insight into the relations between the elements as a whole.

7. Results

7.1 Characterization and location of the samples

Samples consist of sulfide-rich hydrothermal chimneys that were collected by the *Nautile* submersible during dives conducted as part of the Portuguese-French oceanographic mission "Luiz Saldanha," carried out aboard the R/V *Nadir* in 1998. This mission was conducted under the framework of the MOMAR (Monitoring of the Mid-Atlantic Ridge) project, with the primary objective of investigating hydrothermal activity at depths ranging from 850 m to 2800 m, south of the Azores region. The research focused on studying the physical, chemical, and biological characteristics of several hydrothermal vent sites, including the Menez Gwen site (37°45'N), the Lucky Strike site (37°15'N), and the Rainbow site (36°13.8'N). Moreover, the cruise led to the discovery of a new hydrothermal site, the Saldanha site (36°34'N), further advancing the understanding of hydrothermal activity along the Mid-Atlantic Ridge.

A total of nine chimneys were collected from the Rainbow hydrothermal field during dives 3, 4, and 5

Sample's location and respective coordinates can be found in Figure 7.1 and in Table 7.1.

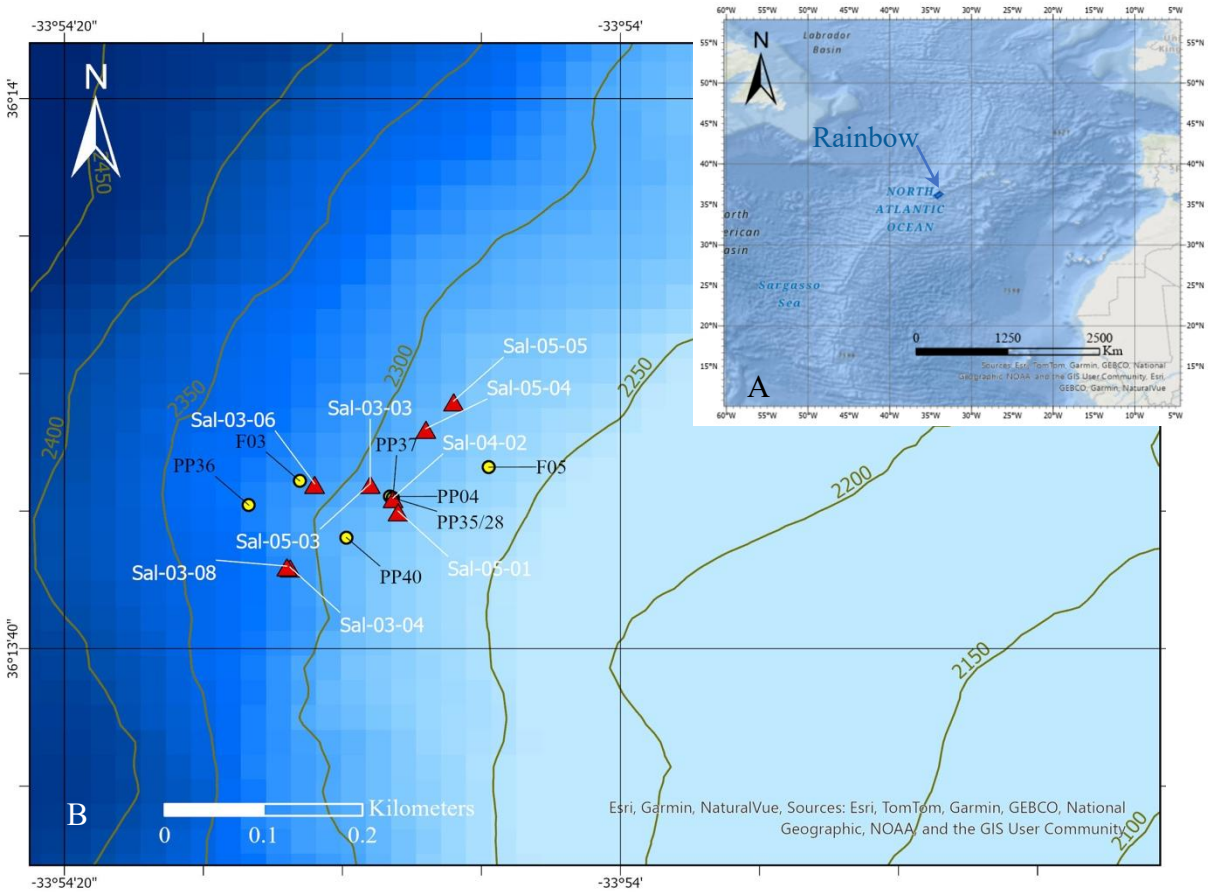

Figure 7.1: (A) Location of the Rainbow hydrothermal field along the MAR. (B) Bathymetric map showing the location of sampling sites, represented by red triangles. Yellow circles indicate markers left by oceanographic missions.

Table 7.1: Samples of chimneys collected at the Rainbow hydrothermal field (including their time/date of retrieval location, depth, as well as nearby markers and brief field remarks, the information was retrieved via the dive reports/recordings).

	Reference	Date and time	Latitude	Longitude	Depth (m)	Markers	Additional remarks
Dive 3	Sal-03-03	16/07/98; 13:34	N 36°13'46"	W 33°54'09"	2335	Near PP39 marker	Well-zoned vent (weakly active /diffuse) located in a very oxidized mound with diffuse flow
	Sal-03-04	16/07/98; 14:18	N 36°13'43"	W 33°54'12"	2360	Close to PP36 and PP40 marker	Chimney with diffuse venting near a fault. Dark, small friable chimneys were observed
	Sal-03-06	16/07/98; 14:58	N 36°13'46"	W 33°54'11"	2311	In the area of the F3 marker	Apparently inactive chimney near an active zone surrounded by serpentinites
	Sal-03-08	16/07/98; 15:26	N 36°13'43"	W 33°54'12"	2305	Close to PP36 and PP40 marker	Active black smoker chimney; T ~355ºC, located in a sulfide mound.
Dive 4	Sal-04-02	17/07/98; 13:07	N 36°13'17"	W 33°53'34"	2299	In the area of the PP35/PP28 marker.	Chimney with weak activity and diffuse venting. Located in a diffuse area of a sulfide mound close to more active zones with black smokers (e.g., Sal-05-01)
Dive 5	Sal-05-01	18/07/98; 10:24	N 36°13'45"	W 33°54'08"	2360	Near PP36 marker	Active back smoker chimney and with a visible concentric zonation
	Sal-05-03	18/07/98; 11:25	N 36°13'46"	W 33°54'09"	2335	In the area of the PP39 marker	Massive fallen chimney, retrieved in the base of a mount of an active black smoker
	Sal-05-04	18/07/98; 12:15	N 36°13'48"	W 33°54'07"	2285	Near PP37 marker	Well-developed chimney with several meters of length and diffuse venting
	Sal-05-05	18/07/98; 14:14	N 36°13'49"	W 33°54'06"	2270	Near F5 marker	Massive sulfide sample from an active chimney from a small black smoker, Nearby fluids was retrieved with a temperature recorded 362ºC

Below is a descriptive summary of the seafloor observations based on the analysis of video footage recorded by the manned submersible *Nautile* and mission Saldanha oceanographic mission' reports.

DIVE 3

During **Dive 3**, the main focus was to set a geological context, providing a comprehensive view of the Rainbow hydrothermal field. Several chimneys' edifices were observed, ranging from vent clusters to isolated edifices, as well as weakly active areas (mostly with diffuse venting and apparently inactive chimneys). Diverse geological samples were collected, including chimneys, basement rocks, and fluids. Chimney edifice samples were taken near the markers PP36, PP39, PP40, and F03. The area where PP40 is located showed the strongest activity. Here, hydrothermal vent fluid samples were collected, and fluid temperatures measured directly in the vent holes recorded 356ºC.

During this dive different samples were collected, including chimneys and basement rocks, along with analysis of the fluids and observations and samples of biological communities near the vents. Observations reveled various degrees of development amongst chimney edifices, ranging from the fluids emanating directly from structural weaknesses (i.e. faults and/or cracks) on the seafloor, to brecciated basements of previous "gothic cathedral"-like structures that had collapsed upon themselves. These collapses formed large and wide structures, showing the different steps of the development of the edifices and the hydrothermal field itself.

Figure 7.2 depicts the herein “gothic cathedral”-like structures, typical in the Rainbow Field, these specific images were taken close to each other during the retrieval of the samples SAL-03-04 and SAL-03-05 (the latter not included in this study) and show diffuse venting. Figure 7.3 highlights the specific location for the retrieval of the sample SAL-03-08, with the main focus on the analyzed plume (~350º), in both cases, the vents were removed from the main structure at the time of the dive (i.e. the vents were broken off the main structure, thus making sure they corresponded to the proper location). During this dive, we were able to observe different colored plumes (ranging from lighter colors up to, as seen in Figure 7.3, pitch black).

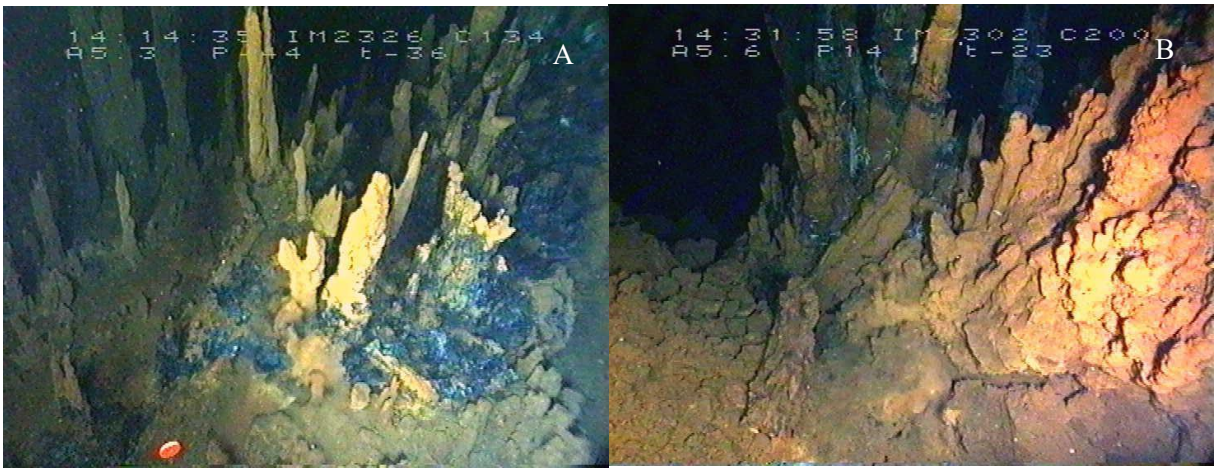

Figure 7.2: "gothic cathedral" like structures where Sal-03-04 (A) and SAL-03-05 (B) were retrieved, respectively. The latter, although not used serves as an example of a well-developed diffuse “gothic cathedral”-like structure, commonly present in the Rainbow hydrothermal field.

Figure 7.3: location of the retrieval of SAL-03-08, showing an active vent.

DIVE 4

The main objective of **Dive** 4 was biological observation, where the interest of the dive was on the different animal species inhabiting near the vents (in this case, mostly fish and shrimp). These animals acted as a biological thermometer as they would only be near active or diffuse vents (i.e. near heat releasing zones). Problems in the recordings of PL04-mobile camera were dully noted in the mission reports, and as such, the attainable information was diminished, however, it was still possible to see both SAL-04-02 samples (part of a chimney) being retrieved during this dive, which happened near to PP35,

in a diffuse venting area of a sulfide mounds where very active black smokers also existed (e.g., Sal-05-01), though the samples were noted as being taken from clusters of weakly active small vents.

DIVE 5

As for the final dive, **Dive 5**, the focus shifted once again to geology, though in this case, with the focus on chimney observation and chimneys retrieval. In this dive we observed not only the top half of the chimney structure being retrieved, but also, the base/foundation upon which it sits. Plume measurements were still conducted (chemical and temperature), mostly in or near the place the respective vents were retrieved, the aforementioned plumes were mostly high temperature, which suggests that this dive was near a more central zone (given the higher heat concentration), when compared to the more fluctuating values we often see in other dives (these temperature values are a great indicator as to what the mineral assemblage might be). Diverse geological samples were collected, including chimneys, basement rocks, and fluids. Chimney edifice samples were taken near the markers PP37 and F5, with the first location also being targeted for biological samples, while the latter being used as a fluid retrieval location, this dive also saw the retrieval of sediments near the F10 marker.

In Figure 7.4 (A) it is observable what once was an active vent, whose activity has now ceased, now not producing heat/releasing chemicals, these relic vent structures are typically characterized by a set of factors, those being (a) a lack of plume, (b) no animals habiting the structure's walls, more specifically, shrimp, that can always be found near large active or diffuse vents, and finally (c) fossilized mussels near the bottom of the structure. Meanwhile in Figure 7.4 (B) a simpler structure is shown, releasing the large plume, a small vent can be observed, this vent's plume temperature and chemical composition were measured, which was followed by the retrieval of sample SAL-05-05.

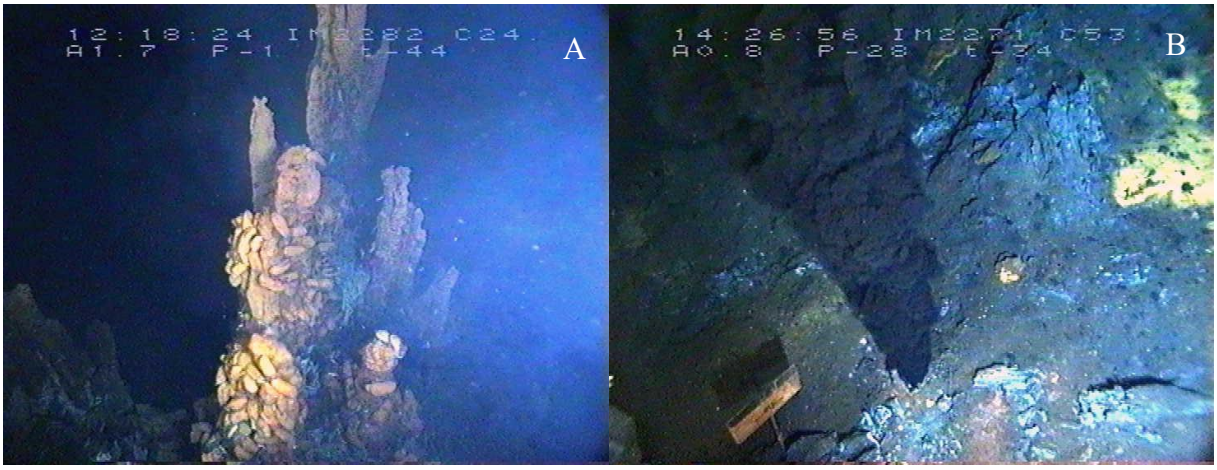

Figure 7.4: Large apparently inactive vent (A) and vigorous active vent (B),where SAL-05-05 was collected.

7.2 Bulk geochemistry

Bulk geochemistry analysis was conducted to attain a general overview of the compositional variations among the analyzed samples. Elementary concentrations can be consulted in the in **APPENDIX IV**. After analyzing the oxide compositions, those were converted into single-element concentration, and all values were standardized to parts per million (ppm). To improve the interpretability of the results, a series of geochemical graphs and tables were created along with comparative analyses incorporation published data from other samples collected also at Rainbow (Fouquet et al., 2010), as well as from other sites with similar characteristics, such as the ones from Logatchev 1 and 2 (Bogdanov et al., 1995;

Fouquet et al., 2010; Krasnov et al., 1995; Mozgova et al., 1999), as well as Tianzuo (Cao et al., 2021), which can be found in **APPENDIX IV**.

In order to further analyze the system's behavior, compositional ratios were also plotted in figure 7.5, which include Ba/Co and Cu/Zn. The Ba/Co ratio of the deposits is indicative of different geological settings, in which an enrichment of Co is typical for ultramafic-hosted deposits, where values near and below 0,1 are strong indicators of ultramafic origin (as per the observations in Sánchez-Mora et al., 2022), with the only value with a ratio above 1 corresponding to the oxide layer of a sample, which further confirms that these samples show strong ultramafic influence. Furthermore, as ultramafic-hosted systems are Cu-enriched, the higher the Cu/Zn ratios, the higher the temperature of the sulfides is presumed, with higher Zn values corresponding to lower temperature associations (in this case, an indicative of Sph-style mineralization), therefore, results show a tendency towards higher Cu contents, with Zn values highlighted only for SAL-03-03 and SAL-03-04 (the two values leaning towards lesser values).

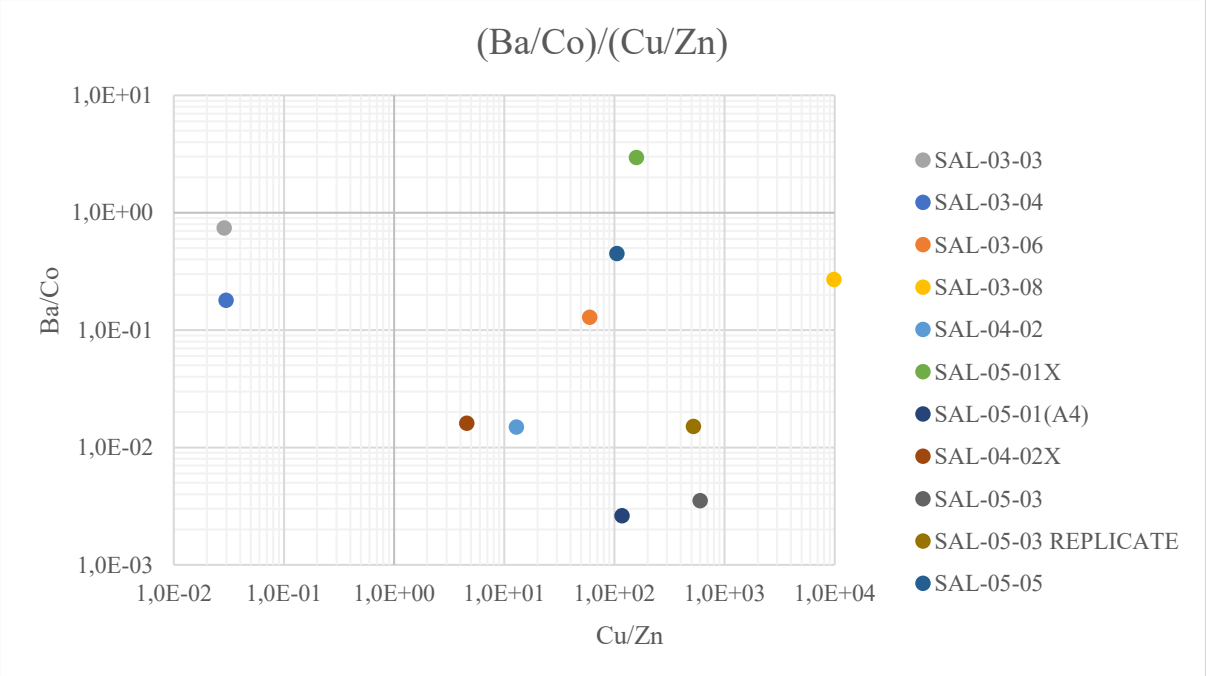

Figure 7.5: Ba/Co and Cu/Zn in the SAL samples

REE were also analyzed, the values were normalized to primitive mantle values proposed by McDonough and Sun (1995). Normalized patterns can be seen in the Figure 7.6 and Eu, Ce anomalies as well ratios between LREE and HREE can be consulted in the Appendix IV.V. Accordingly, the results show the expected Eu anomaly in all samples but SAL-03-04 and SAL-04-02, whose values sit significantly below the remaining, meanwhile Ce values are consistent with the other LREE, while the values might be expected to drop lower. The most surprising values come from SAL-05-01X, where values corresponding to REE, in particular for HREE, are shown to be significantly above the remaining samples (worth referring that since the graph is plotted on a logarithmic scale, the values in some cases are consistently 10x those of the second largest sample, with Tm in particular 5800x above the remaining values, though in this instance is likely due to an error in the analysis).

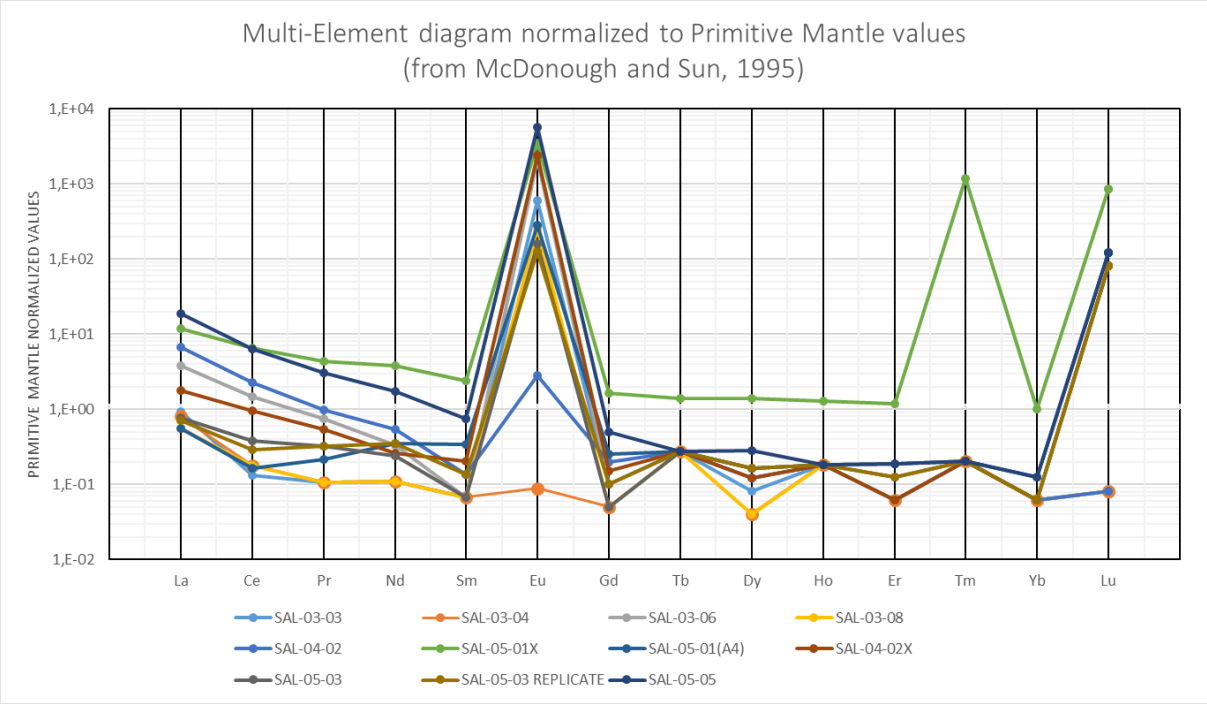

Figure 7.6: Multi-Element diagram of the REE in SAL samples, normalized to Primitive Mantle values (from McDonough and Sun, 1995)

The geochemical data from Rainbow, along with comparable datasets from Logatchev 1, 2 and Tianzuo provide valuable insights into the geochemical variability of the Rainbow field, particularly within the samples analyzed in of this study. As described in the previous chapter 3 Mineralization styles, each sample can be assigned a distinct mineralization style based on the sample description, as such, the geochemical composition of each analysis should serve as an additional indicator as to what mineralization style the sample should belong to, by confirming the previous assumed style.

Figure 7.7 shows the percentual variation between Cu, Fe and Zn. By observing this relation in the SAL samples, three distinct datasets can be seen, the first two samples corresponding to an overwhelming abundance of Zn compared to the two remaining elements and a second batch of samples (n=9) where Zn is negligible and Cu presence is important, in which sample SAL-04-02X is mostly comprised of Fe, which is to be expected since the X serves as an indication that this is an analysis taken on the outer Fe oxide layer. So, excluding the later oxidized sample, it is possible, in conjunction with the predetermined mineralization styles for each sample, to determine that the first two samples (i.e. high Zn content) likely correspond to the sphalerite-rich typology with the Sph-style, while the second group of samples (negligible Zn and considerable amounts of Cu) correspond to copper-rich domains. However, samples to the Cu-style. Samples from the same styles still show geochemical differences, likely due to mineralogical heterogeneities within individual samples.

Furthermore, even though in both hand samples and thin section a singular mineralization style can be attributed to the samples, some samples such as SAL-04-02(1) and SAL-04-02(2) may display different mineral associations and thus different mineralization styles, even though both were retrieved at the same time, as part of SAL-04-02. This fact introduces unexpected variances since for whole rock analysis this set of samples is analyzed as one, therefore, the results may be different than expected if a single thin section was analyzed and so, it is not recommended to base the mineralization styles based on bulk geochemistry, but rather petrographic observation, which reinforces the importance of careful mineralogical studies.

The data from the remaining comparable fields is relevant to compare, as it shows that for Rainbow 1 (n=116), the likely explanation was an heterogenetic mixture of samples from both mineralization styles, which resulted in balanced ratios of Zn and Cu, while Rainbow 2 is much closer to what is seen for SAL-04-02X, and therefore likely an iron crust. Logatchev follows the same patterns as Rainbow 1, with the samples from the field Logatchev 1 showing low Zn contents and thus likely an higher temperature associated to the mineralization process, with the samples from the field Logatchev 2 as the opposite, showing considerable Zn and therefore a lower temperature and presence of sphalerite within the sulfides. The Tianzuo field shows low Cu content and no Zn, this however is to be expected as the main sulfide present in this field is pyrite (FeS_2) unlike the Rainbow and Logatchev 1 and 2 where both chalcopyrite and sphalerite are the more common sulfides. Finally, the ratios are also compared to those of average whole rock values for MORB's, however the large difference in proportions vs other minerals makes the comparison unjustified. Table 7.2 provides depth and temperature for the three fields in comparison.

Table 7.2: Table highlighting depth and temperature for the three fields in comparison

Field	Depth	Temperature	Reference
Logatchev	2900m to 3060m	350 °C	N. Augustin (2008)
Tianzuo	3666 m	335 ◦C	H. Cao et al. (2021)
Rainbow	2270 to 2370 m	365°C	Lein et al. (2001)

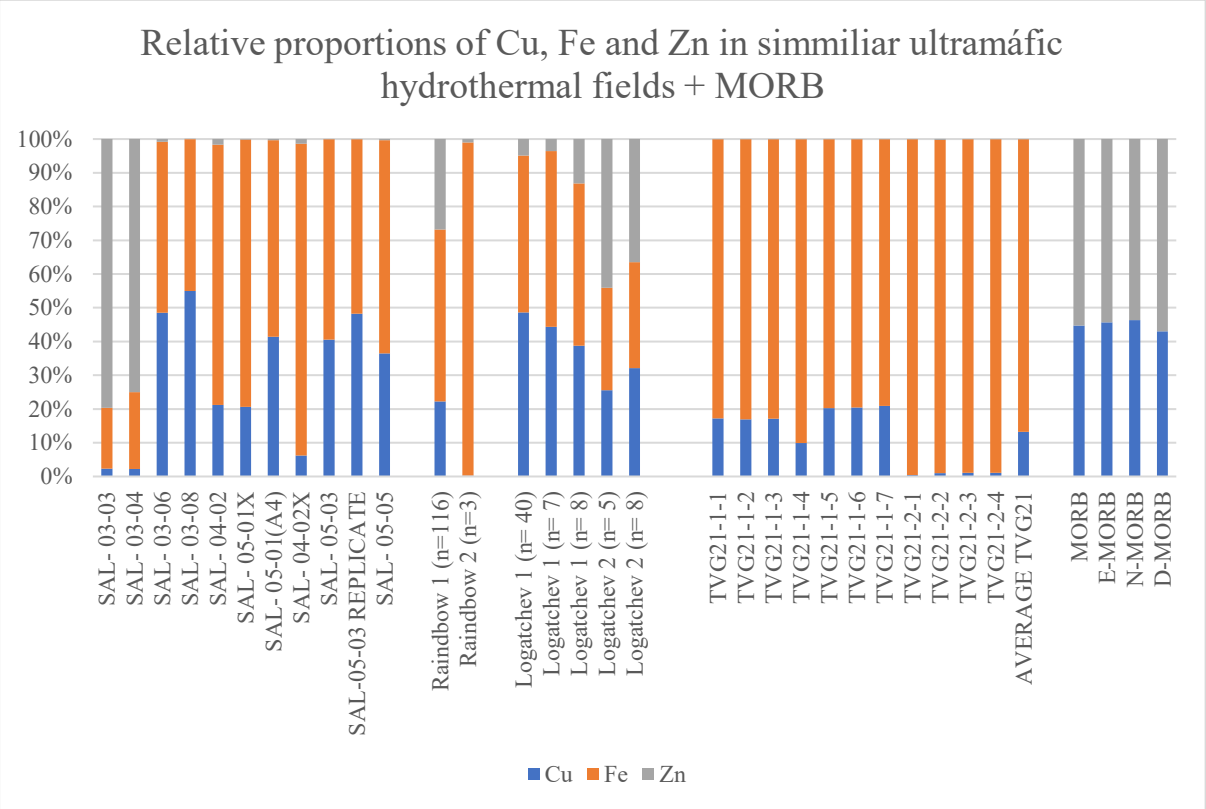

Figure 7.7: Relative proportions of Cu, Fe and Zn for the SAL samples and those of comparative fields, with other Rainbow analysis included, as well as several types of MORB's.

As and Sb, as well as their ratio, also provide important clues to the understanding of what are the dominant processes happening in the seafloor, that affect the vents after their precipitation and a series of information can be inferred from both As rich, as well as Sb rich compositions. Both elements can occur associated to efficient leaching of the host rock, however, high Sb can be associated with the brine phase (as indicated by high chlorine values, to which they often associate), while As with the vapor phase. From the two, Sb is also the more mobile element via post depositional oxidation, which justifies the usage of this ratio, as an high As/Sb ratio can be interpreted as strong water interaction/reworking of the samples (in oxidating environments), therefore, two main factors come into play when analyzing this ratio, those being the phase separation and post depositional oxidation processes (Douvillearb et al., 1998; Fu et al., 2016; Lafay et al., 2016). Figure 7.8 shows these ratios as well as single element presence, with Tianzuo's Sb values notoriously low, which is also to be expected as it consists of an inactive field, where oxidation processes are likely to have leached most of the Sb. The ratios in the Rainbow show a proportionally small variation of As (apart from a single sample, SAL-05-05) when compared to Sb, which may suggest that the greatest influence in this ratio might be the seawater interaction and subsequent reworking and/or oxidation associated processes that may occur.

Overall, the conclusions drawn from whole rock analyses should be limited since their content (including mineralization style) may vary within the same sample (although that cannot be seen in the petrographic samples), resulting from the recovery of the sample often including multiple chimneys, some of which may have not been *in situ* or that may be of different ages and therefore have different compositions, therefore possibly altering the values that should be expected if a sample comprised of a singular mineralization style.

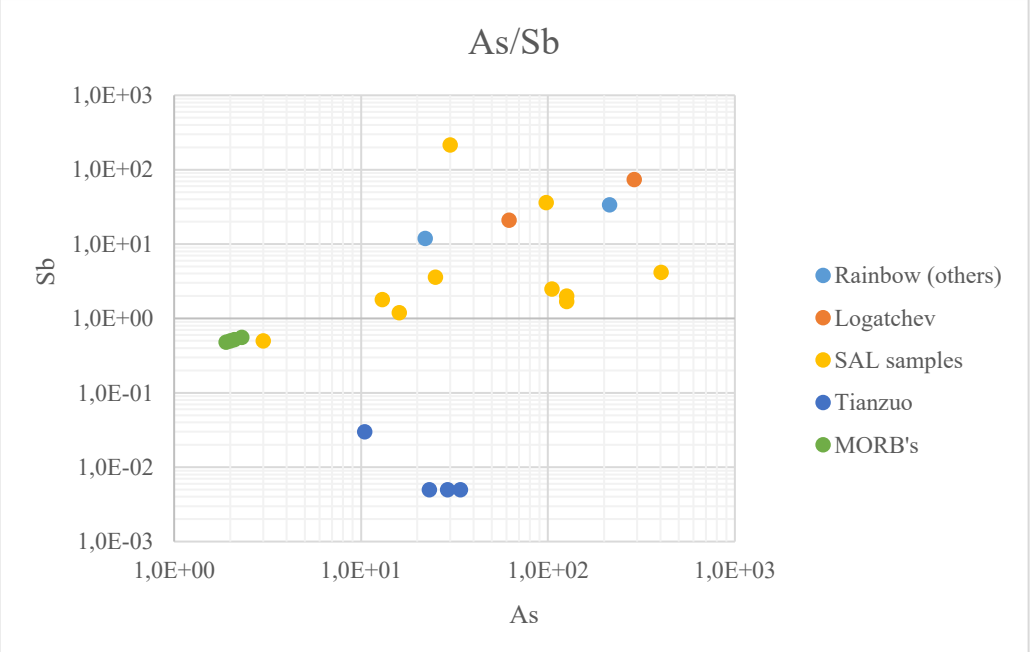

Figure 7.8: As/Sb ratios for Logatchev, Tianzou, Rainbow (this study and others) and MORB's for reference.

7.3 Petrographic and Mineralogical composition

The characterization of the samples was based on petrographic observations, mineral chemistry data, and SEM/EDS analyses.

Some of the samples mentioned were divided into sets of two subsamples (e.g. SAL-03-06(1) and SAL-03-06(2)). The reasoning being either mineral zonation (samples SAL-03-06 and SAL-04-02), or simply due to the sample being too large (samples SAL-05-05) and/or frail (samples SAL-05-01) to be analyzed as one. **Appendix II.II** contains every single EPMA analysis conducted for each sample, presented by element percentage and with the chemical formula of each mineral, presented with S as base, converting the values based on the molar mass of each element.

SAL-03-03 [Sph-style]

The sample SAL 03-03 shows two distinct zones, primarily differentiated by their textural characteristics, as illustrated in Figure 7.9.

The first zone is characterized by cyclic, parallel layers, with each layer showing mineralogical variations between its outer and inner sections. The outer part of each layer is enriched in unaltered sphalerite, with dendritic and oxidized sphalerite gradually replacing it in the inner part of each layer. This pattern repeats itself and is observed across four cyclic layers.

The second zone displays a more disorganized texture in which both sphalerite and the remaining minerals (isocubanite and covellite) are evenly distributed, lacking preferential orientation or spatial arrangement. This results in a uniform mineralogical distribution throughout this zone.

In both zones, isocubanite exsolutions occur within the sphalerite, often forming isocubanite rings or half-ring structures, later shown for the remaining Sph-style samples (e.g. Figure 7.17(A)). Additionally, rare grains of covellite can be found. When sphalerite is in contact with dendritic oxidized sphalerite, the isocubanite exsolutions adopt a semi-circular morphology. Within these exsolutions structures, a distinct iron-rich sphalerite variety can be observed (as verified by the EPMA analysis, presented in **APPENDIX II**.A).

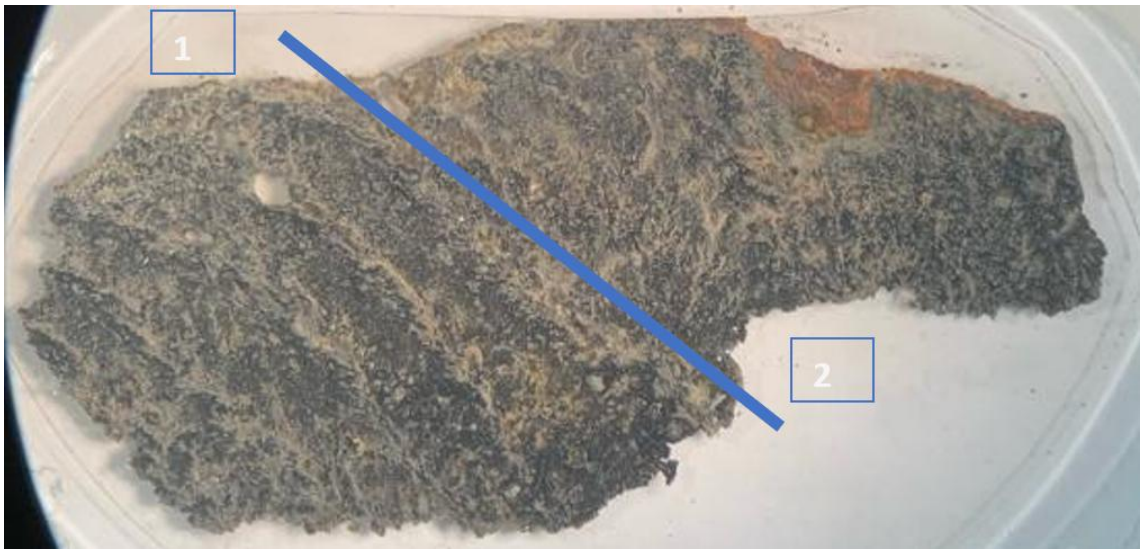

Figure 7.9: Sample SAL-03-03, highlighting the two zones within the sample.

SAL-03-04 [Po-style]

The SAL-03-04 sample is mostly composed of large, tabular pyrrhotite and sphalerite grains, both displaying size variation and occurring ubiquitous throughout the sample, with scattered magnetite. Isocubanite is also commonly present, often occurring in contact with pyrrhotite and sphalerite.

The sample presents high porosity, with euhedral and well-developed mineral grains near the edges of the vent orifice, as shown in Figure 7.10. In contrast, towards the interior of the vent, the porosity decreases, and mineral aggregates occur, composed of varying proportions of pyrrhotite, isocubanite, and sphalerite. Rare sulfates (likely anhydrite) are also observed within the sample.

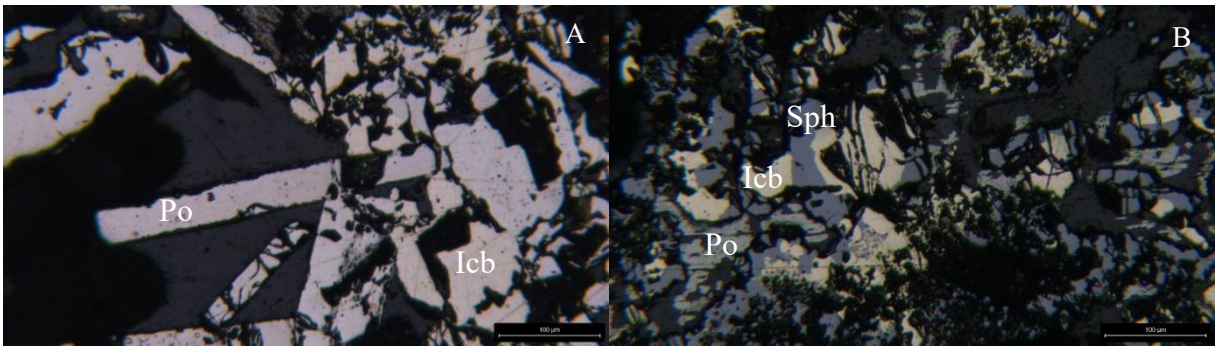

Figure 7.10: Photomicrographs of sample SAL-03-04, showcasing the mineral assemblage, composed of mostly pyrrhotite (Po) as well as isocubanite (Icb) and sphalerite (Sph), in the areas where large euhedral minerals (mostly of pyrrhotite) were able to form (A), as well as the inner zone of the vent where crystals of mostly isocubanite and sphalerite grow in confined spaces and therefore form anhedral crystals alongside anhedral pyrrhotite (B).

SAL-03-06 [both Cu-style (Type-III and -I, respectively)]

Two polished sections were prepared for this sample and labeled as (1) and (2) based on their distinct textural characteristics; section (1), in contrast to section (2) does not exhibit concentric zonation. Figure 7.11 shows the main textual differences in the two subsamples, with each specific samples described below.

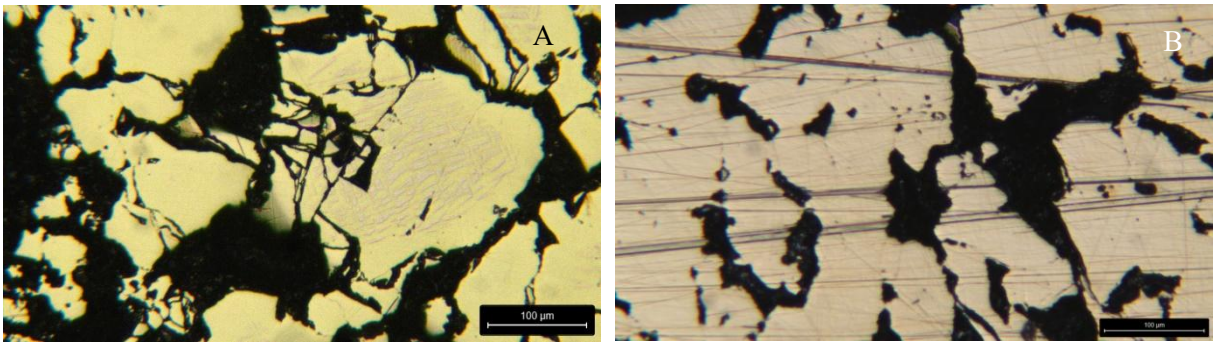

Figure 7.11: Photomicrographs of both sample SAL-03-06(1) (A) and SAL-03-06(2) (B) highlighting textural differences as well as the presence of isocubanite (lighter yellow) within the chalcopyrite (darker yellow) in the sample SAL-03-06(1) (A/B).

The **SAL-03-06 (1)** subsample is composed exclusively of chalcopyrite and isocubanite, with a mineral assemblage similar to SAL 03-06(2). However, the key mineralogical difference is the presence of isocubanite and the absence of sphalerite in SAL-03-06 (1).

Reflected light microscopy revealed that some of the chalcopyrite grains, particularly near the inner zones of the sample, contain internal exsolution structures of isocubanite within the chalcopyrite (e.g. Figure 7.11(A)).

Additionally, this subsample depicts extensive oxidation, especially in the inner zones, which is particularly noticeable in hand sample, which suggests a lower stability of the mineral assemblage, a hypothesis further supported by the presence of internal structures within the larger grains of chalcopyrite.

The **SAL-03-06 (2)** subsample forms a concentric structure and is relatively uniform, consisting of over 90% of the chalcopyrite and it can be divided into four macroscopic layers:

The first three layers are mineralogically identical, composed entirely of chalcopyrite, with only slight textural variations, with the main difference between layers being their porosity, which is generally low, as expected given that this subsample was located in the main discharge point for the vent fluid, one of said layers is presented in Figure 7.11B.

The outermost layer, on the other hand, is composed of sphalerite, possibly wurtzite due to its high Fe content (that combined with Cu represented between 6,1 to 11% of the mineral), intergrown within the chalcopyrite. Textural relationships suggest that chalcopyrite crystallized before sphalerite as sphalerite's presence is greater in alteration prone zones (i.e. around grain borders and holes within the larger grains). The sphalerite shows varying content in both Zn, Fe and Cu, with the latter two inversely proportional to the first as shown in Figure 7.12.

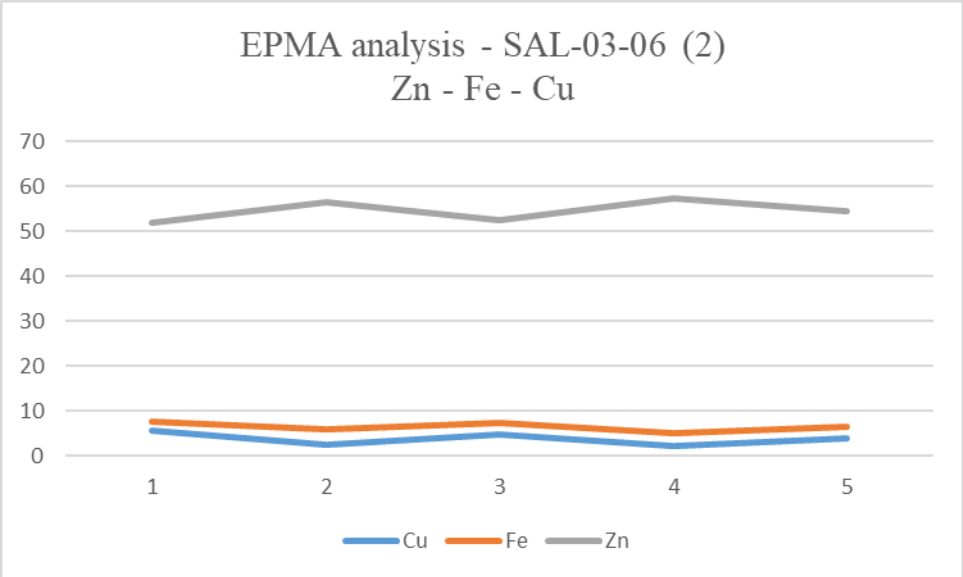

Figure 7.12: EPMA analysis showcasing the variance between Zn - Fe - Cu in sphalerite grains in sample SAL-03-06(2).

SAL-03-08 [Cu-style (Type-I)]

This samples corresponded to a well zoned black smoker chimney wall (T355ºC).

It can be divided in three different zones that vary both their mineralogic and textural content, the core zone, that corresponds to ~80-85% of the sample, is composed exclusively of chalcopyrite.

A middle layer (~12-15% of the sample) is composed of an array of Cu-rich minerals. These minerals are, respectively, chalcopyrite (that is being consumed), digenite, bornite, chalcocite, and pinkish gray chalcocite (intermediate composition between bornite and chalcocite), while also having rare marcasite grains in contact with the final layer.

The outer layer, in contrast to the remaining two, consists of oxides (e.g., magnetite), sulfates, covellite as well as some chalcopyrite and digenite relics.

There is a clear transition from the chalcopyrite to bornite/pinkish gray chalcocite (occurring only in the grain borders and occasionally near the borders) into chalcocite and finally digenite, shown in Figure 7.13, this transition can be seen in areas of the sample where, presumably, there was at some point contact with seawater.

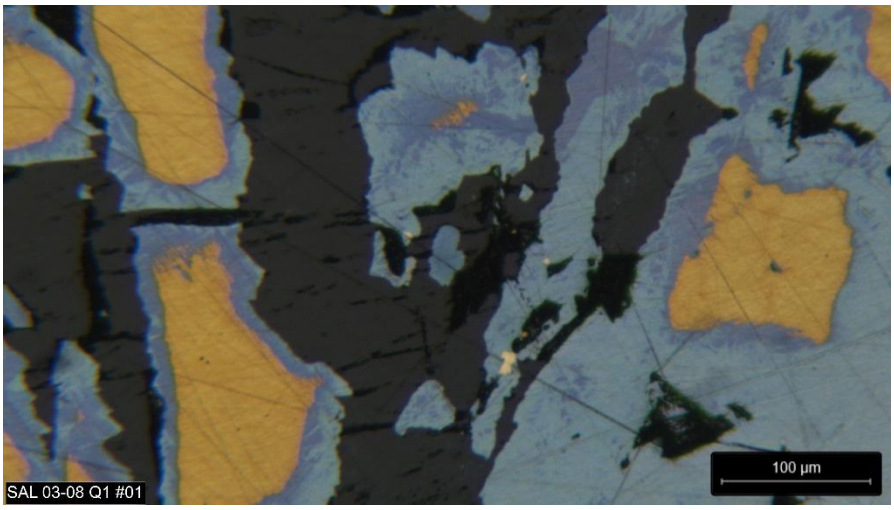

Figure 7.13: Photomicrograph of sample SAL-03-08 showcasing the transition from chalcopyrite to Cu-rich sulfides.

SAL-04-02 [Cu-(Type-III) and Sph-style, respectively]

Two polished sections were prepared for this sample and labeled as (1) and (2) based on their distinct mineralization styles, section (1) belongs to the Cu-style (Type-II), while section (2) belongs to the Sph-style, which means that both mineralogy and texturally the samples show close to no resemblance to each other. Figure 7.14 shows a clear distinction between the two samples and their respective mineralization styles.

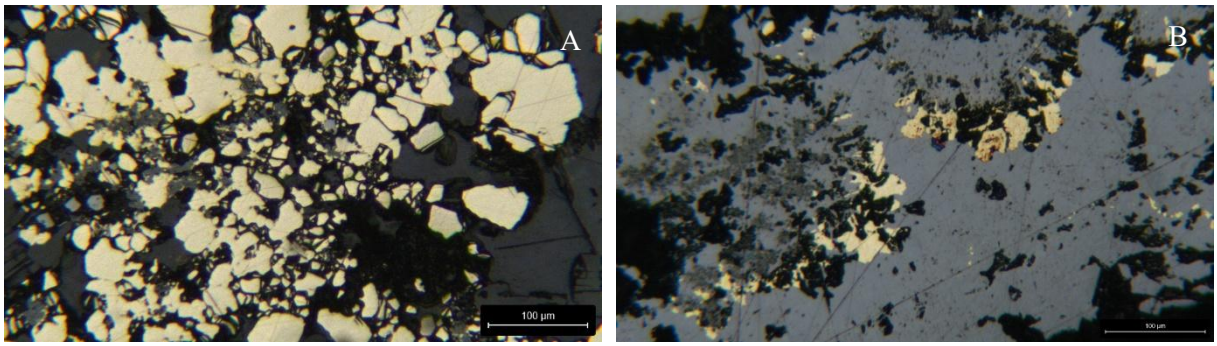

Figure 7.14: Photomicrographs of samples SAL-04-02(1) (A) and SAL-04-02(2) (B), showing the different mineralization styles that characterize both samples.

The **SAL-04-02(1)** subsample is mostly composed of chalcopyrite, which, in rare cases may present isocubanite exsolutions within sulfate matrix (despite the presence of sulfates, chalcopyrite remains the dominant mineral). Aside from these minerals, the sample also presents minor amounts of sphalerite and covellite.

This sample has no direct comparison amongst the other samples (not even the other SAL-04-02 sample (2) as both fall under different mineralization styles) since the presence of isocubanite is so scarce unlike the remaining Cu-style (Type-III) subsamples, making it almost a transition (i.e. the last stage) to Type-I, while at the same time having no unique features.

The **SAL-04-02(2)** subsample is mainly composed of "spotless" (i.e. with little to no impurities) sphalerite (from this point forwards, referred to as Sph-I). Within Sph-I, isocubanite rings are scattered throughout the sample, surrounding a different generation of sphalerite (which from this point forwards shall be referred to as Sph-II). Rare covellite aggregates might also be found near these isocubanite rings. A series of dendritic elongated structures (which were determined by microprobe analysis to be formed as a result of oxidation of sphalerite, that shall be referred to as simply oxidized sphalerite) can also be found, predominantly parallel to each other.

As for the texture, it is similar to what can be found in the second zone of the sample SAL 03-03, where the disposition of the minerals is mostly unorganized, and with no set distribution, possibly due to the large number of small holes, whether those be filled with Sph-II or empty, where fluid would pass.

SAL-05-01 [Cu-style (Type-III)]

Two polished sections were prepared for this sample and labeled as (1) and (2) simply due to the frailty of this sample, which was divided into the two sides of a venting channel as the sample broke in half due to the vibrations associated with the process of sample preparation, both samples, however, can be seen as one.

Due to the nature of the sample, both SAL 05-01(1) and SAL 05-01(2) are difficult to analyze with a microscope, as the samples were prone to also crumble during their preparation, thus leaving a large number of orifices, and a mostly uneven surface to work with, as shown in Figure 7.15.

Regardless, in this sample, some preserved, varying sized grains of chalcopyrite can be seen.

Especially noticeable in the larger grains of chalcopyrite (even though it occurs in the vast majority of them) is the presence of internal structures (i.e. relic minerals) composed of isocubanite, forming exsolution patterns, similar to what's been described for SAL-03-06(1).

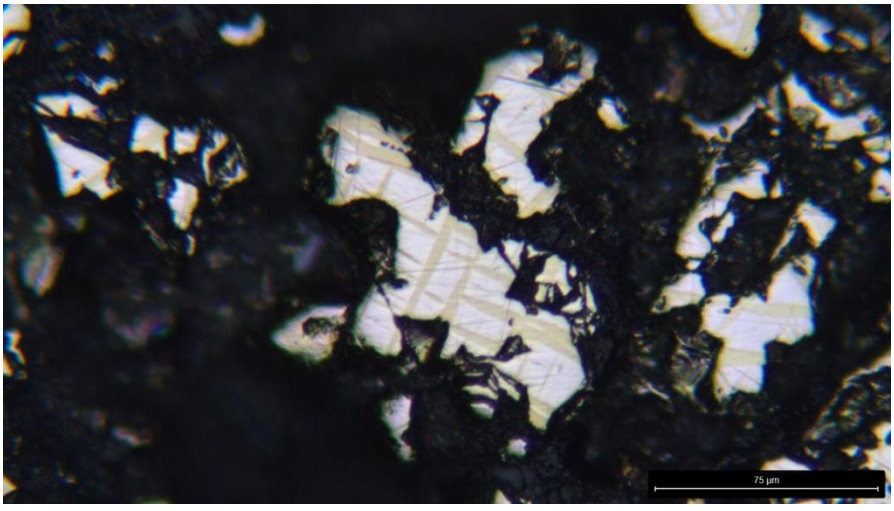

Figure 7.15: Photomicrograph of the sample SAL-05-01, highlighting the large orifices, and uneven surface of the sample. The image also, importantly, highlights the exsolution processes occurring in the sample, where isocubanite is being transformed into chalcopyrite.

SAL-05-03 [Cu-style (Type-III)]

This sample is composed by massive isocubanite grains that is often being replaced by covellite in the grain borders, shown in Figure 7.16.

Rare chalcopyrite is also seen around the borders of the sample, as well as various oxides and sulphates, with the main body of the vent being only composed of isocubanite and covellite.

Different thin sections for this very sample showcase small native gold grains, though after thorough examination none were found in this thin-section.

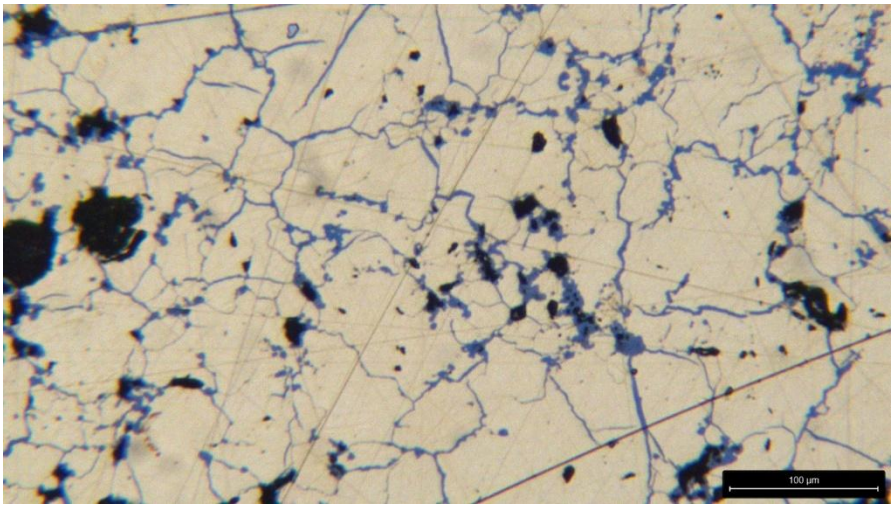

Figure 7.16: Photomicrograph of the sample SAL-05-03, showing the covellite replacement in the isocubanite grain borders.

SAL-05-04 [Sph- and Cu-style (Type-II), respectively]

Two polished sections were prepared for this sample and labeled as (1) and (2) based on their distinct mineralization styles, along with that implies; section (1) belongs to the Sph-style, while section (2) belongs to the Cu-style (Type-II), which means that both mineralogy and texturally the samples show close to no resemblance to each other. Figure 7.17 shows a clear distinction between the two samples and respective mineralization styles.

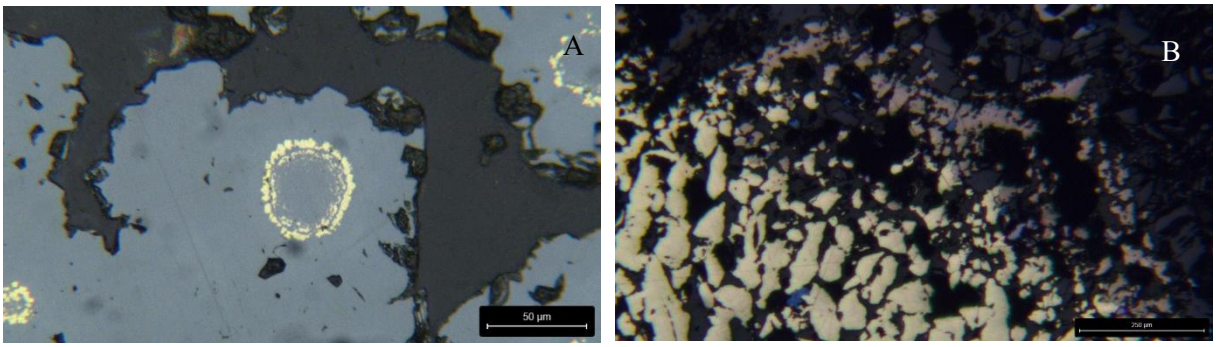

Figure 7.17: Photomicrographs of samples SAL-05-04(1) (A) and SAL-05-04(2) (B), showing the different mineralization styles that characterize both samples. The sample SAL-05-04(1) (A), [Sph- style] dominated by sphalerite and SAL-05-04(2) (B) [Cu-style (Type-II)]dominated by Cu-rich sulfides.

The **SAL-05-04(1)** subsample is mostly composed of colloform oxidized sphalerite as well as Sph-I, with some grains containing intergrowth bands varying between isocubanite and Sph-II throughout repeated layers. Said tendency occurs most frequently in well-developed clusters, where the vents were filled with isocubanite in the outer zone and sphalerite in the interior (in some cases occurring cyclically), thus forming late depositions in previously circulating channels, as shown in Figure 7.17 (A).

The **SAL-05-04(2)** subsample is mostly composed of sulphates, with the sulfide minerals forming concentrical dispositions that consist mostly of chalcopyrite.

In the most inner/recent ring it's observable a transition of chalcopyrite into bornite. It can also be seen throughout the chalcopyrite some scattered grains of covellite and magnetite, usually associated with each other and near the borders of these rings, as demonstrated in Figure 7.17 (B).

The chalcopyrite in the outer rings presents coarse grains and forms clusters of these small crystals, in this case, both indicators of weathering in those grains via alteration and/or evolution of the system and its conditions.

SAL-05-05 [Cu-style (Type-II)]

Two polished sections were prepared for this sample and labeled as (1) and (2), with both sections intersecting the same plain of the vent at slightly different heights (i.e. one of the subsamples is 2-3 cm above the other, both acquired from the same structure).

Thus, the subsamples **SAL 05-05(1)** and **SAL 05-05(2)** are identical, both showing a small quantity of sulfide minerals, when compared with sulfates in the sample.

The main sulfide in the sample is chalcopyrite, which seems to be formed in different generations (with different degrees of physical weathering) and has its deposition confined to the previous and current borders of the sample, where fluid would presumably pass through and thus leaving these depositions of sulfides. These different generations of chalcopyrite are often disposed parallel to each other, separated by the large sulfate matrix.

The only small difference between the samples is the presence of Bornite, Pinkishgray chalcocite, chalcocite, digenite and covellite, as well as magnetite in the outer zone of a single, well developed, chalcopyrite ring in the sample SAL 05-05(2), a close up of that ring is presented in the photomicrograph in Figure 7.18 (A), shown in comparison to a larger chalcopyrite ring in Figure 7.18 (B).

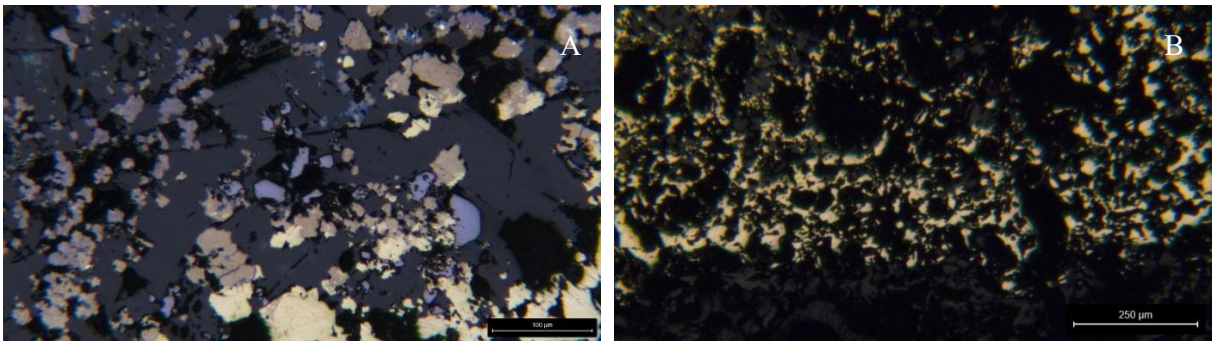

Figure 7.18: Photomicrographs of samples SAL-05-05(2) (A) and SAL-05-05(1) (B), showing chalcopyrite rings at different scales, where in (A) the chalcopyrite ring shows a transition to other Cu-rich sulfides and in (B) an early large chalcopyrite ring that has seemingly suffered significant physical alteration.

Table 7.3 provides a summary of minerals composition of the samples, as well as the corresponding mineralization styles and, when applicable, sub-styles. This table serves as a base for further sample analysis, providing a set of succinct and condensed information free of interpretative bias. The information presented in the table is further complemented by detailed description of each sample above, which aims to enhance the visualization and understanding of its petrographic characteristics, therefore, this table serves not only as a summary of this chapter but also as a guide for easy sample characterization.

Table 7.3: Summary of each sample's minerals composition, as well as the respective mineralization style and (in the pertinent cases) substyle, along with the respective caption.

SAMPLE	Type of Sample	Sphalerite	Chalcopyrite	Isocubanite	Bornite	PG Chalcocite	Chalcocite	Digenite	Covellite	Magnetite	Marcasite	Sulphates	Pyrrhotite	Mineralization Style	
SAL-03-03	Apparently inactive chimney (close to SAL-05-03: active)	XXX		X					x					Sph-style	
SAL-03-04	Diffuse chimney (close to SAL-03-08:active)	XX		XX						X		X	XX	Po-style	
SAL-03-06(1)	Apparently inactive chimney (close to an active zone F3)		XXX	X										Cu-Style	Type-III
SAL-03-06(2)	Apparently inactive chimney (close to an active zone F3)	x	XXX											Cu-Style	Type-I
SAL-03-08	Active chimney (355ºC)		XXX		x	x	x	X	x	x	x	x		Cu-Style	Type-I
SAL-04-02(1)	Diffuse chimney (close to SAL-05-01: active)	x	XX	x					x			XX		Cu-Style	Type-III
SAL-04-02(2)	Diffuse chimney (close to SAL-05-01: active)	XXX		X					x					Sph-style	
SAL-05-01(1)	Active chimney		XX	XX										Cu-Style	Type-III
SAL-05-01(2)	Active chimney		XX	XX										Cu-Style	Type-III
SAL-05-03	Massive sulfide fallen retrieved in the base of a mount of an active smoker		X	XX					X					Cu-Style	Type-III
SAL-05-04(1)	Apparently inactive chimney	XXX		X					x					Sph-style	
SAL-05-04(2)	Apparently inactive		X		x				x	x		XXX		Cu-Style	Type-II
SAL-05-05(1)	Active chimney (364ºC)		X									XXX		Cu-Style	Type-II
SAL-05-05(2)	Active chimney (364ºC)		XX		x	x	x		x	x		XX		Cu-Style	Type-II

	Indicators
Sph-style	Sphalerite >> Isocubanite
Po-style	Pyrrhotite ≥ Sphalerite
Cu-Style	Cu rich minerals

x	Scarce	<5%
X	Present	<25%
XX	Abundant	25~70%
XXX	Extremely Abundant	>70%

8. Revised mineralization styles

The work of Bortnikov et al. (2002) thoroughly explained in chapter 3 Mineralization styles served as a guideline for the microscopic observations , however, the three presented mineralization styles fail to explain the development of the Rainbow samples, whilst simultaneously presenting minerals that were not observed and also missing out on minerals that were verified to occur in the SAL samples, mainly Cu-rich minerals. As such, Bortnikov's work was mainly used to provide clear distinction and guidelines that when interpreted can help distinguish the Rainbow samples into the three main mineralization styles, and so, this chapter presents an updated version based on the observations made using SAL's samples.

As for the minerals referred by Bortnikov et al. (2002) that were not present in the studied samples, those were not taken into consideration for the presented revised mineralization styles, however this doesn't rule out the possibility of their existence in some samples under certain conditions. A prime example of that would be gold grains that were previously described in other thin sections (e.g., SAL-05-03), which after thorough and extensive observations, were not found in the produced samples for this work.

As such, this chapter serves as a more detailed description of each style and sub-style, where not only the styles are dissected but also each of their corresponding minerals are also analyzed.

8.1 Cu-style

Cu-style mineralization is the more complex of the three styles , it is also within the Rainbow samples, whilst also being the more diverse, and thus three sub-styles are proposed, where the main sulfide is either chalcopyrite or isocubanite, with the main difference between the subtypes being which mineral has a greater presence as well as which minerals may arise from the initial mineral,

Regardless of the sub-style, all Cu-style samples showcase a set of sulfide assemblages, mostly consisting of Cu sulfides with varying degrees of both Cu and Fe in the composition, both important indicators of the evolution of the sample.

The description for the three sub-styles is as follows:

8.1.1 Cu-style(Type-I):

This sub typology consists of a range of minerals that; (1) can potentially evolve from chalcopyrite to, ultimately, digenite containing in-between bornite, pinkish-gray chalcocite, chalcocite, all minerals resultant of oxidation that leads to the supergene enrichment, as well as (2) the sink minerals for the expelled elements, such as marcasite and magnetite, with covellite also forming as a result of the supergene oxidation of chalcopyrite, but at lower temperatures. This assemblage is defined by an assemblage of minerals with higher or equal copper content to that of both chalcopyrite and isocubanite. One of the samples that comprise this mineralization sub-style, sample SAL-03-06(2), does not present a Cu enrichment, however, due to having no isocubanite (and thus being stable) nor sulfates, it fits into Cu-style(Type-I) description. This sub-typology presents samples that showcase the various minerals within Cu-style, with the best example being SAL-03-08, in which we see the entire catalog of minerals that may possibly occur from a Cu enrichment.

The corresponding samples are: SAL-03-06(2), SAL-03-08.

8.1.2 Cu-style (Type-II):

This sub style is referred to in the bibliography and chapter 3. Mineralization styles, as "copper-anhydrite substyle" and, unlike what is proposed in the bibliography, where it is used to characterize a Cu-style sulfide assemblage with an outer sulfate layer, in this work, it refers to a sulfate rich mineral assemblage, where the sulfates are proportionally more prevalent than the sulfides (the relation between sulfides and sulfates imposes to the Cu content, i.e. the most important factor when considering these proposed sub-typologies is the proportion of sulfides vs sulfates). The larger prevalence of sulfate minerals suggests strong/important seawater interaction.

In these samples, several generations of sulfide will develop, often with superimposed varying degree of alteration and with the more recent sulfide rings/deposits being well preserved and where often supergene influence can be noted, with the existence of Cu-rich minerals (similar as to what is seen in Cu-rich type-I samples, with chalcopyrite being altered into bornite, pinkish-gray chalcocite, chalcocite and digenite), as a result of supergene enrichment, while in the seemingly early deposits of chalcopyrite, extreme alteration can be noted and is a common factor, especially with grains that are further from the latest (presumed) focal points of fluid flow (i.e. grains outside the most recent fluid circulation channels are presumably older and as they show a greater degree of alteration, also worth noting that multiple focal points of fluid flow can be seen in the same sample).

The corresponding samples are: SAL-05-04(2), SAL-05-05(1) and SAL-05-05(2).

8.1.3 Cu-style(Type-III):

The samples in this last sub-style display a copper deficit in the sulfide mineral assemblage when compared to the remaining type I and type II Cu-rich samples, with isocubanite being the prevalent mineral. This sub-typology can either be almost mono-mineralic (such as sample SAL-05-03) or with the isocubanite being transformed into chalcopyrite, with the remains of isocubanite in the form of internal structures.

These samples, apart from SAL-05-03, whose case is further explained in chapter 10.2 Thin-section interpretation, showcase a great degree of instability, which suggests a limited lifespan of the vent, whether it be because the venting has prematurely ceased, or because, the vent was both young and active upon the sample retrieval. Due to the lack of stability, these samples show great frailty, and as such, the observable grains are, more often than not, isolated as some of the grains have been detached from the sample during the preparation process, not only that, but these samples' surface oxidize quicker than the remaining SAL samples, issues that in both cases increase with the degree of instability, which in this case can be determined by the proportion of isocubanite versus chalcopyrite, with the samples richer in isocubanite being the more unstable, and thus more susceptible to surface weathering (worth noting once again that this refers to the samples in which isocubanite is turning into chalcopyrite, and thus, excludes sample SAL-05-03).

Given the strong presence of unstable isocubanite, it can be proposed that some of it should be considered as ISS (intermediate solid solution, the unstable version of isocubanite).

The corresponding samples are: SAL-03-06(1), SAL-04-02(1), SAL, SAL-05-01(1), SAL-05-01(2) and SAL-05-03.

8.1.4 Cu-style (General remarks)

While there is no given justification in Bortnikov et al, 2002 for the enrichment of Cu within the samples of the Cu-style, by the form of Cu rich sulfides, the logical explanation, with sample SAL-03-08 as the main evidence, would be a supergene enrichment promoted by oxidation of the outer layers (in contact with cold water), this enrichment promotes the mobility of both Fe (iron) and S (sulfur), towards, the outer part of the sample/cracks, where it can either deposit or venture to the seawater, thus prompting a relative Cu enrichment within the "sink" minerals, as Cu is less mobile at the lower temperatures at which S and Fe are highly mobile.

The complete evolution of this system can be seen in the sample SAL-03-08, where the evolution of the minerals is chalcopyrite > bornite > pinkish-gray chalcocite > chalcocite > digenite. In simpler terms, the oxidation front that moves inwards into the sample (whose main mineral is chalcopyrite, composed of Cu, Fe and S) prompts an outwards movement of Fe and S, that are highly mobile at the temperature the process occurs, resulting on a reworking of the primary mineral assemblage that becomes relatively enriched in Cu.

In order to further identify the minerals and respective mineral styles identities, correlation coefficient matrixes were made using the microprobe analysis as reference, where a value of 1 represents a strong correlation between the two elements, 0 a neutral relationship and -1 inverse correlation. These values are particularly relevant in this sort of studies, where a small set of minerals is observed and where each major element in the samples can be strongly related to a single mineral (with the exception of S, which as expected is present in all the sulfides, though in different proportion and therefore can be telling of the sample's tendencies). It is however worth noting that results might be skewered towards certain minerals considering the artificial proportion of data collected for each mineral versus the actual proportion of said minerals within the sample, however, even if with a slight bias, the correlation coefficient matrixes should give a good idea of element correlation for each sample and mineralization styles.

Upon analyzing the values in **APPENDIX V.** and taking into consideration not only the correlation coefficient values, but each element's respective abundance in the samples, a set of element relationships can be drawn. As with the other parameters studied in this thesis, the Cu-style presents the most complex and unique set of correlation coefficient values out of the three mineralization styles, with several elements' compatibility varying depending on the sample as seen in **APPENDIX V.I** for the remaining samples.

Given the larger sample size (n = 172), more elements, whose values were often below the limit detection in most of the analysis for the remaining mineralization styles and some unique samples, could be taken into consideration, and so, more varied and meaningful element relationships could be drawn, nevertheless some elements, such as Bi, Sn, etc. weren't taken into consideration due to not appearing in most samples, thus inflating their correlation values when detected. That said, similar trends to what was seen in the remaining styles prevail, as Zn and Cd show the greatest element correlation, not only that but the lack of affinity Cu has with the other major elements remains, showing a negative correlation coefficient with Fe, S, Zn, as well as Co (whose only noteworthy, positive, relation is with Ni). Unsurprisingly, and complementing the aforementioned supergene enrichment explanation for the appearing of Cu rich sulfides lackluster in both Fe and S, is the affinity of these two elements with each other in the Cu-style samples.

8.2 Cu-style mineralogy:

Isocubanite [$CuFe_2S_3$] – Along with chalcopyrite, these are the two Cu-sulfides predominant in the Cu-style samples and as they tend to represent early sulfides, it can be assumed that they roughly reflect earlier stages of the mineralizing fluid venting through the Rainbow Hydrothermal Field. Isocubanite will evolve to chalcopyrite, which confirms an initial imbalance between the vent's fluid and the mineral. These transformations, when incomplete, often form internal structures (in the form of exsolutions) as seen in most of the Cu-style (Type-III) samples. Isocubanite can also be seen in an almost mono-mineralic arrangement (e.g. SAL-05-03).

Chalcopyrite [$CuFeS_2$] – Chalcopyrite is ubiquitous in the Cu mineralization style and serves as the predecessor for the Cu-rich minerals (i.e. bornite, chalcocite, pinkish gray chalcocite and digenite), as they all evolve from chalcopyrite (at T>500ºC intermediate solid solution [ISS] is the dominant phase on the Cu-Fe-S system, which at lower temperatures ISS decompositions into chalcopyrite, which in turn can be reworked at later stages into Cu-rich minerals). Chalcopyrite also has a fairly high representativity in most of the samples, often being the main sulfide. Due to their similarities, whether those be chemical or optical/textural, chalcopyrite is often difficult to distinguish from isocubanite, and as such, unless in contact with each other and at high ampliations under reflected light, the only way to accurately distinguish both is by microprobe analysis, with isocubanite often evolving to chalcopyrite.

Bornite [Cu_5FeS_4] / Pinkish gray chalcocite[$Cu_{2+3x}Fe_xS_{1+3x}$] / Chalcocite[Cu_2S] / Digenite [Cu_9S_5] - The more reworked Cu- style samples often show Cu rich mineral assemblages. Chalcopyrite undergoes supergene enrichment prompted by interaction with seawater, that removes Fe and S, resulting in a relative enrichment in Cu, forming Bornite / Pinkish gray chalcocite / Chalcocite / Digenite. This transition is observable near where there were previously cracks and/or towards the outer edges of the sample (where sulfates are deposited as they mark where the sulfides from the sample interacted with seawater).

Bornite is the first mineral to form on this transition, and it occurs mostly in samples with a small degree of reworking, furthermore, the smaller percentage of Cu relative to other Cu-rich sulfides indicates that this mineral is the first and thus, a lesser evolved state in the transition towards the Cu enrichment.

A solid solution between bornite and chalcocite (pinkish gray chalcocite) is often present in these samples with a composition varying is in-between both, indicating a transitional state between the two minerals. This association can be found at a greater degree than bornite, especially in the more reworked samples, in which the presence of bornite is less common relative to pinkish gray chalcocite.

The final two minerals are chemically similar and are both shown in the photomicrograph of Figure 8.1. Between the two, chalcocite is the more common Cu-rich sulfide throughout the samples and can easily be mistaken for digenite unless in contact with it, digenite is the final mineral in this supergene enrichment sequence.

In the SAL samples, the main difference between the two minerals is the fact that the first is ubiquitous near the alteration zones and the only occurring near the deep perpendicular cracks to these samples, while the latter occurs only at the outer edges, in direct contact with the sulfates, and previously seawater.

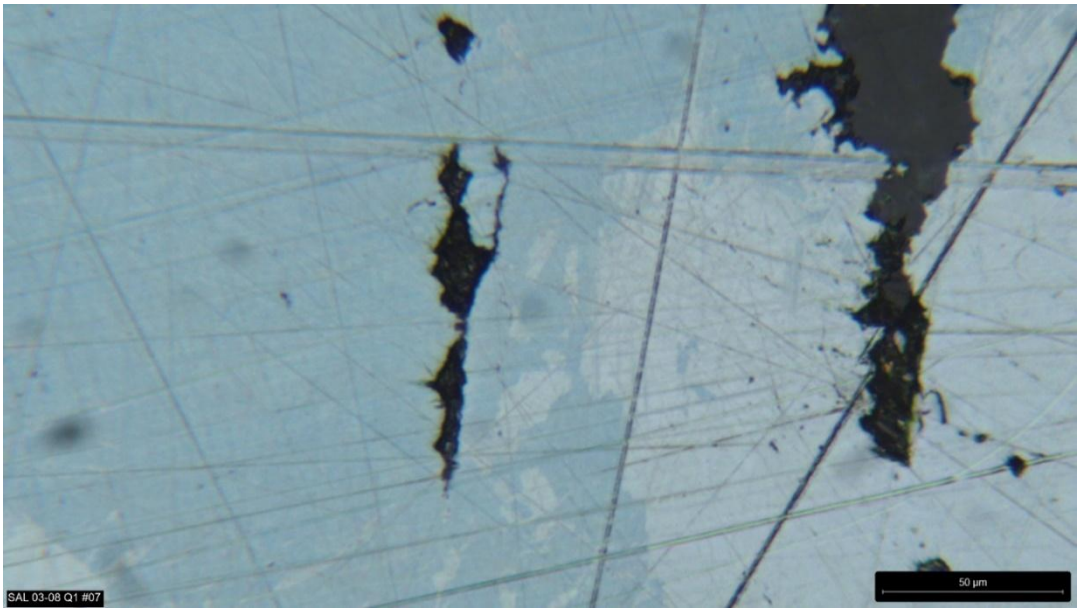

Figure 8.1: Transition from chalcocite (left) to digenite (right) captured in the sample SAL-03-08.

Covellite [CuS] – Covellite is a key mineral when analyzing the Cu- style mineralization style as it gives us information regarding the behavior of the system, particularly because covellite tends to be formed under lower temperature conditions compared to primary Cu-Fe minerals in the system like chalcopyrite. Unlike chalcopyrite, covellite has been depleted in Fe and thus has a greater content in Cu, while roughly maintaining the proportion of S. Covellite in these samples appears to result from the alteration of chalcopyrite, where supergene Cu enrichment of the samples is prompted by seawater oxidation serves as an indirect sink for Cu due to Cu not being mobile at lower temperatures, and thus covellite deposits in place of where the chalcopyrite grains previously were.

Covellite, with the sole exception of sample (SAL-05-03), appears only in contact with sulfates, suggesting that it forms in a later stage, prompted by decreasing temperatures along with seawater interaction. In both SAL-05-05 samples, as well as SAL-05-04, the covellite is often associated with magnetite, which could possibly indicate that the mineral (likely chalcopyrite) that originated the covellite grain is the same as the one that originated the magnetite (this meaning that, from the chalcopyrite interaction with the seawater, the sulfur and copper in the structure of the chalcopyrite remained and were transformed into the covellite, while the iron from the chalcopyrite, in conjunction with the oxygen sequestered from the seawater were converted into the magnetite).

Magnetite [$Fe^{3+}OFe^{2+}{}_2O_3$] – Magnetite's presence helps to illustrate the complexity of the Cu-style mineralization. As aforementioned, magnetite is often associated with covellite, but also (rarely) marcasite. In this mineralization style, magnetite is formed at a later stage, suggesting oxidative conditions, in which magnetite is used as the main sink of iron (e.g. SAL-03-08), where it is surrounded by sulfates, or in contact with covellite.

Marcasite [FeS_2] – Marcasite is rarely observed. Marcasite crystals only formed in the frontiers between the, originally, chalcopyrite transformed into Cu rich minerals (both sulfides as both were formed under a reducing environment driven by the fluid's low pH) and the cracks filled with sulfates (formed as a result of the oxidation prompted by seawater). These small marcasite grains on the border between the

two different environment driven minerals serve as evidence of the Fe mobility, specifically towards the outer parts of the sample and/or to the seawater.

A photomicrograph as well as an EDS map of the same location (rotated 90º left) with a backscattering image with Fe and Cu overlaid is presented in Figure 8.2, and it highlights both magnetite (Mgt), as well as marcasite (Mrc) inside and on the edge of the cracks respectively (even though the marcasite grain is undistinguishable in the EDS image due to grain size), while other minerals are also shown.

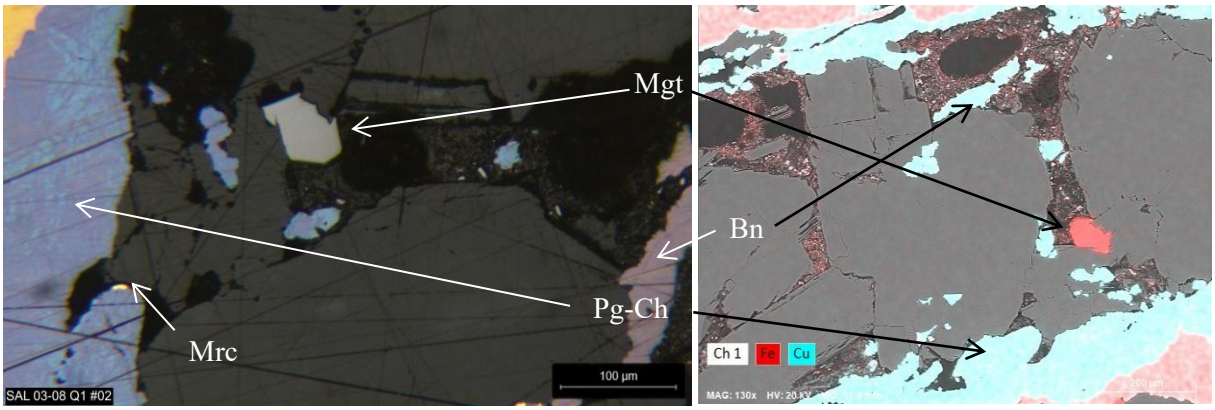

Figure 8.2: Photomicrograph and EDS imaging of a filled crack in sample SAL-03-08, with Mgt (magnetite), Mrc (marcasite), pg-Ch (pinkish gray chalcocite) and Bn (bornite).

Sphalerite [(Zn,Fe)S] – In this mineralization style, the presence of sphalerite represents a later stage of deposition which highlights a decrease in temperature, where the system exhausts most (as only some remains) of the Cu in the system and is left with Fe and S (as the redox conditions don't change as long as there is fluid flow and Fe is still abundant) and Zn (which introduces itself in the system at lower temperatures, when compared to the measured temperatures upwards of 350ºC). The sphalerite deposits itself on the outer part of the vent, where the seawater has a greater influence (in this case, notably in the decrease in temperature), and as it progresses further from the center of the vent a decrease in the Fe and Cu of the sphalerite is verified, which suggests that the liquid remained the same, but simply gradually lost the ability to transport Fe and Cu as the temperature decreased.

8.3 Sph-style

The description for the sphalerite style makes the style out to be quite linear, a *quasi*-monometallic aggregate of reniform and dendritic sphalerite, with the occasional isocubanite, closer to the center, and marcasite, near the outer zone, where we could also see Fe-hydroxides. This simplistic description disregards two key factors in the understanding of this mineralization style, and of the Rainbow Hydrothermal field as a whole, firstly the texture in which the minerals associated with sphalerite present, which is a key to decipher how and why do they appear, and the second factor is the different variants of sphalerite in these samples (respectively Sph-I, Sph-II and oxidized sphalerite).

The sphalerite style consists in fact of large aggregates of sphalerite, that vary between spotless unaltered sphalerite (Sph-I) and chunks of dendritic to sometimes reniform oxidized sphalerite, darker in color, as highlighted in Figure 8.3. Inside this sphalerite, particularly in Sph-I, previously small circulation channels are now filled with Fe-rich late sphalerite (Sph-II) surrounded by isocubanite either in the form of rings or half-rings. Two minerals that also occur in Sph-style mineralization are covellite and galena,

the first of which is a product of alteration in Cu sulfides and thus can be found in association with isocubanite, while galena may rarely occur within Sph-I in singular microscopical size grains.

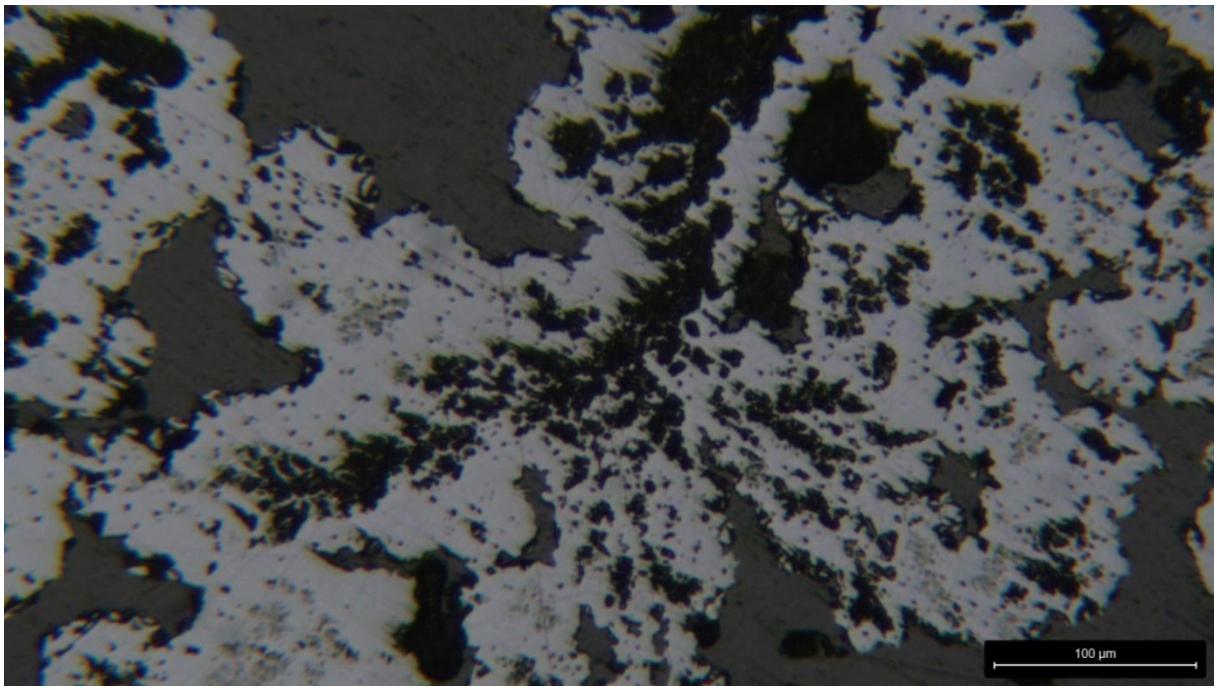

Figure 8.3: Photomicrograph of a Sph-style sample showcasing the differences between unaltered Sph-I and the oxidized sphalerite variation under microscope.

The general tendency in most samples is a large chunk of Sph-I with either occasional single rings, isolated within the Sph-I or half-rings, following in parallel the zones covered in oxidized sphalerite, likely indicating that the same fluid responsible for the oxidation of these sphalerite aggregates, has influence and/or is, in part, the fluid that fills the circulation channels.

In the sample SAL-05-04(1) there is a slight variance in which the Sph-I tends to lean towards a reniform texture, rather than the more common featureless large chunks, and importantly, the Sph-II + isocubanite form not one, but several sets of isocubanite rings surrounding each other, which could indicate that the system is being replenished and since Sph-style mineralization should occur in lower temperature settings and thus further from the main discharge points, where fluid flow is reduced, in order to form these repeating patterns, the liquid would need to be replenished, which could also be an indicator that the isocubanite is the first of the two minerals to deposit as they would form from the same liquid, however with two different immiscible compositions, one for each mineral, isocubanite would be "expelled" to the edges of these circulation channels and deposit first.

The increase of Fe from Sph-I to Sph-II, which is reflected in the microprobe analysis and further highlighted in the EDS imaging with no backscattering, shown in Figure 8.4, where Fe (red) is highlighted, indicate that the two minerals originated from liquids with slightly different compositions (with the second liquid's batch richer in Fe, while also having a minor increase in Cu), implicates that Sph-II composition is influenced by the isocubanite, with the increase in Fe also being a prime indicator that these minerals deposited at slight higher temperatures than Sph-I.

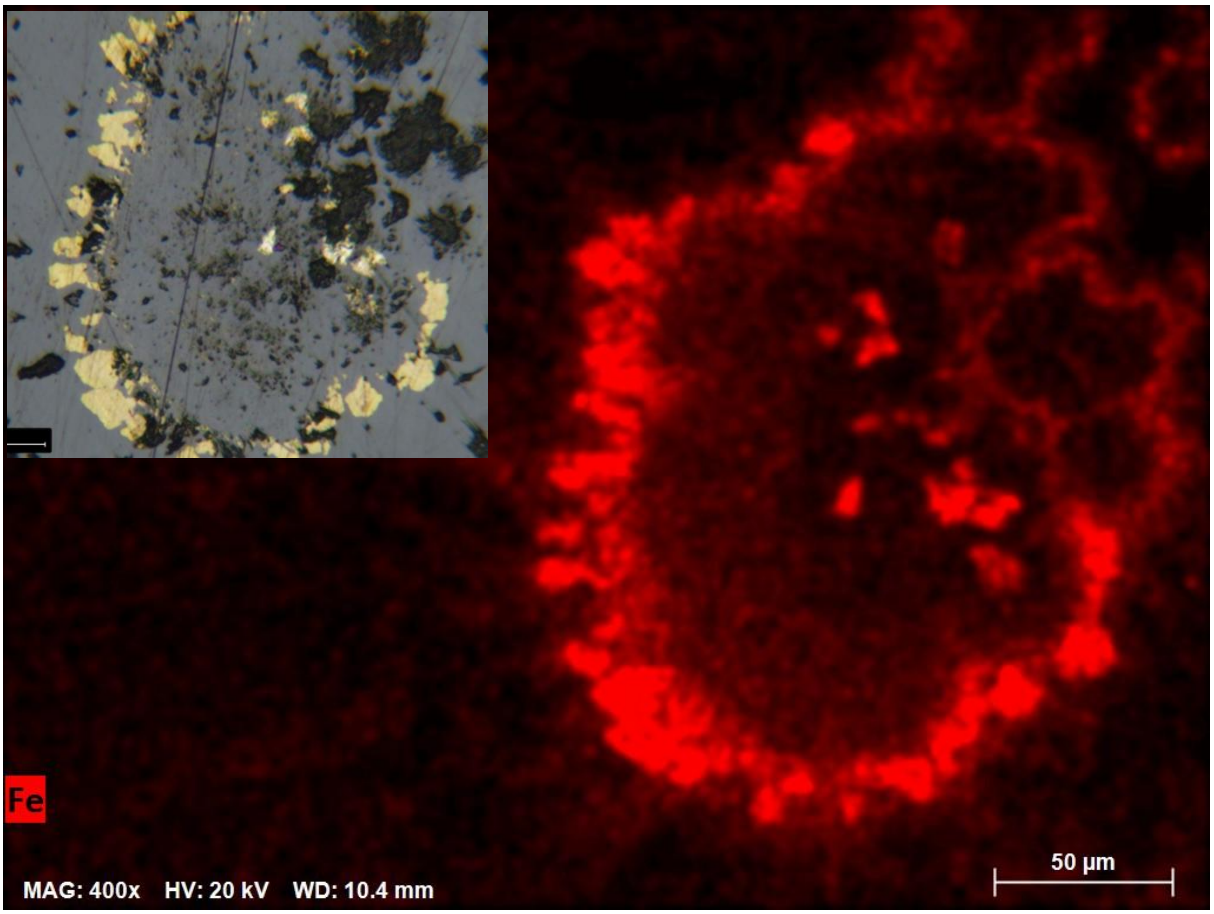

Figure 8.4: EDS map of the sample SAL-03-03, showing the Fe difference between the three mineral phases (Sph-I [a], isocubanite [b] and Sph-II [c]), along with the respective photomicrograph of the same grain.

Regarding representation (i.e. number of samples and analysis), this style is in-between the Po- and Cu-styles, nevertheless, mineral compatibility can still be observed in the correlation coefficient matrixes presented for the Sph-style mineralization.

Upon analyzing the values in **APPENDIX V** and taking into consideration not only the correlation coefficient values, but each element's respective abundance in the samples, a set of element relationships can be drawn. Similarly to the po-style mineralization, two main groups, incompatible with each other form, the first one being Zn + Cd, once again highlighting the affinity of Cd with Zn rich minerals (sphalerites) and the second one consisting of Fe + Co, both showing affinity to Cu and S, which are surprisingly neutral towards each other, likely as a result of the S composition fluctuating only slightly based on whether the analyzed mineral was isocubanite or sphalerite. S also shows a negative correlation coefficient with Pb due to the decrease of S concentration in galena [PbS], compared to the other two minerals, as Pb has an high atomic weight compared to S.

8.4 Sph-style mineralogy:

Sphalerite [(Zn,Fe)S] – As the name suggests, sphalerite is the defining mineral in the Sphalerite mineralization style. Sphalerite occurs in three different textures in these samples, the first one consists of altered sphalerite that suffers from different degrees of oxidation, the second type is Sph-I and is the primary and most abundant sphalerite type in this sample (the aforementioned type of sphalerite is likely Sph-I that suffered oxidation in specific zones that had greater contact with seawater), Sph-I is mostly

featureless and is separated from the third type of sphalerite, Sph-II by rings or half rings of isocubanite, not only that but Sph-II is also richer in both Cu and Fe with an overall increase of up to five times when compared to surrounding Sph-I. This difference in Cu and Fe content highlights variances within the liquid, as Sph-II only forms to fill the fluid channels (along with isocubanite), hence, the more evolved composition, which may derive from isocubanite which is richer in both Fe and Cu.

A photomicrograph as well as two EDS map of Fe (red) and Cu (blue) in the same location, without backscattering to reduce noise, is presented in Figure 8.5 and it highlights the slight variation of Cu and Fe between the Sph-I and Sph-II (separated by isocubanite), especially noticeable in the case of Fe, confirming the increase of both Fe and Cu in the latter Sph-II.

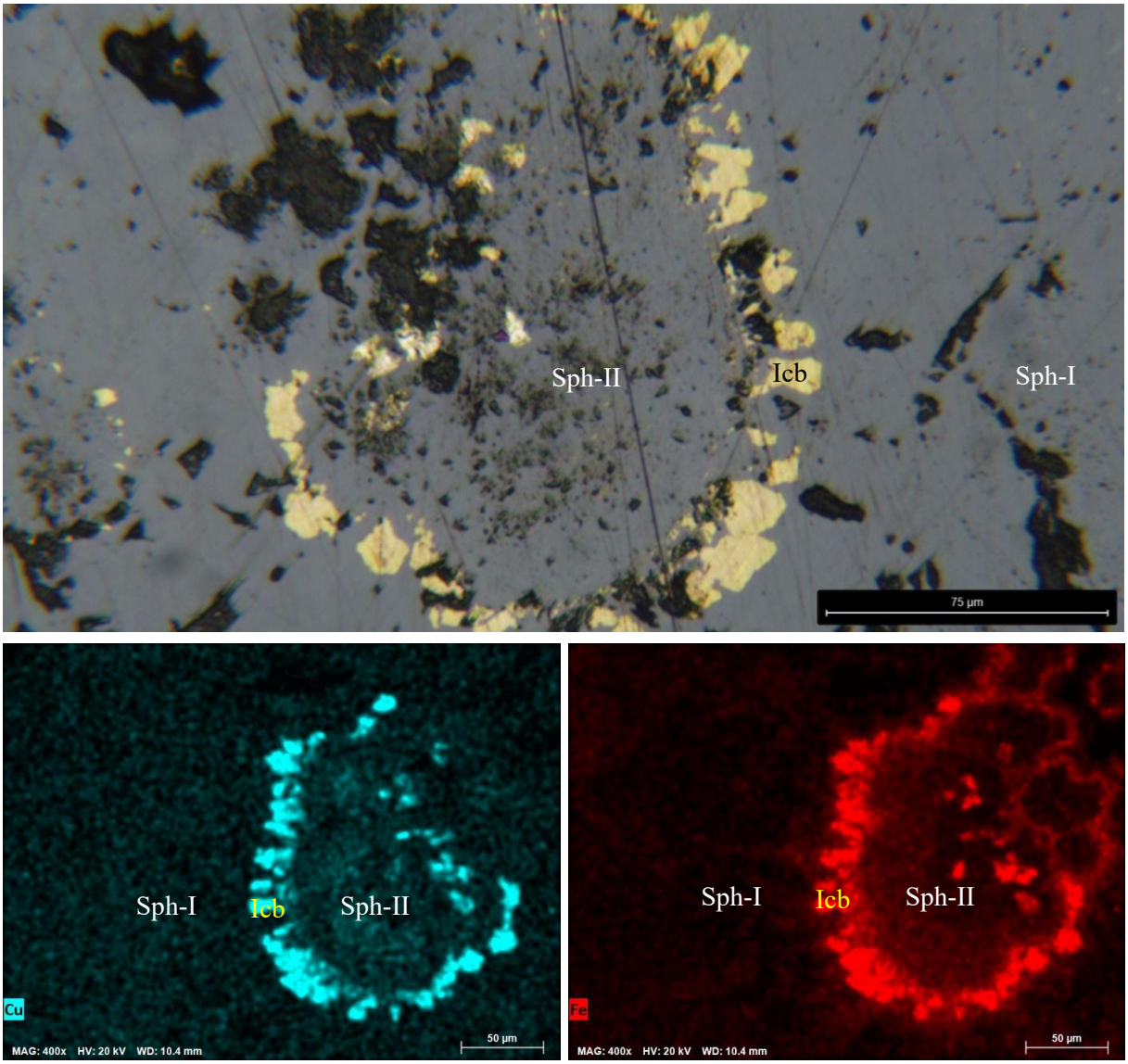

Figure 8.5: Photomicrograph and EDS image (Cu[blue] and Fe[red]) of the sample SAL-03-03 highlighting the compositional differences of Sph-I and Sph-II.

Isocubanite [$CuFe_2S_3$] – All Sph-style samples display Isocubanite surrounding what previously would have been circulation channels either in circles or semi-circles which form either prior or simultaneously to Sph-II (as Sph-II is formed within those circles/semi-circles) and after Sph-I.

Isocubanite (Icb) and Sph-II always form together and given how the two minerals can't form solid solutions, a significant change in the liquid's composition would be necessary to justify the evolutionary process from Sph-I. At first glance, it could be interpreted as simple a second small batch of liquid is either introduced to the system or mixed with the existing circulating fluids that is quickly depleted of it's Cu forming once again sphalerite, but upon further observation of the rings of the sample SAL-05-04(1), a series of rings surrounding each other, cycling between Isocubanite and Sph-II (the second generation of sphalerite) occurs in every filled hole. This pulsation could indicate that the system is being replenished and since Sph-style mineralization should occur in lower temperature settings and therefore further from the main discharge points where fluid flow is reduced, which should imply that in order to form these repeating patterns either the liquid is replenished, or the fluid's flow is weak enough to allow the system to slowly form these rings.

The same way Sph-II is enriched in Cu and Fe due to the interaction with isocubanite, isocubanite also shows a varying relative enrichment in Zn when compared to the standard formula.

Covellite [CuS] - Covellite is scarce and forms around Isocubanite. It's likely the last mineral to be formed and represents Cu accumulations resulting from the cooling of the sample in conjunction with the seawater interactions, it is likely that these samples could suffer a similar process to the supergene enrichment mentioned for Cu-style, but to a much smaller degree (both in temperature and in element mobility).

8.5 Po-style

Pyrrhotite style has a broad characterization, with the original description stating pyrrhotite covering from 10 upwards to 100% of the sample and showing different minerals associated with it, which includes both sphalerite, isocubanite and chalcopyrite (the main minerals in the other mineralization styles).

The original description for the po-style is on par with what can be seen in the sample SAL-03-04, where in fact , it displays large, elongated euhedral grains of pyrrhotite, often within the same grains as isocubanite in the outer edges of the sample, where minerals have space to fully grow, while closer to the center, where the grains are more compact and have less space to develop, the sample is composed of a mixture of physically altered, elongated pyrrhotite crystals, in contact with isocubanite and sphalerite aggregates, often occurring within the same grains.

In chapter 3 Mineralization styles, it is referred the possibility of finding chalcopyrite with the isocubanite, and while that may be true, the fact did not occur within this sample, but given the behavior of the aggregates of chalcopyrite and isocubanite observable in the Cu-poor style sample, it seems highly probable that isocubanite and chalcopyrite could co-exist in an exsolution in some of the samples, with the main deciding factor being likely the fluid's temperature and whether or not the same fluid is capable of forming chalcopyrite before the pyrrhotite, contrary to what can be seen in the Cu-poor mineralization style, as the general trend in this samples is a decrease in Cu, unlike in Cu-style mineralization.

Pyrrhotite has a large amplitude when it comes to temperature of formation, as its presence is dependent on the fS and $fO2$, since it is a REDOX sensitive mineral, however, the presence of Zn (associated to lower temperatures) and lackluster presence of Cu (associated with higher temperature assemblages), imply that this association should be defined as of intermediate temperature between the remaining two, so the greater take-away from this sort of samples is that they aren't directly in contact with the heat source, as it is demonstrated in Figure 8.6, but rather in a zone in which Fe and S have a greater presence

as they are more compatible with lower temperatures that stem from this mineral zonation, while still having considerably higher temperatures than those associated to sphalerite rich zones.

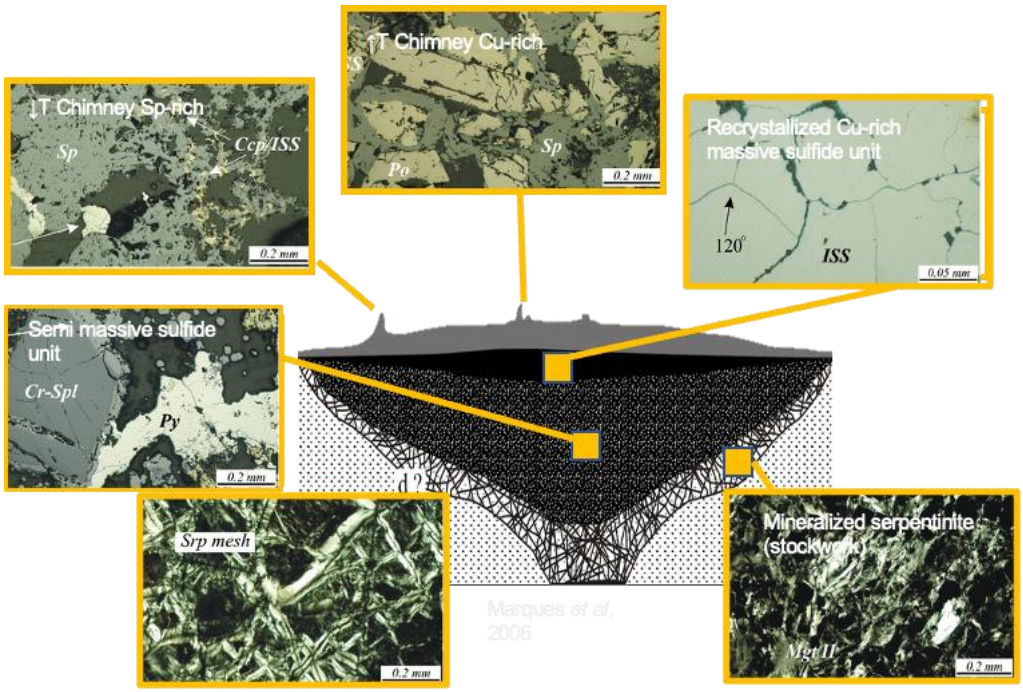

Figure 8.6: Schematic view of the Rainbow hydrothermal field and the presumed deposit type, with special emphasis on the evolution of sulfide minerals further from the central point, where fluid discharge and heat tend to be greater (after Marques et al., 2006).

The sample size, due to SAL-03-04 representing the sole Po-style sample, is reduced compared to the other mineralization styles, which results in more extreme values for the correlation coefficient matrixes.

Upon analyzing the values in **APPENDIX V**. and taking into consideration not only the correlation coefficient values, but each element's respective abundance in the samples, two groups can be observed. Those two groups have a strong incompatibility with each other (i.e. will not the simultaneously observed), with the element groups consisting on one side of Cd + Zn, and the other group S + Fe + Co, which reflect the composition of the main minerals in the assemblage and thus the values are to be expected, as the content in S increases with Fe due to the analyzed pyrrhotite and isocubanite crystals, while both elements tend to diminish, when compared to Zn in the sphalerite crystals. This data also highlights the strong correlation of Cd with the sphalerites and Co with the Fe sulfides, as well as their respective negative correlation with each other.

8.6 Po-style mineralogy:

Pyrrhotite [$Fe^{2+}_{0.95}S$] - Pyrrhotite is the defining mineral in this mineralization style. As only one sample for this style was analyzed, even if the mineralization style is presented in the bibliography as somewhat linear, the proposed interpretations can be refuted given enough counter evidence. In sample SAL-03-04, the pyrrhotite crystals come in two different settings, when they have space to grow at the time of their deposition, they form large euhedral tabular crystals that usually connect to each other by one of the thin edges of the crystal, on the other hand if the minerals don't have the space to fully grow they tend to form smaller anhedral clusters, often in the form of exsolutions with isocubanite. Pyrrhotite is an indicator of a low temperature setting.

Sphalerite [(Zn,Fe)S] – The sphalerite in these samples is featureless and forms in exsolutions with isocubanite (both minerals were at a certain point in equilibrium, but due to the lowering temperature and changing conditions separate, yet remain within the same crystal). In this sample pyrrhotite is the dominant mineral, nevertheless it isn't necessarily the case, as sphalerite can be predominant when compared to pyrrhotite. Sphalerite tends to not be in contact with pyrrhotite

Isocubanite [$CuFe_2S_3$] - The isocubanite is difficult to distinguish from pyrrhotite, when not aware of the presence of both minerals in the sample. It appears in various forms, whether it be in form of exsolutions in large crystals with either pyrrhotite or sphalerite, of in anhedral crystals by itself. Crystals displaying isocubanite are often "broken" and more altered than those composed of mainly pyrrhotite.

Magnetite [$Fe^{3+}OFe^{2+}{}_2O_3$] - Magnetite is present in these samples in small quantities, likely formed as a result of oxidative conditions which would be present at later stages of the vent's lifespan.

The three main minerals in the po-style mineralization are shown in Figure 8.7, in a setting where pyrrhotite is quite frail due to the alteration and isocubanite and sphalerite are presented occupying the same grains. Near the bottom left border is also possible to see the transition between isocubanite and pyrrhotite in a grain also composed of sphalerite.

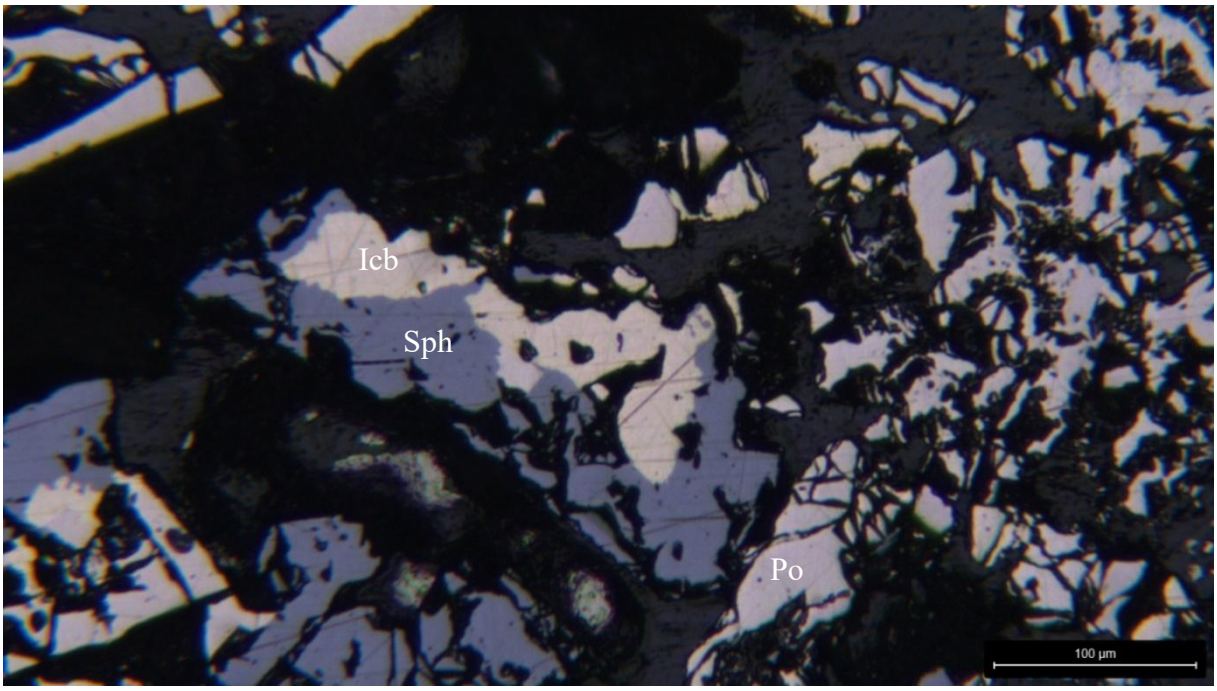

Figure 8.7: Photomicrograph of the sample SAL-03-04 showcasing the disposition of sphalerite (Sph), pyrrhotite (Po) and isocubanite (Icb) in the po-style mineralization.

9. *In-situ* S isotopes ($\delta^{34}S$) composition

A total of 56 in-situ $\delta^{34}S$ isotope analyses were conducted across six samples. The selection of the samples, locations of the spot analyses on the samples, and the phase mineral analyzed was guided by the textural characteristics of the samples. Samples with high porosity were excluded from analysis due to the impossibility of performing reliable measurements. When possible, compositional profiles of the vent walls were performed. Limitations in the number of analytical spots were primarily due to the quality of the minerals but also due to constraints imposed by the available budget for analyses. The number of analyses per mineral is present in Table 9.1.

Table 9.1: Summary of analyses made per mineral in each sample.

Sample	Number of analyses per mineral
SAL-03-03	6 analyses on Sph-I, 2 on Sph-II, and 3 on isocubanite
SAL-03-08	14 analyses on chalcopyrite and 3 on chalcocite across a vent wall
SAL-04-02(2)	3 analyses on Sph-I, 1 on Sph-II, and 2 on isocubanite
SAL-05-01	8 analyses on a mix of chalcopyrite and isocubanite
SAL-05-03	6 analyses on isocubanite (randomly selected grains)
SAL-05-05	8 analyses on chalcopyrite

The precise locations of these analyses within each sample, along with a table of all $\delta^{34}S$ values, can be found in **APPENDIX V.I**. The $\delta^{34}S$ values of the Rainbow hydrothermal vent samples display clear distinctions between different mineral phases and mineralization styles as can be seen in the Figure 9.1.

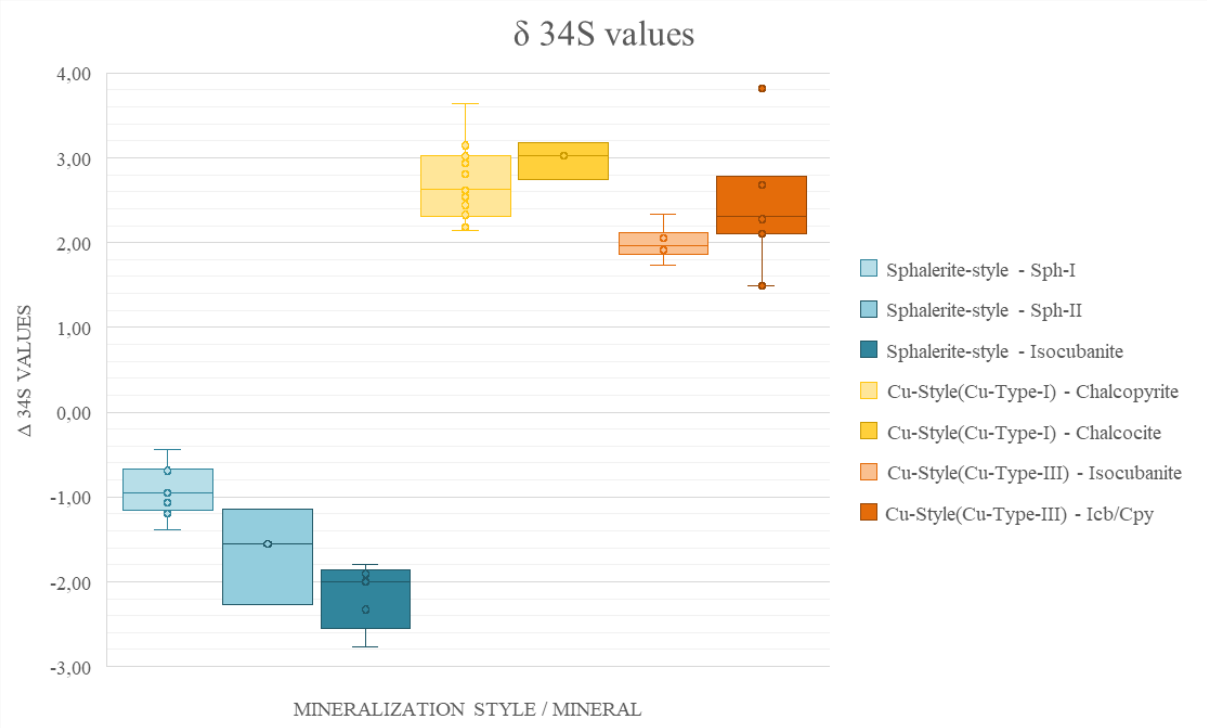

Figure 9.1: Boxplot showing the $\delta^{34}S$ composition of sulfide minerals of the Rainbow samples grouped by mineralization styles and mineral phases. Sphalerite-style minerals (Sph-I, Sph-II, and isocubanite) Cu-style minerals (chalcopyrite, chalcocite, and isocubanite) display consistently positive $\delta^{34}S$ values.

Together, the $\delta^{34}S$ composition of the analyzed samples ranges from -2.77‰ to 3.82‰, with a mean ± standard deviation (std. dev.) of 1,41 ± 1,91‰ and a median of 2.21‰.

Sphalerite exhibits $\delta^{34}S$ values, in this case, below zero, ranging from -0.44‰ to -2.27‰ and should be divided into two distinct categories. Fe-rich sphalerite, Sph-II (mean ± std. dev. = -1,66 ± 0,57‰; median = -1,55‰), tends to exhibit more negative δ34S values compared to Fe-poor sphalerite, Sph-I (mean ± std. dev. = -0,93 ± 0,3‰; median = -0,95‰), with Sph-II values showing a stronger resemblance to isocubanite (from Sph-style) values.

Isocubanite $\delta^{34}S$ values range from -2.77‰ to 2.33‰, depending on the mineralization style. In Sphalerite-style samples, isocubanite $\delta^{34}S$ values range from -1.91‰ to -2.77‰ (mean ± std. dev. = -0.93 ± 0.30‰; median = -0.95‰), while in Cu-rich deposits, $\delta^{34}S$ values range from 1.49‰ to 2.33‰ (mean ± std. dev. = 1.92 ± 0.26‰; median = 1.94‰).

Chalcopyrite is characteristic of Cu-rich deposits and $\delta^{34}S$ values are consistently positive, ranging from +2.15‰ to +3.64‰ (mean ± std. dev. = 2.70 ± 0.39‰; median = 2.63‰).

Chalcocite is characteristic of Cu-rich deposits and boasts the highest $\delta^{34}S$ values ranging from 2.74‰ to 3.18‰ (mean ± std. dev. = 2,98 ± 0,22‰; median = 3,03‰).

Considering the style of mineralization, sulfide minerals analyzed in Sphalerite-style samples (n = 17) exhibit $\delta^{34}S$ values ranging from -2.77‰ to -0.44‰ (mean ± std. dev. = 1,42 ± 0,66‰; median = -1,19‰). In contrast, Cu-style samples (n = 42) show more positive and consistent $\delta^{34}S$ values, ranging from 1.49‰ to 3.82‰ (mean ± std. dev. = 2,56 ± 0,55‰; median = 2,58‰).

All the values are shown in Table 9.2 and 9.3 that serve as a summary for these observations.

Table 9.2: Mean, Standard Deviation, Median, Count, Minimum and Maximum values for each of the analyzed mineral groups

Mineral Group	Mean	Std Dev	Median	Count	Min	Max
Chalcocite (Cu-style - Type-I)	2,98	0,22	3,03	3	2,74	3,18
Chalcopyrite (Cu-style - Type-I)	2,7	0,39	2,63	22	2,15	3,64
Icb/Cpy (Cu-style - Type-III)	2,58	0,74	2,32	10	1,49	3,82
Isocubanite (Cu-style - Type-III)	1,92	0,26	1,94	7	1,49	2,33
Isocubanite (Sph-style)	-2,16	0,39	-2	5	-2,77	-1,8
Sphalerite-I (Sph-style)	-0,93	0,3	-0,95	9	-1,39	-0,44
Sphalerite-II (Sph-style)	-1,66	0,57	-1,55	3	-2,27	-1,15

Table 9.3: Mean, Standard Deviation, Median, Count, Minimum and Maximum values for each of the analyzed mineralization stye

Mineral Group	Mean	Std Dev	Median	Count	Min	Max
Sph-style	-1,42	0,66	-1,19	17	-2,77	-0,44
Cu-style	2,56	0,55	2,58	42	1,49	3,82

10. Samples' Interpretation

10.1 Whole-rock analysis interpretation

As mentioned in chapter 7.2 Bulk geochemistry, the data for whole rock analysis was further developed into Ba/Co and Cu/Zn ratio graphs, PCA for both REE and for the most important elements, multi-element diagrams for REE values (normalized to primitive mantle values from Mcdonough & Sun, 1995),

The PCA analysis, shown in Figure 10.1 and 10.3 provide further complement to the correlation coefficient matrixes presented in **APPENDIX V** to interpret the correlation between the variables in this data, the first step is to analyze the horizontal axis (PC 1), which represents the greater affinity or lack thereof, followed by the vertical axis (PC 2), also representing the same traits, but to a lesser degree.

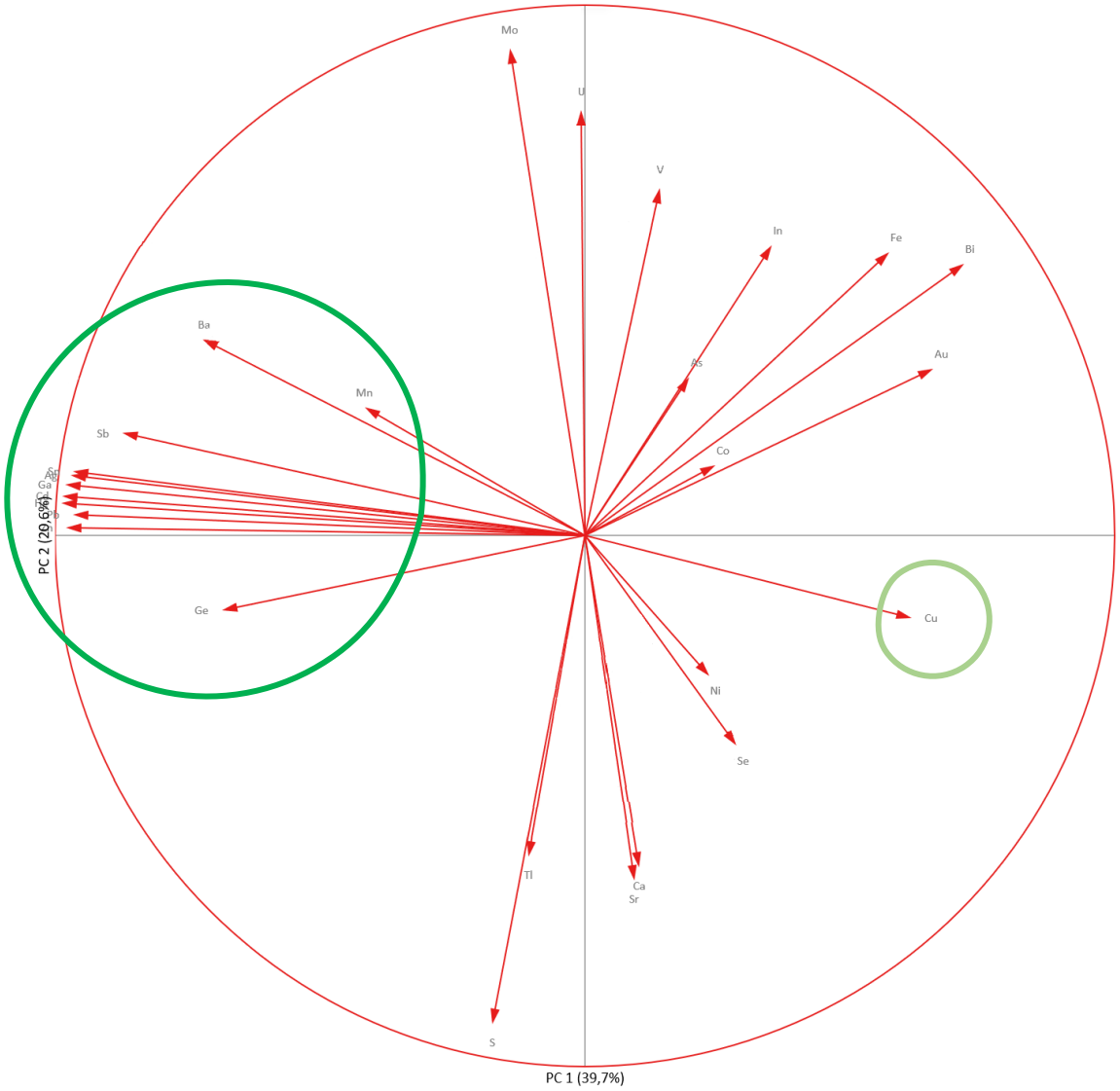

Figure 10.1: PCA analysis of relevant elements in the SAL samples, in the form of whole-rock geochemistry, often analyzed in works regarding hydrothermal fields of similar nature.

To interpret PC 1, the first observation must be to the large cluster of elements situated on the left of the PCA graph, represented in dark green, these elements can be seen as a cluster (composed of Zn and elements that will be associated with it), given their proximity to each other, which illustrates their affinity (i.e. if one element is present, the likelihood of the other elements also being present increases, furthermore, these elements should vary proportionally to each other), on the opposite end stands Cu, the furthest in the PC 1 axis to this cluster, which indicates a strong aversion to these elements, meaning, the presence of Cu, will in all likelihood mean that the other cluster of elements is not present or if present, it is in small quantity, this observation meets what is seen in the SAL samples, in which, Cu minerals show a weak affinity for Zn minerals, and both elements are only found together in Zn minerals, in which Cu may exist in small quantities (with a much smaller presence than in the Cu minerals, in which Zn and the affiliated elements are not present), similarly to Cu, these elements also show a lack of affinity to Fe, albeit smaller, which can be explained by Fe showing in greater amounts when in Cu minerals, rather than Zn minerals. The lack of Cu in Fe minerals should also be one of the reasons for both elements to not have greater affinity.

The remaining minerals are mostly either isolated or in pairs, likely due to the analyzed samples having all three mineralization styles (since these analysis compromise of all the whole-rock geochemistry data, unlike the correlation coefficient matrixes for individual samples and mineralization styles, produced via EPMA data), which implies that the elements affinity and lack thereof won't be as assertive, regardless, PC 2 still provides insightful information regarding how some elements cannot correlate to S, such as Mo and U, with the latter being particularly relevant as U only occurs in later stages of the process as a result of contact with seawater (*post*-deposition of sulfides). A lack of affinity between S and Fe is also shown, likely due to the iron (Fe) oxides that are present in the borders of the samples, in which S does not occur.

These observations go along with what has been observed in the correlation coefficient matrixes and though said matrixes present more detailed data (as they also serve as base for PCA analysis) they are not only harder to analyze but focus on the relation between two elements towards each other in isolation.

Table 10.1: Average composition of SAL samples, Logatchev (1 and 2), Rainbow (others) and TVG21 (Tianzuo)

	Cu	Fe	Zn
Average SAL samples	29%	56%	16%
Mean Logatchev	41%	45%	14%
Rainbow (others)	22%	51%	27%
AVERAGE TVG21	13%	87%	0%

Table 10.1 highlights the analyzed minerals in Figure 7.7 and summarizes the elemental distribution per field, this approach allows for a more generalist approach to each field, which in this case allows to see a broader characterization of each field instead of the usual individual sample analysis. As such a few conclusions can be drawn, a) The SAL samples fall within the acceptable ranges of Rainbow (others) to be considered similar, and with a greater sample size, the results should only be closer; b) The Logatchev samples show a slight increase in Cu/Fe compared to the SAL samples, but otherwise the values indicate a somewhat strong geochemical correlation between the two fields; c) Finally, TVG21 samples distinguish themselves from the SAL samples for the incredibly high proportion of Fe when compared to Cu and the total lack of Zn, which comes as a result of a totally different geochemical and mineral signature, with the main sulfide as pyrite, with both the Rainbow and Logatchev with chalcopyrite and sphalerite as the main sulfides.

Figure 10.2 presents Cu/Zn and Ba/Co ratios for each of the analysis in the **Appendix IV.III**, with said values projected against each other in a logarithmic scale graph, with Ba/Co ratio serving as an indicator of different geological settings (where Co is a typical indicator for ultramafic-hosted deposits), and Cu/Zn ratios as a temperature indicator (where higher Cu values as an indicator of higher temperatures and higher Zn values associated to lower temperatures, usually <250°C). This projection highlights a trend in these samples where higher Cu/Zn correlates to lower Ba/Co, meaning there is a strong correlation between higher Cu content (i.e., higher temperatures) to higher Co (i.e., the geological setting being of ultramafic nature).

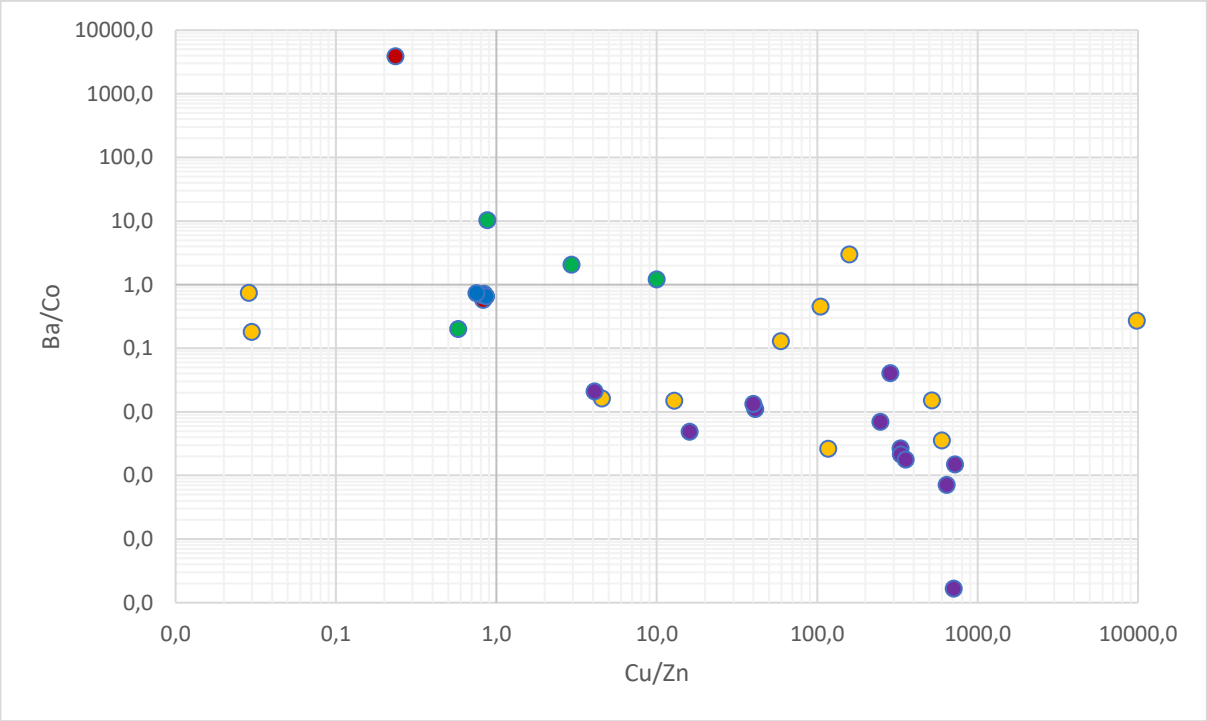

*Figure 10.2: Cu/Zn and Ba/Co reasons for each of the analysis in the **Appendix IV.3**, with said values projected against each other in a logarithmic scale graph.*

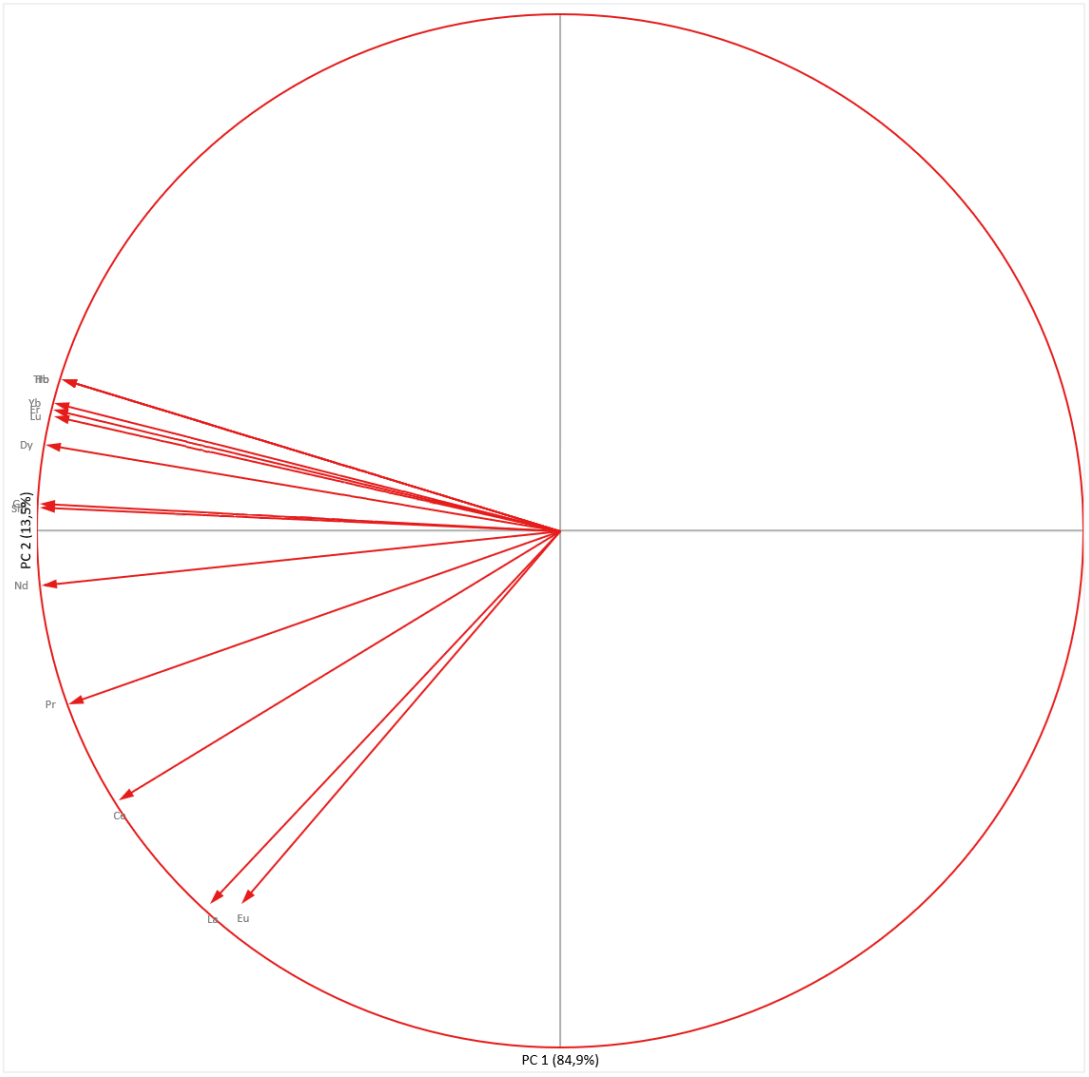

Figure 10.3: REE values projected into a PCA analysis graph, showcasing the affinity of each element.

The interpretation for this PCA graph is quite simple, with all elements showing relative affinity towards each other as expected, with only Eu, La and Ce showing a slight variation, to be expected as they often vary more than the remaining REE, whom otherwise share an expected high affinity.

10.2 Thin-section interpretation

Thin-section interpretation uses, naturally, microscopic observations as the basis for interpretating the minerals and textural relationships, however, EPMA and SEM/EDS analysis conducted on the samples provide further context as well as verify the compositions of each mineral and/or section.

SAL-03-03

The sample SAL-03-03 is Sph-style sample, and it can be divided into two zones with different behaviors. The first zone consists of sequential pulses of fluid interaction that originate four repeating sections (in regards to the mineral assemblage and texture), where the outer part of each layer (towards the vent) is rich in sphalerite (Sph-I), with less significant occurrences of dendritic oxidized sphalerite whereas in the inner part of each layer this tendency is reversed with the Sph-I present diminishing

abruptly in relation to its oxidized counterpart, it is also in this area that the typical isocubanite half-rings, surrounding the Fe-rich sphalerite (Sph-II) occur.

In the second zone all the minerals are evenly distributed in a chaotic setting, with the exception of Sph-II, which cannot occur except when surrounded by isocubanite rings.

These zones allude to the existence of a main pathway for fluid flow, which would form the cycling parallel layers (first zone), and a diffuse venting system for the same sample (second zone), which would justify this spread disposition of the channels and the remaining minerals.

In both zones covellite grains tend to occur next to isocubanite, indicating that they form as a result of its alteration at a later stage.

SAL-03-04

The sample SAL-03-04 is the sole representative of the po-style and the sample shows internal differences regarding the deposition of the minerals.

In the outer zone, where the grains have enough space to develop, large, elongated euhedral crystals of pyrrhotite form, often, within the same grain as isocubanite, which tends to form larger anhedral aggregates.

Near the center of the sample, space is tighter and therefore the minerals deposit in aggregates, with the main differences being the introduction of sphalerite, in contact with isocubanite, as well as pyrrhotite's grains showcasing a high degree of physical alteration, while still often being in contact with isocubanite.

SAL-03-06(1)

Sample SAL-03-06(1) is a Cu-style sample (Cu-poor), and similarly to both SAL-05-01(1) and SAL-05-01(2), it is only composed of isocubanite and chalcopyrite, which occur within the same grain in the form of an exsolution.

This sample shows a later stage of the vent's evolution (i.e. is a more mature vent) than the samples SAL-05-01, as it not only has a smaller relative proportion of isocubanite, but also, isocubanite can only be found in the center of the crystals, which indicates that the alteration occurs from the outside of the grain borders inwards (as every mineral is less stable in the borders due to open links in the chemical structure which makes the mineral less stable in those regions), whereas in the SAL-05-01 samples, both chalcopyrite and isocubanite appear indiscriminately within the grain with Figure highlighting this relative proportion of both minerals within the sample.

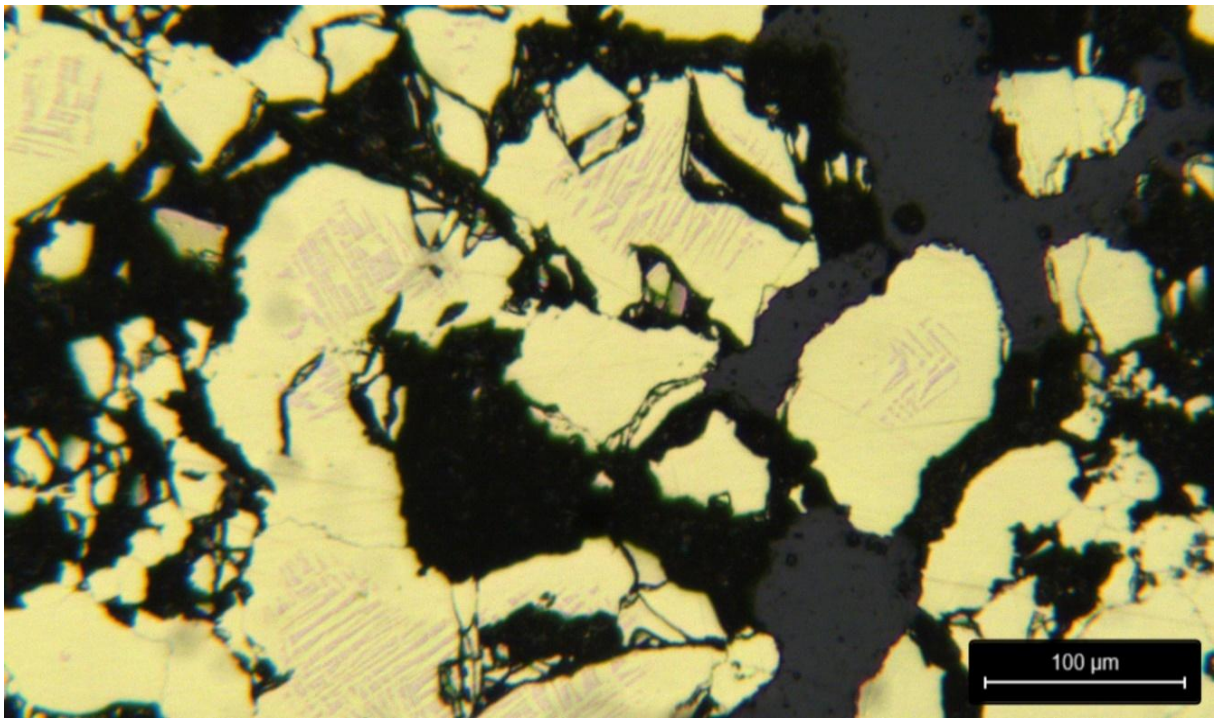

Figure 10.2: Relative proportion of chalcopyrite (yellow) and isocubanite (whiteish) in sample SAL-03-06(1).

SAL-03-06(2)

The sample SAL-03-06(2) is a Cu-style sample (Cu-rich) composed however of only two minerals, chalcopyrite and sphalerite. This sample is rather unique and is comprised of 4 chalcopyrite layers, with the outer one having sphalerite within the chalcopyrite grains. These 4 rings are only discernable by the porosity they present, and can also be identified via hand sample, however, chemically, the differences are minor, with the composition of chalcopyrite in each ring being roughly the same as the others. Apart from the last ring where we see Fe rich sphalerite, we can assume that all the remaining rings derive from the same liquid, and were formed under similar conditions, whereas at least for the last layer the conditions and liquid's temperature would presumably have changed. The sample tarnishes from oxidation with ease, which can usually be a sign of the chalcopyrite instability.

SAL-03-08

The sample SAL-03-08 is the most important sample of the Cu-style mineralization, as it is the sample in which the entire mineral assemblage of Cu-rich sulfides is observable, and thus is the sample that provides the most information available. The sample consists of a large chalcopyrite body, growing from the focal venting point towards the outer sulfate rich edge. The chalcopyrite, in contact with seawater, as indicated by the precipitation of sulfates in the outer zone and filling the cracks, suffers a supergene enrichment prompted by oxidation of the chalcopyrite, due to the difference between the original vent's fluid and seawater pH, forming Cu-rich minerals, those being bornite, pinkishgray chalcocite, chalcocite, and digenite. These newly formed minerals begin their transformation on the edges of the chalcopyrite grains, where the contact with seawater can be maximized, and the samples are more unstable (due to incomplete links in the chemical structure of the mineral), as such the sample shows a pattern in which, the Cu-rich minerals evolve in the aforementioned order, with bornite(rare) and pinkish-gray chalcocite mostly in contact with the chalcopyrite, and chalcocite and digenite in contact with the sulfates (though mostly the digenite) in the more evolved zones. Near the cracks, both magnetite and marcasite can be observed as sinks for the Fe and in marcasite's case, also S, of the supergene

enrichment. Occasionally, covellite can be formed, from a previously unaltered chalcopyrite grain, which occurs in the sulfate outer zone, highlighting significant variance in temperature from the vent's plume and the outer edge of the sample, as covellite should form at temperatures below the recorded vent's temperature (355º C).

In Figure 10.3, a zone of chalcopyrite exposed to one of the perpendicular cracks, filled with sulfates, that pass through the sample is shown, and the aforementioned evolution can be seen, though in this case, as the area between the chalcopyrite and the sulfates is reduced, at least when compared to what can be seen near the outer zones of the sample, the minerals in display are also reduced if compared to the total mineral assemblage, still, it is clear that the evolution is prompted by the sulfate zones, that alter the chalcopyrite, forming, in this case, pinkishgray chalcocite in the grain borders, with the fully developed chalcocite in contact with the sulfates. It is worth noting that, as previously mentioned, pinkishgray chalcocite is a solid solution between bornite and chalcocite, whose composition is in-between both.

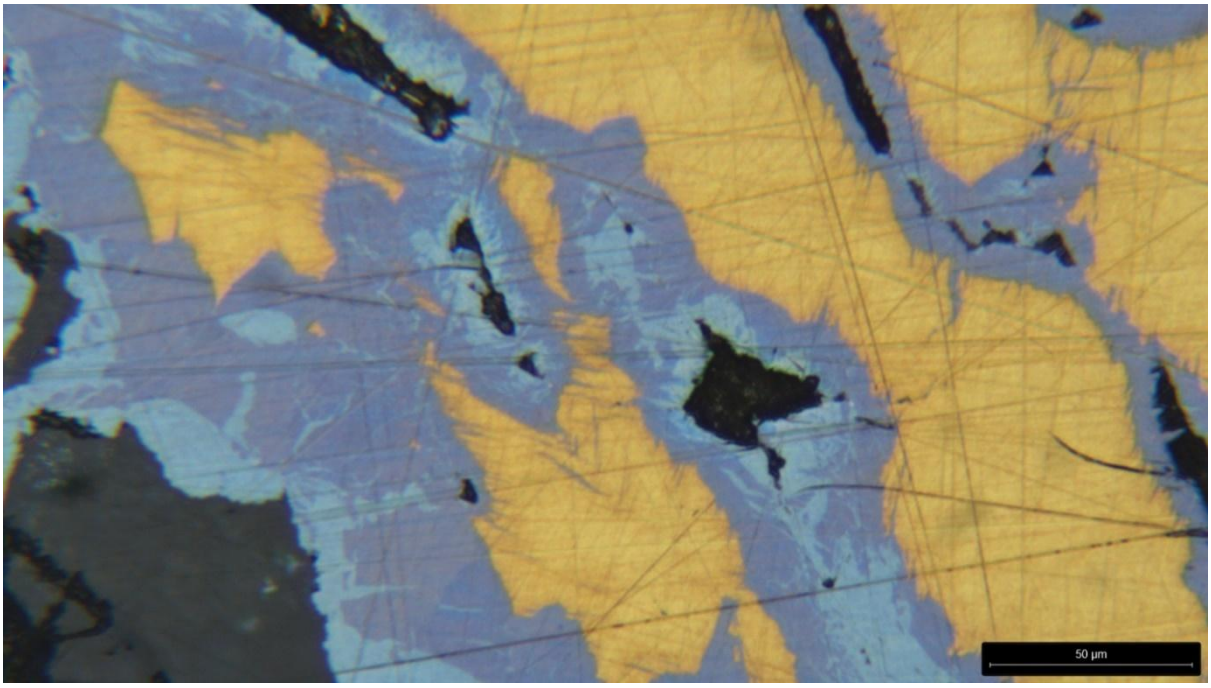

Figure 10.3: Transition between chalcopyrite and Cu-rich sulfides prompted by interaction with a crack in sample SAL-03-08.

The variation in the elements in the different minerals can be easily visualized in Figure which corresponds to a cross-section of the sample SAL-03-08 in which the relative proportion of each element in the passing mineral can be observed, with C representing the holes. The SEM/EDS imaging from the same figure. is also able to clarify any doubts that may arise to the evolution of the Cu-rich minerals from the interaction of chalcopyrite with the cracks where sulfates are deposited. The clearest image highlights the correlation of Cu and Fe in the samples, in which a higher Fe content is shown inside the cracks with the sulfates and in the chalcopyrite (as it is the mineral with the highest Fe and lowest Cu composition of the Cu sulfides) and a higher Cu content in the Cu-rich minerals.

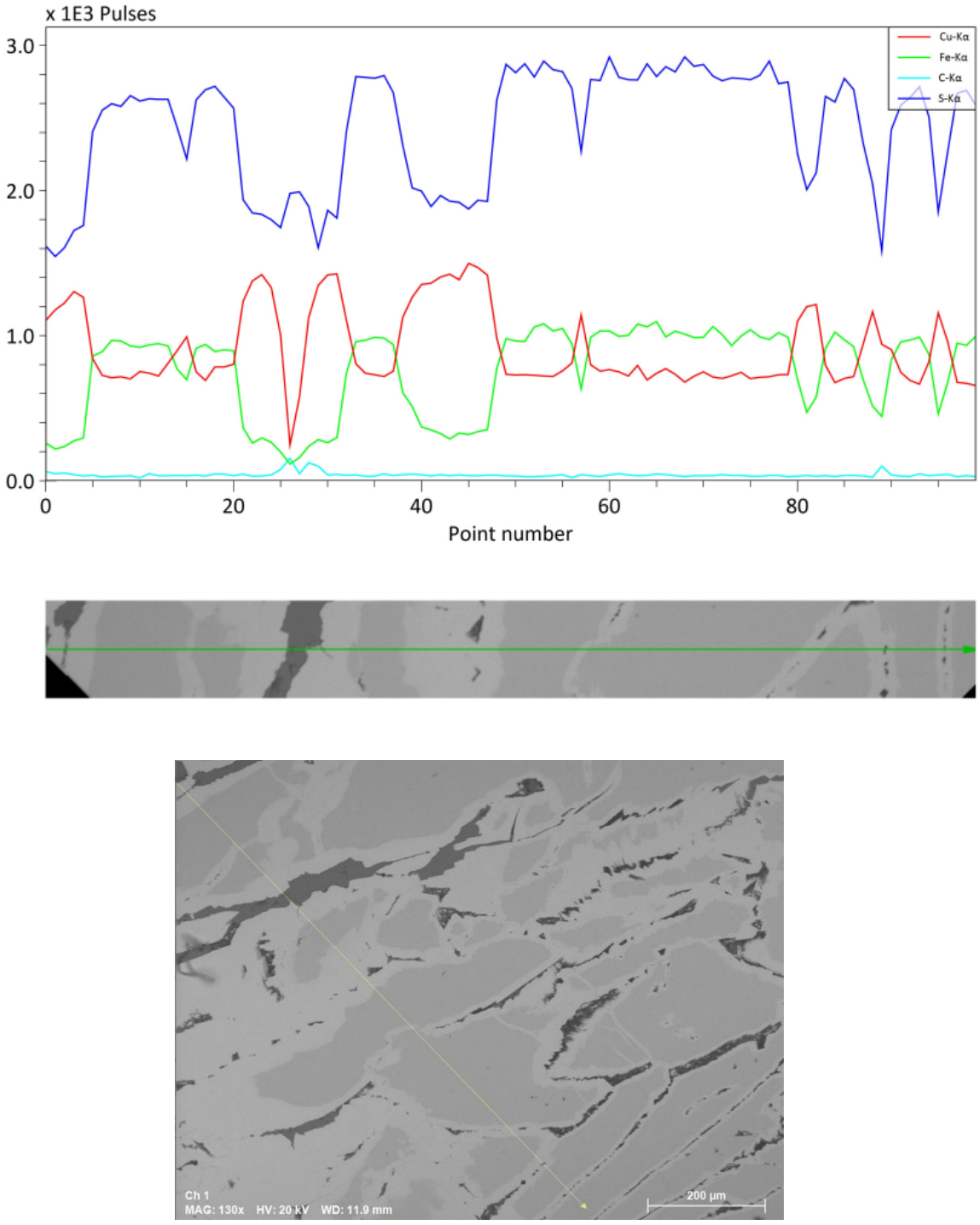

Figure 10.4: profile of EDS image, showcasing the variance in Cu, Fe and S in a zone affected by seawater interaction through cracks (dark grey), along with chalcopyrite (grey) and chalcocite (light grey).

SAL-04-02(1)

The sample SAL-04-02(1) represents a Cu-style (Cu-poor) sample, as it is mostly composed of chalcopyrite, which may present isocubanite exsolutions, however, the sample's isocubanite is present in such small quantities that this sample is close enough to the other sub-typologies, therefore not being the perfect example for neither of them. Regardless, this sample will still be considered as a Cu-poor sample, whose maturity is tricky to analyze, as in one hand the sample does have the smaller isocubanite proportion, but in the other hand, the grains that present isocubanite have an ubiquitous distribution of

the mineral within the crystals, which would indicate low maturity. Aside from the referred minerals, the sample also presents minor sphalerite, covellite and sulfates.

SAL-04-02(2)

The sample SAL-04-02(2) is the typical Sph-style sample, in which both the mineral assemblage and texture are "the standard" for this mineralization styles. As such, the sample consists of a large sphalerite body, in which two different types of sphalerites can be identified, the more common spotless sphalerite (Sph-I) and darker oxidized sphalerite (most likely previous Sph-I), and residing within this body, a set of late isocubanite rings, filled with Fe rich sphalerite (Sph-II). These filled rings represent a later deposition within the samples marking the filling of circulation holes, the filled holes in this sample have a random distribution, which indicate that there wasn't a sole, focal discharge point of fluid, but rather, diffuse venting.

The sample also presented an exterior Fe-oxide layer (crust), that likely formed at a later stage.

SAL-05-01

The sample SAL-05-01(1) and SAL-05-01(2) are perfect examples of immature vents (i.e. not fully developed), in which we see isocubanite being transformed into chalcopyrite.

Both samples show an unprecedent degree of instability, not only in hand samples, but also upon microscopic analysis. As for the hand samples, not only was the production of said samples quite difficult, as they would crumble and dismantle during preparation, leaving the thin surface uneven with a series of cavities and an overall irregular surface, but also upon microscopic analysis, the samples highlighted what was already evident, excessive holes and uprooting of the grains from the sample. Figure 10.5 presents a preserved grain with significant ampliation that withstood the process of abrasion of the sample in great amplification to show the relationship between isocubanite and chalcopyrite in these samples, with the chalcopyrite veinlets developing perpendicular to each other which end up ultimately engulfing the entire grain, after consuming the entirety of the isocubanite. It is also possible to observe in the figure how the chalcopyrite parallel lines seemingly merge.

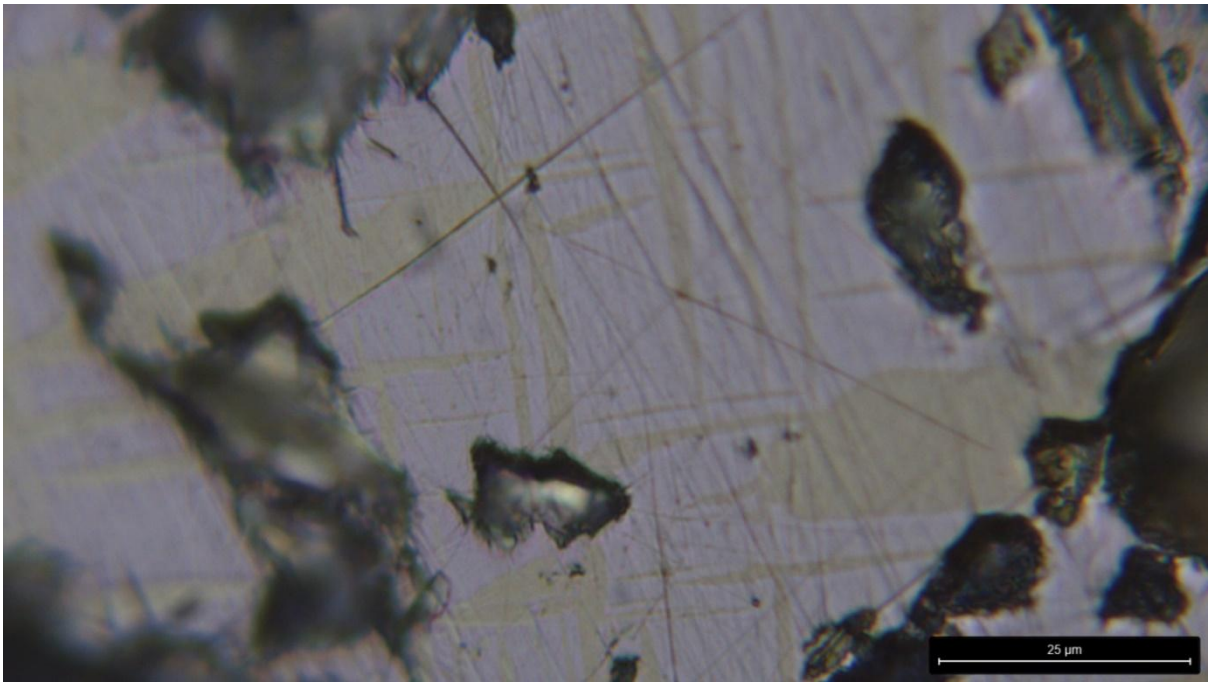

Figure 10.5: Photomicrograph for the close-up of a grain containing unstable isocubanite (white) suffering alteration to chalcopyrite (yellow) in the sample SAL-05-01(1).

SAL-05-03

The sample SAL-05-03 highlights the deficiencies of the isocubanite grains after formation when the temperature drops, as the veinlets of covellite surrounding the grains are most likely resultant from the instability existent prior to the diminishing of heat, which was ultimately caused by interaction the seawater has with vent and in particular with the minerals within, in which seawater enters in contact with the edge of the copper minerals, where they are more unstable, and depletes them of Cu, forming covellite. This can occur as a consequence of the system's temperature not instantly dropping, resulting in the system not being immediately closed, thus giving time for the instabilities to be exposed and alterations to the system to occur. This sample greatly differs from the remaining Cu-poor samples, as this sample's isocubanite is in comparison much more stable with the environment around it, with the borders slightly unstable but the overall mineral assemblage showing a great degree of stability, furthermore, since covellite is likely to have formed in the early stages of the process, the excess Cu that would be required to transform isocubanite into chalcopyrite was exhausted in the formation of covellite.

An interesting remark regarding this sample is that SAL-05-03 is the only sample in which covellite is formed not in contact with sulfites, not only that, it is also the only Cu-style sample in which isocubanite can be seen as stable to pseudo-stable.

Figure 10.6 highlights the covellite veinlets serving as grain borders, showcasing the fluid's interactions with each of the grains, and despite what is mentioned regarding a greater degree of stability compared to the remaining Cu-poor samples, the instability of the isocubanite can be testified, in thin section, by the slight color variances which can only be noticeable at higher resolutions as shown in the photomicrograph.

Furthermore, the sample exhibits an iron oxide crust, close to 1mm in thickness, marking the outer edge of the sample.

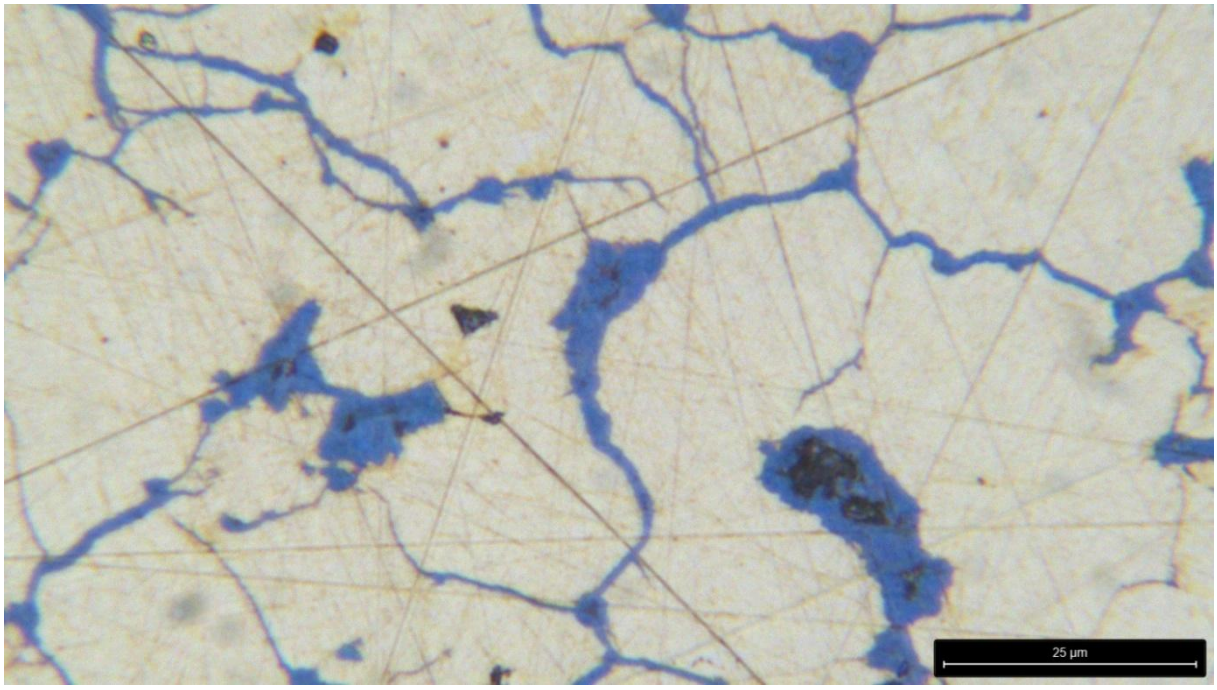

Figure 10.6: Close-up of the sample SAL-05-03, highlighting the pseudo-instability of the isocubanite which is marked by the slight color variations within the isocubanite, regardless, in this sample, isocubanite appears much more stable, when compared to the remaining samples, furthermore it shows covellite in the grain borders, where alteration has a greater effect.

SAL-05-04(1)

This sample falls under the category of Sph-style samples, which for the most part are all identical, as such, the description won't vary much from what has been previously stated for the equivalent samples. So, as expected, sample SAL-05-04(1) is composed of a large sphalerite body, which represents the primary mineral deposition event, where featureless sphalerite (Sph-I) and oxidized sphalerite (which is likely to have previously been Sph-I) can be found. The second mineralization event still consists of isocubanite rings around a newly-formed sphalerite, rich in Fe (Sph-II).

However, in this case, there is a noticeable difference, instead of a single isocubanite ring, there are multiple rings surrounding the sphalerite, forming a loop of rings, as shown in Figure 10.7. The figure also highlights the difference between the spotless sphalerite (Sph-I) and the Fe rich variance (Sph-II). Figure presents a single filled hole, in which the looping of the rings is clearer. This information can be one of the keys to the understanding of this second wave of liquid that reaches the samples and leads to the deposition of two different minerals, formed, presumably, in the same temporal interval, therefore alluding to the immiscibility of the two minerals and several liquid discharges separated through time in this sample.

From these images, in particular Figure 10.8, where besides the cycling pattern (mostly on the left side), rings next to each other also seem to form, it seems likely that there is somehow a frequent delivery in small batches of liquid, that in this case, cannot full fill the circulation channels, and therefore allow for later batches to come in and form new rings inside the already partially filled holes.

Similar to samples SAL-04-02(2) and SAL-05-03, this sample has an iron oxide crust close to 1mm in thickness.

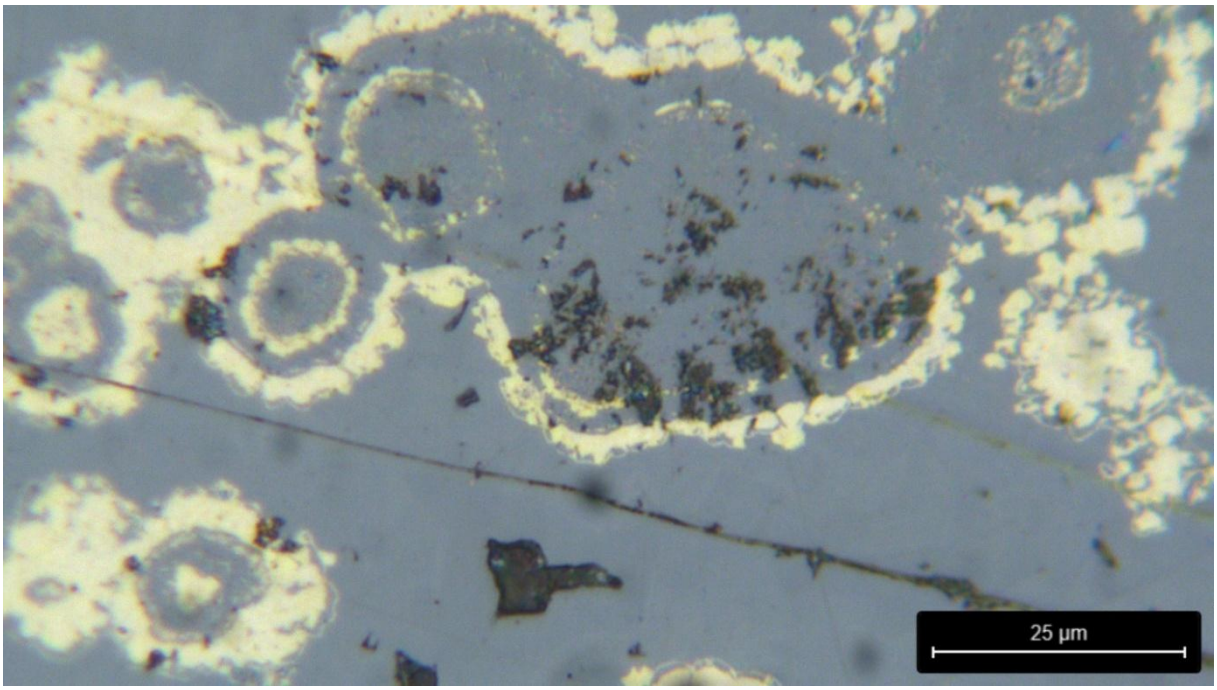

Figure 10.7: Multiple isocubanite rings in the same large structure in sample SAL-05-04(1).

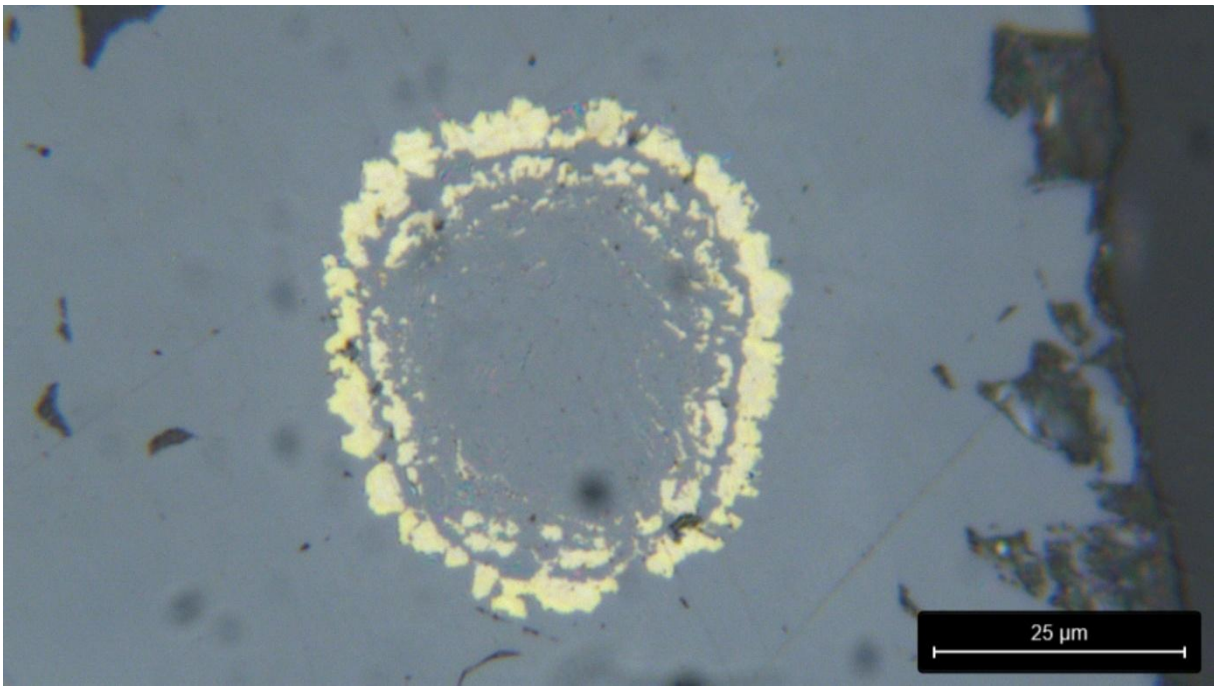

Figure 10.8: Multiple isocubanite rings surrounding each other in the same structure in sample SAL-05-04(1).

SAL-05-04(2)

The sample SAL-05-04(2) is particularly interesting from a mineralogic standpoint as there is a clear transition from a severely altered set clusters made of chalcopyrite closer the outer edge, to a preserved more recent, large ring of chalcopyrite, near the center, that towards the outer zones, is altered to bornite, in perfect preservation conditions, by the same supergene enrichment process already discussed for other samples, however, in an early stage, which means that the only non-sulfate minerals, besides

chalcopyrite and bornite are covellite and magnetite, in small quantities, near the bornite-chalcopyrite frontier.

The remaining of the sample is composed of sulfates, which represent the greater part of the sample.

A photomicrograph as well as three EDS maps of Fe (red) and Cu (blue) and the combination of both in the same location, with backscattering so that the grains are well defined, is presented in Figure , and it highlights the evolution of Cu and Fe between the original chalcopyrite and the Cu-rich bornite, while also showing where exactly covellite and magnetite form.

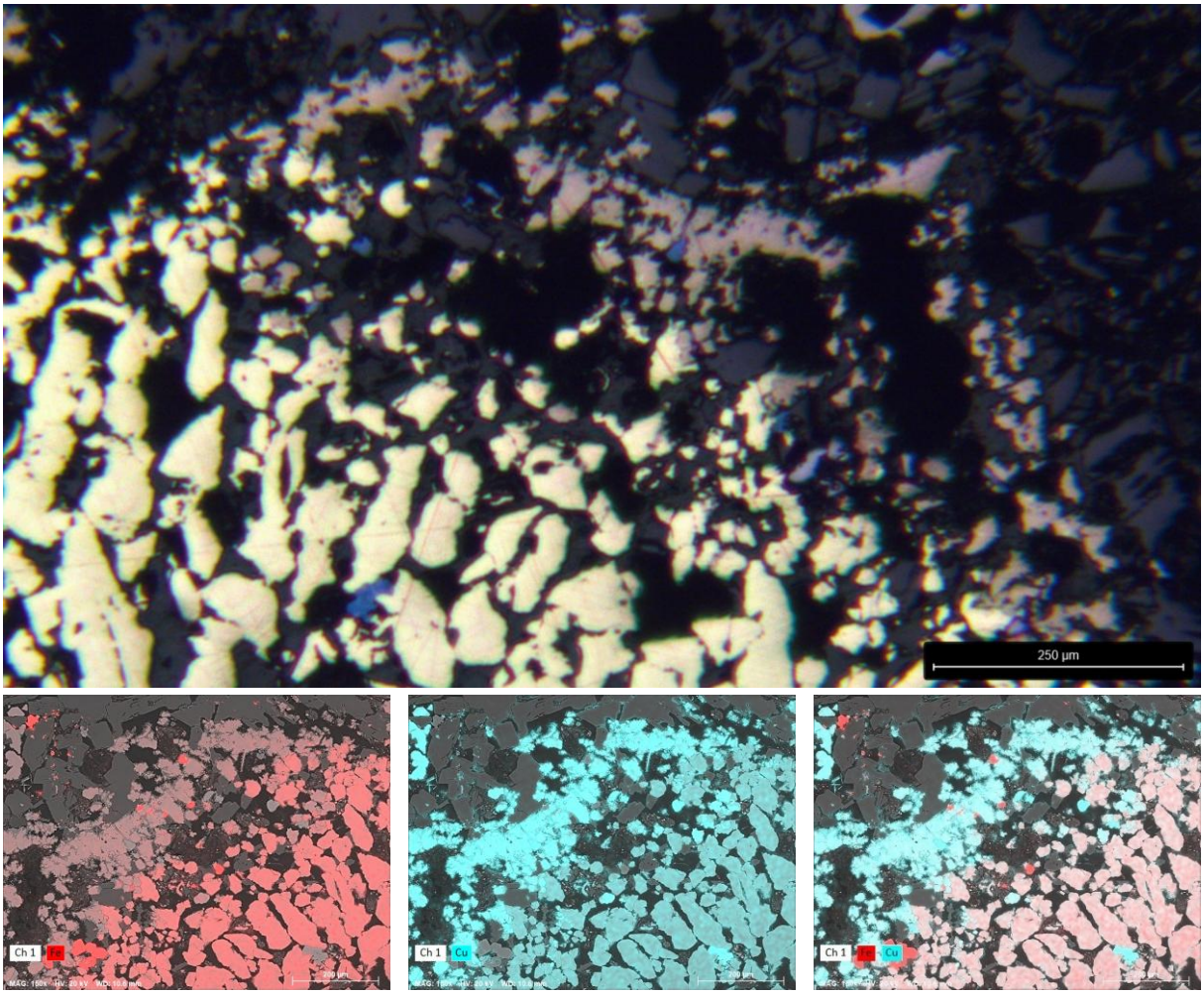

Figure 10.9: Photomicrograph and EDS imaging (photomicrograph for Fe[red], Cu[blue] and both) of the sample SAL-05-04(2) highlighting the transition from chalcopyrite to bornite (left to right in the photomicrograph), while simultaneously showing the compositional differences of both minerals, along with magnetite and covellite.

SAL-05-05(1) and **SAL-05-05(2)**

Both SAL-05-05 samples are composed almost exclusively of chalcopyrite rings in a sulfate matrix, making them the typical Cu-style(Sulfates) samples. Similarly to what is seen in the sample SAL-05-04(2), the tendency in both SAL-05-05(1) and SAL-05-05(2) samples persists in which older chalcopyrite clusters have tendentially suffered more alteration, while the newer chalcopyrite tends to remain unaltered, with the main difference being that in these samples, chalcopyrite will appear in rings or half rings around what was presumably the remains of latest (at the time) vent conduits. The difference

between newer unaltered clusters and older altered ones can be seen in Figure 10.10, where, in the same sample, SAL-05-05(1), different stages of deposition can clearly be interpreted, with the same exact tendency in the sample SAL-05-05(2).

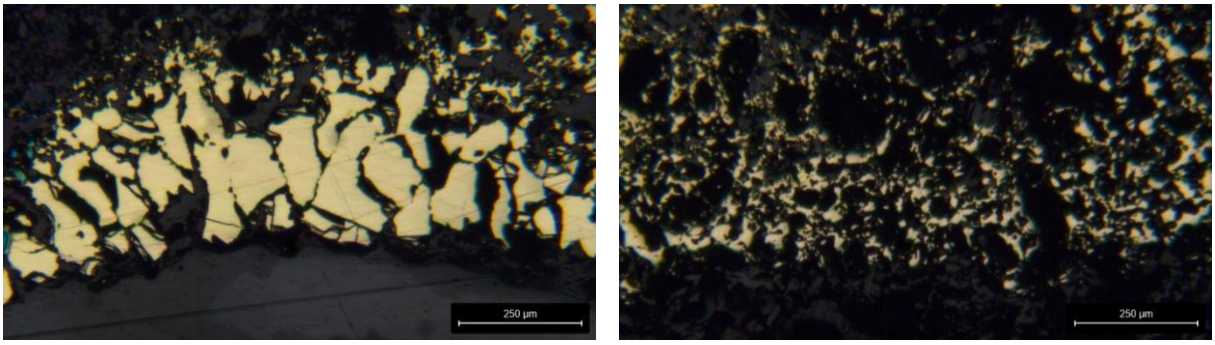

Figure 10.10: Unaltered (left) vs altered (right) chalcopyrite in the samples SAL-05-05, highlighting the alteration over time of the samples.

While both samples are identical, in one of the more developed rings of the sample SAL-05-05(2), a supergene enrichment occurred, and bornite, pinkishgray chalcocite and chalcocite and rare digenite can be seen, with once again, both covellite and magnetite forming as a result of this process. This sample showcases the perfect example of the bornite to pinkishgray chalcocite transition as presented in figure 10.11, where this transition can be seen at a great ampliation, which allows an observation of grains still in the transition between the two different mineral phases.

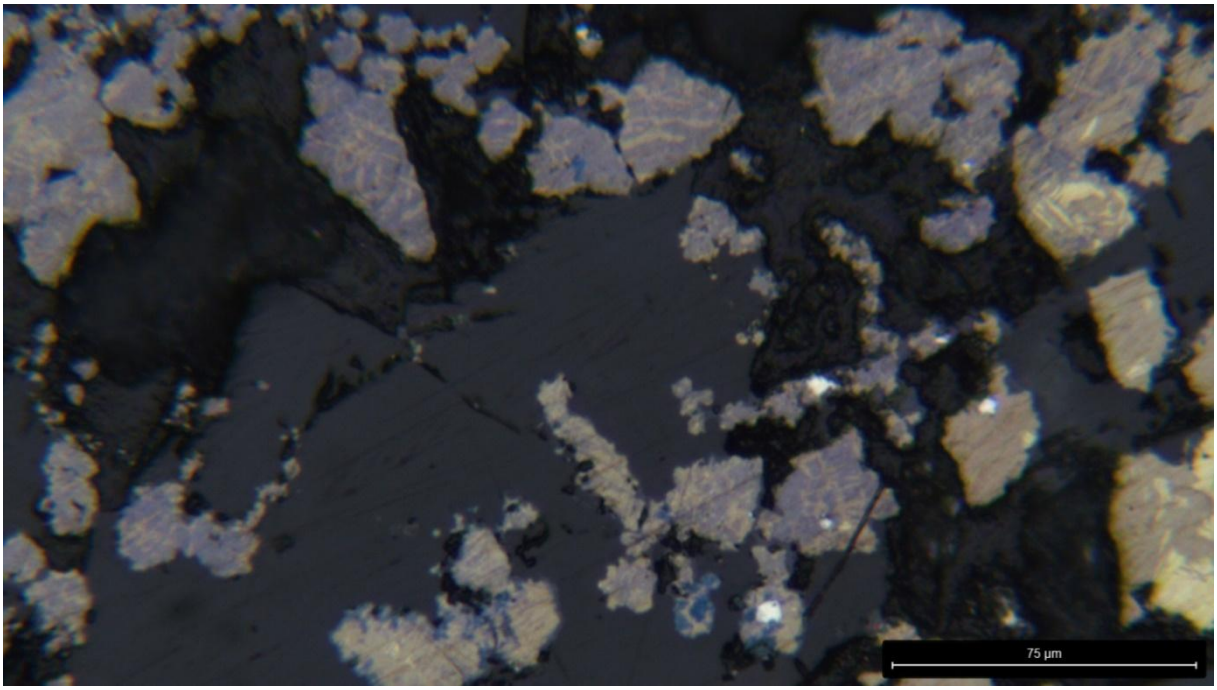

Figure 10.11: Transition from chalcopyrite to bornite to chalcocite (right to left) in the sample SAL-05-05(2), highlighting the increase in Cu in the mineral assemblage.

11. *In-situ* S isotopes - $\delta^{34}S$

For the purpose of this work, 56 in-situ isotope $\delta^{34}S$ analysis were made, distributed by 6 of the SAL samples, those being SAL-03-03 (6 on Sph-I, 2 on Sph-II and 3 on isocubanite), SAL-03-08 (14 on chalcopyrite and 3 on chalcocite), SAL-04-02(2) (3 on Sph-I, 1 on Sph-II and 2 on isocubanite), SAL-05-01 (8 in a mix between chalcopyrite and isocubanite), SAL-05-03 (6 on isocubanite) and SAL-05-05 (8 on chalcopyrite). The precise location of each of the analysis in the respective sample, as well as a table with the full $\delta^{34}S$ values is present in the **APPENDIX VI.II**, with the exception of sample SAL-05-03, in which the results were taken from random isocubanite grains.

As it is often observed in these samples, the determining factors in the sample's behavior are the mineralization style and the maturation of the samples (i.e. how evolved the samples are), as such, focusing on these factors presents more objective division for these samples, which apart from sample SAL-05-01 all fall under the category of mature samples, which means that the sample SAL-05-01 must have its own category when presenting these results. This is in line with what's been mentioned in chapter 4. Sulfur Isotopes as Geochemical Tracers of Mineralizing Processes, when the question of how the variation of $\delta^{34}S$ ‰ in Rainbow sulfides regarding age and activity of the vents is posed in Table 4.1. which already provides an insight into how the sphalerite will behave versus chalcopyrite, in other words how the Sph and Cu-style minerals will fare.

As such, Figure 9.1 presented once again, shows a clear distinction between the two main mineralization styles in Sph and Cu style, with the latter having two of its sub-styles represented.

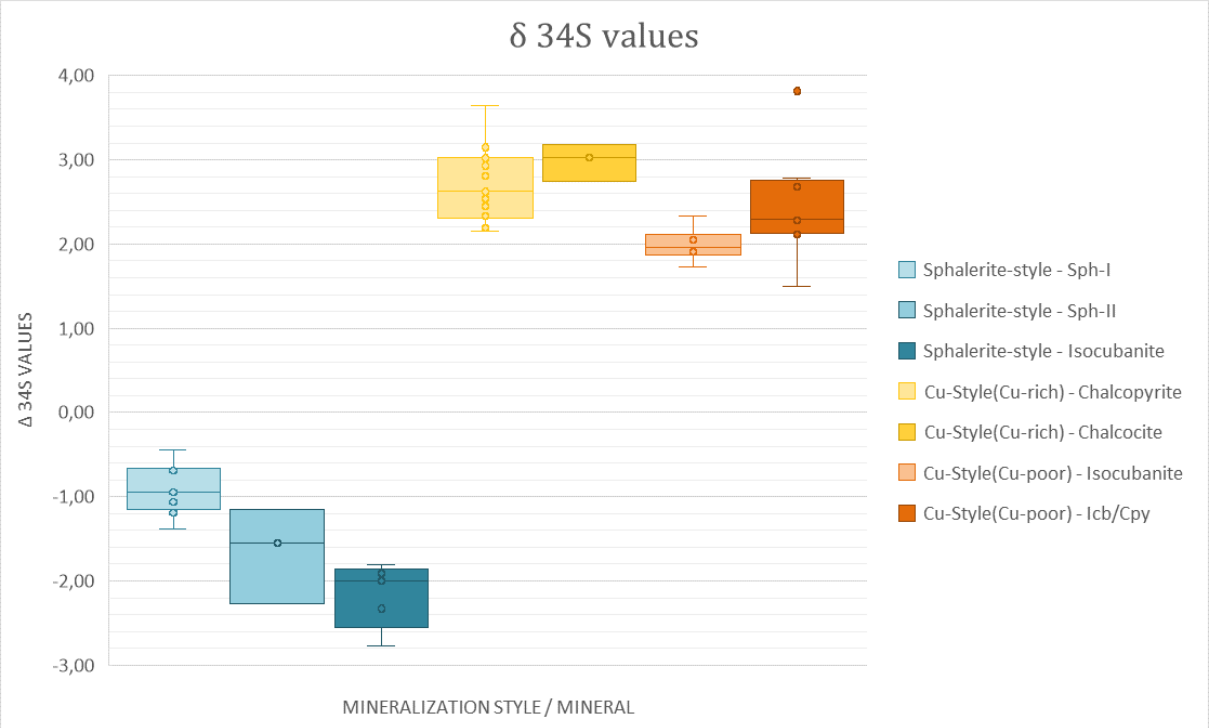

Figure 9.1: Boxplot showing the $\delta^{34}S$ composition of sulfide minerals of the Rainbow samples grouped by mineralization styles and mineral phases. Sphalerite-style minerals (Sph-I, Sph-II, and isocubanite) Cu-style minerals (chalcopyrite, chalcocite, and isocubanite) display consistently positive $\delta^{34}S$ values, the figure is once again shown to highlight the noticeable difference between the $\delta^{34}S$ values for both mineralization styles

The first noticeable feature in the comparison graph presented in Figure 11.1 is how slim each row is (i.e. how precise the values proved to be), with a variance that remains close to an order of magnitude below some of the other values, this fact likely stems from something that was previously mentioned,

the $\delta^{34}S$ values were taken *in-situ*, which is reflected in the precision of the SAL values, however, the same cannot be said for the remaining presented samples, given how large the $\delta^{34}S$ intervals are.

Furthermore, it is clear that the minerals from the Cu-style mineralization style only appear with values above zero, contrary to the Sph-style mineralization values that sit below zero. This is important as a relative positive enrichment is expected in these type of samples, therefore implying unique conditions for the Sph-style minerals, not only that but in this figure, seawater is also represented on the far right, as to highlight its influence during the deposition and reworking of the samples, the large distance between the seawater and the minerals also showcases how much they differ and why, in an environment where seawater is virtually infinite and the samples are in constant interaction/contact with it, the $\delta^{34}S$ values of the minerals tend to increase over time.

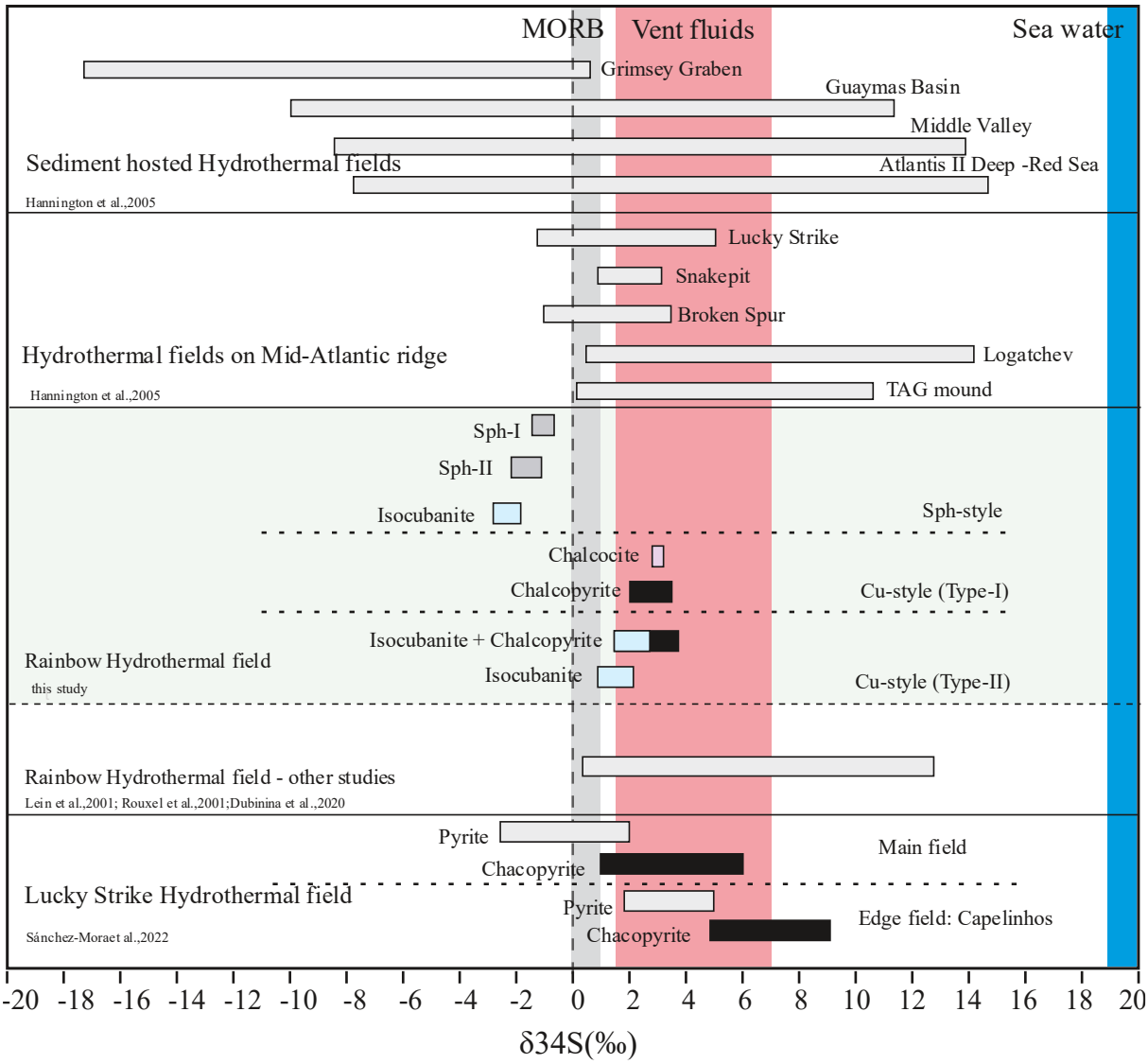

Figure 11.1: $\delta^{34}S$ values for MAR samples of various fields, amongst which Rainbow's SAL samples are included (green).

11.1 Cu-style:

The first conclusion that can be drawn is that there are higher $\delta^{34}S$ values for higher Cu content and subsequently lower S/Fe content.

Chalcocite has an high $\delta^{34}S$ value due to the fractioning that happens during the supergene enrichment, more precisely during the leaching of S from the chalcopyrite, where the lighter S isotopes tend to move away from the chalcopyrite, leaving behind the heavier isotopes.

Following the same logic, it can be concluded that the higher $\delta^{34}S$ values in chalcopyrite occur near zones where contact with seawater is evident by the presence of sulfates (e.g. near the outer edges and large, fluid flowing holes), which again, as a result from interactions with seawater leads to the fractioning of $\delta^{34}S$. This variation is clear and can be observed near cracks and close to the outer edge in sample SAL-03-08.

As per Dang et al.,(2024): "Previous experimental simulation and theoretical calculations have indicated the incorporation of sulfur derived from reductive seawater sulfate could result in an elevation of $\delta^{34}S$ values in associated fluids. Specifically, during the process of the mixing of upwelling fluids (350℃) with circumambient seawater (2℃), the $\delta^{34}S$ values of the fluids are expected to increase from approximately 1－1.5‰ to 1.5－4.5‰".

These observations align with the data provided and further justify the increase in $\delta^{34}S$ that chalcocite suffers after evolving from chalcopyrite, not only that, but it also encourages the discussion of whether the chalcopyrite in Cu-rich samples may have evolved from isocubanite (which is likely as isocubanite may originate from ISS - intermediate solid solution), especially considering that the Cu-poor SAL samples provide different stages of the evolution from isocubanite to chalcopyrite. Even the values from isocubanite, while stable, were most likely enriched, as the covellite in the analyzed samples in contact with the isocubanite grains is likely resultant of seawater interaction, thus staying in line with the previous statement.

If we were to take Isocubanite values in this samples as a whole, it would be hard to objectively analyze as the samples present in some cases an unstable version of the mineral also known as intermediate solid solution (ISS), which leads to varying results. Not only that, but when considering only the analyses labeled as "Cu-Style(Cu-poor) - Icb/Cpy", the analyses themselves don't indicate whether the analyzed mineral was chalcopyrite or isocubanite as the two can be quite difficult to distinguish under SEM imaging.

Upon further analysis, it is clear that a greater degree of stability from the samples has a strong correlation to the constrained $\delta^{34}S$ values. As such, the significance of the analysis can be inferred by the varying degree of reworking and stability that can be interpreted from the samples.

Regarding specifically Cu-poor samples SAL-05-01, even if the goal was to try to identify the correct minerals, the results would still be to be scattered and unpredictable, likely due to the fact that these samples show a faint evolution and therefore can be regarded as being extremely immature in their evolution/reworking process.

The polar opposite would be Cu-rich samples such as SAL-03-08, which shows the highest degree of reworking amongst all the samples, and, as such demonstrates quite a predictable evolution of the $\delta^{34}S$ values, particularly when taken into context the placement of the analyses shown in Figure 11.1 (that can be further analyzed by the data provided in **APPENDIX VI)**, as the values presented reflect, not only the mineral analyzed, but also the proximity to places where the seawater would have interacted with the sample (i.e. outer edge, cracks and holes). Another example would be sample SAL-05-03, which presents the most coherent results, where out of 6 randomly chosen isocubanite grains, the $\delta^{34}S$

values only vary 0,39‰, between 1,94 and 2,33‰. Meanwhile, "Cu-Style(Cu-poor) - Icb/Cpy" $\delta^{34}S$ values vary between 3,82 and 1,49‰, representing a fluctuation of 2,33‰.

Overall there is a predictability in these values, where, taking into consideration only the stable samples, it is almost possible to identify the mineral by the $\delta^{34}S$ value alone, with the biggest take-aways being the possibility to understand the mineral behavior simply by observing the variance in the $\delta^{34}S$ values. Another important fact to notice is the evolution of the $\delta^{34}S$ values directly corelating to the increase in Cu and subsequent decrease in Fe/S, though in this case the reason behind this correlation would be that both occur from the same cause, the evolution (i.e. subsequent reworking) of the minerals within the sample.

11.2 Sph style:

Once again for the Sph-style, the first thing that jumps out is the evolution of the $\delta^{34}S$ values, that can also be seen decreasing with the increase in Fe, similar to what is seen on the Cu-style samples.

Sph-style sample's maturity is hard to assess, as the variation amongst the samples is virtually non-existent, which could be interpreted as the samples simply showing a decent degree of maturity (which might likely be the case as all the samples show the deposition of both early and late minerals, whose existence implies a certain degree of evolution), nevertheless, while the results may present some degree of variance, they fall into specific zones, characteristic of each mineral.

As such, the evolution of the $\delta^{34}S$ values, while less restricted, falls under the same constricts of Cu-style.

The first mineral to deposit, Sph-I, is poor in both Fe and Cu, when compared to Sph-II and isocubanite, invalidating the possibility that the $\delta^{34}S$ values would somehow be related to Cu content. However, in order to understand these values, a brief recapitulation must be made as the evolution of the samples seems once again to be the kay factor. In a first instance, the sample deposits the "standard" sphalerite, Sph-I, whose value is higher than both Sph-II and isocubanite, as they represent late minerals, richer in Fe and thus, likely of lower temperature associations and a more evolved liquid, that was suffered a higher degree of fractionation from the source and couldn't carry the heavier $\delta^{34}S$ (i.e. at an higher temperature the liquid with minimal fractionation is able to move an heavier $\delta^{34}S$, while after multiple instances of fractionation, the colder liquid with a decreased ability to transport elements becomes more selective, which leads to the increase of $\delta^{34}S$ values for the late minerals).

This would imply that isocubanite and Sph-II came in the same liquid and were mixable at the temperature of the liquid, but not at the temperature it deposited, thus differentiating the two minerals, and leaving behind the heavier $\delta^{34}S$ in the Sph-II, and expelling to the outer edge of this circulation channel the lighter $\delta^{34}S$ within the isocubanite, which would perhaps justify the overlap in the values. It is worth noting however that the value closer to isocubanite values is clear to be Sph-II, while the other two are in a zone that could be open to debate (even though they appear to indeed be Sph-II).

Biogenic reduction does not appear to be a particularly important factor, since the values within the same mineralization style appear to be within precise intervals (i.e. are somewhat predictable), though their influence cannot be ruled out as a justification for the negative values.

These observations for the Sph-style seem to disprove what's been mentioned in chapter 4. Sulfur Isotopes as Geochemical Tracers of Mineralizing Processes:

"Dubinina et al. (2020) provides evidence that the $\delta^{34}S$ values for early sulfides seems to always be 1-2 ‰ lower than for late sulfides,[…] thus attributing the variation in $\delta^{34}S$ solely to the fluid evolution".

It is clear from these observations that the evolution of each mineral within the sample is not only crucial to the understanding of the samples as a whole, but also crucial to the understanding of the evolution of the Rainbow field and not simply the fluid evolution as previously suggested. It is also clear that this evolution takes a big role in determining the $\delta^{34}S$ values for each mineral, and that the lack of maturity disrupts the otherwise fairly predictable values of $\delta^{34}S$.

Nor Fe nor Cu contents are an influential factor in $\delta^{34}S$, however, they are partially a product of the same constricts that influence $\delta^{34}S$, those being the evolution of the liquid and the sample.

In the case of the possibility of Cu-rich samples evolving from Cu-poor samples is disproved, a new argument must be provided as to explain why would chalcopyrite $\delta^{34}S$ values be higher than for isocubanite, but since it can't be as of now neither proved nor disproved that all chalcopyrite must evolve from isocubanite, both sub-styles shall remain, and the reasoning behind isocubanite $\delta^{34}S$ values shall remain in question.

It may however simply be a reflex of the higher temperature and subsequent ease to transport material (which is known to happen in Cu-rich vents), including heavier isotopes, compared to Cu-poor samples, that likely formed under lower temperatures.

12.Conclusions

Three main sulfide mineralization styles are recognized as the surface expression of hydrothermal system that makes the Rainbow vent field in the Mid-Atlantic Ridge, south of the Azores. In broad terms these mineralized rocks likely share the overall genetic process, with the sole difference being either the temperature, the degree of evolution and distance to the main fluid pathway.

To address this, each sample was meticulously studied, in which resulted the detailed petrographic descriptions, that serves as a foundation for the interpretation of the geochemical analyses. These analyses complement the information and add to the geochemical nature of each mineralization style, adding a layer of certainty to the mineralogical conclusions (namely the interpretation of the reworking of the samples) proposed to justify the intricate processes occurring in the Rainbow Hydrothermal Field.

Petrography suggests the existence of three different mineralization styles, to whom several minerals may be associated, which can be separated into three different overall mineral assemblages. As such the three mineral styles previously were defined as Cu-style (further subdivided in three sub-styles), Sph-style and Po-style, with Po-style as the only one not being presented in this work with significant changes.

The correlation coefficient matrixes offer insight as to which elements present or not compatibility towards each other and with 4 major elements representing the greater part of the samples (those being Cu, Fe, Zn and S), it becomes possible to draw relationships between each element, and the respective minerals/ mineralization styles.

In Cu-style samples Cu often shows a very negative correlation, with the remaining three elements, this happens for two reasons, the first one being the general incompatibility between Cu-rich sulfides and sphalerite (ZnS), hence, the only Cu sulfide commonly in contact with sphalerite being isocubanite and in rare cases chalcopyrite (though the latter is simply a reflection of liquid evolution), the other reason stems from how Cu-rich assemblages form, a supergene enrichment in which Cu, the more stable element at high temperatures remains, whilst Fe and S, less stable, migrate outwards of the sample.

As for the Sph-style samples, Zn's behavior largely describes the overall behavior of the samples as they are almost mono-mineralic sphalerite aggregates.

As the data demonstrates, the values for S remain stable regardless of the analyzed mineral and thus, there is no correlation between S and Zn, nor positive, nor negative, the same however can't be said for Cu and Fe, as both elements showcase a strong negative correlation towards Zn, justifiable on two factors, the first would be the obvious compositional difference from isocubanite [CuFe2S3] and sphalerite [(Zn,Fe)S], in which Fe is only accessory, with the second hidden in the compositional differences between the spotless Sph-I and the Fe rich Sph-II, which also happens to present a slight increase in Cu, proportionate to the increase in Fe and since S is unaltered regardless of the mineral's composition (in the main minerals of these samples, thus excluding the microscopic galena grains analyzed), Zn has to decrease in the sample to accommodate the two elements. It is also worth noting that this is the only instance throughout the three mineralization styles in which Cu shows a positive correlation with any of the remaining three main elements.

As for the po-style, Fe should naturally be the main focus, as it not only is present in every mineral, but is also the main element found in pyrrhotite.

Unlike in other mineralization styles, the minerals' composition in sample SAL-03-04 (the only po-style representative) all have a slight variance in S values, and those are directly proportional to the values of Fe, which indicates an extremely high correlation with all the minerals, having significant quantities of S, with Fe and Zn disputing over which is the remaining major element, their proportion becomes

indirectly proportional and thus, these two elements shows a strong negative correlation with each other, finally Cu is only present in isocubanite and as per usual, has a weak correlation with the remaining three elements.

These sets of observations help, not only to understand each mineralization style's behavior, but also reflect a few tendencies for the overall field, namely the way Cu behaves, showing great negative correlation with most major elements, which could be indicative of either the tendency for Cu to deposit at an higher initial rate at first and then either being exhausted quickly or the system simply not being capable to efficiently transport Cu (due to temperature decreases) or, most likely, a mixture of both factors.

Furthermore, the values in correlation coefficient matrixes for each sample presented in **APPENDIX V.II**, share the same tendencies with each individual analysis as well as the overall results, showcasing how this data can be used to identify and understand each mineralization style.

$\delta^{34}S$ values represent an important portion of this thesis' work and help uncover information about not only the evolution of the Rainbow field but also any similar field, as such, these results and trends should be interpreted for each of the mineralization styles in which they were analyzed, in order to further support the conclusions that the microscopical and chemical analyses provided.

For the two different analyzed mineralization styles, $\delta^{34}S$ show a notorious difference, even if the same mineral is analyzed. As such, these analyses should be made always considering the mineralization style to whom they belong, as that clearly proves to be the more influential factor in these values.

In Cu-style samples, an easy to observe trend consists of higher Cu compositions corresponding to a higher S isotopic value. Specifically in the sample SAL-03-08, the isotopic values within chalcopyrite are related to the degree of influence of fluids, whether those be in form of holes or if the sample was near the altered zones (i.e. near cracks and/or the outer edge, where the seawater had a greater effect), where the most relevant transformations occur.

Higher Cu is resultant of element leaching by supergene enrichment (prompted by the interaction with the oxidizing seawater) and thus, the smaller weight isotopes will present an increased relative mobility and therefore a higher Cu elemental proportion will reflect an increase in isotopic values, further augmented by the degree of evolution of the Cu sulfide. It is worth noting that the Cu proportion is the main identifier of each mineral and the relation with the sample's evolution is simply regarding the fact that Cu, the same way as the heavier $\delta^{34}S$ tend to remain in the sample rather than escaping.

As the leaching process progresses, lighter isotopes will escape the system, while heavier ones will be trapped, thus creating a "false" isotope S^{34} enrichment, which does not reflect the liquid's behavior, but rather the sample's interaction with the seawater and the sample's own evolution (i.e. this increase is post-deposition and so does not reflect the behavior of the liquid).

Therefore, for the Cu-style samples, one of two possibilities should occur:

Either all Cu-style samples stem from isocubanite with different degrees of evolution/reworking, meaning that all chalcopyrite should have evolved from isocubanite and, thus, the $\delta^{34}S$ increase from one mineral to the other in a process similar to what has been described for the evolution of chalcopyrite to Cu-rich sulfides, or, conversely, both minerals deposit as they are directly from the liquid and chalcopyrite, likely due to fractioning in the liquid and forming tendentially at higher temperatures, simply has a greater capability transport heavier S isotopes.

In Sph-style samples, inversely to Cu-style, it is possible to observe a trend consisting of lower Cu compositions corresponding to a higher S isotopic value.

However, in Sph-style samples it is clear that the greatest factor involved in the determination of the isotopic values is the evolution of the liquid that originates the mineral phase in question, with greater

evolution being associated with lower temperature phases that would hinder the capabilities of transport of the liquid, thus limiting such transport to lighter isotopes.

For isocubanite's description, presented in chapters 8.3 and 8.4, it is mentioned that during the evolution of the Sph-style, isocubanite, surrounding Sph-II, should logically be the first of the two minerals to deposit and since they both share the same liquid, though both are immiscible with one another this results in the deposition of the two different mineral phases, however, $\delta^{34}S$ values in isocubanite are lower than in Sph-II, which could allude to the possibility of an initial deposition of both minerals, still at high temperatures (at which they would be partially miscible) followed by a decrease in the temperature that would see the two mineral forms differentiating from the initial composition, with isocubanite being "expelled" outwards leaving behind part of the Fe, Cu and importantly the heavier $\delta^{34}S$. Alternatively, these values may simply be due to the constricts of each mineral and how much their transport/deposition capability.

A rather interesting factor is how by watching the isotopic values for different minerals and understanding their deposition order, as well as the (evolutionary) order of the mineral styles, it is possible (to a certain degree) to predict the mineral in question, or at the very least, a range of possible minerals and even the order in which minerals deposit (considering the mineralization style has been identified) having only access to their $\delta^{34}S$ values, which suggests that the understanding of $\delta^{34}S$ values may be the key to understanding the deposition order/evolution of these hydrothermal systems.

While this work provides a lot of answers and clues regarding the Rainbow hydrothermal field's behavior and evolution, some questions still remain, especially in regard to the association of the same mineral phases in different mineralization styles, namely sphalerite as it not only plays an extremely important role in the Sph-style , but also features in the remaining mineralization styles.

This question stems from the difference between Sph-I and Sph-II in Sph-style mineralization (and how they compare to po and Cu-style), which is easily identifiable given a basic understanding of the samples, while also highlighting the expected evolution of the liquid, and while this sphalerite evolution is only noticeable in Sph-style mineralization, the same evolution principles could apply to the remaining liquid phases that are in the origin of different mineralization styles.

A varying degree of Fe within the Cu-style sphalerites in sample SAL-03-06(2) was also noticed, but it most certainly represents the evolution of the liquid and its increasing capacity to transport Fe at lower temperatures, as its presence seemingly increases further from the main venting orifice. However, due to a small sample size and the absence of isocubanite, it is hard to directly link the sphalerite in these samples with Sph-I and Sph-II, it is possible to say however that their composition and behavior close resembles Sph-II since their chemical composition is closer related (as it shows higher Fe and Cu proportions when compared to typical Sph-I values) as well as the required association to Cu sulfides, from which they may include partially some elements that may justify the Fe and Cu increase.

All which begs the question, is the composition of the sphalerite in Cu-style samples closer to that of Sph-II due to the evolution of the liquid (as it also represents a later stage of deposition, at least when compared to the inner layers in these samples), or is it a product of element absorption from the surrounding Cu and Fe sulfides? The same question should be asked of the sphalerites in po-style mineralization, yet, due to the small sample size, the values should not be taken into consideration.

While this may be a difficult question to answer, the understanding of the greatest takeaway from this thesis may serve as a basis for a future resolution, as such it is extremely important to note that two different types of evolution can be traced in the studied samples, and the approach towards the Rainbow samples, should always be to identify, if possible, traces of these two different types of evolution which were already vital to the understanding of the SAL samples.

The first type is the evolution post-deposition, in which different minerals evolve within the sample, forming different minerals, even though the minerals share the same liquid/origin, with this evolution process occurring post deposition. The clearer examples would be the supergene enrichment of Cu-style samples, as well as the evolution of isocubanite into chalcopyrite in Cu-poor samples. This evolutionary process offers insight into the vent's behavior and how it evolves/reacts in an intricate system consisting of vent minerals, plume and surrounding seawater, with time also having a significant, yet hard to quantify, contribution.

The second studied type of evolution consists of the liquid's evolution (i.e. pre-deposition), which gives each vent its unique composition. This more linear evolutionary process is reflected in two aspects of the vents' samples, firstly their mineralization style, and secondly, the possible different stages of deposition of the minerals within the samples. The first aspect is directly correlated to the fluid's temperature and distance to the main fluid flowing channels for the Rainbow hydrothermal field, which in turn influence the fractioning of the liquid, in other words, its evolution, which is the crucial factor in identifying different stages of mineral deposition. The second aspect mostly reflects the exhaustion of certain elements and diminishing transport capacity at lower temperatures of certain elements, which once again stems directly from the liquid's fractionating processes.

While both types of evolutions come in play for all the mineralization styles, to each style it is possible to attribute one type of evolution that has the greater influence in each of the mineralization styles.

For Cu-style and all its sub-typologies, the common factor as well as their main differentiation point comes from the evolution within the sample post-deposition, as such, it mostly fits with the first type of evolution. Meanwhile, for the remaining two mineralization styles (Sph and Po-styles), the main differentiation comes from pre-deposition factors, namely the evolution of the liquid and the influence in transport of the distance from the focal point of fluid flow, combined with temperature. Therefore, both pre- and post-deposition differentiation should be interpreted in order to fully understand not only the process which leads to the deposition of certain mineralization styles, but also the existence of each mineral.

In order to simplify and further develop the information for future studies, a systematic approach should be followed when trying to determine and identify new samples retrieved from the Rainbow hydrothermal field:

- Identify the main mineral within the sample, as it should provide a first approximation as to what is the mineralization style of the sample;
- Determine the secondary minerals and respective proportions to verify and provide a suitable mineralization style to the sample;
- Verify the textural characteristics of the sample, as well as the deposition order of each mineral if possible;
- Determine, if possible, the degree of maturity of the sample.

This approach would help simplify the understanding of mineral interactions and sample evolution overall for the new samples, all while providing meaningful information which would aid in the association of any new samples to the existing ones and possibly create a database of these samples, which would also simplify the analyses of the Rainbow hydrothermal field and any comparable fields.

13.Bibliography

Allen, D. E., & Seyfried, W. E. (2003). Compositional controls on vent fluids from ultramafic-hosted hydrothermal systems at mid-ocean ridges: An experimental study at 4 00°C, 500 bars. *Geochimica et Cosmochimica Acta*, *67*(8), 1531–1542. https://doi.org/10.1016/S0016-7037(02)01173-0

Allen, D. E., & Seyfried, W. E. (2004). Serpentinization and heat generation: Constraints from Lost City and Rainbow hydrothermal systems. *Geochimica et Cosmochimica Acta*, *68*(6), 1347–1354. https://doi.org/10.1016/j.gca.2003.09.003

Alt, J. C., & Anderson, T. F. (1989). *The geochemistry of sulfur in a 1.3 km section of hydrothermally altered oceanic crust, DSDP Hole 504B* (Vol. 53).

Alt, J. C., & Shanks, W. C. (1998). Sulfur in serpentinized oceanic peridotites: Serpentinization processes and microbial sulfate reduction. *Journal of Geophysical Research: Solid Earth*, *103*(5), 9917–9929. https://doi.org/10.1029/98jb00576

Alt, J. C., & Shanks, W. C. (2003). *Serpentinization of abyssal peridotites from the MARK area, Mid-Atlantic Ridge: Sulfur geochemistry and reaction modeling*. http://zonvark.wustl.edu/

Alt, J. C., Shanks, W. C., & Jackson, M. C. (1993). Cycling of sulfur in subduction zones: The geochemistry of sulfur in the Mariana Island Arc and back-arc trough. In *Earth and Planetary Science Letters* (Vol. 119).

Alveirinho Dias, Á., Relvas, J., A. Marques, A. F., Qiu, W., Barriga, F., Ribeiro, L., & Calado, A. (2022). Variability of the hydrothermal fields within the Portuguese seafloor (MAR). *Goldschmidt2022 Abstracts*. https://doi.org/10.46427/gold2022.11686

Andreani, M., Escartin, J., Delacour, A., Ildefonse, B., Godard, M., Dyment, J., Fallick, A. E., & Fouquet, Y. (2014). Tectonic structure, lithology, and hydrothermal signature of the rainbow massif (Mid-Atlantic Ridge 36° 14'N). *Geochemistry, Geophysics, Geosystems*, *15*(9), 3543–3571. https://doi.org/10.1002/2014GC005269

Baker, E. T., Resing, J. A., Haymon, R. M., Tunnicliffe, V., Lavelle, J. W., Martinez, F., Ferrini, V., Walker, S. L., & Nakamura, K. (2016). How many vent fields? New estimates of vent field populations on ocean ridges from precise mapping of hydrothermal discharge locations. *Earth and Planetary Science Letters*, *449*, 186–196. https://doi.org/10.1016/j.epsl.2016.05.031

Barriga, F. J. A. S., Costa, I., & Relvas, J. M. R. S. (1997). *The Rainbow serpentinites and serpentinite-sulphide stockwork (Mid-Atlantic Ridge, AMAR segment): A preliminary report of the FLORES results Ocean Drilling Program Leg 170, JOIDES Resolution View project Blue Mining: breakthrough solutions for sustainable deep sea mining View project*. https://www.researchgate.net/publication/285075681

Beaulieu, S. E., Baker, E. T., & German, C. R. (2015). Where are the undiscovered hydrothermal vents on oceanic spreading ridges? *Deep-Sea Research Part II: Topical Studies in Oceanography*, *121*, 202–212. https://doi.org/10.1016/j.dsr2.2015.05.001

Beaulieu, S. E., Baker, E. T., German, C. R., & Maffei, A. (2013). An authoritative global database for active submarine hydrothermal vent fields. *Geochemistry, Geophysics, Geosystems*, *14*(11), 4892–4905. https://doi.org/10.1002/2013GC004998

Beaulieu, S., & Szafranski, K. (2020, March 25). *InterRidge Global Database of Active Submarine Hydrothermal Vent Fields, Version 3.4.* Szafranski, K. https://doi.org/10.1594/PANGAEA.917894

Bogdanov, Y., Sagalevitch, A., Chernyaev, E., Ashadze, A., Gurvich, E., Lukashin, V., & Peresypkin, V. (1995). A study of the hydrothermal field at 14 45′ N on the Mid-Atlantic Ridge using the “MIR” submersibles. *BRIDGE Newsl*, *9*, 9–13.

Bortnikov, N., Vikentev, I. V, Lein, A., Shirshov, P. P., & Sagalevich, A. (2002). *Article in Geology of Ore Deposits ·*. https://www.researchgate.net/publication/286407411

Brunner, B., & Bernasconi, S. M. (2005). A revised isotope fractionation model for dissimilatory sulfate reduction in sulfate reducing bacteria. *Geochimica et Cosmochimica Acta*, *69*(20), 4759–4771. https://doi.org/10.1016/j.gca.2005.04.015

Campbell, A. C., Palmer, M. R., Klinkhammer, G. P., & Bowers, T. S. (1988). Chemistry of hot springs on the Mid-Atlantic Ridge. *Nature*, *335*(6190), 514–519.

Canales, J. P., Dunn, R. A., Arai, R., & Sohn, R. A. (2017). Seismic imaging of magma sills beneath an ultramafic-hosted hydrothermal system. *Geology*, *45*(5), 451–454. https://doi.org/10.1130/G38795.1

Canfield, D. E. (2001). Biogeochemistry of sulfur isotopes. *Reviews in Mineralogy and Geochemistry*, *43*(1), 607–638.

Cannat, M. (1993). Emplacement of mantle rocks in the seafloor at mid-ocean ridges. *Journal of Geophysical Research*, *98*(B3), 4163–4172. https://doi.org/10.1029/92JB02221

Cao, H., Sun, Z., Jiang, Z., Dong, A., Geng, W., Zhang, X., Li, X., Yan, D., & Liu, W. (2021). Source origin and ore-controlling factors of hydrothermal sulfides from the Tianzuo hydrothermal field, Southwest Indian Ridge. *Ore Geology Reviews*, *134*. https://doi.org/10.1016/j.oregeorev.2021.104168

Cherkashov, G., Bel’Tenev, V., Ivanov, V., Lazareva, L., Samovarov, M., Shilov, V., Stepanova, T., Glasby, G. P., & Kuznetsov, V. (2008a). Two new hydrothermal fields at the mid-atlantic ridge. *Marine Georesources and Geotechnology*, *26*(4), 308–316. https://doi.org/10.1080/10641190802400708

Cherkashov, G., Bel’Tenev, V., Ivanov, V., Lazareva, L., Samovarov, M., Shilov, V., Stepanova, T., Glasby, G. P., & Kuznetsov, V. (2008b). Two new hydrothermal fields at the mid-atlantic ridge. *Marine Georesources and Geotechnology*, *26*(4), 308–316. https://doi.org/10.1080/10641190802400708

Corliss, J. B., Dymond, J., Gor John M Edmond, L. I., von Herzen, R. P., Bal Kenneth Green, R. D., Williams, D., Bainbri Kathy Crane, A., van A, T. H., Corliss J Dymond, J. B., Gordon are, L. I., Herzen, von, Ballard, R. D., Bainbridge, A., & Crane, K. (1979). *Submarine Thermal Sprir on the Galapagos 1R* (Vol. 203).

Dang, Y., Li, C., Ye, J., Yang, Y., Wang, S., Zhao, Q., Li, B., Guan, Y., Fan, L., & Shi, X. (2024). Mineralogy and sulfur isotopic compositions of sulfides from Yunzang (25.3°S) hydrothermal field, South Mid-Atlantic Ridge: Implications for formation mechanism and maturation of sulfide chimneys. *Ore Geology Reviews*, *171*. https://doi.org/10.1016/j.oregeorev.2024.106187

Dias, Á. (2009). *Geochemistry of deep-sea hydrothermal sediments from the Saldanha and Lucky Strike hydrothermal fields (Mid-Atlantic Ridge)*.

Dias, Á. S., & Barriga, F. J. A. S. (2006). Mineralogy and geochemistry of hydrothermal sediments from the serpentinite-hosted Saldanha hydrothermal field (36°34′N; 33°26′W) at MAR. *Marine Geology*, *225*(1–4), 157–175. https://doi.org/10.1016/j.margeo.2005.07.013

Dias, Á. S., Früh-Green, G. L., Bernasconi, S. M., & Barriga, F. J. A. S. (2011). Geochemistry and stable isotope constraints on high-temperature activity from sediment cores of the Saldanha hydrothermal field. *Marine Geology*, *279*(1–4), 128–140. https://doi.org/10.1016/j.margeo.2010.10.017

Dias, Á. S., Mills, R. A., Taylor, R. N., Ferreira, P., & Barriga, F. J. A. S. (2008). Geochemistry of a sediment push-core from the Lucky Strike hydrothermal field, Mid-Atlantic Ridge. *Chemical Geology*, *247*(3–4), 339–351. https://doi.org/10.1016/j.chemgeo.2007.10.015

Dick, H. J. B., Lin, J., & Schouten, H. (2003). *An ultraslow-spreading class of ocean ridge*. www.nature.com/nature

Ding, T., Tao, C., Ágata, &, Dias, A., Liang, J., Chen, J., Wu, B., Ma, D., Zhang, R., Wang, J., Liao, S., Wang, Y., Yang, W., Liu, J., Li, W., Zhang, G., & Huang, H. (2021). Sulfur isotopic compositions of sulfides along the Southwest Indian Ridge: implications for mineralization in ultramafic rocks. *Mineralium Deposita*, *56*, 991–1006. https://doi.org/10.1007/s00126-020

Douville, E., Charlou, J. L., Oelkers, E. H., Bienvenu, P., Colon, C. F. J., Donval, J. P., Fouquet, Y., Prieur, D., & Appriou, P. (2002). *The rainbow vent fluids (36°14VN, MAR): the influence of ultramafic rocks and phase separation on trace metal content in Mid-Atlantic Ridge hydrothermal f luids*. www.elsevier.com/locate/chemgeo

Douvillearb, E., Apprioub, P., Charloua, J.-K., Donvala, J.-P., & Hureauafb, D. (1998). *Le comportement de I'arsenic (As) et de I'antimoine (Sb) dans les fluides provenant de diffkents systgmes hydrothermaux ockaniques As and Sb bebaviour in jluids from various deep-sea hydrothermal systems*.

Dubinina, E. O., Bortnikov, N. S., Stavrova, O. O., & Kossova, S. A. (2020). Sulfur Isotope Fractionation During Sulfide Generation in the Hydrothermal Submarine Systems: The Case of Logatchev, Krasnov, and Rainbow Hydrothermal Fields, Mid-Atlantic Ridge. *Geology of Ore Deposits*, *62*(5), 351–371. https://doi.org/10.1134/S1075701520050025

Dunn, R. A., Arai, R., Eason, D. E., Canales, J. P., & Sohn, R. A. (2017). Three-Dimensional Seismic Structure of the Mid-Atlantic Ridge: An Investigation of Tectonic, Magmatic, and Hydrothermal Processes in the Rainbow Area. *Journal of Geophysical Research: Solid Earth*, *122*(12), 9580–9602. https://doi.org/10.1002/2017JB015051

Fontaine, F. J., Cannat, M., & Escartin, J. (2008). Hydrothermal circulation at slow-spreading mid-ocean rigdes: The role of along-axis variations in axial lithospheric thickness. *Geology*, *36*(10), 759–762. https://doi.org/10.1130/G24885A.1

Fouquet, Y., Barriga, F., Char, J. L., Elderfield, H., German, C. R., Ondreas, H., Parson, L., Re, J., Ribeiro, A., Sclwltz, A., Apprioua, R., Cambon, P., Donva, J. P., Douvilld, E., Lrmdtm, J. Y., Normand, A., Pelle, H., Portsevercr, E., Richesl, S., … Sur Yve, G. (1998). *FLORES diving cruise with the Nautile near the Azores-First dives on the Rainbow field: hydrothermal seawater/mantle interaction*. http://www.l~s.jussieu.fr/-intridge/irn.htm

Fouquet, Y., Cambon, P., Etoubleau, J., Charlou, J. L., Ondréas, H., Barriga, F. J. A. S., Cherkashov, G., Semkova, T., Poroshina, I., Bohn, M., Donval, J. P., Henry, K., Murphy, P., & Rouxel, O. (2010). Geodiversity of hydrothermal processes along the mid-atlantic ridge and ultramafic-hosted mineralization: A new type of oceanic Cu-Zn-Co-Au volcanogenic massive sulfide deposit. *Geophysical Monograph Series*, *188*, 321–367. https://doi.org/10.1029/2008GM000746

Fouquet, Y., Cherkashov, G., Charlou, J. L., Ondréas, H., Birot, D., Cannat, M., Bortnikov, N., Silantyev, S., Sudarikov, S., Cambon-Bonavita, M. A., Desbruyères, D., Fabri, M. C., Querellou, J., Hourdez, S., Gebruk, A., Sokolova, T., Hoisé, E., Mercier, E., Kohn, C., … Buffi Er, E. (2008). INTERNATIONAL RESEARCH Serpentine cruise-ultramafic hosted hydrothermal deposits on the Mid-At-lantic Ridge: First submersible studies on Ashadze 1 and 2, Logatchev 2 and Krasnov vent fields. In *InterRidge News* (Vol. 16).

Fouquet, Y., Jean-Luc, C., Jean-Pierre, D., Radford-Knoery, J., Pelle, P., Ondreas, H., Lourenco, N., Segonzac, M., & Tivey, M. (1994). A Detailed Study of the Lucky Strike Hydrothermal Site and Discovery of a New Hydrothermal Site: Menez Gwen; Preliminary Results of the DIV Al Cruise (5-29 May, 1994). *LnterRidge News*, *3*(2), 14–17.

Foustoukos, D. I., & Seyfried, W. E. (2007). Fluid phase separation processes in submarine hydrothermal systems. *Reviews in Mineralogy and Geochemistry*, *65*, 213–239. https://doi.org/10.2138/rmg.2007.65.7

Fu, Z., Wu, F., Mo, C., Deng, Q., Meng, W., & Giesy, J. P. (2016). Comparison of arsenic and antimony biogeochemical behavior in water, soil and tailings from Xikuangshan, China. *Science of the Total Environment*, *539*, 97–104. https://doi.org/10.1016/j.scitotenv.2015.08.146

Gale, A., Dalton, C. A., Langmuir, C. H., Su, Y., & Schilling, J. G. (2013). The mean composition of ocean ridge basalts. *Geochemistry, Geophysics, Geosystems*, *14*(3), 489–518. https://doi.org/10.1029/2012GC004334

German, C. R., & Damm, K. L. Von. (2003). Hydrothermal processes. *The Oceans and Marine Geochemistry, Edited by H. Elderfield.*, *6*(Treatise on Geochemistry). https://doi.org/http://dx.doi.org/10.1016/B0-08-043751-6/06109-0

German, C. R., Klinkhammer, G. P., & Rudnickf. (1996). The Rainbow hydrothermal plume, 36º15'N, MAR. *GEOPHYSICAL RESEARCH LETTERS*, *23*(21), 2979–2982.

German, C. R., & Seyfried, W. E. (2013). Hydrothermal Processes. In *Treatise on Geochemistry: Second Edition* (Vol. 8, pp. 191–233). Elsevier Inc. https://doi.org/10.1016/B978-0-08-095975-7.00607-0

Goldhaber, M. B., & Kaplan, I. R. (1980). MECHANISMS OF SULFUR INCORPORATION AND ISOTOPE FRACTIONATION DURING EARLY DIAGENESIS IN SEDIMENTS OF THE GULF OF CALIFORNIA*. In *Marine Chemistry* (Vol. 9).

Gràcia, E., Charlou, J. L., Radford-Knoery, J., & Parson, L. M. (2000). Non-transform offsets along the Mid-Atlantic Ridge south of the Azores (38°N–34°N): ultramafic exposures and hosting of hydrothermal vents. *Earth and Planetary Science Letters*, *177*(1–2), 89–103. https://doi.org/10.1016/S0012-821X(00)00034-0

Hannington, M. D., De Ronde, C. E. J., & Petersen, S. (2005). Sea-Floor Tectonics and Submarine Hydrothermal Systems. In *Economic Geology 100th Anniversary*.

Haymon, R. M. (1983). Growth history of hydrothermal black smoker chimneys. *Nature*, *301*(5902), 695–698.

Herzig, P. M., Hannington, M. D., & Arribas, A. (1998). *Sulfur isotopic composition of hydrothermal precipitates from the Lau back-arc: implications for magmatic contributions to sea¯oor hydrothermal systems*.

Humphris, S. E., Herzig, P. M., Miller, D. J., Alt, J. C., Becker, K., Brown, D., ..., & Zhao, X. (1995). The internal structure of an active sea-floor massive sulphide deposit. *Nature*, *377*(6551), 713–716.

Humphris, S. E., & Mccollom, T. (1998a). *THE DISCOVERY OF HYDROTHERMAL VENTS 25th Anniversary CD-ROM The Cauldron Beneath the Seafloor: Percolating Through Volcanic Subsurface Rocks, Seawater is Chemically Transformed into Hydrothermal Fluid* (Vol. 41, Issue 2).

Humphris, S. E., & Mccollom, T. (1998b). *THE DISCOVERY OF HYDROTHERMAL VENTS 25th Anniversary CD-ROM The Cauldron Beneath the Seafloor: Percolating Through Volcanic Subsurface Rocks, Seawater is Chemically Transformed into Hydrothermal Fluid* (Vol. 41, Issue 2).

Jamieson, J. W., & Gartman, A. (2020). Defining active, inactive, and extinct seafloor massive sulfide deposits. *Marine Policy*, *117*. https://doi.org/10.1016/j.marpol.2020.103926

Janecky, D. R. (1988). *Computational modeling of chemical and sulfur isotopic reaction processes in seafloor hydrothermal systems: chimneys, massive sulfides, and subjacent alteration zones*. https://www.researchgate.net/publication/279705585

Kase, K., Yamamoto, M., & Shibata, T. (1990). *Copper-rich sulfide deposit near 23°N, Mid-Atlantic Ridge: chemical composition, mineral chemistry, and sulfur isotopes*. *106*, 163–177.

Kelley, D. S., Karson, J. A., Blackman, D. K., Früh-Green, G. L., Butterfield, D. A., Lilley, M. D., Olson, E. J., Schrenk, M. O., Roe, K. K., Lebon, G. T., & Rivizzigno, P. (2001). An off-axis hydrothermal vent field near the Mid-Atlantic Ridge at 30° N. *Nature*, *412*(6843), 145–149. https://doi.org/10.1038/35084000

Klinkhammer, G. P., Elderfield, H., Edmond, J. M., & Mitra, A. (1994). Geochemical implications of rare earth element patterns in hydrothermal fluids from mid-ocean ridges. In *Geochimica et Cosmochimica Acta* (Vol. 58, Issue 23).

Knott, R., Fallick, A. E., Rickard, D., & Backer, H. (1995). *Mineralogy and sulphur isotope characteristics of a massive sulphide boulder, Galapagos Rift, 85~*. http://sp.lyellcollection.org/

Konn, C., Donval, J. P., Guyader, V., Germain, Y., Alix, A.-S., Roussel, E., & Rouxel, O. (2021). *Extending the dataset of fluid geochemistry of the Menez Gwen, Lucky Strike, Rainbow, TAG and Snake Pit hydrothermal vent fields: 2 investigation of temporal stability and organic contribution*.

Koschinsky, A. (2016). Hydrothermal vent fluids (Seafloor). In *Encyclopedia of Earth Sciences Series: Vol. Part 2* (pp. 339–344). Springer Netherlands. https://doi.org/10.1007/978-94-007-6644-0_17-1

Krasnov, S. G., Poroshina, I. M., & Cherkashev, G. A. (1995). Geological setting of high-temperature hydrothermal activity and massive sulphide formation on fast- and slow-spreading ridges. *Geological Society Special Publication*, *87*, 17–32. https://doi.org/10.1144/GSL.SP.1995.087.01.03

Lafay, R., Montes-Hernandez, G., Janots, E., Munoz, M., Auzende, A. L., Gehin, A., Chiriac, R., & Proux, O. (2016). Experimental investigation of As, Sb and Cs behavior during olivine serpentinization in hydrothermal alkaline systems. *Geochimica et Cosmochimica Acta*, *179*, 177–202. https://doi.org/10.1016/j.gca.2016.02.014

Lein, A. Y., Ulyanova, N. V, Ulyanov, A. A., Cherkashev, G. A., & Stepanova, T. V. (2001). Mineralogy and geochemistry of sulfide ores in ocean-floor hydrothermal fields associated with serpentinite protrusions. In *RUSSIAN JOURNAL OF EARTH SCIENCES* (Vol. 3, Issue 5). http://rjes.agu.org/v03/TJE01068/TJE01068.htm

Liao, S., Tao, C., Dias, Á. A., Liu, J., Su, X., Lv, S., Jamieson, J. W., Zhou, J., Deng, X., Liang, J., Yang, W., Li, W., & Yang, X. (2024). Sediment geochemistry reveals abundant off-axis hydrothermal fields on the ultraslow-spreading Southwest Indian Ridge. *Earth and Planetary Science Letters*, *643*, 118916. https://doi.org/10.1016/j.epsl.2024.118916

Liao, S., Tao, C., Li, H., Barriga, F. J. A. S., Liang, J., Yang, W., Yu, J., & Zhu, C. (2018). Bulk geochemistry, sulfur isotope characteristics of the Yuhuang-1 hydrothermal field on the ultraslow-spreading Southwest Indian Ridge. *Ore Geology Reviews*, *96*, 13–27. https://doi.org/10.1016/j.oregeorev.2018.04.007

Lowell, R. P., & Rona, P. A. (2002). Seafloor hydrothermal systems driven by the serpentinization of peridotite. *Geophysical Research Letters*, *29*(11), 26-1-26–4. https://doi.org/10.1029/2001GL014411

Marques, A. F. A., Barriga, F., Chavagnac, V., & Fouquet, Y. (2006). Mineralogy, geochemistry, and Nd isotope composition of the Rainbow hydrothermal field, Mid-Atlantic Ridge. *Mineralium Deposita*, *41*(1), 52–67. https://doi.org/10.1007/s00126-005-0040-8

Marques, A. F. A., Barriga, F. J. A. S., & Scott, S. D. (2007). Sulfide mineralization in an ultramafic-rock hosted seafloor hydrothermal system: From serpentinization to the formation of Cu-Zn-(Co)-rich massive sulfides. *Marine Geology*, *245*(1–4), 20–39. https://doi.org/10.1016/j.margeo.2007.05.007

McCollom, T. M., Klein, F., Robbins, M., Moskowitz, B., Berquó, T. S., Jöns, N., Bach, W., & Templeton, A. (2016). Temperature trends for reaction rates, hydrogen generation, and partitioning of iron during experimental serpentinization of olivine. *Geochimica et Cosmochimica Acta*, *181*, 175–200. https://doi.org/10.1016/j.gca.2016.03.002

Mcdonough, F., & Sun, S. (1995). The composition of the Earth. *Chemical Geology*, *120*(3–4), 223–253. https://doi.org/https://doi.org/10.1016/0009-2541(94)00140-4

Melchert, B., Devey, C. W., German, C. R., Lackschewitz, K. S., Seifert, R., Walter, M., Mertens, C., Yoerger, D. R., Baker, E. T., Paulick, H., & Nakamura, K. (2008). First evidence for high-temperature off-axis venting of deep crustal/mantle heat: The Nibelungen hydrothermal field, southern Mid-Atlantic Ridge. *Earth and Planetary Science Letters*, *275*(1–2), 61–69. https://doi.org/10.1016/j.epsl.2008.08.010

Mottl, M. J., Geof, C., & Wheat, =rey. (1994). Hydrothermal circulation through mid-ocean ridge flanks: Fluxes of heat and magnesium*. In *Geochimica et Cosmochimica Acta* (Vol. 58, Issue 10).

Mozgova, N., Efimov, A., Borodaev, Y. S., Krasnov, S., Cherkashov, G. A., Stepanova, T. V., & Ashadze, A. M. (1999). Mineralogy and chemistry of massive sulfides from the Logatchev hydrothermal field (14 degrees 45'N Mid-Atlantic Ridge). *Exploration and Mining Geology*, *8*, 379–395.

Murton, B. J., Lehrmann, B., Dutrieux, A. M., Martins, S., de la Iglesia, A. G., Stobbs, I. J., Barriga, F. J. A. S., Bialas, J., Dannowski, A., Vardy, M. E., North, L. J., Yeo, I. A. L. M., Lusty, P. A. J., & Petersen, S. (2019). Geological fate of seafloor massive sulphides at the TAG hydrothermal field (Mid-Atlantic Ridge). In *Ore Geology Reviews* (Vol. 107, pp. 903–925). Elsevier B.V. https://doi.org/10.1016/j.oregeorev.2019.03.005

Pat Shanks, W. C. (2013). Stable Isotope Geochemistry of Mineral Deposits. In *Treatise on Geochemistry: Second Edition* (Vol. 13, pp. 59–85). Elsevier Inc. https://doi.org/10.1016/B978-0-08-095975-7.01103-7

Petersen, S., Lehrmann, B., & Murton, B. J. (2018). Modern seafloor hydrothermal systems: New perspectives on ancient ore-forming processes. *Elements*, *14*(5), 307–312. https://doi.org/10.2138/gselements.14.5.307

Rainbow - InterRidge Vents Database Ver. 3.4. (2020). https://vents-data.interridge.org/ventfield/rainbow

Rees, C. E., Jenkins, W. J., & Monster, J. (1978). *The sulphur isotopic composition of ocean water sulphate** (Vol. 42). Pergamon Press. Printed m Great Britam.

Rouxel, O., Shanks, W. C., Bach, W., & Edwards, K. J. (2008). Integrated Fe- and S-isotope study of seafloor hydrothermal vents at East Pacific Rise 9-10°N. *Chemical Geology*, *252*(3–4), 214–227. https://doi.org/10.1016/j.chemgeo.2008.03.009

Sakai, H., Des Marais, D. J., Ueda, A., & Moored, J. G. (1984). *Concentrations and isotope ratios of carbon, nitrogen and sulfur in ocean-floor basalts* (Vol. 48). Pe@amon Press Ltd.

Sánchez-Mora, D., Jamieson, J., Cannat, M., Escartín, J., & Barreyre, T. (2022). Effects of Substrate Composition and Subsurface Fluid Pathways on the Geochemistry of Seafloor Hydrothermal

Deposits at the Lucky Strike Vent Field, Mid-Atlantic Ridge. *Geochemistry, Geophysics, Geosystems*, *23*(5). https://doi.org/10.1029/2021GC010073

Seal, R. R. (2006). Sulfur isotope geochemistry of sulfide minerals. In *Reviews in Mineralogy and Geochemistry* (Vol. 61, pp. 633–677). https://doi.org/10.2138/rmg.2006.61.12

Seward, T. M., Williams-Jones, A. E., & Migdisov, A. A. (2014). The Chemistry of Metal Transport and Deposition by Ore-Forming Hydrothermal Fluids. In *Treatise on Geochemistry: Second Edition* (Vol. 13, pp. 29–57). Elsevier Inc. https://doi.org/10.1016/B978-0-08-095975-7.01102-5

Seyefried, W. E., Ding, K., & Berndt, M. E. (1991). *Phase equilibria constraints on the chemistry of hot spring fluids at mid-acean ridges* (Vol. 55). Pe@amon Press pk.

Seyfried Jr, W. E., & Dibble Jr, W. E. (1980). Seawater-peridotite interaction at 300°C and 500 bars: implications for the origin of oceanic serpentinites. *Geochimica et Cosmochimica Acta*, *44*, 309–321.

Seyfried, W. E., Pester, N. J., Tutolo, B. M., & Ding, K. (2015). The Lost City hydrothermal system: Constraints imposed by vent fluid chemistry and reaction path models on subseafloor heat and mass transfer processes. *Geochimica et Cosmochimica Acta*, *163*, 59–79. https://doi.org/10.1016/j.gca.2015.04.040

Tao, C., Guo, Z., Liang, J., Ding, T., Yang, W., Liao, S., Chen, M., Zhou, F., Chen, J., Wang, N., Liu, X., & Zhou, J. (2023). Sulfide metallogenic model for the ultraslow-spreading Southwest Indian Ridge. *Science China Earth Sciences*, *66*(6), 1212–1230. https://doi.org/10.1007/s11430-023-1108-7

Tivey, M. (2007). *Generation of Seafloor Hydrothermal Vent Fluids and associated Mineral Deposits*. https://doi.org/https://doi.org/10.5670/oceanog.2007.80

Toffolo, L., Nimis, P., Tret'yakov, G. A., Melekestseva, I. Y., & Beltenev, V. E. (2020). Seafloor massive sulfides from mid-ocean ridges: Exploring the causes of their geochemical variability with multivariate analysis. In *Earth-Science Reviews* (Vol. 201). Elsevier B.V. https://doi.org/10.1016/j.earscirev.2019.102958

Vent Fields list all - InterRidge Vents Database Ver. 3.4. (2020). https://vents-data.interridge.org/ventfields_list_all

Whitney, D. L., Teyssier, C., Rey, P., & Buck, W. R. (2013). Continental and oceanic core complexes. *Geological Society of America Bulletin*, *125*(3–4), 273–298. https://doi.org/10.1130/B30754.1

Woodruff, L. G., & Shanks, W. C. (1988). Sulfur isotope study of chimney minerals and vent fluids from 21°N, East Pacific Rise: Hydrothermal sulfur sources and disequilibrium sulfate reduction. *Journal of Geophysical Research: Solid Earth*, *93*(B5), 4562–4572. https://doi.org/10.1029/jb093ib05p04562

Woods, A. W., & Delancey, J. R. (1992). The heat and fluid transfer associated with the flanges on hydrothermal venting structures. *Earth and Planetary Science Letters, Elsevier Science Publishers B.V, Amsterdam*, *112*, 117–129.

Zhao, Y., Ding, W., Manatschal, G., Wei, X., Ding, H., Tong, Z., & Zhao, J. (2024). Unraveling the link between magma and deformation during slow seafloor spreading. *Tectonophysics*, *889*. https://doi.org/10.1016/j.tecto.2024.230473

APPENDICES

APPENDIX I: Rainbow chimney samples - *Descriptive summary, locations, and conducted analyses.*

APPENDIX II: Mineral Chemistry - Electron probe microanalysis (EPMA) in sulfide phases.

APPENDIX III: Mineral Composition - Scanning electron microscopy and energy dispersive spectroscopy (SEM/EDS).

APPENDIX IV: Bulk geochemistry.

APPENDIX V: Correlation Coefficient matrixes.

APPENDIX VI: *In-situ* Sulfur (S) isotopic analysis.

APPENDIX VII: Posters derived from the research conducted on this thesis.

APPENDIX I: Rainbow chimney samples - *Descriptive summary, locations, and conducted analyses.*

Note: petrographic observation and EPMA analysis are not mentioned as those were conducted for all samples.

<table>
<tr><td colspan="4">SAL-03-03</td></tr>
<tr><td>Hand Samples</td><td colspan="2">  </td><td>  </td></tr>
<tr><td colspan="2">Sample description + Observations</td><td colspan="2">Mount for polished thin sections</td></tr>
<tr><td colspan="2">Chimney fragment

-Dark, friable chimney fragments with oxides in the outer part. The sample is mainly composed of Sphalerite and possibly isocubanite. The Sphalerite forms a granular and dendritic texture.</td><td colspan="2">  </td></tr>
<tr><td colspan="2">Coordinates (lat; long)</td><td colspan="2">volume (cm3)</td></tr>
<tr><td colspan="2">- N 36°13'46"; W 33°54'09"</td><td colspan="2">- 10x6x2cm; 8x6x15cm; 8x6x15cm</td></tr>
<tr><td>- Whole chemistry</td><td>- SEM/EDS analysis</td><td colspan="2">In-situ S isotopic analysis (per mineral + total)</td></tr>
<tr><td>- ✓ (yes)</td><td>- ✓ (yes)</td><td colspan="2">Icb – 3 Sph-I - 6 Sph-II - 2 Total - 11</td></tr>
</table>

<table>
<tr><td colspan="4">SAL-03-04</td></tr>
<tr><td>Hand Samples</td><td colspan="2">  </td><td>  </td></tr>
<tr><td colspan="2">Sample description + Observations</td><td colspan="2">Mount for polished thin sections</td></tr>
<tr><td colspan="2">Chimney fragment

- The chimney fragments are covered by a Fe-Mn oxide crust with brown and reddish colors. Mineral zonation is visible within these fragments. The outer wall of the chimney is composed of sphalerite (possibly weathered to covellite) and exhibits a dark color. The inner wall is irregular and contains pyrrhotite and isocubanite/chalcopyrite.</td><td colspan="2">  </td></tr>
<tr><td colspan="2">Coordinates (lat; long)</td><td colspan="2">volume (cm3)</td></tr>
<tr><td colspan="2">- N 36°13'43"; W 33°54'12"</td><td colspan="2">- 8x6x3cm; 7x6x2cm</td></tr>
<tr><td>- Whole chemistry</td><td>- SEM/EDS analysis</td><td colspan="2">In-situ S isotopic analysis (per mineral + total)</td></tr>
<tr><td>✓ (yes)</td><td>x (no)</td><td colspan="2">x (no)</td></tr>
</table>

<table>
<tr><td colspan="4">SAL-03-06</td></tr>
<tr><td>Hand Samples</td><td colspan="2">  </td><td> 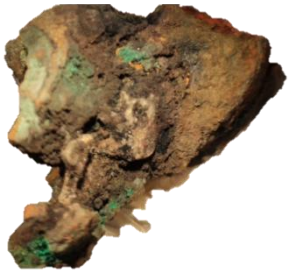 </td></tr>
<tr><td colspan="3">Sample description + Observations</td><td>Mount for polished thin sections</td></tr>
<tr><td colspan="3">Seemingly inactive chimney

- There is an oxidation layer both in the outer and inner parts. In the less oxidized zones, it is possible to observe Atacamite (green), Covellite (blue), Isocubanite, and seemingly some sphalerite. The growth of chalcopyrite is perpendicular to the chimney walls.

- Two different thin samples.</td><td> 
  </td></tr>
<tr><td colspan="2">Coordinates (lat; long)</td><td colspan="2">volume (cm3)</td></tr>
<tr><td colspan="2">- N 36°13'46"; W 33°54'11"</td><td colspan="2">- 6x4x3cm; 4x3x0,5cm; 5x3x0,5cm, and others fragments</td></tr>
<tr><td>- Whole chemistry</td><td>- SEM/EDS analysis</td><td colspan="2">In-situ S isotopic analysis (per mineral + total)</td></tr>
<tr><td>✓ (yes)</td><td>X (no)</td><td colspan="2">X (no)</td></tr>
</table>

<table>
<tr><td colspan="4">SAL-03-08</td></tr>
<tr><td>Hand Samples</td><td colspan="2">  </td><td>  </td></tr>
<tr><td colspan="2">Sample description + Observations</td><td colspan="2">Mount for polished thin sections</td></tr>
<tr><td colspan="2">Active chimney fragments (fluid temperature measured in-situ = 350ºC)

- There is an inward concentric zonation with the following mineralization:
Outer oxidized zone composed of iron oxides (Magnetite, hematite) and some chalcopyrite;
Middle zone connecting the other layers where we can observe a vuggy layer containing Cu-rich sulfides and sulfates;
Inner zone composed of Isocubanite and/or chalcopyrite crystals.</td><td colspan="2"> 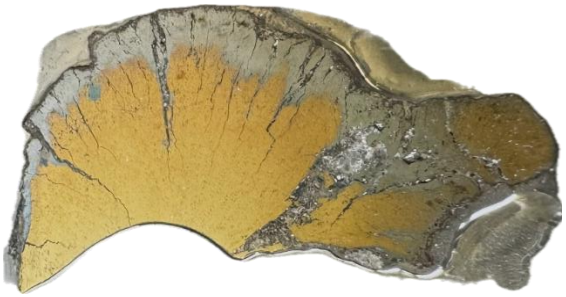 </td></tr>
<tr><td colspan="2">Coordinates (lat; long)</td><td colspan="2">volume (cm3)</td></tr>
<tr><td colspan="2">- N 36°13'43"; W 33°54'12"</td><td colspan="2">- 10x7x3 cm and other fragments</td></tr>
<tr><td>- Whole chemistry</td><td>- SEM/EDS analysis</td><td colspan="2">In-situ S isotopic analysis (per mineral + total)</td></tr>
<tr><td>✓ (yes)</td><td>✓ (yes)</td><td colspan="2">Cpy - 14 Ch - 3
Total - 17</td></tr>
</table>

<table>
<tr><td colspan="4">SAL-04-02</td></tr>
<tr><td>Hand Samples</td><td colspan="2">  </td><td></td></tr>
<tr><td colspan="2">Sample description + Observations</td><td colspan="2">Mount for polished thin sections</td></tr>
<tr><td colspan="2">Chimney fragment

- These friable samples fragments are composed of isocubanite and/or chalcopyrite, pyrrhotite, and sphalerite. Copper sulfide appears to be associated with euhedral crystals of sulfates (anhydrite and/or barite).

- Two different thin samples.</td><td colspan="2"> 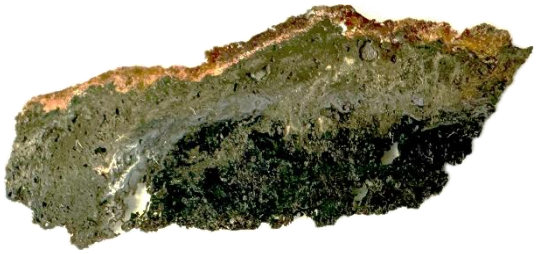
 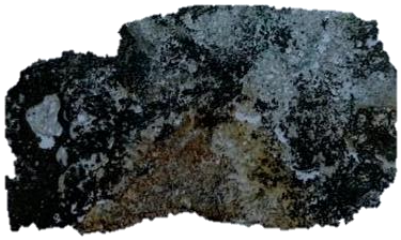 </td></tr>
<tr><td colspan="2">Coordinates (lat; long)</td><td colspan="2">volume (cm3)</td></tr>
<tr><td colspan="2">- N 36°13'17"; W 33°53'34"</td><td colspan="2">- 12x7x1cm; 7x4x1cm; 7x5x15cm; 8x6x3cm; 22x20x25cm, and others</td></tr>
<tr><td>- Whole chemistry</td><td>- SEM/EDS analysis</td><td colspan="2">In-situ S isotopic analysis (per mineral + total)</td></tr>
<tr><td>✓ (yes)</td><td>X (no)</td><td colspan="2">Icb – 2 Sph-I - 3 Sph-II - 1
Total - 6</td></tr>
</table>

<table>
<tr><td colspan="4">SAL-05-01</td></tr>
<tr><td>Hand Samples</td><td colspan="2">  </td><td>  </td></tr>
<tr><td colspan="2">Sample description + Observations</td><td colspan="2">Mount for polished thin sections</td></tr>
<tr><td colspan="2">Massive Sulphide (part of a larger block), likely from an inactive chimney at the base of a larger structure.

- A large block of vuggy rock composed of chalcopyrite/isocubanite and likely sphalerite. The thick external crust consists of iron oxides, sulfates and atacamite. There is a small portion containing covellite and native copper.

- Two different thin samples.</td><td colspan="2"> 
  </td></tr>
<tr><td colspan="2">Coordinates (lat; long)</td><td colspan="2">volume (cm3)</td></tr>
<tr><td colspan="2">- N 36°13'45"; W 33°54'08"</td><td colspan="2">- 19x15x7cm; 18x14x6cm; 15x7x5cm; 8x6x3cm; 22x20x15cm</td></tr>
<tr><td>- Whole chemistry</td><td>- SEM/EDS analysis</td><td colspan="2">In-situ S isotopic analysis (per mineral + total)</td></tr>
<tr><td>✓ (yes)</td><td>x (no)</td><td colspan="2">Cpy / Icb – 8
Total - 8</td></tr>
</table>

<table>
<tr><td colspan="4">SAL-05-03</td></tr>
<tr><td>Hand Samples</td><td colspan="2">  </td><td></td></tr>
<tr><td colspan="2">Sample description + Observations</td><td colspan="2">Mount for polished thin sections</td></tr>
<tr><td colspan="2">Apparently inactive Chimney - part of a larger structure

- The oxidized external crust, measuring 2 mm, exhibits brownish to ochre colors. The sulfide portion is primarily composed of isocubanite. Near the fractures that cut through the rock, there are small vuggy areas, composed of sphalerite and covellite.</td><td colspan="2"> 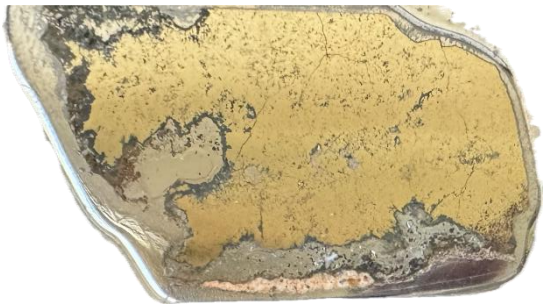 </td></tr>
<tr><td colspan="2">Coordinates (lat; long)</td><td colspan="2">volume (cm3)</td></tr>
<tr><td colspan="2">- N 36°13'46"; W33°54'09"</td><td colspan="2">- 8x6x5cm; 8x7x5cm; and 2 small fragments</td></tr>
<tr><td>- Whole chemistry</td><td>- SEM/EDS analysis</td><td colspan="2">In-situ S isotopic analysis (per mineral + total)</td></tr>
<tr><td>✓ (yes)</td><td>✓ (yes)</td><td colspan="2">Icb – 6
Total - 6</td></tr>
</table>

<table>
<tr><td colspan="4">SAL-05-04</td></tr>
<tr><td>Hand Samples</td><td colspan="2">  </td><td>  </td></tr>
<tr><td colspan="2">Sample description + Observations</td><td colspan="2">Mount for polished thin sections</td></tr>
<tr><td colspan="2">Apparently inactive and oxidized chimney fragments

- Several friable fragments exhibit significant alteration cape (3 mm) and are composed of iron oxides. In the inner part of the chimney, there are sphalerite and chalcopyrite without visible zoning in hand samples. Atacamite crystals are present in some fragments.

- Two different thin samples.</td><td colspan="2"> 
  </td></tr>
<tr><td colspan="2">Coordinates (lat; long)</td><td colspan="2">volume (cm3)</td></tr>
<tr><td colspan="2">- N 36°13'48"; W 33°54'07"</td><td colspan="2">- 9x8x2,5cm; 7x4x2,5cm; 6x6x3cm and other fragments</td></tr>
<tr><td>- Whole chemistry</td><td>- SEM/EDS analysis</td><td colspan="2">In-situ S isotopic analysis (per mineral + total)</td></tr>
<tr><td>X (no)</td><td>✓ (yes)</td><td colspan="2">X (no)</td></tr>
</table>

<table>
<tr><td colspan="4">SAL-05-05</td></tr>
<tr><td>Hand Samples</td><td colspan="2">  </td><td> 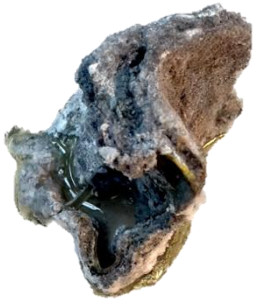 </td></tr>
<tr><td colspan="3">Sample description + Observations</td><td>Mount for polished thin sections</td></tr>
<tr><td colspan="3">Chimney fragments - full section (355ºC)

- The fluid circulation channels are visible. The typical oxidized crust is not present in the sample. The fragments are quite friable. The dominant sulphide is chalcopyrite in the form of rings and half rings, near the closed fluid circulation channels. The inner zone of the chimney is filled with anhydrite surrounded by a thin red oxide mineral ring.

- Two different thin samples.</td><td> 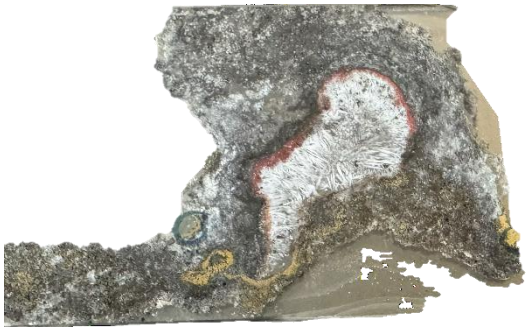
  </td></tr>
<tr><td colspan="2">Coordinates (lat; long)</td><td colspan="2">volume (cm3)</td></tr>
<tr><td colspan="2">- N 36°13'49"; W 33°54'06"</td><td colspan="2">- 11x7x5cm; 14x6x4cm; several fragments</td></tr>
<tr><td>- Whole chemistry</td><td>- SEM/EDS analysis</td><td colspan="2">In-situ S isotopic analysis (per mineral + total)</td></tr>
<tr><td>✓ (yes)</td><td>x (no)</td><td colspan="2">Cpy – 8
Total - 8</td></tr>
</table>

x

APPENDIX II: Mineral Chemistry - *Electron probe microanalysis (EPMA) in sulfide phases*.

Appendix. II.I: Standard data used to calibrate EPMA for microprobe analysis in sulfide minerals.

Element	Standard name	Mass (%)	ZAF Fac.	Z	A	F
Bi	15kV_2AV_42	100,0000	2,6972	3,4515	0,7815	1,0000
Ga	15kV_2AV_18	48,2000	7,1090	12,3103	0,5775	1,0000
Pb	15kV_ABAY_24	86,6000	2,7233	3,4515	0,7890	1,0000
Au	15kV_2AV_39	100,0000	3,3936	4,5502	0,7458	1,0000
Ag	15kV_2AV_26	100,0000	1,5455	1,7832	0,8667	1,0000
Ge	15kV_2AV_17	100,0000	6,8011	10,7887	0,6304	1,0000
Cd	15kV_2AV_27	100,0000	1,4230	1,6272	0,8745	1,0000
Mo	15kV_2AV_22	100,0000	2,5362	3,1014	0,8177	1,0000
In	15kV_2AV_28	78,7600	1,1831	1,3760	0,8598	1,0000
As	15kV_2AV_18	51,8000	3,4462	9,3860	0,3672	1,0000
Sn	15kV_2AV_29	100,0000	1,1695	1,3157	0,8889	1,0000
S	15kV_ABAY_44	28,3200	2,3647	3,1046	0,7576	1,0000
Ni	15kV_2AV_14	100,0000	0,1256	0,1271	0,9882	1,0000
Se	15kV_2AV_19	100,0000	5,7742	8,4543	0,6830	1,0000
Zn	15kV_2AV_16	100,0000	0,0673	0,0679	0,9919	1,0000
Fe	15kV_2AV_12	100,0000	0,2282	0,2320	0,9836	1,0000
Sb	15kV_2AV_30	100,0000	1,0643	1,1886	0,8954	1,0000
Mn	15kV_2AV_11	100,0000	0,3045	0,3104	0,9808	1,0000
Co	15kV_2AV_13	100,0000	0,1755	0,1780	0,9860	1,0000
W	15kV_2AV_34	100,0000	0,0646	0,0661	0,9783	1,0000
Te	15kV_2AV_31	100,0000	0,9795	1,0865	0,9015	1,0000
Cu	15kV_2AV_15	100,0000	0,0956	0,0966	0,9901	1,0000

Appendix II.II: Compositional variation of sulfide phases.

	Bi	Ga	Pb	Au	Ag	Ge	Cd	Mo	In	As	Sn	S	Ni	Se	Zn	Fe	Sb	Mn	Co	W	Te	Cu	Chemical Formula
SAMPLE 03-06(1)	0,00	0,00	0,00	0,00	0,00	0,00	0,00	0,01	0,00	0,00	0,00	35,39	0,03	0,06	0,08	31,18	0,00	0,00	0,07	0,00	0,00	33,65	Fe(0,506)Cu(0,48)S
	0,00	0,03	0,03	0,00	0,04	0,02	0,00	0,01	0,01	0,00	0,00	35,45	0,06	0,03	0,12	31,47	0,00	0,00	0,04	0,00	0,02	33,41	Fe(0,51)Cu(0,476)S
	0,00	0,02	0,02	0,03	0,01	0,00	0,00	0,00	0,02	0,00	0,00	35,46	0,01	0,07	0,02	31,52	0,00	0,04	0,07	0,00	0,02	33,22	Fe(0,51)Cu(0,473)S
	0,00	0,03	0,04	0,00	0,00	0,00	0,00	0,01	0,00	0,00	0,00	35,49	0,04	0,15	0,00	31,51	0,00	0,00	0,08	0,00	0,00	33,61	Fe(0,51)Cu(0,478)S
	0,00	0,00	0,00	0,00	0,01	0,00	0,00	0,00	0,01	0,00	0,00	35,15	0,05	0,00	0,05	30,98	0,01	0,07	0,08	0,00	0,00	33,65	Fe(0,506)Cu(0,483)S
	0,00	0,00	0,00	0,00	0,02	0,00	0,00	0,03	0,00	0,00	0,00	35,40	0,00	0,00	0,03	31,99	0,00	0,00	0,10	0,00	0,01	32,83	Fe(0,519)Cu(0,468)S
	0,00	0,00	0,10	0,01	0,00	0,00	0,00	0,04	0,02	0,02	0,00	35,35	0,02	0,01	0,00	31,92	0,00	0,00	0,14	0,00	0,01	32,86	Fe(0,519)Cu(0,469)S
	0,00	0,03	0,01	0,05	0,00	0,00	0,00	0,00	0,00	0,00	0,00	35,68	0,03	0,00	0,01	33,99	0,00	0,00	0,25	0,04	0,05	31,14	Fe(0,547)Cu(0,441)S
	0,00	0,05	0,06	0,01	0,01	0,00	0,00	0,00	0,00	0,00	0,00	35,77	0,00	0,00	0,04	35,74	0,00	0,00	0,37	0,00	0,00	28,37	Fe(0,574)Cu(0,4)S
	0,00	0,02	0,03	0,02	0,03	0,01	0,00	0,03	0,03	0,00	0,00	35,76	0,02	0,01	0,00	35,70	0,00	0,00	0,64	0,00	0,00	27,85	Fe(0,573)Cu(0,393)S
	0,00	0,00	0,03	0,00	0,01	0,00	0,00	0,02	0,00	0,00	0,00	35,54	0,01	0,01	0,00	31,34	0,00	0,00	0,17	0,07	0,00	33,00	Fe(0,507)Cu(0,469)S
	0,00	0,00	0,02	0,03	0,00	0,00	0,00	0,00	0,00	0,00	0,00	35,36	0,00	0,00	0,01	31,14	0,00	0,00	0,10	0,00	0,00	33,40	Fe(0,506)Cu(0,477)S
	0,00	0,00	0,01	0,02	0,00	0,00	0,00	0,00	0,02	0,00	0,00	34,83	0,00	0,00	0,07	30,69	0,00	0,00	0,06	0,00	0,00	33,15	Fe(0,506)Cu(0,48)S
	0,00	0,02	0,00	0,00	0,02	0,00	0,00	0,00	0,03	0,00	0,00	34,83	0,00	0,00	0,12	30,75	0,00	0,00	0,07	0,00	0,00	33,14	Fe(0,507)Cu(0,48)S
	Bi	**Ga**	**Pb**	**Au**	**Ag**	**Ge**	**Cd**	**Mo**	**In**	**As**	**Sn**	**S**	**Ni**	**Se**	**Zn**	**Fe**	**Sb**	**Mn**	**Co**	**W**	**Te**	**Cu**	**Chemical Formula**
SAMPLE 03-06(2)	0,00	0,00	0,11	0,01	0,00	0,01	0,00	0,06	0,02	0,00	0,00	34,87	0,02	0,08	0,01	30,29	0,04	0,00	0,19	0,20	0,02	32,81	Fe(0,499)Cu(0,475)S
	0,00	0,04	0,09	0,03	0,02	0,00	0,00	0,00	0,01	0,00	0,00	34,78	0,05	0,11	0,01	30,12	0,00	0,00	0,10	0,03	0,00	33,16	Fe(0,497)Cu(0,481)S
	0,00	0,06	0,00	0,00	0,01	0,00	0,00	0,09	0,00	0,00	0,00	34,80	0,05	0,08	0,09	29,95	0,00	0,04	0,12	0,00	0,05	33,19	Fe(0,494)Cu(0,481)S
	0,00	0,00	0,00	0,00	0,04	0,00	0,00	0,03	0,06	0,00	0,00	34,97	0,07	0,07	0,11	30,37	0,00	0,00	0,16	0,04	0,00	33,21	Fe(0,499)Cu(0,479)S
	0,00	0,00	0,11	0,00	0,00	0,02	0,00	0,05	0,00	0,02	0,00	35,03	0,10	0,05	0,00	30,35	0,00	0,00	0,40	0,00	0,05	33,11	Fe(0,498)Cu(0,477)S
	0,00	0,00	0,00	0,00	0,00	0,00	0,00	0,07	0,00	0,00	0,00	34,31	0,14	0,03	0,00	30,12	0,00	0,01	0,07	0,00	0,01	32,18	Fe(0,504)Cu(0,473)S
	0,00	0,00	0,00	0,00	0,02	0,01	0,00	0,04	0,00	0,00	0,00	34,95	0,04	0,09	0,09	30,41	0,00	0,00	0,11	0,12	0,00	33,66	Fe(0,5)Cu(0,486)S
	0,00	0,03	0,00	0,00	0,00	0,02	0,00	0,00	0,00	0,00	0,00	35,35	0,04	0,07	0,06	30,55	0,00	0,01	0,17	0,07	0,00	33,58	Fe(0,496)Cu(0,479)S
	0,00	0,00	0,01	0,04	0,04	0,00	0,00	0,03	0,00	0,00	0,00	35,30	0,01	0,14	0,07	30,74	0,00	0,02	0,05	0,00	0,00	34,09	Fe(0,5)Cu(0,487)S
	0,00	0,00	0,02	0,02	0,01	0,01	0,00	0,05	0,00	0,02	0,00	35,32	0,00	0,00	0,14	30,70	0,00	0,00	0,08	0,00	0,00	33,67	Fe(0,499)Cu(0,481)S
	0,00	0,00	0,00	0,00	0,00	0,00	0,00	0,04	0,00	0,00	0,00	35,28	0,07	0,00	0,22	30,60	0,00	0,00	0,08	0,12	0,02	33,95	Fe(0,498)Cu(0,486)S
	0,00	0,00	0,00	0,02	0,02	0,03	0,00	0,02	0,00	0,00	0,00	35,17	0,03	0,00	4,28	28,89	0,05	0,00	0,19	0,00	0,00	28,79	Zn(0,06)Fe(0,472)Cu(0,413)S

	0,00	0,00	0,00	0,00	0,00	0,00	0,00	0,09	0,02	0,00	0,00	34,79	0,06	0,16	0,03	30,55	0,00	0,03	0,16	0,01	0,00	33,08	Fe(0,504)Cu(0,48)S
	0,00	0,00	0,00	0,00	0,02	0,00	0,00	0,05	0,00	0,00	0,00	34,52	0,03	0,14	0,00	30,33	0,00	0,00	0,12	0,00	0,00	33,37	Fe(0,505)Cu(0,488)S
	0,00	0,00	0,00	0,00	0,00	0,00	0,00	0,04	0,00	0,00	0,00	34,73	0,00	0,11	0,01	30,38	0,00	0,00	0,06	0,00	0,00	33,44	Fe(0,503)Cu(0,486)S
	0,00	0,01	0,00	0,00	0,00	0,00	0,00	0,06	0,03	0,00	0,00	34,56	0,06	0,09	0,07	30,36	0,00	0,00	0,11	0,16	0,00	33,34	Fe(0,504)Cu(0,487)S
	0,00	0,00	0,00	0,00	0,01	0,00	0,00	0,06	0,01	0,00	0,00	34,65	0,04	0,13	0,03	30,40	0,00	0,01	0,11	0,04	0,00	33,31	Fe(0,504)Cu(0,485)S
	0,00	0,00	0,03	0,01	0,00	0,00	0,00	0,06	0,01	0,00	0,00	34,91	0,00	0,07	0,04	30,44	0,00	0,06	0,09	0,09	0,02	33,34	Fe(0,501)Cu(0,482)S
	0,00	0,09	0,00	0,00	0,03	0,00	0,00	0,02	0,00	0,00	0,00	34,84	0,13	0,09	0,02	29,82	0,00	0,00	0,66	0,00	0,00	32,79	Fe(0,492)Cu(0,475)S
	0,00	0,01	0,00	0,00	0,00	0,01	0,00	0,06	0,00	0,00	0,00	34,96	0,07	0,20	0,01	30,41	0,00	0,04	0,08	0,00	0,05	33,55	Fe(0,5)Cu(0,484)S
	0,00	0,00	0,00	0,03	0,00	0,01	0,00	0,03	0,00	0,00	0,00	34,85	0,07	0,07	0,18	30,20	0,00	0,04	0,34	0,03	0,00	32,70	Fe(0,498)Cu(0,474)S
	0,00	0,03	0,01	0,01	0,01	0,01	0,00	0,04	0,00	0,00	0,00	34,89	0,07	0,11	0,06	30,22	0,00	0,03	0,29	0,03	0,02	33,09	Fe(0,497)Cu(0,479)S
	0,00	0,00	0,00	0,00	0,03	0,00	0,00	0,07	0,00	0,00	0,00	35,22	0,04	0,02	0,11	30,28	0,00	0,00	0,09	0,00	0,02	33,68	Fe(0,494)Cu(0,483)S
	0,00	0,01	0,03	0,04	0,02	0,02	0,00	0,04	0,00	0,01	0,00	35,27	0,01	0,00	0,13	30,37	0,00	0,00	0,07	0,05	0,00	33,98	Fe(0,495)Cu(0,486)S
	0,00	0,00	0,03	0,02	0,00	0,00	0,00	0,07	0,00	0,00	0,00	35,16	0,01	0,02	0,09	30,17	0,00	0,00	0,08	0,00	0,00	34,03	Fe(0,493)Cu(0,489)S
	0,00	0,00	0,00	0,01	0,00	0,00	0,00	0,05	0,00	0,00	0,00	35,32	0,00	0,00	0,24	30,39	0,01	0,00	0,09	0,07	0,00	33,87	Fe(0,494)Cu(0,484)S
	0,00	0,00	0,02	0,02	0,01	0,00	0,00	0,06	0,00	0,00	0,00	35,24	0,02	0,01	0,14	30,30	0,00	0,00	0,08	0,03	0,01	33,89	Fe(0,494)Cu(0,485)S
	0,00	0,00	0,08	0,01	0,00	0,00	0,39	0,06	0,00	0,00	0,04	33,47	0,00	0,00	51,82	7,83	0,02	0,02	0,35	0,00	0,00	5,67	Zn(0,76)Fe(0,134)Cu(0,086)S
	0,00	0,00	0,00	0,00	0,02	0,00	0,28	0,02	0,00	0,00	0,04	33,39	0,00	0,00	56,43	6,06	0,00	0,01	0,40	0,00	0,06	2,70	Zn(0,829)Fe(0,104)S
	0,00	0,00	0,24	0,04	0,08	0,00	0,28	0,05	0,03	0,00	0,00	33,34	0,00	0,00	52,54	7,36	0,04	0,00	0,36	0,00	0,00	4,76	Zn(0,773)Fe(0,127)Cu(0,072)S
	0,00	0,00	0,03	0,00	0,00	0,02	0,11	0,03	0,00	0,00	0,00	33,26	0,00	0,00	57,34	5,03	0,00	0,03	0,41	0,00	0,03	2,31	Zn(0,846)Fe(0,087)S
	0,00	0,00	0,09	0,01	0,02	0,00	0,26	0,04	0,01	0,00	0,02	33,36	0,00	0,00	54,53	6,57	0,01	0,01	0,38	0,00	0,02	3,86	Zn(0,802)Fe(0,113)Cu(0,058)S
	Bi	**Ga**	**Pb**	**Au**	**Ag**	**Ge**	**Cd**	**Mo**	**In**	**As**	**Sn**	**S**	**Ni**	**Se**	**Zn**	**Fe**	**Sb**	**Mn**	**Co**	**W**	**Te**	**Cu**	**Chemical Formula**
SAMPLE 03-08	0,00	0,00	0,01	0,00	0,00	0,00	0,00	0,03	0,00	0,01	0,00	34,99	0,13	0,24	0,03	31,24	0,00	0,00	0,05	0,00	0,00	32,44	Fe(0,513)Cu(0,468)S
	0,00	0,00	0,00	0,00	0,03	0,00	0,00	0,09	0,00	0,00	0,00	34,84	0,09	0,22	0,00	30,64	0,00	0,00	0,05	0,00	0,00	33,27	Fe(0,505)Cu(0,482)S
	0,00	0,00	0,07	0,00	0,02	0,00	0,00	0,07	0,00	0,05	0,00	34,84	0,13	0,17	0,04	30,59	0,00	0,00	0,06	0,00	0,00	33,06	Fe(0,504)Cu(0,479)S
	0,00	0,00	0,02	0,00	0,00	0,01	0,00	0,02	0,00	0,01	0,00	34,90	0,22	0,22	0,00	30,42	0,00	0,00	0,02	0,00	0,00	32,56	Fe(0,501)Cu(0,471)S
	0,00	0,00	0,00	0,00	0,00	0,00	0,00	0,07	0,01	0,00	0,00	34,82	0,04	0,18	0,00	30,16	0,00	0,00	0,01	0,20	0,00	32,93	Fe(0,497)Cu(0,477)S
	0,00	0,00	0,00	0,00	0,00	0,00	0,00	0,02	0,00	0,02	0,00	26,06	0,00	0,11	0,01	11,40	0,01	0,00	0,04	0,11	0,04	61,70	Fe(0,251)Cu(1,195)S
	0,00	0,01	0,11	0,03	0,01	0,00	0,00	0,07	0,00	0,00	0,00	34,53	0,10	0,20	0,00	30,15	0,00	0,02	0,02	0,00	0,00	33,55	Fe(0,502)Cu(0,49)S
	0,00	0,04	0,00	0,01	0,00	0,00	0,00	0,04	0,05	0,00	0,00	26,19	0,03	0,13	0,00	12,11	0,02	0,00	0,00	0,00	0,00	59,06	Fe(0,266)Cu(1,138)S
	0,00	0,02	0,00	0,00	0,00	0,00	0,00	0,07	0,00	0,00	0,00	34,68	0,10	0,13	0,00	30,13	0,00	0,00	0,03	0,00	0,00	33,46	Fe(0,499)Cu(0,487)S

0,00	0,00	0,00	0,00	0,00	0,00	0,03	0,05	0,00	0,00	0,00	24,55	0,00	0,09	0,06	7,12	0,00	0,01	0,00	0,00	0,00	65,94	Fe(0,167)Cu(1,356)S
0,00	0,00	0,00	0,03	0,00	0,01	0,00	0,06	0,00	0,00	0,00	23,93	0,01	0,00	0,00	5,69	0,03	0,02	0,00	0,09	0,01	68,77	Fe(0,137)Cu(1,451)S
0,07	0,00	0,02	0,00	0,01	0,00	0,00	0,07	0,00	0,00	0,00	23,37	0,00	0,11	0,12	4,58	0,00	0,04	0,00	0,02	0,00	69,50	Fe(0,113)Cu(1,501)S
0,01	0,00	0,00	0,00	0,04	0,02	0,00	0,01	0,01	0,00	0,00	21,12	0,00	0,08	0,12	0,01	0,02	0,00	0,00	0,00	0,00	76,11	Cu(1,819)S
0,03	0,00	0,04	0,05	0,02	0,00	0,04	0,03	0,00	0,00	0,00	21,10	0,00	0,10	0,00	0,01	0,02	0,00	0,00	0,00	0,00	75,78	Cu(1,813)S
0,00	0,00	0,00	0,01	0,08	0,00	0,01	0,05	0,01	0,00	0,00	21,19	0,00	0,09	0,05	0,10	0,00	0,00	0,00	0,00	0,00	76,52	Cu(1,823)S
0,00	0,05	0,08	0,00	0,00	0,00	0,00	0,04	0,00	0,00	0,00	34,60	0,01	0,23	0,00	30,15	0,00	0,00	0,02	0,00	0,04	33,34	Fe(0,501)Cu(0,486)S
0,03	0,00	0,00	0,04	0,02	0,01	0,00	0,00	0,02	0,00	0,00	25,66	0,00	0,15	0,00	11,35	0,00	0,01	0,00	0,00	0,01	61,56	Fe(0,254)Cu(1,211)S
0,00	0,00	0,05	0,04	0,00	0,01	0,00	0,03	0,00	0,00	0,02	26,10	0,00	0,13	0,16	10,98	0,05	0,01	0,00	0,00	0,00	61,59	Fe(0,242)Cu(1,191)S
0,00	0,02	0,00	0,00	0,00	0,01	0,00	0,06	0,00	0,00	0,00	26,02	0,00	0,17	0,13	11,22	0,00	0,00	0,01	0,00	0,00	62,18	Fe(0,248)Cu(1,206)S
0,00	0,00	0,00	0,00	0,02	0,00	0,00	0,01	0,00	0,00	0,01	25,92	0,00	0,11	0,12	10,90	0,00	0,00	0,00	0,03	0,00	62,51	Fe(0,241)Cu(1,217)S
0,00	0,00	0,00	0,00	0,02	0,00	0,00	0,01	0,00	0,00	0,00	25,95	0,08	0,01	0,00	10,57	0,04	0,00	0,02	0,01	0,00	62,35	Fe(0,234)Cu(1,213)S
0,00	0,00	0,00	0,01	0,05	0,00	0,01	0,03	0,00	0,00	0,00	25,59	0,00	0,04	0,03	10,38	0,00	0,02	0,00	0,01	0,00	62,19	Fe(0,233)Cu(1,226)S
0,00	0,01	0,00	0,00	0,00	0,00	0,00	0,03	0,00	0,00	0,00	34,73	0,07	0,18	0,03	29,95	0,00	0,00	0,01	0,00	0,00	34,04	Fe(0,495)Cu(0,495)S
0,00	0,00	0,06	0,00	0,00	0,02	0,00	0,06	0,00	0,00	0,06	33,24	47,11	0,03	0,00	1,09	0,00	0,05	4,35	0,00	0,00	6,06	Ni(0,775)Co(0,071)Cu(0,092)S
0,00	0,00	0,02	0,01	0,00	0,00	0,00	0,00	0,00	0,00	0,00	34,16	0,07	0,18	0,13	28,38	0,00	0,00	0,00	0,00	0,00	37,02	Fe(0,477)Cu(0,547)S
0,00	0,04	0,03	0,00	0,05	0,00	0,00	0,06	0,00	0,00	0,00	34,84	0,00	0,11	0,00	30,21	0,00	0,00	0,02	0,01	0,00	33,97	Fe(0,498)Cu(0,492)S
0,02	0,05	0,00	0,00	0,01	0,05	0,00	0,02	0,02	0,00	0,00	25,89	0,00	0,10	0,05	11,42	0,00	0,00	0,01	0,00	0,01	61,63	Fe(0,253)Cu(1,202)S
0,00	0,02	0,00	0,02	0,02	0,00	0,00	0,00	0,00	0,01	0,00	25,81	0,00	0,09	0,07	11,09	0,00	0,02	0,00	0,00	0,00	62,16	Fe(0,247)Cu(1,216)S
0,03	0,02	0,03	0,00	0,00	0,01	0,00	0,04	0,00	0,00	0,00	26,12	0,01	0,10	0,12	11,74	0,00	0,00	0,01	0,00	0,00	62,19	Fe(0,258)Cu(1,202)S
0,00	0,05	0,00	0,04	0,05	0,00	0,00	0,04	0,00	0,00	0,00	35,30	0,06	0,17	0,11	30,91	0,00	0,00	0,01	0,04	0,02	35,51	Fe(0,503)Cu(0,508)S
0,00	0,02	0,05	0,00	0,02	0,00	0,00	0,03	0,00	0,00	0,00	25,80	0,06	0,16	0,07	11,39	0,00	0,00	0,00	0,00	0,00	61,67	Fe(0,254)Cu(1,207)S
0,07	0,00	0,00	0,00	0,00	0,00	0,00	0,04	0,04	0,02	0,00	23,16	0,01	0,08	0,15	0,03	0,00	0,00	0,00	0,21	0,00	75,55	Cu(1,647)S
0,00	0,02	0,00	0,00	0,02	0,00	0,03	0,04	0,04	0,00	0,07	33,31	0,05	0,07	0,12	0,08	0,05	0,00	0,00	0,00	0,03	65,18	Cu(0,988)S
0,00	0,00	0,03	0,00	0,00	0,00	0,00	0,03	0,00	0,00	0,02	32,08	0,02	0,10	0,04	0,07	0,00	0,02	0,00	0,00	0,01	65,32	Cu(1,028)S
0,00	0,00	0,00	0,04	0,02	0,00	0,01	0,00	0,00	0,00	0,00	32,54	0,00	0,13	0,00	0,00	0,00	0,00	0,00	0,00	0,00	66,21	Cu(1,027)S
0,00	0,00	0,00	0,00	0,04	0,00	0,01	0,00	0,00	0,00	0,00	20,81	0,03	0,10	0,12	0,12	0,05	0,01	0,02	0,00	0,00	76,64	Cu(1,859)S
0,00	0,00	0,00	0,00	0,00	0,00	0,00	0,01	0,02	0,01	0,00	20,96	0,03	0,06	0,00	0,01	0,04	0,00	0,00	0,00	0,00	77,57	Cu(1,868)S
0,00	0,00	0,00	0,00	0,00	0,00	0,00	0,01	0,00	0,00	0,00	21,02	0,00	0,07	0,07	0,03	0,01	0,02	0,00	0,00	0,00	77,66	Cu(1,865)S
0,00	0,00	0,00	0,01	0,06	0,00	0,00	0,02	0,00	0,00	0,00	33,16	0,00	0,09	0,09	0,08	0,04	0,00	0,01	0,00	0,00	65,80	Cu(1,002)S
0,02	0,00	0,00	14,04	0,19	0,00	0,06	0,00	0,00	0,00	0,06	18,14	0,00	0,00	0,00	0,36	0,00	0,00	0,00	0,00	0,04	45,76	Au(0,126)Cu(1,273)S

0,00	0,03	0,01	0,00	0,00	0,00	0,00	0,00	0,04	0,00	0,00	0,22	0,19	0,00	0,02	10,72	0,03	0,01	0,01	0,00	0,00	52,87	Ga(0,068)Ni(0,491)Fe(28,644)Cu(124,133)S
0,00	0,00	0,02	0,00	0,00	0,00	0,00	0,04	0,00	0,00	0,00	34,93	0,04	0,12	0,00	30,71	0,00	0,03	0,03	0,00	0,00	34,66	Fe(0,505)Cu(0,501)S
0,00	0,00	0,08	0,00	0,06	0,00	0,00	0,01	0,00	0,00	0,01	24,90	0,00	0,14	0,14	8,23	0,00	0,03	0,01	0,00	0,00	68,05	Fe(0,19)Cu(1,38)S
0,00	0,00	0,04	0,01	0,05	0,00	0,02	0,06	0,02	0,00	0,00	24,78	0,00	0,11	0,08	7,27	0,00	0,00	0,01	0,00	0,00	70,85	Fe(0,169)Cu(1,443)S
0,00	0,00	0,08	0,00	0,00	0,00	0,00	0,03	0,03	0,00	0,00	23,87	0,06	0,13	0,03	5,91	0,00	0,00	0,02	0,14	0,00	69,20	Fe(0,142)Cu(1,463)S
0,00	0,00	0,00	0,00	0,05	0,00	0,00	0,04	0,00	0,00	0,00	35,26	0,17	0,23	0,06	31,05	0,00	0,00	0,03	0,26	0,04	32,65	Fe(0,506)Cu(0,467)S
0,00	0,00	0,05	0,00	0,01	0,00	0,00	0,03	0,00	0,00	0,00	35,20	0,17	0,21	0,00	30,54	0,00	0,01	0,06	0,08	0,00	33,29	Fe(0,498)Cu(0,477)S
0,00	0,00	0,00	0,03	0,01	0,00	0,00	0,00	0,00	0,03	0,00	35,05	0,46	0,22	0,00	30,55	0,00	0,00	0,02	0,00	0,00	33,03	Fe(0,501)Cu(0,476)S
0,00	0,00	0,08	0,07	0,01	0,00	0,00	0,05	0,00	0,00	0,00	35,06	0,39	0,18	0,00	30,35	0,03	0,01	0,06	0,07	0,00	33,51	Fe(0,497)Cu(0,482)S
0,00	0,00	0,01	0,06	0,00	0,00	0,00	0,02	0,02	0,00	0,00	34,80	0,15	0,18	0,00	30,00	0,00	0,02	0,01	0,00	0,00	34,16	Fe(0,495)Cu(0,496)S
0,00	0,01	0,00	0,00	0,05	0,00	0,00	0,02	0,00	0,00	0,00	34,73	0,01	0,27	0,00	30,18	0,00	0,02	0,01	0,00	0,00	34,42	Fe(0,499)Cu(0,5)S
0,00	0,00	0,10	0,05	0,00	0,00	0,00	0,00	0,00	0,00	0,00	34,64	0,40	0,22	0,07	30,06	0,00	0,01	0,04	0,07	0,04	34,40	Fe(0,498)Cu(0,501)S
0,00	0,00	0,11	0,03	0,00	0,00	0,00	0,00	0,00	0,00	0,00	34,85	0,01	0,15	0,09	30,51	0,00	0,00	0,02	0,01	0,00	34,68	Fe(0,503)Cu(0,502)S
0,00	0,00	0,00	0,01	0,03	0,00	0,00	0,00	0,00	0,00	0,00	34,87	0,05	0,23	0,00	30,40	0,00	0,00	0,00	0,00	0,00	34,75	Fe(0,501)Cu(0,503)S
0,00	0,00	0,04	0,00	0,02	0,01	0,00	0,00	0,00	0,00	0,00	34,84	0,05	0,16	0,00	30,35	0,00	0,03	0,00	0,01	0,00	34,93	Fe(0,5)Cu(0,506)S
0,00	0,00	0,00	0,04	0,00	0,00	0,00	0,03	0,00	0,00	0,00	34,90	0,07	0,14	0,02	30,56	0,00	0,01	0,04	0,16	0,00	34,91	Fe(0,503)Cu(0,505)S
Bi	**Ga**	**Pb**	**Au**	**Ag**	**Ge**	**Cd**	**Mo**	**In**	**As**	**Sn**	**S**	**Ni**	**Se**	**Zn**	**Fe**	**Sb**	**Mn**	**Co**	**W**	**Te**	**Cu**	**Chemical Formula**
0,00	0,00	0,00	0,00	0,00	0,00	0,00	0,05	0,00	0,00	0,00	35,31	0,06	0,00	0,07	35,36	0,02	0,03	0,28	0,00	0,00	26,78	Fe(0,575)Cu(0,383)S
0,00	0,00	0,03	0,02	0,01	0,01	0,00	0,04	0,01	0,04	0,00	35,90	0,02	0,00	0,12	39,97	0,00	0,00	0,54	0,00	0,03	22,42	Fe(0,639)Cu(0,315)S
0,00	0,00	0,07	0,00	0,00	0,00	0,00	0,00	0,01	0,01	0,00	36,38	0,00	0,00	0,11	43,50	0,00	0,00	0,71	0,11	0,00	19,03	Fe(0,687)Cu(0,264)S
0,00	0,01	0,00	0,00	0,07	0,02	0,00	0,00	0,00	0,01	0,00	35,69	0,05	0,04	0,19	39,02	0,00	0,00	0,43	0,00	0,03	24,14	Fe(0,628)Cu(0,341)S
0,03	0,00	0,03	0,06	0,04	0,00	0,00	0,00	0,00	0,00	0,00	35,37	0,00	0,00	0,13	33,38	0,00	0,00	0,21	0,09	0,00	28,30	Fe(0,542)Cu(0,404)S
0,00	0,00	0,00	0,00	0,02	0,00	0,00	0,00	0,00	0,02	0,00	35,66	0,00	0,00	0,04	37,09	0,00	0,00	0,36	0,00	0,00	25,93	Fe(0,597)Cu(0,367)S
0,00	0,00	0,00	0,08	0,00	0,00	0,00	0,04	0,01	0,00	0,00	36,28	0,00	0,00	0,14	43,42	0,00	0,03	0,67	0,23	0,02	19,13	Fe(0,687)Cu(0,266)S
0,00	0,00	0,00	0,00	0,03	0,00	0,00	0,00	0,00	0,00	0,00	35,54	0,05	0,01	0,09	37,02	0,00	0,00	0,33	0,00	0,00	26,16	Fe(0,598)Cu(0,372)S
0,01	0,00	0,00	0,03	0,00	0,00	0,00	0,00	0,00	0,00	0,00	36,11	0,00	0,00	0,08	43,43	0,00	0,00	0,64	0,02	0,00	19,31	Fe(0,691)Cu(0,27)S
0,00	0,00	0,00	0,07	0,00	0,00	0,00	0,01	0,03	0,02	0,00	35,96	0,00	0,00	0,10	41,32	0,00	0,03	0,59	0,06	0,00	20,80	Fe(0,66)Cu(0,292)S
0,00	0,00	0,00	0,09	0,03	0,00	0,00	0,01	0,01	0,00	0,00	35,22	0,02	0,00	0,02	33,86	0,00	0,00	0,18	0,00	0,00	29,07	Fe(0,552)Cu(0,417)S
0,00	0,01	0,00	0,00	0,00	0,00	0,00	0,02	0,00	0,00	0,00	35,32	0,00	0,05	0,06	33,80	0,00	0,00	0,17	0,06	0,00	28,29	Fe(0,55)Cu(0,404)S
0,00	0,05	0,03	0,00	0,00	0,00	0,00	0,00	0,00	0,00	0,00	36,01	0,00	0,01	0,21	43,33	0,00	0,02	0,76	0,00	0,00	18,82	Fe(0,691)Cu(0,264)S
0,00	0,00	0,02	0,01	0,00	0,00	0,00	0,00	0,04	0,00	0,00	35,24	0,05	0,00	0,11	32,71	0,00	0,03	0,17	0,00	0,00	30,41	Fe(0,533)Cu(0,436)S

SAMPLE 05-01(1)

	0,00	0,00	0,07	0,01	0,00	0,00	0,00	0,02	0,00	0,05	0,00	36,05	0,00	0,00	0,10	42,85	0,00	0,00	0,89	0,03	0,00	19,26	Fe(0,683)Cu(0,27)S
	0,00	0,00	0,00	0,00	0,01	0,00	0,00	0,00	0,00	0,00	0,00	36,04	0,01	0,00	0,14	40,81	0,00	0,00	0,94	0,09	0,00	19,45	Fe(0,65)Cu(0,272)S
	0,00	0,00	0,04	0,00	0,04	0,01	0,00	0,02	0,00	0,00	0,00	35,65	0,03	0,00	0,13	35,39	0,00	0,03	0,33	0,00	0,00	28,52	Fe(0,57)Cu(0,404)S
	0,00	0,00	0,05	0,00	0,00	0,00	0,00	0,01	0,00	0,00	0,00	35,50	0,00	0,00	0,15	37,66	0,03	0,00	0,60	0,19	0,00	24,01	Fe(0,609)Cu(0,341)S
	0,00	0,00	0,00	0,00	0,04	0,00	0,00	0,02	0,00	0,01	0,00	35,41	0,00	0,00	0,00	36,51	0,00	0,00	0,26	0,00	0,02	27,73	Fe(0,592)Cu(0,395)S
	0,00	0,00	0,04	0,00	0,02	0,00	0,00	0,00	0,00	0,03	0,00	35,98	0,02	0,00	0,03	42,92	0,00	0,00	0,84	0,04	0,01	19,55	Fe(0,685)Cu(0,274)S
	Bi	**Ga**	**Pb**	**Au**	**Ag**	**Ge**	**Cd**	**Mo**	**In**	**As**	**Sn**	**S**	**Ni**	**Se**	**Zn**	**Fe**	**Sb**	**Mn**	**Co**	**W**	**Te**	**Cu**	**Chemical Formula**
SAMPLE 05-03	0,00	0,00	0,05	0,00	0,01	0,00	0,00	0,01	0,00	0,00	0,00	32,64	0,01	0,05	0,10	34,03	0,02	0,00	0,41	0,00	0,00	30,51	Fe(0,599)Cu(0,472)S
	0,00	0,00	0,05	0,00	0,10	0,00	0,00	0,00	0,00	0,00	0,00	31,30	0,03	0,05	0,11	21,90	0,00	0,01	0,26	0,00	0,00	40,76	Fe(0,402)Cu(0,657)S
	0,00	0,01	0,10	0,05	0,00	0,00	0,00	0,03	0,02	0,00	0,00	35,66	0,00	0,04	0,06	39,28	0,00	0,02	0,48	0,00	0,00	24,12	Fe(0,633)Cu(0,341)S
	0,00	0,00	0,00	0,02	0,02	0,00	0,00	0,03	0,00	0,00	0,00	35,47	0,05	0,07	0,04	39,28	0,00	0,00	0,49	0,06	0,02	23,89	Fe(0,636)Cu(0,34)S
	0,00	0,00	0,00	0,02	0,01	0,00	0,00	0,08	0,00	0,00	0,00	34,63	0,00	0,00	0,00	37,82	0,00	0,03	0,43	0,00	0,00	26,16	Fe(0,627)Cu(0,381)S
	0,00	0,00	0,13	0,01	0,00	0,00	0,00	0,04	0,00	0,00	0,00	1,93	0,01	0,03	0,80	29,81	0,00	0,00	0,17	0,00	0,00	18,01	Zn(0,204)Fe(8,872)Cu(4,711)S
	0,00	0,00	0,00	0,00	0,02	0,00	0,00	0,00	0,00	0,00	0,00	6,55	0,05	0,02	0,97	36,09	0,00	0,00	0,17	0,01	0,01	21,53	Zn(0,073)Fe(3,163)Cu(1,658)S
	0,00	0,00	0,05	0,01	0,00	0,00	0,00	0,00	0,00	0,00	0,01	7,15	0,00	0,03	0,09	0,66	0,01	0,00	0,01	0,00	0,00	65,41	Fe(0,053)Cu(4,621)S
	0,00	0,03	0,00	0,00	0,00	0,00	0,00	0,00	0,00	0,00	0,00	35,50	0,00	0,03	0,06	39,70	0,00	0,00	0,52	0,00	0,00	24,00	Fe(0,642)Cu(0,341)S
	0,00	0,06	0,00	0,04	0,00	0,00	0,00	0,01	0,07	0,00	0,00	35,09	0,00	0,00	0,06	35,39	0,00	0,00	0,46	0,00	0,01	28,12	Fe(0,579)Cu(0,404)S
	0,00	0,01	0,00	0,00	0,02	0,00	0,00	0,02	0,00	0,00	0,00	35,13	0,01	0,09	0,04	38,60	0,00	0,00	0,47	0,17	0,00	23,72	Fe(0,631)Cu(0,341)S
	0,00	0,00	0,00	0,02	0,03	0,00	0,00	0,04	0,00	0,00	0,00	35,43	0,00	0,14	0,13	38,94	0,00	0,00	0,51	0,14	0,00	24,07	Fe(0,631)Cu(0,343)S
	0,00	0,02	0,04	0,02	0,05	0,00	0,00	0,04	0,08	0,00	0,00	35,54	0,02	0,18	0,00	39,21	0,00	0,00	0,50	0,16	0,01	24,22	Fe(0,634)Cu(0,344)S
	0,00	0,00	0,16	0,00	0,00	0,00	0,00	0,00	0,00	0,00	0,00	34,85	0,00	0,04	0,01	37,85	0,07	0,03	0,48	0,15	0,01	24,49	Fe(0,624)Cu(0,355)S
	0,00	0,00	0,00	0,02	0,02	0,00	0,00	0,06	0,03	0,00	0,00	35,33	0,00	0,00	0,01	39,92	0,00	0,00	0,49	0,00	0,00	24,59	Fe(0,649)Cu(0,351)S
	Bi	**Ga**	**Pb**	**Au**	**Ag**	**Ge**	**Cd**	**Mo**	**In**	**As**	**Sn**	**S**	**Ni**	**Se**	**Zn**	**Fe**	**Sb**	**Mn**	**Co**	**W**	**Te**	**Cu**	**Chemical Formula**
SAMPLE 05-04(2)	0,00	0,00	0,04	0,00	0,00	0,00	0,00	0,02	0,00	0,00	0,00	32,70	0,00	0,00	0,02	5,62	0,00	0,01	0,04	0,02	0,00	60,50	Fe(0,099)Cu(0,934)S
	0,00	0,00	0,00	0,00	0,03	0,00	0,01	0,02	0,00	0,00	0,00	33,11	0,00	0,03	0,03	10,31	0,02	0,00	0,10	0,03	0,00	54,93	Fe(0,179)Cu(0,838)S
	0,00	0,02	0,03	0,03	0,00	0,02	0,00	0,02	0,01	0,00	0,00	30,65	0,01	0,05	0,02	10,86	0,00	0,00	0,09	0,06	0,00	52,17	Fe(0,204)Cu(0,859)S
	0,00	0,00	0,00	0,00	0,00	0,00	0,04	0,00	0,04	0,00	0,00	33,60	0,00	0,00	0,14	1,04	0,00	0,00	0,02	0,04	0,01	63,79	Cu(0,958)S
	0,00	0,00	0,00	0,00	0,01	0,00	0,00	0,00	0,00	0,00	0,00	34,82	0,10	0,07	0,04	31,00	0,00	0,00	0,53	0,00	0,00	32,27	Fe(0,511)Cu(0,468)S
	0,00	0,01	0,00	0,00	0,00	0,00	0,00	0,05	0,00	0,00	0,00	35,51	0,00	0,02	0,07	37,91	0,00	0,01	0,42	0,00	0,03	25,49	Fe(0,613)Cu(0,362)S
	0,00	0,00	0,00	0,00	0,01	0,02	0,00	0,00	0,00	0,01	0,00	35,29	0,00	0,04	0,14	37,22	0,00	0,00	0,40	0,14	0,00	24,04	Fe(0,606)Cu(0,344)S

	0,00	0,00	0,00	0,00	0,03	0,00	0,00	0,00	0,00	0,00	0,00	33,84	0,00	0,00	0,06	9,53	0,03	0,01	0,08	0,00	0,00	54,79	Fe(0,162)Cu(0,817)S
	0,00	0,00	0,00	0,00	0,00	0,00	0,00	0,07	0,00	0,00	0,00	35,11	0,02	0,06	0,09	36,11	0,00	0,00	0,76	0,02	0,00	24,91	Fe(0,591)Cu(0,358)S
	0,00	0,00	0,02	0,00	0,00	0,00	0,00	0,03	0,00	0,00	0,00	34,59	0,00	0,02	0,09	32,91	0,00	0,05	0,58	0,02	0,00	27,73	Fe(0,546)Cu(0,405)S
	0,00	0,00	0,01	0,01	0,00	0,00	0,00	0,04	0,00	0,05	0,00	35,18	0,03	0,07	0,15	32,61	0,00	0,00	0,31	0,00	0,01	29,88	Fe(0,532)Cu(0,429)S
	0,00	0,00	0,02	0,02	0,04	0,01	0,00	0,02	0,00	0,01	0,00	35,22	0,09	0,06	0,00	35,07	0,00	0,00	0,43	0,02	0,00	26,60	Fe(0,572)Cu(0,381)S
	Bi	**Ga**	**Pb**	**Au**	**Ag**	**Ge**	**Cd**	**Mo**	**In**	**As**	**Sn**	**S**	**Ni**	**Se**	**Zn**	**Fe**	**Sb**	**Mn**	**Co**	**W**	**Te**	**Cu**	**Chemical Formula**
SAMPLE 05-05(2)	0,00	0,00	0,01	0,00	0,00	0,00	0,00	0,00	0,00	0,00	0,00	35,58	0,25	0,23	0,01	36,46	0,05	0,03	0,46	0,00	0,00	26,56	Fe(0,589)Cu(0,377)S
	0,00	0,00	0,01	0,00	0,00	0,00	0,00	0,01	0,00	0,00	0,00	35,26	0,18	0,14	0,00	31,14	0,00	0,00	0,37	0,21	0,01	32,50	Fe(0,507)Cu(0,465)S
	0,00	0,01	0,03	0,00	0,00	0,00	0,00	0,02	0,02	0,00	0,00	29,99	0,00	0,01	0,09	6,02	0,00	0,03	0,06	0,00	0,00	64,45	Fe(0,115)Cu(1,085)S
	0,00	0,02	0,00	0,00	0,00	0,00	0,00	0,01	0,01	0,03	0,00	29,18	0,02	0,08	0,03	6,76	0,00	0,00	0,00	0,00	0,00	63,67	Fe(0,133)Cu(1,102)S
	0,00	0,01	0,00	0,00	0,04	0,00	0,00	0,01	0,01	0,03	0,00	30,73	0,00	0,00	0,04	7,55	0,01	0,02	0,12	0,01	0,00	60,53	Fe(0,141)Cu(0,994)S
	0,00	0,03	0,02	0,00	0,00	0,00	0,00	0,03	0,00	0,00	0,00	35,73	0,01	0,05	0,04	38,32	0,00	0,02	0,61	0,11	0,00	24,90	Fe(0,616)Cu(0,352)S
	0,00	0,00	0,00	0,00	0,01	0,00	0,00	0,00	0,00	0,00	0,00	35,42	0,07	0,10	0,07	36,61	0,01	0,01	0,57	0,09	0,00	25,94	Fe(0,594)Cu(0,37)S
	0,00	0,00	0,00	0,00	0,04	0,00	0,00	0,02	0,00	0,02	0,00	35,37	0,20	0,15	0,03	37,18	0,00	0,01	0,55	0,00	0,00	25,36	Fe(0,604)Cu(0,362)S
	0,00	0,01	0,09	0,00	0,00	0,00	0,00	0,00	0,00	0,01	0,00	35,18	0,05	0,06	0,08	32,04	0,00	0,03	0,53	0,03	0,00	31,20	Fe(0,523)Cu(0,448)S
	0,00	0,00	0,06	0,00	0,00	0,00	0,00	0,02	0,00	0,01	0,00	35,47	0,09	0,24	0,00	39,33	0,00	0,00	0,52	0,07	0,00	23,16	Fe(0,637)Cu(0,33)S
	0,00	0,01	0,00	0,00	0,00	0,00	0,00	0,00	0,00	0,03	0,00	35,16	0,05	0,04	0,13	30,47	0,00	0,02	1,04	0,00	0,00	32,74	Fe(0,498)Cu(0,47)S
	0,00	0,04	0,14	0,00	0,07	0,00	0,00	0,06	0,00	0,00	0,00	35,84	0,02	0,02	0,00	39,98	0,00	0,03	0,50	0,00	0,01	23,20	Fe(0,641)Cu(0,327)S
	0,00	0,05	0,04	0,00	0,10	0,00	0,00	0,01	0,00	0,00	0,00	35,38	0,42	0,26	0,14	37,98	0,04	0,00	0,41	0,00	0,00	24,17	Fe(0,617)Cu(0,345)S
	0,00	0,00	0,14	0,00	0,03	0,03	0,00	0,02	0,00	0,00	0,00	35,39	0,21	0,07	0,02	37,37	0,00	0,00	0,34	0,00	0,00	25,02	Fe(0,606)Cu(0,357)S
	0,00	0,00	0,01	0,04	0,04	0,03	0,00	0,01	0,00	0,00	0,00	35,52	0,26	0,13	0,00	37,16	0,00	0,01	0,37	0,00	0,01	25,17	Fe(0,601)Cu(0,358)S
	0,00	0,00	0,00	0,01	0,00	0,02	0,00	0,00	0,00	0,02	0,00	34,77	0,16	0,01	0,00	28,82	0,00	0,00	1,97	0,18	0,00	32,38	Fe(0,476)Cu(0,47)S
	0,00	0,04	0,01	0,00	0,00	0,02	0,00	0,04	0,00	0,03	0,00	31,60	0,00	0,00	0,02	13,86	0,02	0,02	0,01	0,00	0,06	52,26	Fe(0,252)Cu(0,835)S
	0,00	0,00	0,02	0,00	0,00	0,00	0,00	0,01	0,00	0,00	0,00	30,23	0,00	0,00	0,10	8,54	0,00	0,00	0,01	0,12	0,00	57,50	Fe(0,162)Cu(0,96)S
	0,00	0,00	0,00	0,00	0,00	0,00	0,00	0,03	0,00	0,02	0,00	30,21	0,01	0,07	0,09	7,60	0,00	0,02	0,00	0,00	0,00	60,97	Fe(0,144)Cu(1,019)S
	0,00	0,01	0,08	0,04	0,03	0,00	0,00	0,01	0,02	0,00	0,00	29,52	0,01	0,06	0,08	5,01	0,00	0,00	0,04	0,22	0,00	55,82	Fe(0,097)Cu(0,955)S
	0,00	0,01	0,09	0,00	0,00	0,00	0,00	0,02	0,01	0,00	0,00	31,53	0,00	0,03	0,02	12,58	0,00	0,01	0,05	0,00	0,02	51,53	Fe(0,229)Cu(0,825)S
	0,00	0,00	0,15	0,03	0,03	0,00	0,00	0,01	0,00	0,00	0,00	31,53	0,03	0,00	0,10	11,84	0,00	0,00	0,03	0,00	0,02	52,25	Fe(0,216)Cu(0,836)S
	0,00	0,00	0,00	0,00	0,02	0,00	0,00	0,00	0,00	0,00	0,00	31,26	0,01	0,00	0,08	11,37	0,04	0,00	0,00	0,00	0,00	53,97	Fe(0,209)Cu(0,872)S

	Bi	Ga	Pb	Au	Ag	Ge	Cd	Mo	In	As	Sn	S	Ni	Se	Zn	Fe	Sb	Mn	Co	W	Te	Cu	Chemical Formula
SAMPLE 03-03	0,00	0,00	0,05	0,00	0,05	0,00	0,11	0,01	0,06	0,00	0,00	32,89	0,00	0,02	62,05	1,76	0,01	0,00	0,04	0,00	0,02	0,59	Zn(0,925)S
	0,00	0,00	0,00	0,00	0,00	0,00	0,43	0,01	0,00	0,00	0,00	33,25	0,02	0,00	59,83	3,71	0,01	0,02	0,00	0,00	0,00	0,80	Zn(0,883)Fe(0,064)S
	0,00	0,00	0,08	0,00	0,02	0,00	0,28	0,01	0,00	0,00	0,03	32,96	0,00	0,02	52,71	7,98	0,04	0,01	0,07	0,00	0,00	2,33	Zn(0,785)Fe(0,139)S
	0,00	0,00	0,14	0,00	0,03	0,00	0,47	0,00	0,00	0,01	0,04	31,59	0,00	0,01	53,80	5,57	0,02	0,00	0,04	0,00	0,00	2,36	Zn(0,836)Fe(0,101)S
	0,00	0,00	0,08	0,01	0,03	0,02	0,13	0,02	0,00	0,00	0,01	20,49	0,05	0,02	31,64	1,87	0,00	0,03	0,04	0,06	0,00	0,27	Zn(0,758)Fe(0,052)S
	0,07	0,00	0,05	0,00	0,09	0,00	0,08	0,00	0,05	0,02	0,04	23,06	0,00	0,00	28,71	1,04	0,06	0,01	0,07	0,00	0,01	0,16	Zn(0,611)S
	0,00	0,00	0,00	0,05	0,03	0,00	0,17	0,03	0,00	0,01	0,00	33,36	0,00	0,03	65,04	1,81	0,03	0,03	0,04	0,06	0,00	0,93	Zn(0,957)S
	0,00	0,00	0,08	0,00	0,00	0,00	0,00	0,04	0,02	0,01	0,00	35,21	0,06	0,00	1,98	38,87	0,00	0,02	0,70	0,12	0,00	18,42	Fe(0,634)Cu(0,264)S
	0,00	0,00	0,00	0,07	0,03	0,00	0,40	0,05	0,00	0,00	0,00	33,62	0,01	0,02	62,32	4,23	0,08	0,05	0,06	0,00	0,00	0,85	Zn(0,909)Fe(0,072)S
	0,00	0,00	0,12	0,00	0,00	0,00	0,50	0,00	0,00	0,00	0,01	33,34	0,00	0,00	56,92	5,75	0,10	0,01	0,06	0,00	0,00	0,72	Zn(0,838)Fe(0,099)S
	0,00	0,00	0,00	0,00	0,00	0,00	0,41	0,04	0,01	0,00	0,02	33,58	0,00	0,00	57,86	5,96	0,03	0,00	0,08	0,00	0,00	0,20	Zn(0,845)Fe(0,102)S
	0,00	0,00	0,02	0,00	0,01	0,00	0,29	0,00	0,00	0,00	0,00	33,65	0,00	0,00	62,17	3,81	0,07	0,00	0,08	0,00	0,01	0,43	Zn(0,906)Fe(0,065)S
	0,00	0,00	0,00	0,00	0,00	0,00	0,16	0,00	0,00	0,00	0,00	33,27	0,00	0,00	61,91	2,61	0,00	0,03	0,06	0,00	0,00	0,45	Zn(0,913)S
	0,00	0,00	0,15	0,00	0,02	0,00	0,09	0,02	0,00	0,01	0,00	33,15	0,00	0,00	62,99	0,63	0,01	0,01	0,01	0,00	0,08	0,89	Zn(0,932)S
	0,00	0,00	0,10	0,00	0,00	0,02	0,00	0,02	0,00	0,00	0,00	35,08	0,00	0,00	2,83	35,30	0,00	0,00	0,52	0,00	0,00	20,64	Fe(0,578)Cu(0,297)S
	0,02	0,00	0,06	0,00	0,03	0,00	0,13	0,05	0,03	0,00	0,02	33,14	0,04	0,00	63,09	1,55	0,00	0,00	0,04	0,00	0,00	0,66	Zn(0,934)S
	0,00	0,00	0,00	0,05	0,01	0,00	0,00	0,07	0,00	0,00	0,01	33,54	0,00	0,00	65,49	0,39	0,00	0,00	0,00	0,00	0,00	0,04	Zn(0,958)S
	0,00	0,00	0,02	0,00	0,05	0,00	0,03	0,02	0,00	0,00	0,00	30,85	0,00	0,00	58,92	1,09	0,00	0,03	0,00	0,00	0,02	0,19	Zn(0,937)S
	0,02	0,00	0,00	0,04	0,03	0,00	0,10	0,05	0,00	0,00	0,00	32,10	0,00	0,00	61,66	1,07	0,00	0,04	0,00	0,00	0,00	0,04	Zn(0,942)S
	0,00	0,00	38,79	0,00	0,01	0,01	0,00	0,00	0,00	0,00	0,00	13,52	0,00	0,00	16,28	0,96	0,00	0,00	0,03	0,07	0,01	0,17	Pb(0,444)Zn(0,591)S
	0,00	0,00	42,17	0,00	0,01	0,03	0,00	0,00	0,00	0,00	0,00	13,20	0,00	0,00	15,52	1,01	0,04	0,00	0,01	0,00	0,03	0,13	Pb(0,494)Zn(0,577)S
	0,00	0,00	0,00	0,00	0,04	0,02	0,00	0,02	0,00	0,00	0,22	33,41	0,01	0,00	10,89	30,97	0,00	0,00	0,57	0,00	0,00	17,87	Zn(0,16)Fe(0,532)Cu(0,27)S
	0,00	0,00	0,01	0,00	0,05	0,00	0,27	0,00	0,04	0,02	0,13	33,80	0,00	0,04	48,76	14,40	0,02	0,00	0,37	0,00	0,00	0,42	Zn(0,708)Fe(0,245)S
	0,00	0,00	0,00	0,03	0,01	0,00	0,00	0,03	0,00	0,00	0,00	35,40	0,00	0,01	1,90	37,54	0,00	0,00	0,58	0,07	0,00	21,35	Fe(0,609)Cu(0,304)S
	0,00	0,00	0,01	0,00	0,01	0,00	0,32	0,03	0,00	0,00	0,00	33,69	0,00	0,04	56,59	8,24	0,00	0,05	0,17	0,00	0,02	0,31	Zn(0,824)Fe(0,14)S
	0,00	0,00	0,08	0,00	0,04	0,00	0,37	0,00	0,00	0,03	0,04	32,96	0,03	0,00	58,54	4,93	0,04	0,02	0,05	0,02	0,00	1,00	Zn(0,871)Fe(0,086)S
	0,00	0,00	0,03	0,03	0,00	0,03	0,03	0,00	0,02	0,01	0,00	34,81	0,00	0,00	11,06	29,93	0,06	0,00	0,34	0,00	0,08	20,29	Zn(0,156)Fe(0,494)Cu(0,294)S
	0,00	0,00	0,00	0,00	0,00	0,00	0,15	0,05	0,00	0,01	0,00	32,99	0,00	0,02	62,37	1,99	0,02	0,00	0,05	0,00	0,05	0,90	Zn(0,928)S

	0,00	0,00	0,05	0,00	0,05	0,00	0,41	0,03	0,00	0,00	0,13	33,67	0,06	0,00	50,62	12,36	0,03	0,00	0,17	0,00	0,02	1,23	Zn(0,738)Fe(0,211)S
	0,00	0,00	0,00	0,04	0,01	0,00	0,00	0,01	0,00	0,01	0,00	35,47	0,06	0,00	1,44	37,71	0,00	0,00	0,59	0,00	0,00	20,80	Fe(0,611)Cu(0,296)S
	0,00	0,00	0,05	0,00	0,00	0,00	0,25	0,03	0,00	0,00	0,00	33,49	0,00	0,00	58,93	5,43	0,00	0,03	0,07	0,00	0,01	0,56	Zn(0,863)Fe(0,093)S
	0,00	0,00	0,13	0,01	0,00	0,00	0,00	0,02	0,00	0,00	0,23	34,43	0,00	0,03	7,18	36,24	0,00	0,00	0,64	0,02	0,00	12,53	Zn(0,102)Fe(0,605)Cu(0,184)S
	0,00	0,00	0,00	0,00	53,49	0,00	0,00	0,00	0,07	0,00	0,00	19,07	0,00	0,01	5,50	7,03	0,00	0,00	0,04	0,00	0,00	8,06	Ag(0,834)Zn(0,142)Fe(0,212)Cu(0,213)S
	0,00	0,00	0,06	0,00	57,61	0,00	0,00	0,00	0,00	0,00	0,00	18,20	0,01	0,01	5,00	6,02	0,00	0,00	0,07	0,16	0,00	8,48	Ag(0,941)Zn(0,135)Fe(0,19)Cu(0,235)S
	0,00	0,00	0,05	0,00	0,04	0,00	0,56	0,03	0,00	0,00	0,05	33,09	0,00	0,00	57,19	6,46	0,04	0,01	0,07	0,00	0,05	0,91	Zn(0,848)Fe(0,112)S
	0,00	0,00	0,00	0,00	0,00	0,00	0,00	0,04	0,00	0,00	0,00	35,82	0,00	0,00	1,92	38,30	0,00	0,00	0,63	0,00	0,02	19,98	Fe(0,614)Cu(0,282)S
	0,00	0,00	0,00	0,00	0,04	0,00	0,34	0,06	0,00	0,02	0,00	33,72	0,01	0,03	60,71	4,40	0,01	0,00	0,04	0,00	0,00	0,17	Zn(0,883)Fe(0,075)S
	0,00	0,00	0,11	0,00	0,23	0,00	0,12	0,00	0,00	0,00	0,00	29,85	0,03	0,00	48,46	4,39	0,00	0,01	0,08	0,00	0,00	0,69	Zn(0,797)Fe(0,084)S
	Bi	**Ga**	**Pb**	**Au**	**Ag**	**Ge**	**Cd**	**Mo**	**In**	**As**	**Sn**	**S**	**Ni**	**Se**	**Zn**	**Fe**	**Sb**	**Mn**	**Co**	**W**	**Te**	**Cu**	**Chemical Formula**
SAMPLE 04-02(2)	0,00	0,00	0,11	0,01	0,00	0,00	0,19	0,02	0,01	0,00	0,02	33,32	0,02	0,00	62,04	3,09	0,07	0,03	0,07	0,00	0,00	0,54	Zn(0,913)Fe(0,053)S
	0,00	0,00	0,00	0,02	0,09	0,01	0,60	0,00	0,00	0,00	0,23	33,04	0,01	0,00	54,00	8,99	0,09	0,00	0,09	0,00	0,00	1,34	Zn(0,802)Fe(0,156)S
	0,00	0,00	0,00	0,03	0,05	0,00	0,09	0,02	0,00	0,01	0,02	32,74	0,00	0,00	63,36	1,52	0,06	0,02	0,04	0,12	0,00	0,88	Zn(0,949)S
	0,00	0,00	0,05	0,00	0,03	0,00	0,46	0,04	0,00	0,00	0,11	33,24	0,02	0,00	55,70	8,46	0,00	0,00	0,08	0,00	0,00	0,73	Zn(0,822)Fe(0,146)S
	0,00	0,00	0,02	0,00	0,00	0,00	0,58	0,01	0,02	0,02	0,09	33,05	0,03	0,01	55,95	7,46	0,00	0,05	0,11	0,00	0,01	1,33	Zn(0,831)Fe(0,13)S
	0,00	0,00	0,00	0,01	0,01	0,00	0,25	0,04	0,00	0,00	0,00	33,54	0,03	0,03	61,50	2,79	0,00	0,00	0,03	0,00	0,00	0,32	Zn(0,9)S
	0,00	0,00	0,01	0,00	0,01	0,00	0,29	0,02	0,00	0,00	0,12	33,97	0,00	0,00	54,43	9,20	0,00	0,05	0,25	0,00	0,02	0,68	Zn(0,786)Fe(0,156)S
	0,00	0,00	0,00	0,03	0,02	0,00	0,28	0,00	0,00	0,00	0,14	34,53	0,00	0,00	55,77	9,31	0,10	0,00	0,28	0,00	0,00	0,46	Zn(0,792)Fe(0,155)S
	0,00	0,00	0,02	0,00	0,04	0,00	0,34	0,02	0,00	0,00	0,15	33,65	0,03	0,00	55,05	7,98	0,02	0,00	0,21	0,00	0,00	0,47	Zn(0,802)Fe(0,136)S
	0,00	0,00	0,06	0,03	0,08	0,01	0,16	0,06	0,00	0,00	0,00	33,07	0,03	0,00	60,74	3,03	0,00	0,00	0,04	0,00	0,00	0,30	Zn(0,901)Fe(0,053)S
	0,00	0,00	0,17	0,03	0,00	0,01	0,31	0,03	0,00	0,00	0,21	33,48	0,00	0,00	52,23	10,63	0,07	0,01	0,19	0,04	0,00	1,58	Zn(0,765)Fe(0,182)S
	0,01	0,00	0,07	0,00	0,04	0,00	0,35	0,02	0,01	0,00	0,01	33,27	0,00	0,02	53,78	9,59	0,11	0,01	0,17	0,00	0,02	1,09	Zn(0,793)Fe(0,166)S
	0,00	0,00	0,00	0,06	0,06	0,00	0,27	0,00	0,00	0,00	0,06	34,55	0,05	0,00	51,37	12,95	0,00	0,00	0,30	0,00	0,00	0,73	Zn(0,73)Fe(0,215)S
	0,00	0,00	0,09	0,00	0,42	0,00	0,15	0,03	0,00	0,00	0,14	32,10	0,00	0,00	45,14	10,52	0,10	0,00	0,23	0,00	0,00	8,41	Zn(0,69)Fe(0,188)Cu(0,132)S
	0,00	0,00	0,00	0,00	0,00	0,00	0,16	0,03	0,00	0,00	0,00	33,54	0,00	0,00	57,66	6,23	0,07	0,00	0,23	0,00	0,00	0,51	Zn(0,844)Fe(0,107)S
	0,00	0,00	0,06	0,00	0,01	0,00	0,00	0,00	0,00	0,00	0,11	35,07	0,00	0,00	6,07	32,38	0,00	0,00	0,30	0,18	0,00	25,17	Zn(0,085)Fe(0,53)Cu(0,362)S
	0,00	0,00	0,00	0,00	0,01	0,00	0,07	0,02	0,00	0,00	0,49	33,85	0,00	0,00	20,43	29,16	0,02	0,02	0,44	0,00	0,01	11,09	Zn(0,296)Fe(0,495)Cu(0,165)S
	0,00	0,00	0,00	0,00	0,07	0,00	0,21	0,00	0,00	0,00	0,17	35,70	0,00	0,00	23,83	24,97	0,07	0,00	0,39	0,00	0,00	17,36	Zn(0,328)Fe(0,402)Cu(0,245)S

	0,00	0,00	0,11	0,00	0,00	0,02	0,42	0,04	0,02	0,01	0,58	33,82	0,05	0,00	52,89	9,37	0,13	0,03	0,17	0,00	0,00	0,98	Zn(0,767)Fe(0,159)S
	0,00	0,00	0,00	0,01	0,00	0,00	0,21	0,08	0,00	0,00	0,00	33,83	0,00	0,00	59,02	4,96	0,00	0,01	0,09	0,00	0,04	0,65	Zn(0,856)Fe(0,084)S
	0,00	0,00	0,00	0,04	0,03	0,00	0,38	0,00	0,00	0,00	0,01	34,46	0,00	0,00	54,90	8,45	0,03	0,00	0,09	0,00	0,03	0,52	Zn(0,782)Fe(0,141)S
	0,00	0,00	0,15	0,00	0,04	0,00	0,41	0,00	0,01	0,00	0,18	33,38	0,00	0,00	54,93	7,51	0,06	0,02	0,06	0,00	0,01	0,87	Zn(0,807)Fe(0,129)S
	0,00	0,00	0,00	0,01	0,02	0,00	0,25	0,02	0,00	0,00	0,00	34,16	0,02	0,01	59,91	4,77	0,10	0,04	0,08	0,00	0,01	0,26	Zn(0,86)Fe(0,08)S
	Bi	**Ga**	**Pb**	**Au**	**Ag**	**Ge**	**Cd**	**Mo**	**In**	**As**	**Sn**	**S**	**Ni**	**Se**	**Zn**	**Fe**	**Sb**	**Mn**	**Co**	**W**	**Te**	**Cu**	**Chemical Formula**
SAMPLE 05-04(1)	0,00	0,00	0,19	0,00	0,20	0,01	0,27	0,01	0,04	0,00	0,04	33,58	0,00	0,01	60,26	4,50	0,05	0,00	0,02	0,00	0,04	0,84	Zn(0,881)Fe(0,077)S
	0,00	0,00	0,09	0,00	0,15	0,03	0,27	0,03	0,00	0,02	0,01	33,27	0,01	0,00	59,73	4,69	0,04	0,01	0,01	0,00	0,00	0,89	Zn(0,881)Fe(0,081)S
	0,00	0,00	0,13	0,00	0,19	0,00	0,29	0,03	0,00	0,02	0,03	33,27	0,00	0,00	61,73	3,60	0,01	0,00	0,03	0,00	0,01	0,57	Zn(0,91)Fe(0,062)S
	0,00	0,00	0,02	0,01	0,00	0,00	0,00	0,01	0,02	0,00	0,24	35,82	0,00	0,02	2,98	38,60	0,00	0,00	0,37	0,00	0,00	18,86	Fe(0,619)Cu(0,266)S
	0,00	0,00	0,00	0,00	0,00	0,00	0,00	0,01	0,00	0,00	0,20	35,46	0,00	0,02	3,13	37,87	0,01	0,00	0,32	0,00	0,02	19,83	Fe(0,613)Cu(0,282)S
	0,00	0,00	0,04	0,00	0,11	0,00	0,36	0,02	0,00	0,00	0,42	34,24	0,00	0,00	29,01	21,15	0,00	0,00	0,15	0,00	0,00	11,35	Zn(0,416)Fe(0,355)Cu(0,167)S
	0,00	0,00	0,02	0,00	0,17	0,00	0,31	0,01	0,00	0,02	0,13	34,12	0,00	0,00	36,06	18,59	0,00	0,01	0,09	0,00	0,00	8,31	Zn(0,518)Fe(0,313)Cu(0,123)S
	0,00	0,05	0,08	0,05	0,06	0,00	0,00	0,00	0,00	0,00	0,18	35,96	0,08	0,00	1,30	39,94	0,00	0,00	0,41	0,02	0,00	18,78	Fe(0,638)Cu(0,264)S
	0,00	0,00	0,04	0,00	0,02	0,00	0,00	0,03	0,00	0,00	0,12	35,69	0,00	0,01	6,62	37,55	0,00	0,01	0,37	0,12	0,02	16,78	Zn(0,091)Fe(0,604)Cu(0,237)S
	0,00	0,00	0,00	0,01	0,10	0,00	0,22	0,02	0,00	0,00	0,22	35,24	0,00	0,02	25,06	27,64	0,00	0,00	0,26	0,00	0,06	7,87	Zn(0,349)Fe(0,45)Cu(0,113)S
	0,00	0,00	0,10	0,00	0,00	0,00	0,00	0,01	0,00	0,00	0,19	35,14	0,03	0,00	6,03	30,04	0,00	0,00	0,19	0,06	0,00	21,43	Zn(0,084)Fe(0,491)Cu(0,308)S
	0,00	0,00	0,04	0,00	0,05	0,02	0,00	0,03	0,00	0,00	0,19	35,65	0,05	0,00	16,21	28,15	0,00	0,02	0,21	0,00	0,00	16,87	Zn(0,223)Fe(0,454)Cu(0,239)S
	0,00	0,00	0,23	0,04	0,06	0,04	0,26	0,01	0,00	0,01	0,14	33,91	0,00	0,01	51,61	10,58	0,01	0,01	0,07	0,00	0,02	2,33	Zn(0,747)Fe(0,179)S
	0,00	0,00	0,12	0,00	0,02	0,00	0,26	0,07	0,00	0,01	0,10	33,96	0,00	0,00	47,58	14,20	0,05	0,05	0,12	0,00	0,05	2,57	Zn(0,687)Fe(0,24)S
	0,00	0,00	0,19	0,00	0,26	0,00	0,17	0,01	0,00	0,00	0,07	33,30	0,00	0,00	57,81	5,53	0,05	0,00	0,01	0,00	0,00	0,74	Zn(0,852)Fe(0,095)S
	0,03	0,00	0,00	0,00	0,13	0,02	0,48	0,03	0,01	0,00	0,17	33,64	0,00	0,00	52,88	10,02	0,00	0,01	0,09	0,00	0,00	1,16	Zn(0,771)Fe(0,171)S
	0,00	0,00	0,10	0,00	0,12	0,00	0,17	0,04	0,02	0,00	0,02	33,29	0,00	0,00	60,68	4,01	0,03	0,00	0,02	0,00	0,00	0,29	Zn(0,894)Fe(0,069)S
	0,00	0,00	0,36	0,02	0,25	0,00	0,22	0,07	0,00	0,02	0,04	32,97	0,00	0,00	60,88	3,07	0,00	0,00	0,03	0,00	0,00	0,99	Zn(0,906)Fe(0,054)S
	0,10	0,00	0,21	0,00	0,00	0,00	0,08	0,02	0,02	0,00	0,00	10,69	0,00	0,00	0,73	0,07	0,05	0,00	0,00	0,08	0,00	0,03	S
	0,06	0,00	0,00	0,00	0,03	0,00	0,00	0,03	0,00	0,00	0,02	9,97	0,00	0,00	0,65	0,04	0,05	0,00	0,00	0,00	0,00	0,05	S
	0,00	0,01	0,00	0,04	0,00	0,00	0,00	0,00	0,00	0,00	0,00	52,73	0,00	0,02	0,28	43,07	0,00	0,00	1,29	0,03	0,00	0,00	Fe(0,469)S
	0,00	0,00	0,00	0,00	0,05	0,00	0,00	0,00	0,00	0,01	0,00	52,24	0,00	0,00	0,11	43,87	0,00	0,00	0,99	0,00	0,00	0,00	Fe(0,482)S
	0,00	0,00	0,03	0,00	0,02	0,00	0,00	0,00	0,02	0,00	0,00	52,79	0,00	0,00	0,25	43,82	0,00	0,00	0,86	0,06	0,00	0,00	Fe(0,477)S

0,00	0,00	0,35	0,01	0,02	0,02	0,00	0,00	0,00	0,01	0,00	33,17	0,00	0,00	54,71	3,16	0,02	0,02	0,04	0,00	0,04	0,04	Zn(0,809)Fe(0,055)S
0,00	0,00	0,47	0,00	0,05	0,01	0,00	0,05	0,05	0,00	0,00	33,00	0,00	0,00	54,68	1,56	0,00	0,00	0,03	0,00	0,00	0,00	Zn(0,813)S
0,00	0,00	0,12	0,00	0,00	0,00	0,00	0,07	0,02	0,03	0,00	32,24	0,00	0,00	48,17	2,54	0,00	0,00	0,05	0,00	0,00	0,00	Zn(0,733)S
0,00	0,00	0,03	0,00	0,03	0,03	0,10	0,01	0,03	0,00	0,00	33,84	0,01	0,01	53,56	10,92	0,00	0,00	0,09	0,00	0,00	0,57	Zn(0,777)Fe(0,185)S
0,00	0,00	0,00	0,00	0,10	0,00	0,24	0,00	0,00	0,00	0,05	33,60	0,00	0,00	52,59	11,28	0,00	0,04	0,13	0,00	0,00	0,66	Zn(0,768)Fe(0,193)S
0,00	0,03	0,00	0,00	0,04	0,00	0,00	0,04	0,00	0,00	0,28	35,14	0,00	0,00	1,83	39,00	0,00	0,00	0,58	0,00	0,00	19,52	Fe(0,637)Cu(0,28)S
0,00	0,00	0,05	0,01	0,17	0,00	0,06	0,02	0,00	0,00	0,06	33,67	0,00	0,01	57,22	6,99	0,02	0,01	0,05	0,00	0,00	0,47	Zn(0,834)Fe(0,119)S
0,00	0,00	0,09	0,05	0,07	0,00	0,13	0,02	0,00	0,00	0,00	33,83	0,04	0,00	54,25	10,02	0,05	0,02	0,07	0,00	0,00	0,65	Zn(0,787)Fe(0,17)S
0,00	0,03	0,00	0,00	0,01	0,00	0,00	0,00	0,00	0,01	0,30	35,09	0,01	0,00	2,76	30,06	0,00	0,00	0,06	0,10	0,00	28,52	Fe(0,492)Cu(0,41)S
0,00	0,00	0,10	0,00	0,16	0,00	0,33	0,04	0,00	0,03	0,06	33,22	0,00	0,00	52,40	10,30	0,01	0,00	0,08	0,00	0,03	1,10	Zn(0,774)Fe(0,178)S
0,00	0,00	0,21	0,00	0,05	0,00	0,29	0,00	0,00	0,00	0,03	33,81	0,03	0,00	53,23	10,68	0,00	0,01	0,07	0,00	0,00	0,73	Zn(0,772)Fe(0,181)S
0,00	0,00	0,21	0,00	0,14	0,00	0,01	0,03	0,02	0,02	0,00	32,94	0,00	0,00	60,97	3,14	0,00	0,00	0,04	0,00	0,00	0,16	Zn(0,908)Fe(0,055)S

	Bi	Ga	Pb	Au	Ag	Ge	Cd	Mo	In	As	Sn	S	Ni	Se	Zn	Fe	Sb	Mn	Co	W	Te	Cu	Chemical Formula
SAMPLE 03-04	0,00	0,00	0,00	0,00	0,01	0,00	0,00	0,00	0,00	0,00	0,00	37,83	0,00	0,00	0,07	59,31	0,00	0,02	1,33	0,00	0,01	0,02	Fe(0,901)S
	0,00	0,00	0,07	0,02	0,00	0,00	0,00	0,01	0,00	0,00	0,00	37,84	0,00	0,00	0,00	59,37	0,00	0,01	1,11	0,00	0,03	0,05	Fe(0,901)S
	0,00	0,00	0,10	0,01	0,00	0,00	0,00	0,04	0,00	0,00	0,00	37,70	0,00	0,00	0,00	59,90	0,00	0,00	0,72	0,00	0,00	0,06	Fe(0,913)S
	0,00	0,00	0,00	0,02	0,02	0,00	0,00	0,03	0,00	0,00	0,00	38,30	0,04	0,00	0,00	60,46	0,00	0,00	0,93	0,00	0,00	0,02	Fe(0,907)S
	0,00	0,00	0,00	0,00	0,00	0,00	0,00	0,04	0,00	0,00	0,00	35,52	0,00	0,00	0,16	42,06	0,00	0,00	0,90	0,04	0,00	18,61	Fe(0,68)Cu(0,264)S
	0,00	0,00	0,05	0,00	0,00	0,00	0,14	0,08	0,00	0,00	0,00	33,75	0,03	0,00	41,47	14,23	0,00	0,03	0,46	0,00	0,00	0,66	Zn(0,603)Fe(0,242)S
	0,00	0,00	0,05	0,01	0,00	0,01	0,00	0,03	0,00	0,00	0,00	38,24	0,00	0,00	0,03	59,93	0,00	0,01	0,96	0,24	0,00	0,00	Fe(0,9)S
	0,02	0,00	0,00	0,00	0,00	0,00	0,09	0,02	0,03	0,03	0,00	32,63	0,01	0,00	28,22	25,86	0,00	0,00	0,63	0,00	0,00	3,23	Zn(0,424)Fe(0,455)S
	0,00	0,00	0,00	0,04	0,02	0,00	0,00	0,02	0,01	0,00	0,00	35,57	0,03	0,01	0,25	42,12	0,00	0,00	0,81	0,00	0,00	17,97	Fe(0,68)Cu(0,255)S
	0,00	0,00	0,00	0,00	0,02	0,02	0,00	0,00	0,00	0,00	0,00	35,72	0,01	0,00	0,26	41,83	0,00	0,00	0,89	0,11	0,03	18,08	Fe(0,673)Cu(0,256)S
	0,00	0,00	0,00	0,00	0,00	0,00	0,00	0,02	0,00	0,01	0,00	36,15	0,03	0,00	0,94	41,51	0,00	0,00	1,15	0,00	0,00	20,43	Fe(0,66)Cu(0,285)S
	0,00	0,00	0,02	0,00	0,03	0,00	0,00	0,06	0,00	0,00	0,00	35,45	0,00	0,00	0,84	41,13	0,00	0,02	0,89	0,00	0,00	21,13	Fe(0,666)Cu(0,301)S

APPENDIX III: Mineral Composition - *Scanning electron microscopy and energy dispersive spectroscopy (SEM/EDS).*

Appendix III.I: *Sample SAL-03-03.*

Appendix III.I.a: *SEM imaging of sample SAL-03-03.*

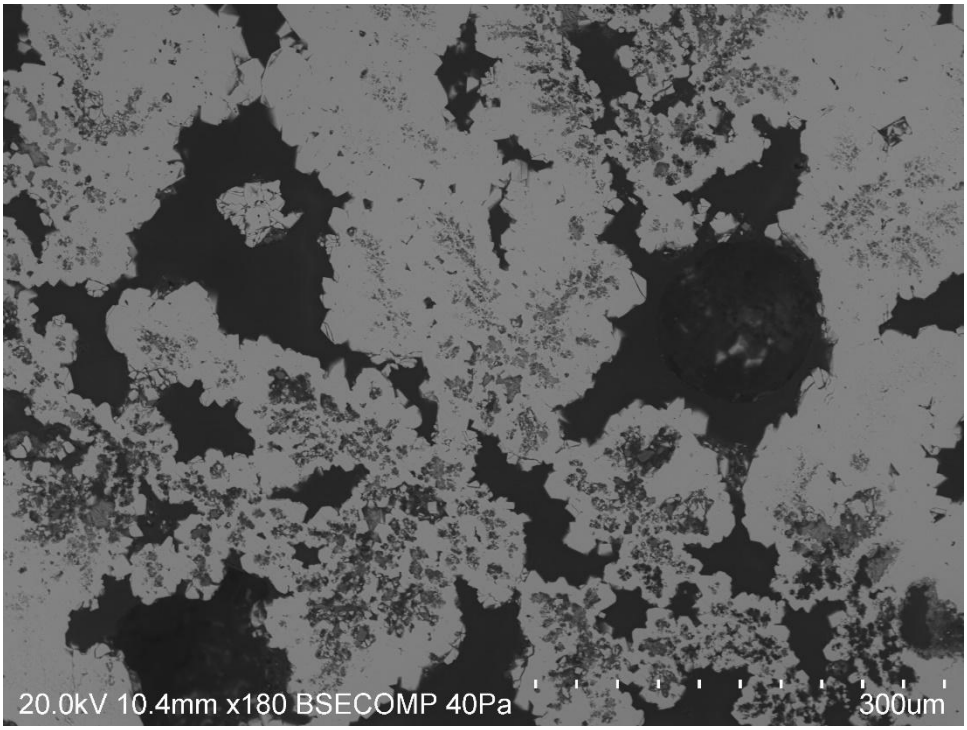

Appendix III.I.b: *EDS imaging of sample SAL-03-03 with backscattering.*

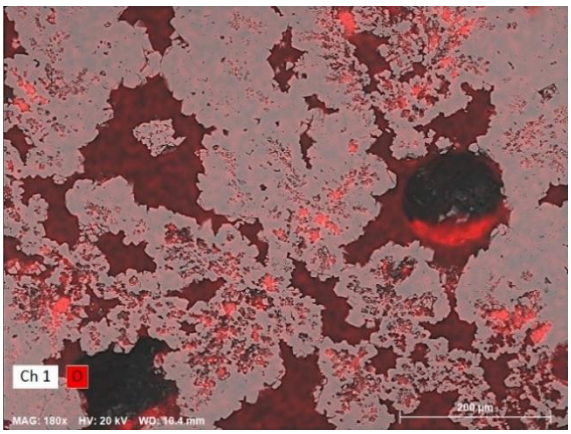

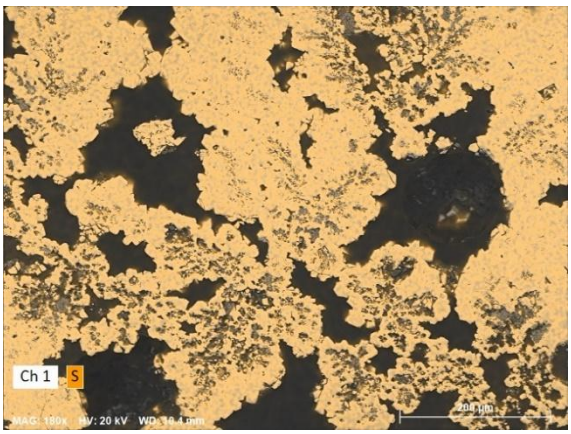

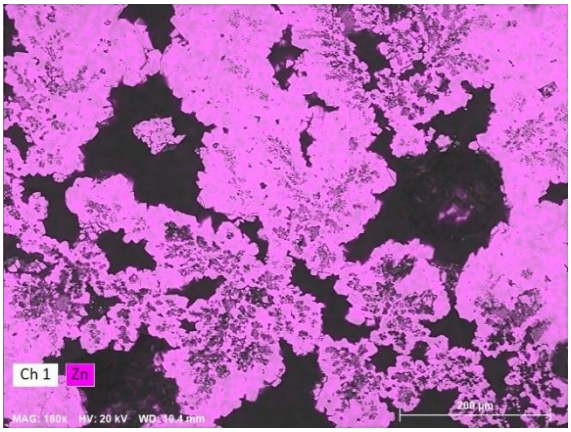
Ch 1 Zn
MAG: 180x HV: 20 kV WD: 10.4 mm
200 µm

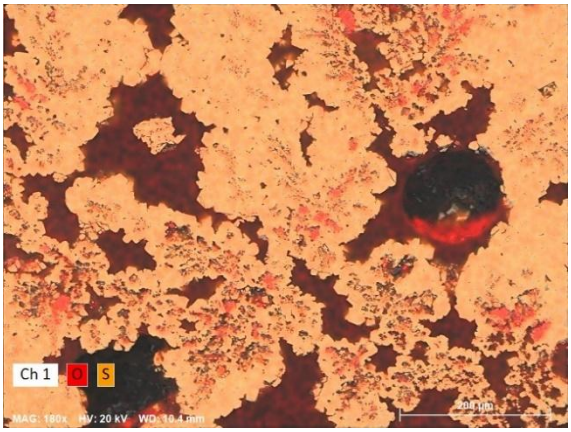
Ch 1 O S
MAG: 180x HV: 20 kV WD: 10.4 mm
200 µm

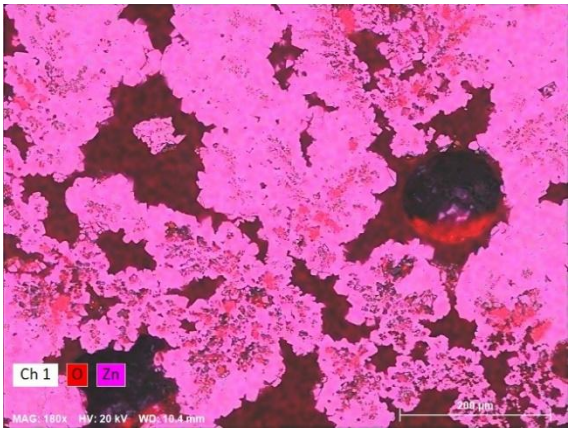
Ch 1 O Zn
MAG: 180x HV: 20 kV WD: 10.4 mm
200 µm

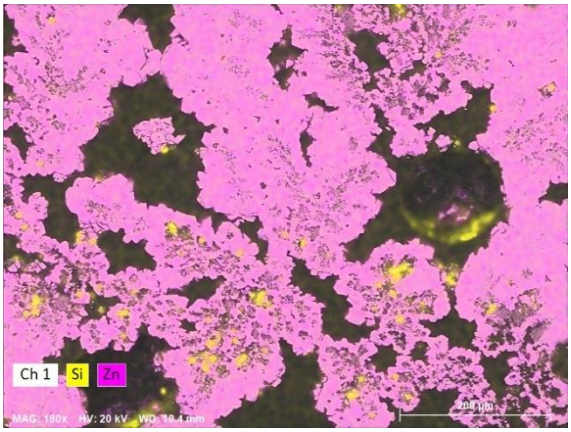
Ch 1 Si Zn
MAG: 180x HV: 20 kV WD: 10.4 mm
200 µm

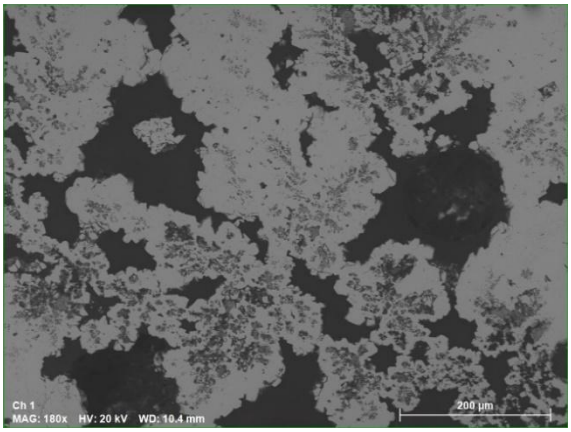
Ch 1
MAG: 180x HV: 20 kV WD: 10.4 mm
200 µm

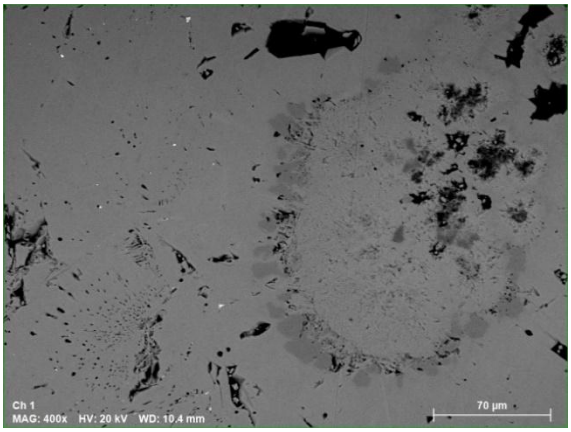
Ch 1
MAG: 400x HV: 20 kV WD: 10.4 mm
70 µm

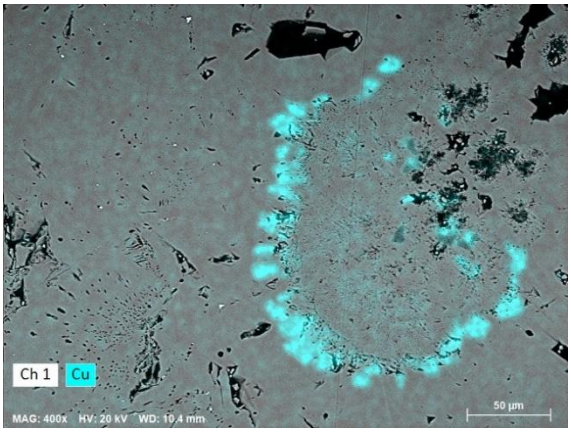
Ch 1 Cu
MAG: 400x HV: 20 kV WD: 10.4 mm
50 µm

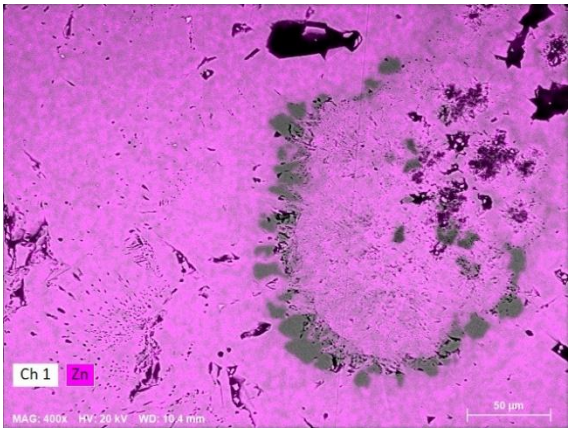
Ch 1 Zn
MAG: 400x HV: 20 kV WD: 10.4 mm
50 µm

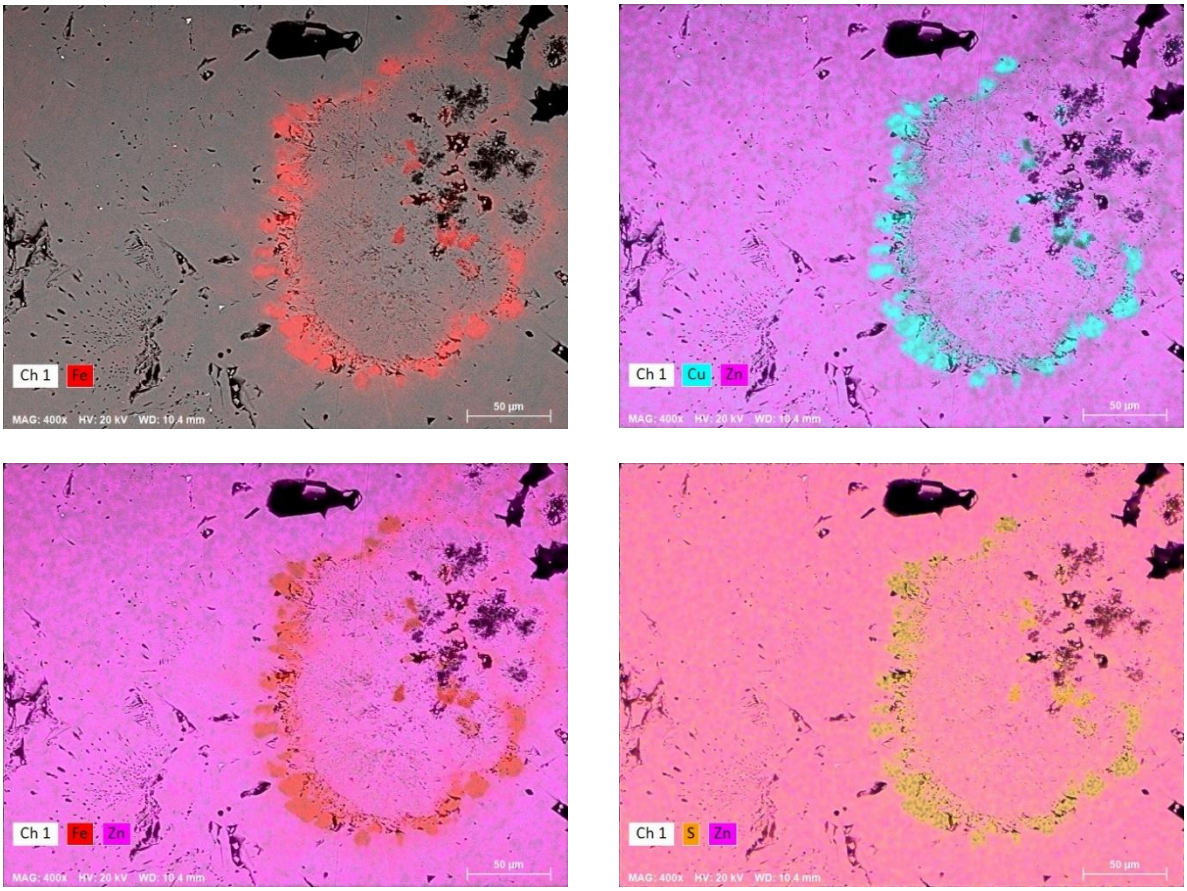

Appendix III.I.c: *EDS imaging of sample SAL-03-03 without backscattering.*

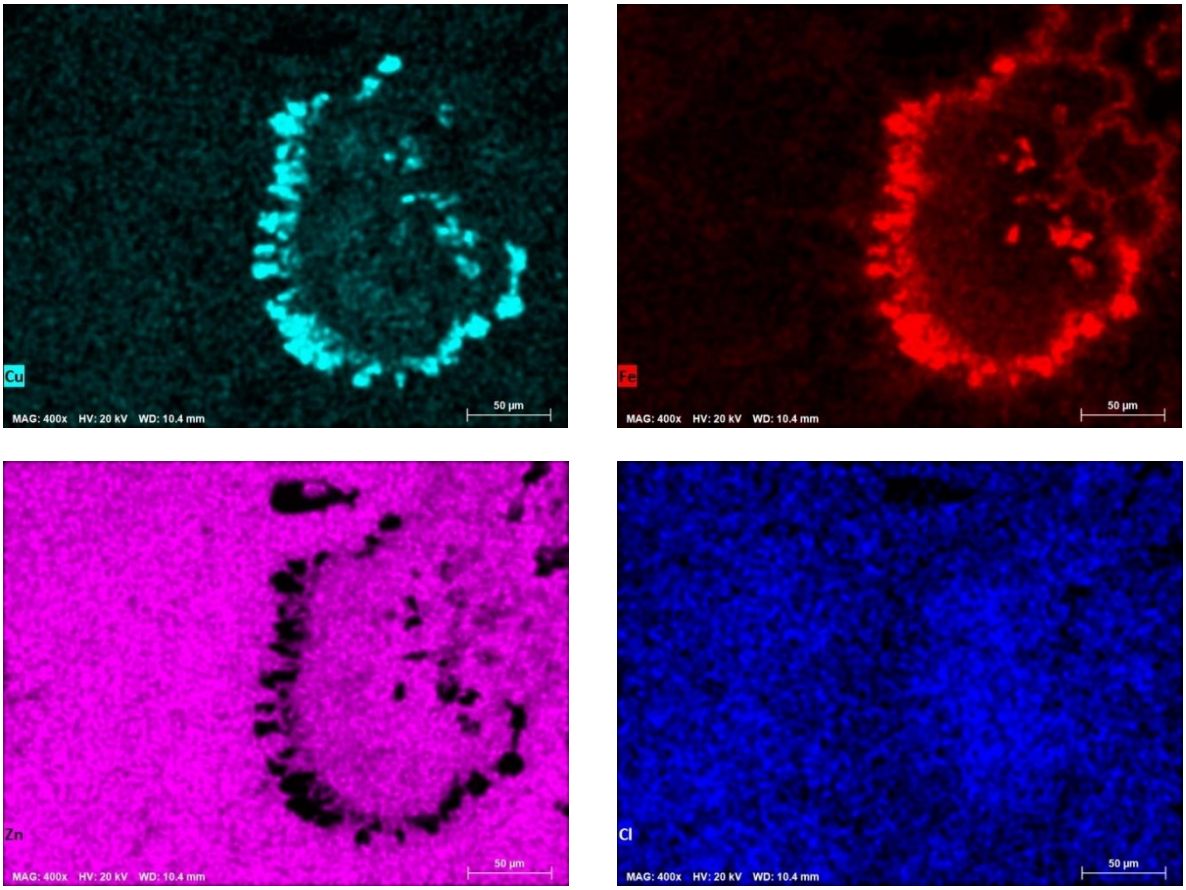

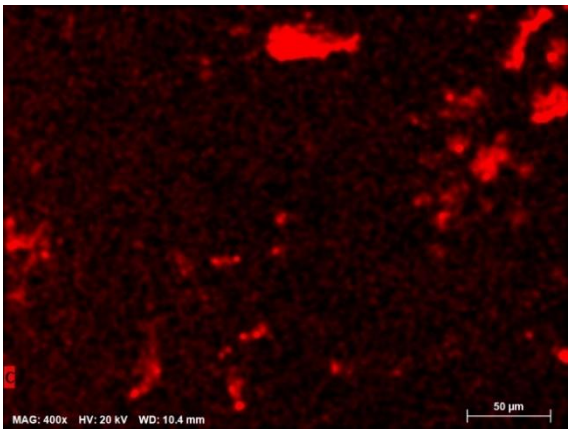

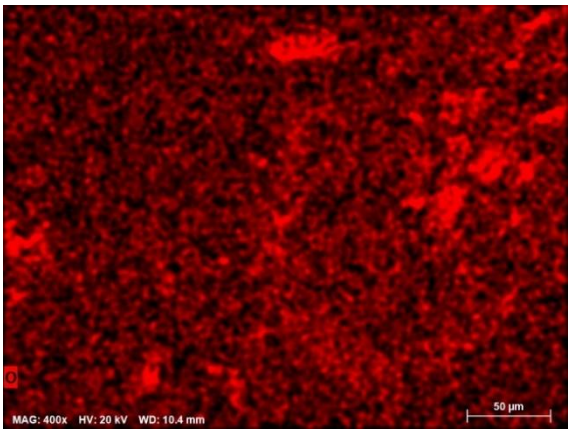

Appendix III.II: *Sample SAL-03-08.*

Appendix III.II.a: *SEM imaging of sample SAL-03-08.*

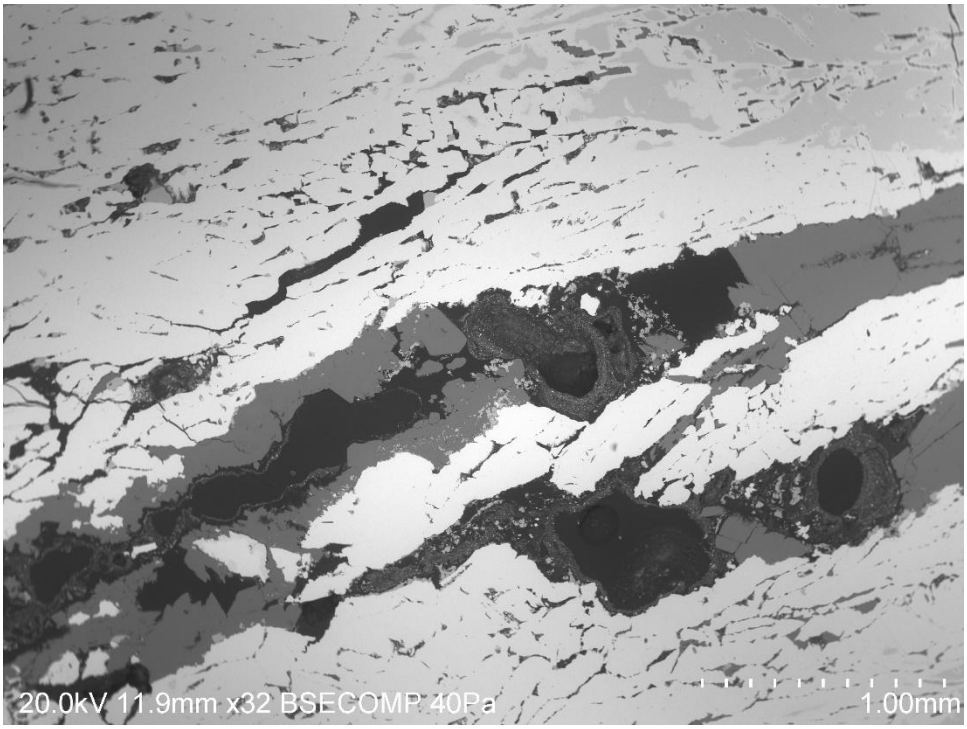

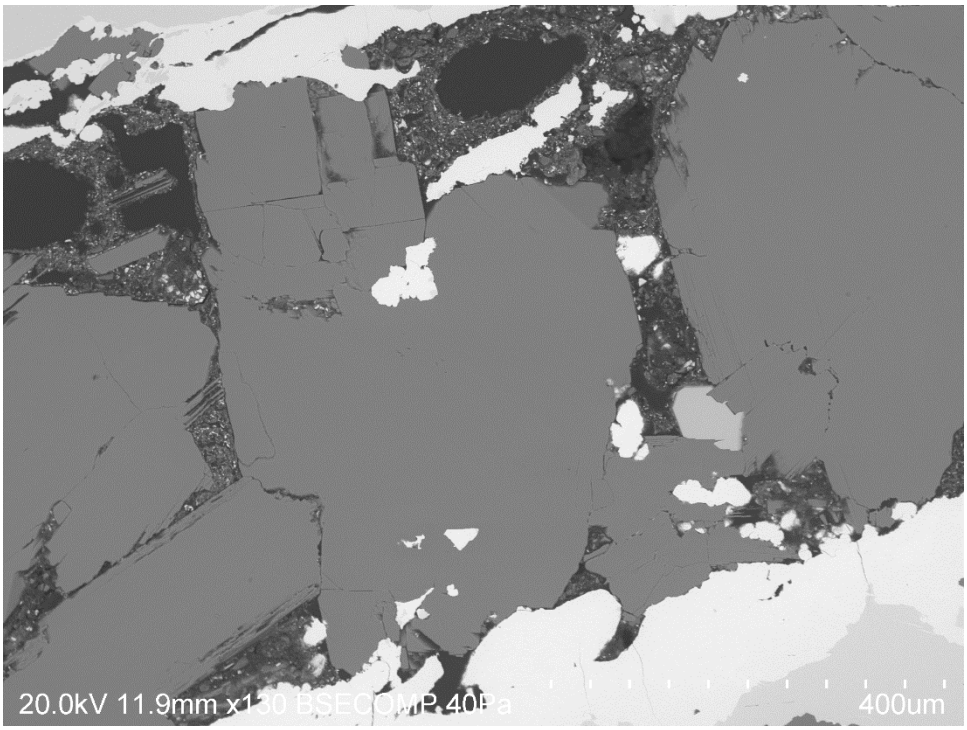
400um

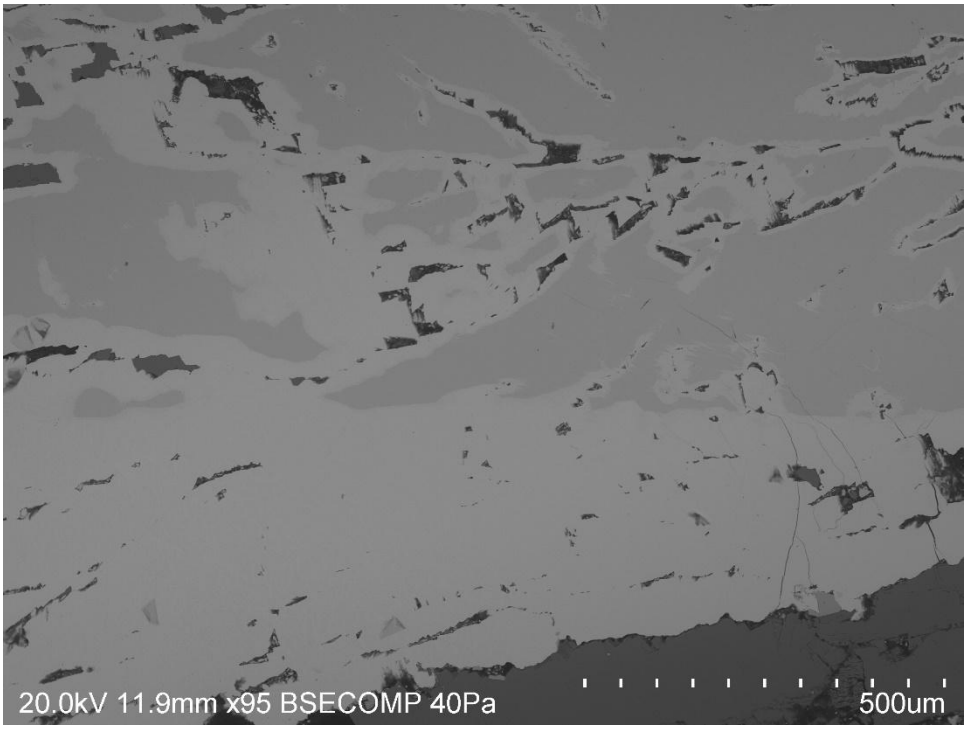
20.0kV 11.9mm x95 BSECOMP 40Pa
500um

Appendix III.II.b: *EDS imaging of sample SAL-03-08 with backscattering.*

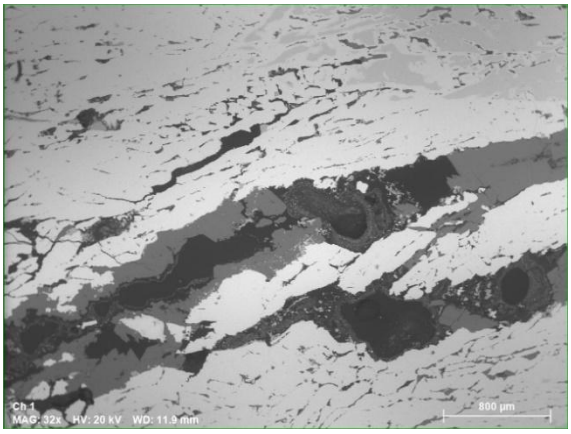

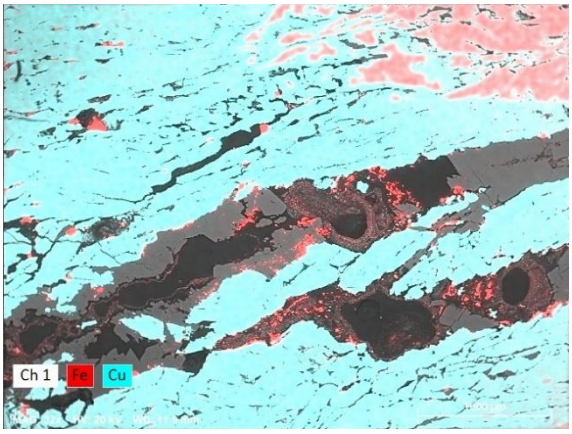

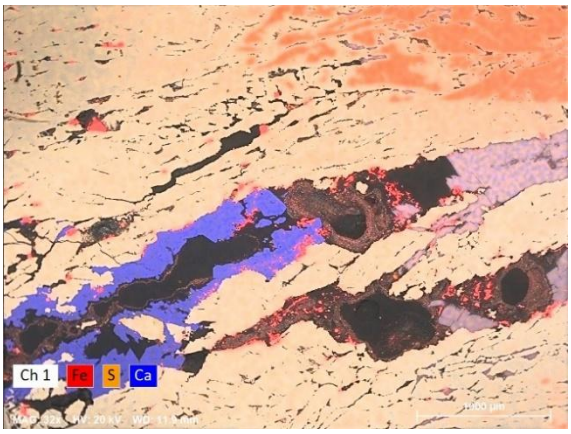

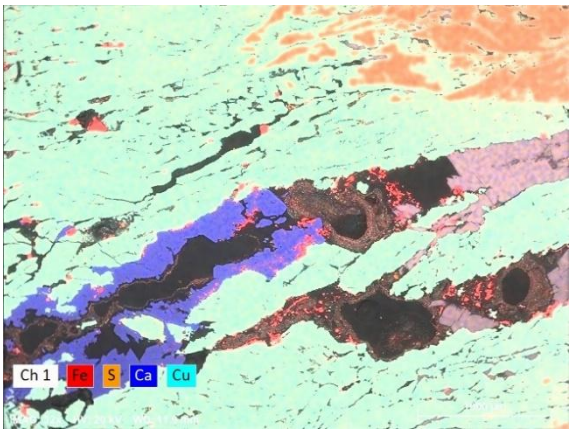

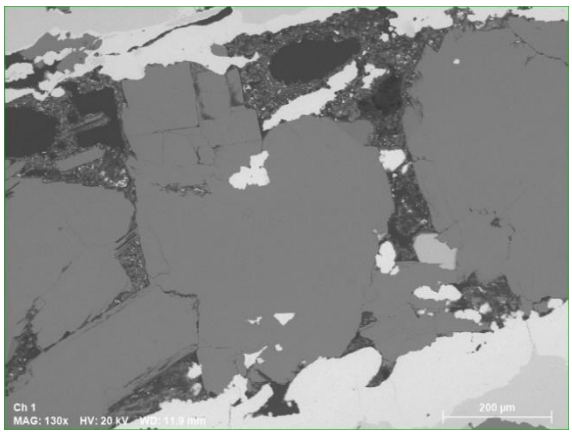

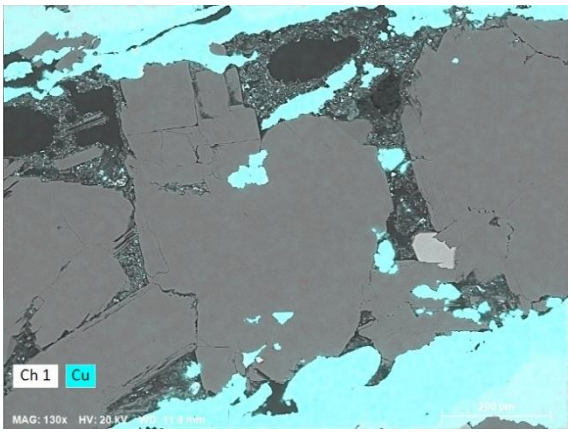

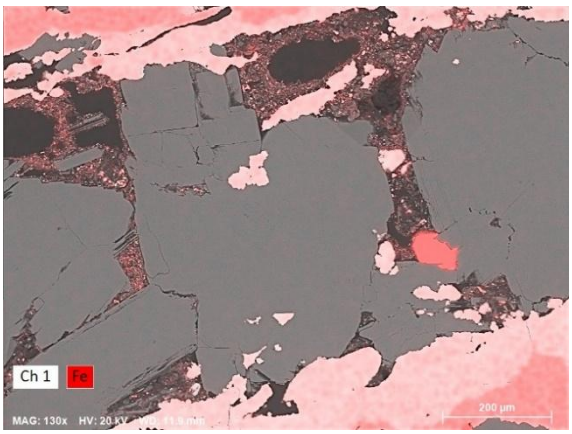

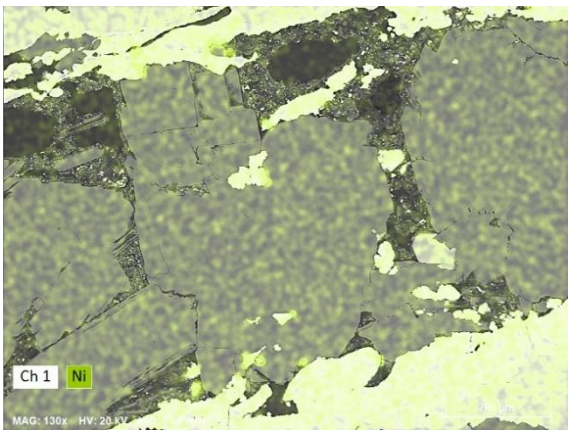

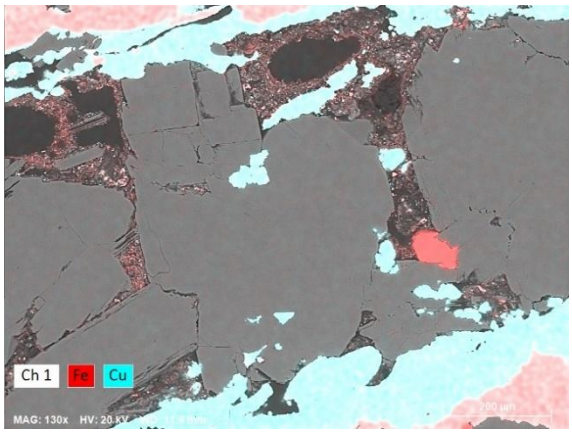
Ch 1
Fe
Cu

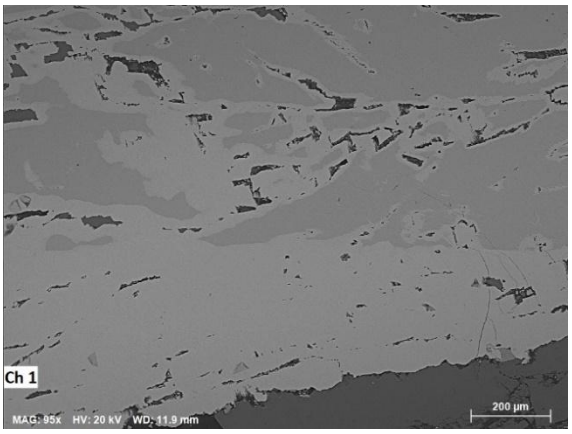
Ch 1
MAG: 95x HV: 20 kV WD: 11.9 mm
200 µm

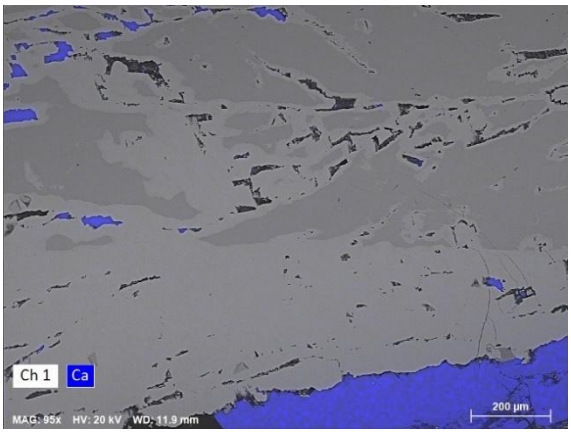
Ch 1
Ca
MAG: 95x HV: 20 kV WD: 11.9 mm
200 µm

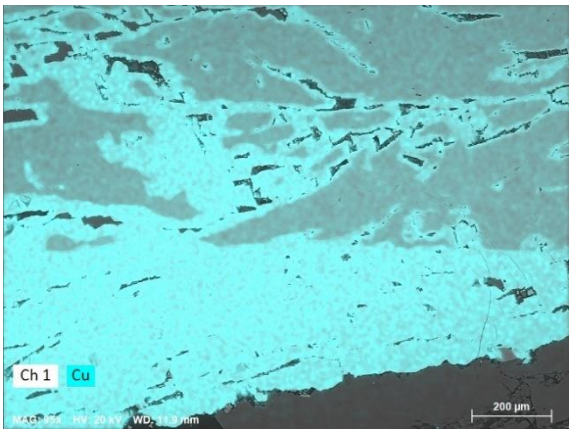
Ch 1
Cu
200 µm

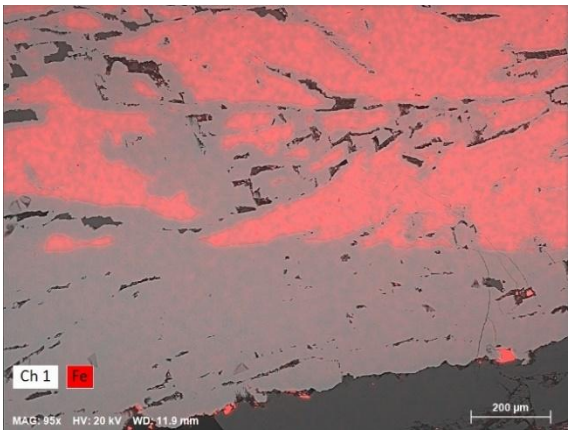
Ch 1
Fe
MAG: 95x HV: 20 kV WD: 11.9 mm
200 µm

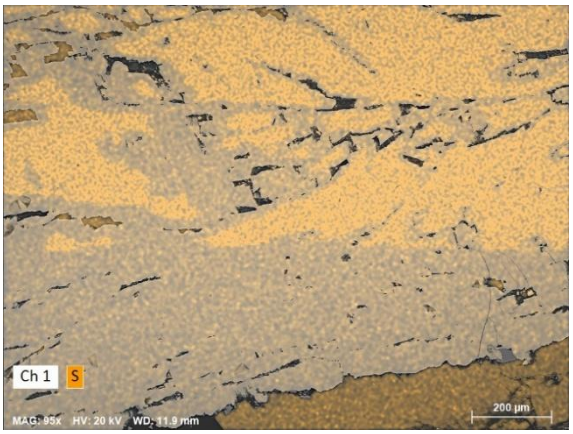
Ch 1
S
MAG: 95x HV: 20 kV WD: 11.9 mm
200 µm

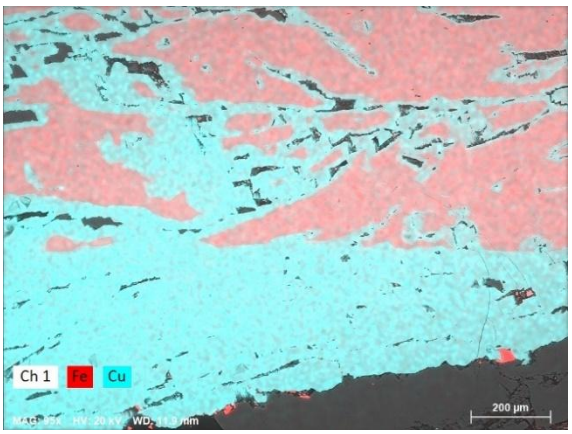
Ch 1
Fe
Cu
200 µm

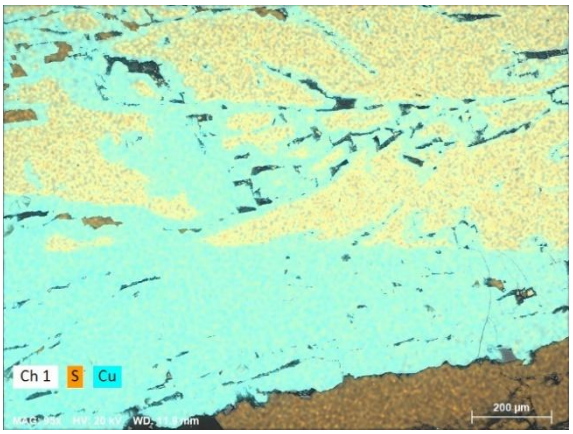
Ch 1
S
Cu
200 µm

Appendix III.II.c: *EDS imaging of sample SAL-03-08 without backscattering.*

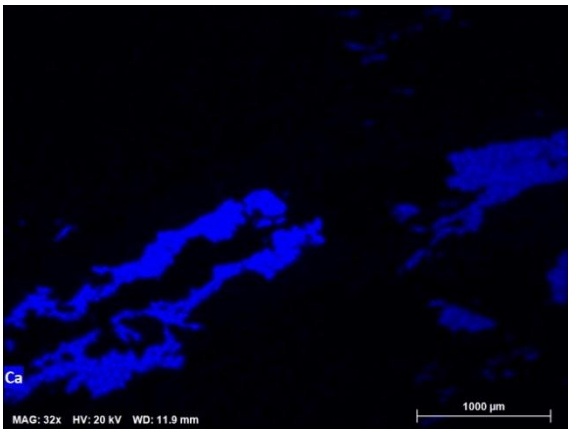

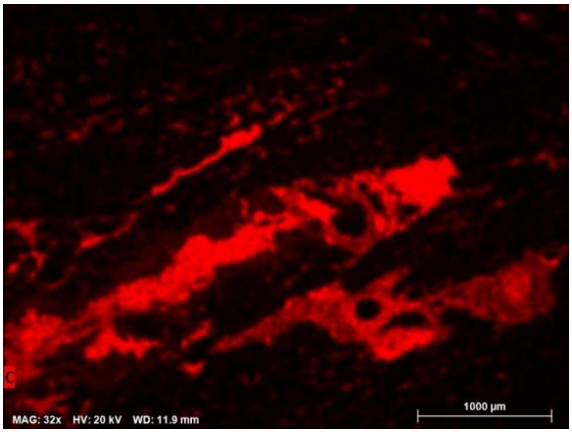

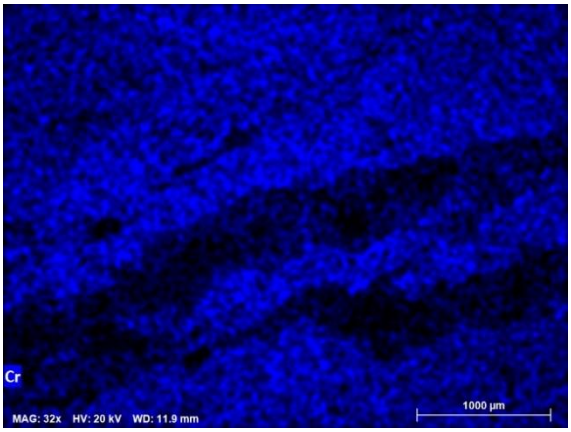

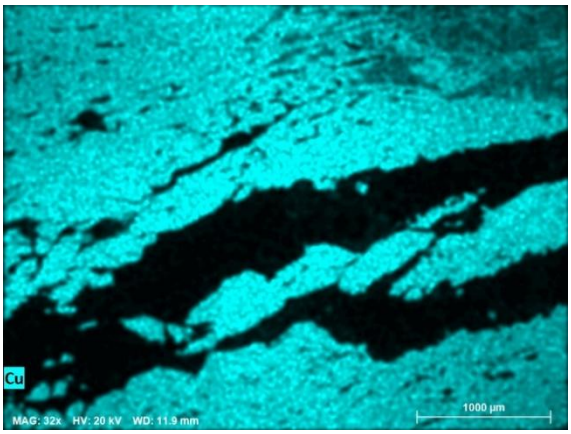

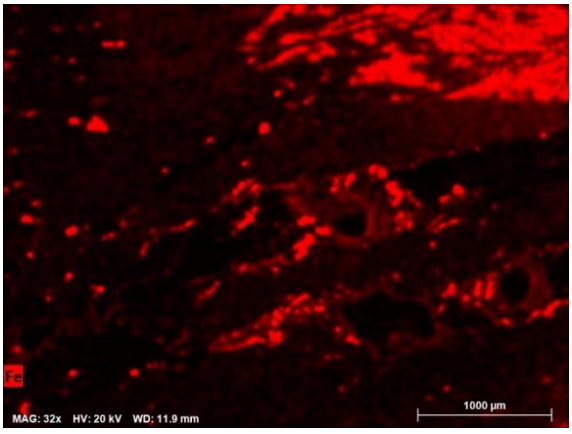

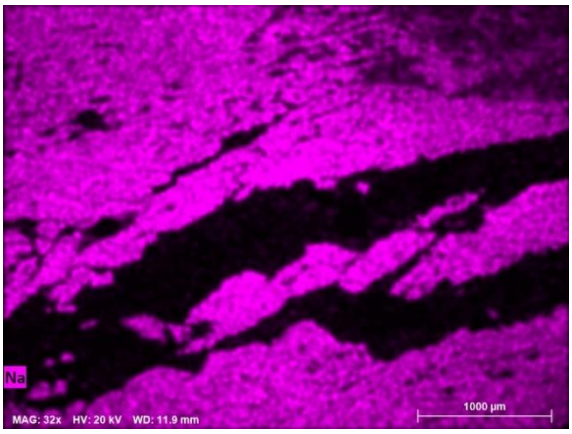

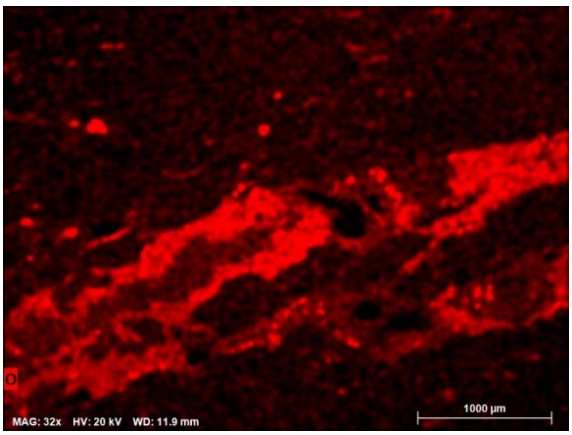

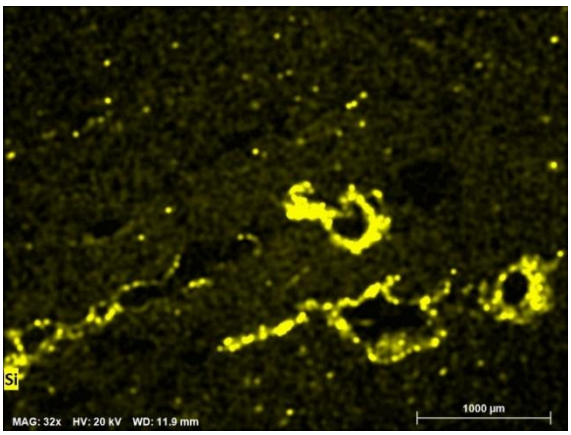

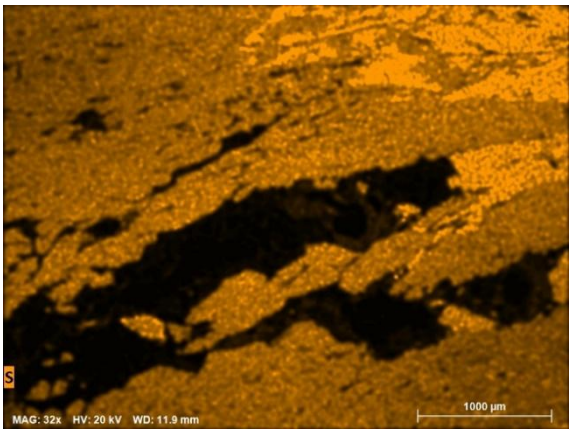
S
MAG: 32x HV: 20 kV WD: 11.9 mm
1000 µm

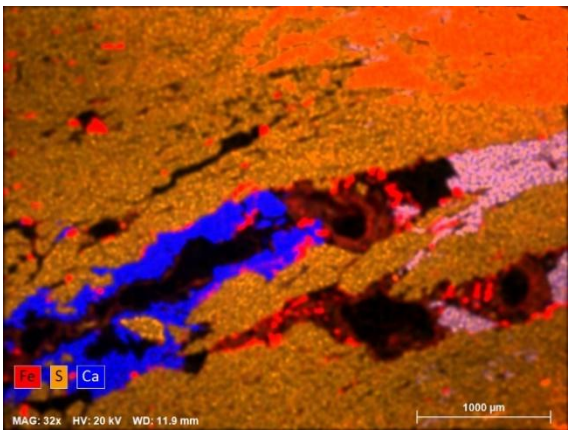
Fe
S
Ca
MAG: 32x HV: 20 kV WD: 11.9 mm
1000 µm

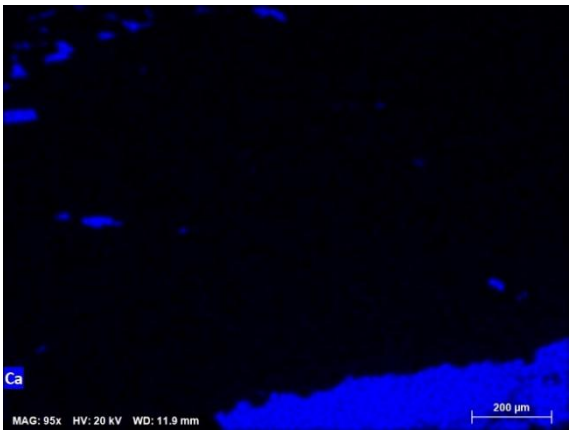
Ca
MAG: 95x HV: 20 kV WD: 11.9 mm
200 µm

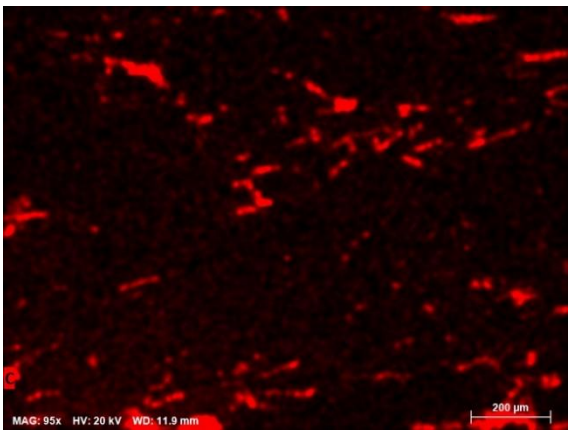
C
MAG: 95x HV: 20 kV WD: 11.9 mm
200 µm

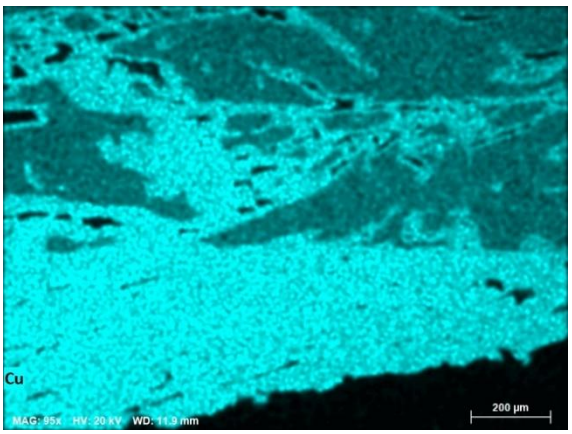
Cu
MAG: 95x HV: 20 kV WD: 11.9 mm
200 µm

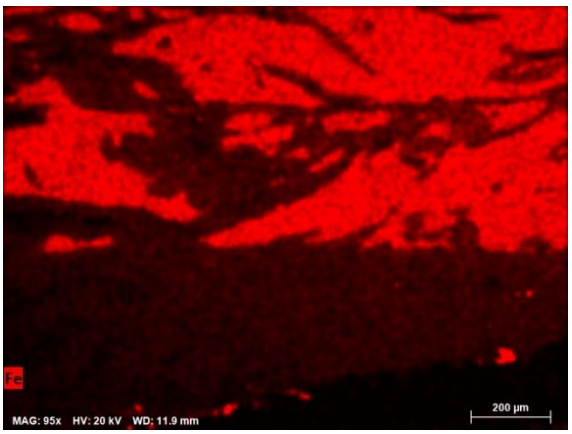
Fe
MAG: 95x HV: 20 kV WD: 11.9 mm
200 µm

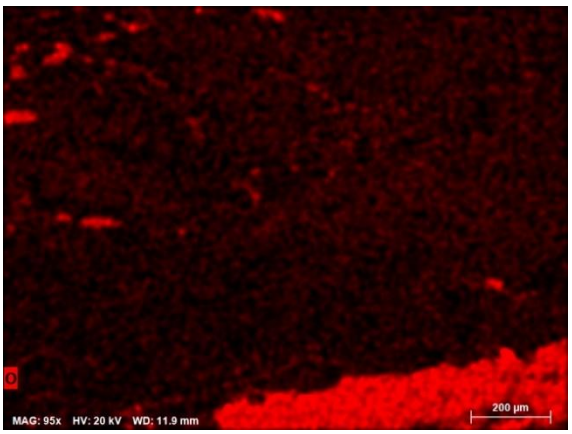
O
MAG: 95x HV: 20 kV WD: 11.9 mm
200 µm

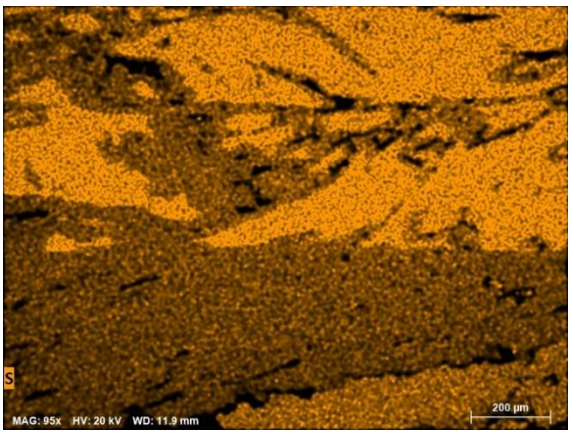
S
MAG: 95x HV: 20 kV WD: 11.9 mm
200 µm

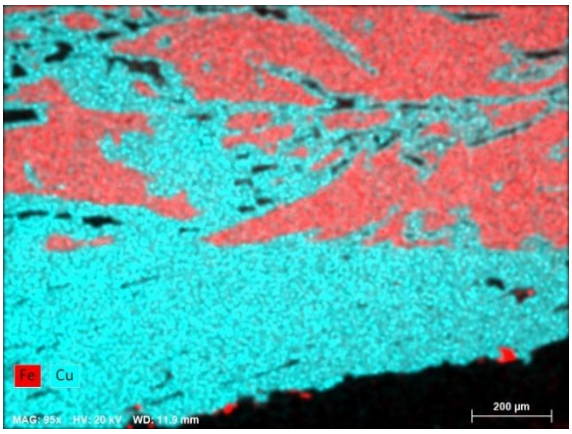

Appendix III.III: *Sample SAL-05-03.*

Appendix III.III.a: *SEM imaging of sample SAL-05-03.*

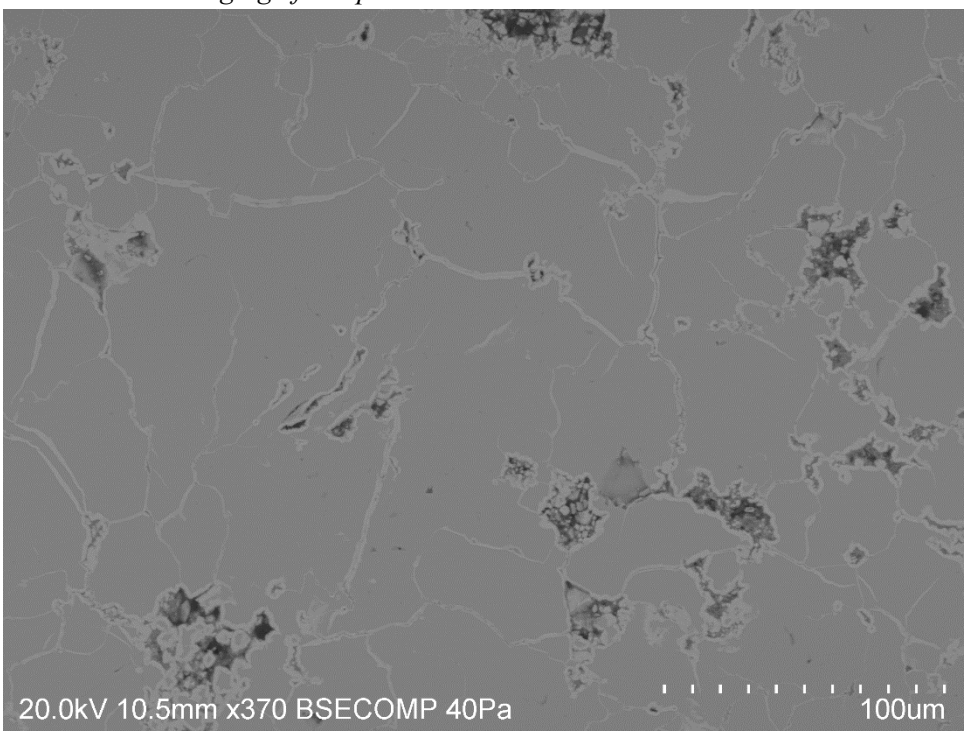

Appendix III.III.b: *EDS imaging of sample SAL-05-03 with backscattering.*

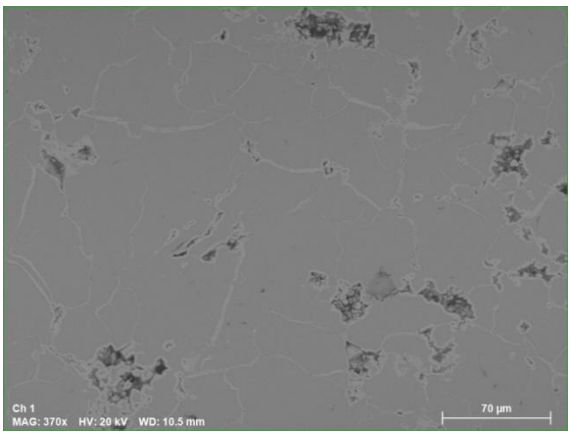

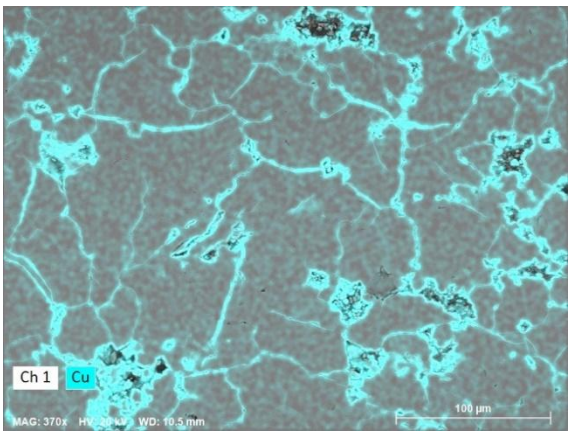

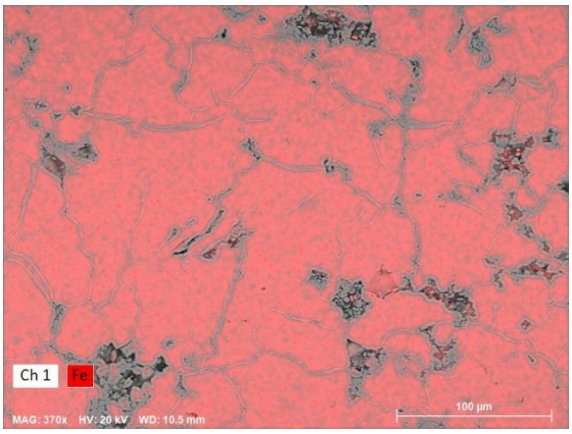
Ch 1
Fe
100 µm

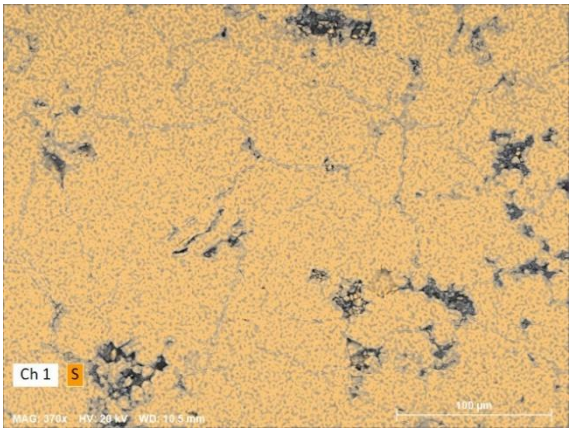
Ch 1
S
100 µm

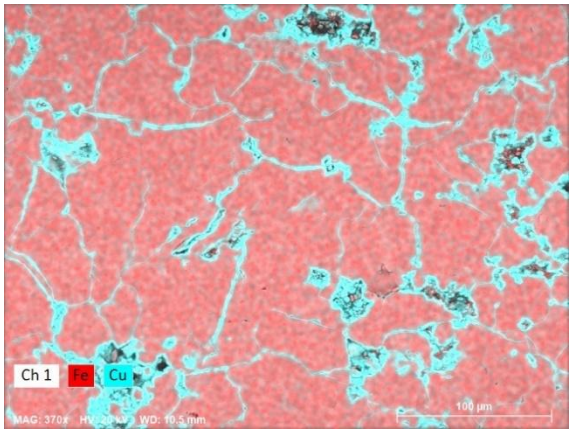
Ch 1
Fe
Cu
100 µm

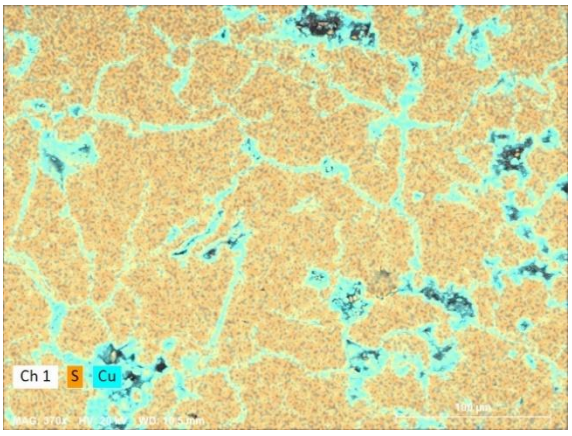
Ch 1
S
Cu

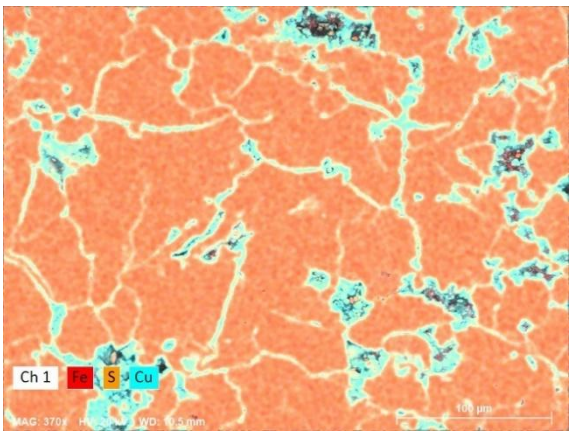
Ch 1
Fe
S
Cu
100 µm

Appendix III.IV: *Sample SAL-05-04(2).*

Appendix III.IV.a: *SEM imaging of sample SAL-05-04(2).*

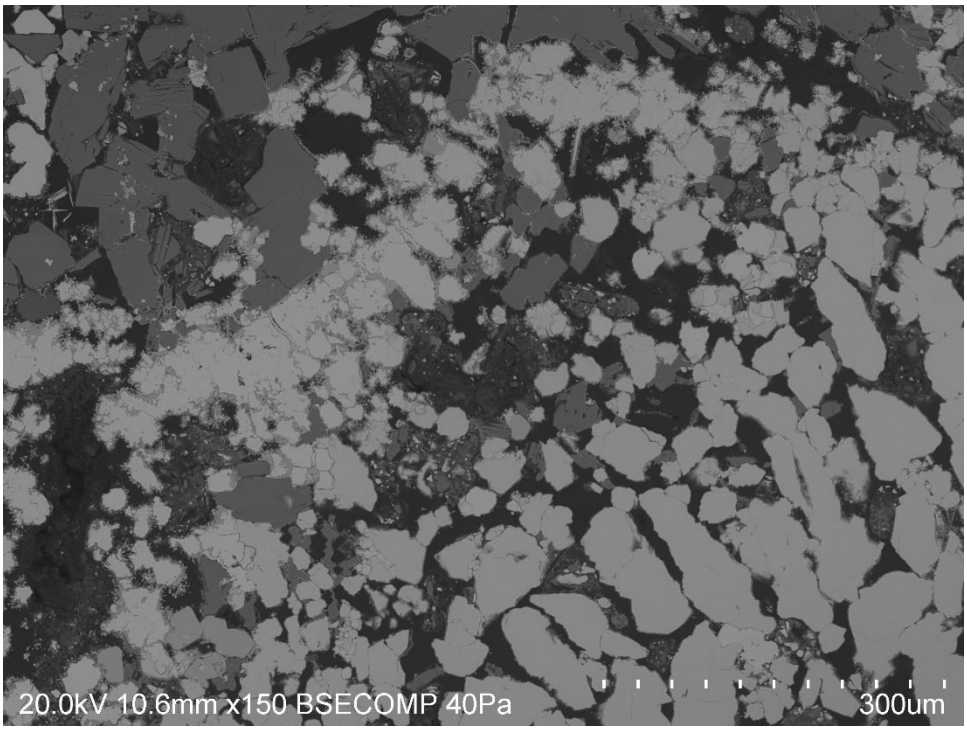

Appendix III.IV.b: *EDS imaging of sample SAL-05-03 with backscattering.*

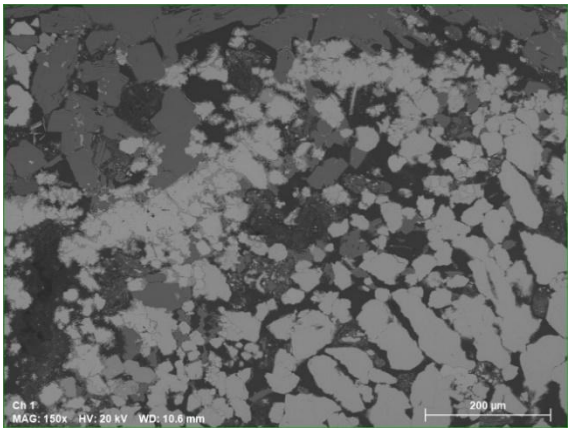

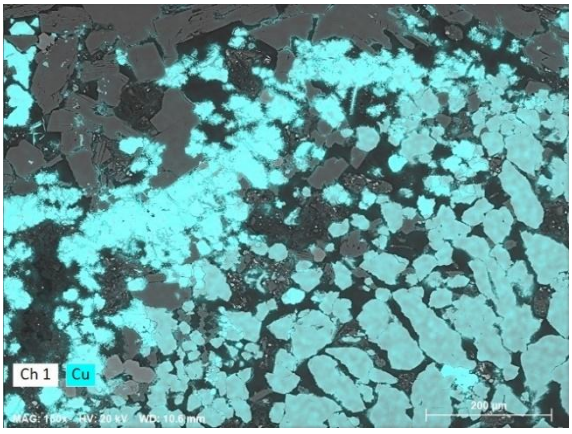

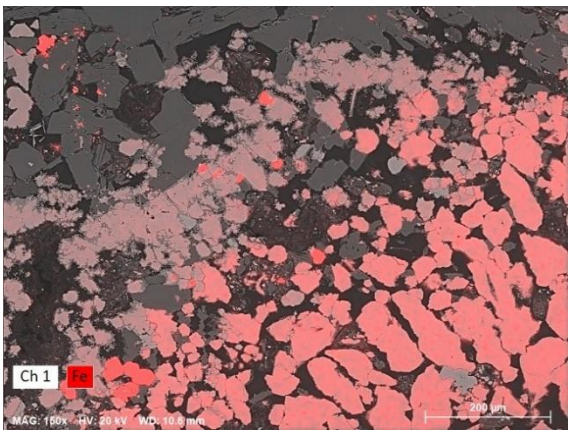

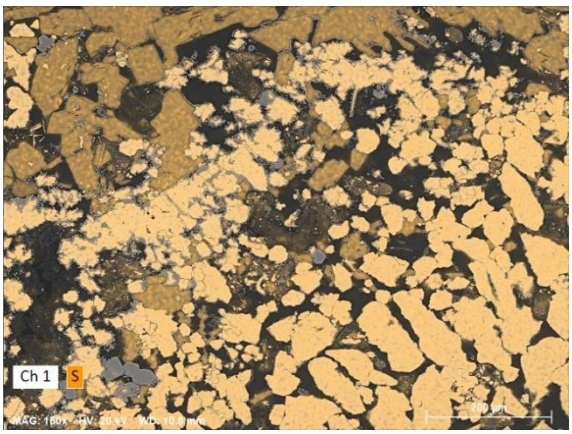

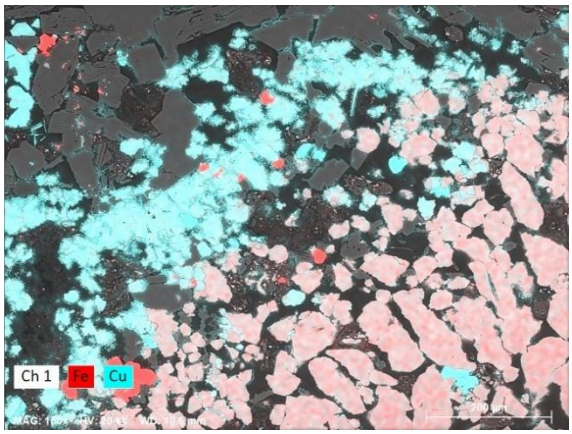

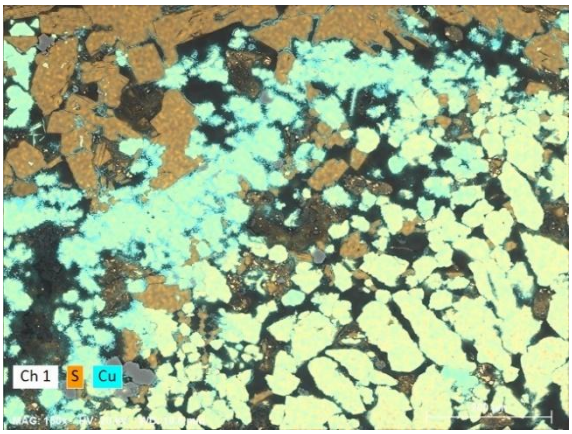

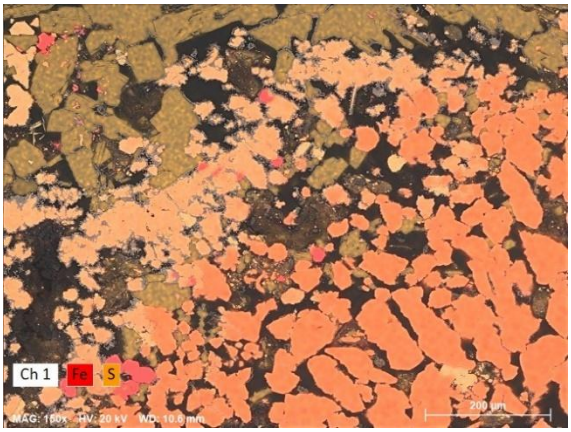

Appendix III.IV.c: *EDS imaging of sample SAL-05-03 without backscattering.*

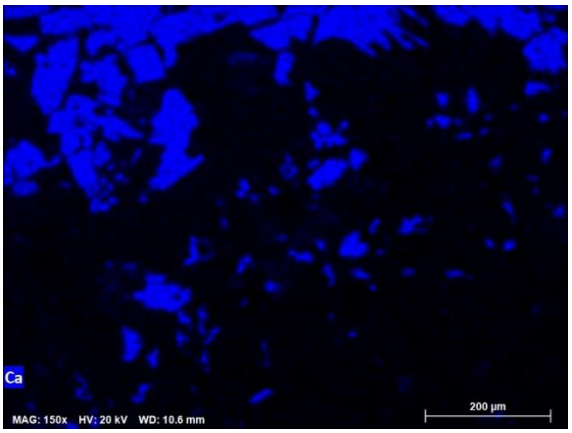

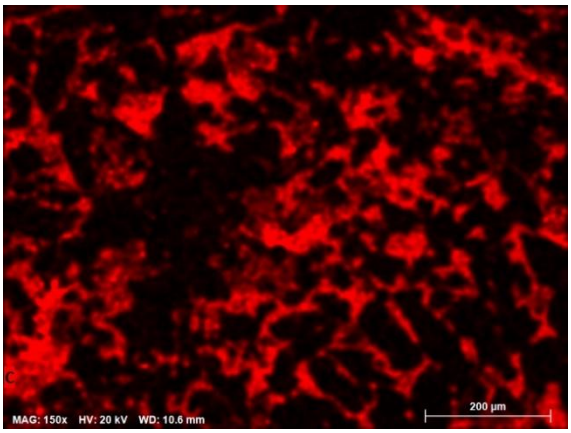

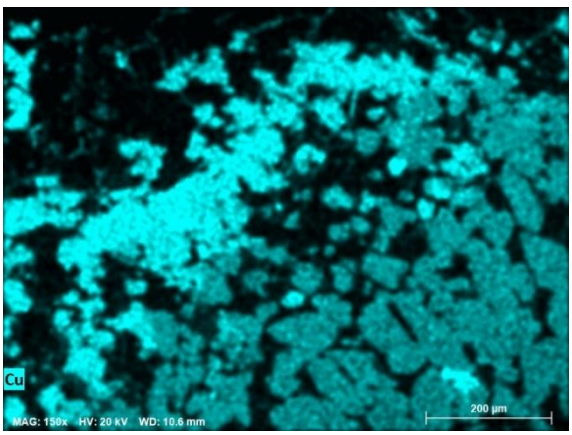

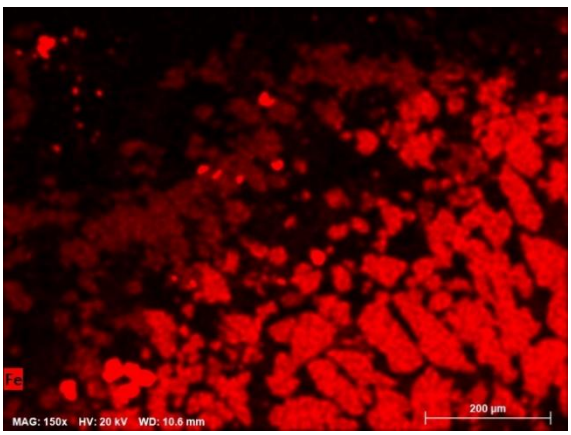

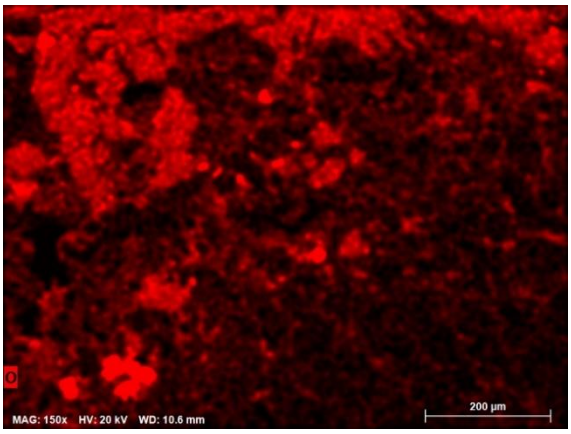
O
MAG: 150x HV: 20 kV WD: 10.6 mm
200 µm

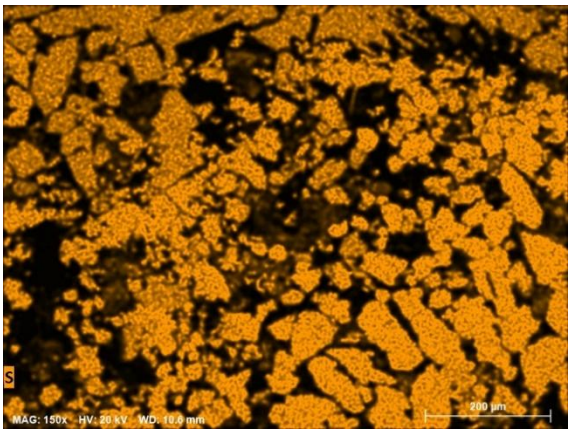
S
MAG: 150x HV: 20 kV WD: 10.6 mm
200 µm

APPENDIX IV: Bulk geochemistry.

Appendix IV.1: Oxide Composition of Rainbow samples.

Sample name	SiO2 (wt %)	Al2O3 (wt %)	MnO (wt %)	MgO (wt %)	CaO (wt %)	Na2O (wt %)	K2O (wt %)	TiO2 (wt %)	P2O5 (wt %)	$Fe_2O_3^{(T)}$ (wt %)	Fe2O3 (wt %)	FeO (wt %)
Det. limit	*0,01*	*0,01*	*0,001*	*0,01*	*0,01*	*0,01*	*0,01*	*0,001*	*0,01*	*0,01*	*0,01*	*0,1*
SAL- 03-03	0,2	0,02	0,022	0,07	0,12	0,07	0,01	< 0.001	0,03	9,28	1,05	7,4
SAL- 03-04	0,05	< 0.01	0,01	0,03	0,03	0,05	< 0.01	< 0.001	0,01	13,37	5,2	7,3
SAL- 03-06	0,17	< 0.01	0,017	0,08	0,13	0,07	< 0.01	< 0.001	0,02	44,7	38,1	5,9
SAL- 03-08	0,16	< 0.01	0,08	0,17	4,51	< 0.01	< 0.01	< 0.001	< 0.01	38,81	32,69	5,5
SAL- 04-02	0,03	< 0.01	0,01	0,06	13,95	0,06	< 0.01	< 0.001	0,03	38,78	13,98	22,3
SAL- 04-02X	0,07	< 0.01	0,02	0,02	0,09	0,02	< 0.01	0,001	0,01	73,78	43,5	27,2
SAL- 05-01X	1,75	0,12	0,05	0,64	0,09	0,57	0,1	0,02	0,33	63,12	61,01	1,9
SAL- 05-01(A4)	0,22	0,02	0,02	0,14	0,06	0,52	0,06	< 0.001	0,02	41,51	36,95	4,1
SAL- 05-03	0,31	0,01	0,01	0,06	0,05	0,03	< 0.01	< 0.001	0,04	47,54	27,19	18,3
SAL-05-03R	0,31	0,01	0,04	0,05	0,05	0,03	< 0.01	< 0.001	0,02	46,46	42,24	3,8
SAL- 05-05	0,05	< 0.01	0,008	1,31	33,34	0,32	< 0.01	< 0.001	< 0.01	5,29	2,96	2,1

Data form other sites

Appendix IV.II.: Elemental Composition of rainbow samples – The composition of SAL samples.

Concentration in ppm	S	Ca	V	Mn	Fe	Co	Ni	Cu	Zn	Ga	Ge	As	Se
SAL- 03-03	82959,4	857,6	8,0	170380,6	122428,4	925,0	2,0	15500,0	540000,0	194,0	25,3	30,0	< 0,5
SAL- 03-04	207703,6	214,4	< 5	77,4	150257,9	2870,0	1,0	14800,0	495000,0	119,0	106,0	98,0	< 0,5
SAL- 03-06	119864,2	929,1	6,0	131657,8	358507,9	1910,0	1180,0	344000,0	5770,0	5,0	4,7	13,0	590,0
SAL- 03-08	139079,0	32233,0	< 5	619,6	314202,1	233,0	867,0	384000,0	39,0	< 1	< 0,5	< 1	1330,0
SAL- 04-02	144569,0	99700,8	< 5	77,4	444580,5	3420,0	< 1	122000,0	9460,0	3,0	0,6	25,0	30,0
SAL- 05-01X	11101,9	643,2	228,0	387,2	456251,0	224,0	16,0	119000,0	748,0	3,0	3,6	105,0	39,0
SAL- 05-01(A4)	97294,3	428,8	6,0	154,9	322204,4	4970,0	< 1	229000,0	1950,0	8,0	2,5	403,0	45,5
SAL- 04-02X	68014,5	643,2	12,0	139402,3	727470,3	3350,0	< 1	48800,0	10700,0	5,0	3,0	16,0	5,5
SAL- 05-03	117119,2	357,4	8,0	77,4	474758,4	3120,0	< 1	324000,0	540,0	3,0	0,9	126,0	237,0
SAL-05-03 REPLICATE	118339,2	357,4	9,0	309,8	354494,4	3440,0	< 1	331000,0	636,0	7,0	1,0	126,0	233,0
SAL- 05-05	208008,6	238281,3	< 5	61956,6	53323,5	453,0	61,0	30800,0	293,0	< 1	< 0,5	3,0	30,5

Sr	Mo	Ag	Cd	In	Sn	Sb	Ba	Sr	Pb	Au	Hg	Tl	Pb	Bi	reference:
50,0	32,0	832,0	1830,0	< 0,1	875,0	216,0	686,0	50,0	648,0	0,0	3,0	< 0,05	648,0	< 0,1	(this study)
32,0	14,0	415,0	1130,0	0,2	407,0	36,2	515,0	32,0	650,0	1,4	2,0	0,1	650,0	< 0,1	(this stydy)
27,0	15,0	32,3	12,7	19,4	27,0	1,8	246,0	27,0	45,0	12,9	< 1	0,1	45,0	4,9	(this stydy)
461,0	< 2	3,9	< 0,5	1,8	6,0	< 0,1	63,0	461,0	7,0	0,4	< 1	0,1	7,0	0,3	(this stydy)
903,0	4,0	46,1	27,3	5,5	37,0	3,6	51,0	903,0	18,0	8,3	< 1	0,1	18,0	4,9	(this stydy)
30,0	49,0	2,3	< 0,5	29,3	10,0	2,5	662,0	30,0	51,0	7,4	< 1	0,1	51,0	6,8	(this stydy)
7,0	32,0	26,4	3,6	5,3	24,0	4,2	13,0	7,0	14,0	6,9	< 1	< 0,05	14,0	8,9	(this stydy)
8,0	44,0	37,3	22,3	2,3	22,0	1,2	54,0	8,0	27,0	5,0	< 1	< 0,05	27,0	5,0	(this stydy)
3,0	8,0	6,6	< 0,5	2,8	11,0	1,7	11,0	3,0	14,0	8,7	< 1	0,1	14,0	5,4	(this stydy)
4,0	8,0	< 0,5	0,7	2,7	11,0	2,0	52,0	4,0	9,0	8,6	< 1	< 0,05	9,0	4,8	(this stydy)
2212,0	3,0	2,5	< 0,5	2,3	2,0	0,5	203,0	2212,0	< 5	1,8	< 1	0,1	< 5	2,7	(this stydy)

Appendix IV.III.: Elemental Composition of hydrothermal sulfide samples, along with average MORB compositions for reference – The composition samples from Rainbow (previous studies: Fouquet et al., 2010), Logatchev 1 and 2 (Bogdanov et al., 1995; Fouquet et al., 2010; Krasnov et al., 1995; Mozgova et al., 1999) and Tianzuo (Cao et al., 2021), as well as MORB (Gale et al., 2013), included for comparison. All oxide values were converted to the respective elements.

	VALUES IN ppm	S	Ca	V	Mn	Fe	Co	Ni	Cu	Zn	Ga	Ge	As	Se
Rainbow (others)	**Raindbow 1 (n=116)**	327500,0	26900,0		453,0	285600,0	5086,0	490,0	124300,0	149900,0	0,0	12,0	214,0	186,0
	Raindbow 2 (n=3)	312700,0	2200,0		2407,0	321000,0	42,0	177,0	800,0	3400,0	0,0	0,0	22,0	10,0
		S	**Ca**	**V**	**Mn**	**Fe**	**Co**	**Ni**	**Cu**	**Zn**	**Ga**	**Ge**	**As**	**Se**
Logatchev	**Logatchev 1 (n= 40)**	263600,0	28600,0		602,0	244000,0	500,0	92,0	254700,0	25500,0	23,0	12,0	62,0	625,0
	Logatchev 1 (n= 7)	N/A	N/A		N/A	222600,0	329,0	N/A	189600,0	15100,0	N/A	N/A	N/A	N/A
	Logatchev 1 (n= 8)	N/A	N/A		179,0	286000,0	778,0	20,0	231000,0	78500,0	N/A	N/A	389,0	N/A
	Logatchev 2 (n= 5)	209000,0	3700,0		100,0	175500,0	500,0	20,0	147200,0	254000,0	43,0	50,0	522,0	N/A
	Logatchev 2 (n= 8)	332400,0	12700,0		508,0	196800,0	49,0	31,0	200500,0	227800,0	32,0	19,0	289,0	1314,0
		S	**Ca**	**V**	**Mn**	**Fe**	**Co**	**Ni**	**Cu**	**Zn**	**Ga**	**Ge**	**As**	**Se**
Tianzuo	**TVG21-1-1**		100,0	3,6	52,2	342300,0	2400,0	5,0	71000,0	100,0			34,0	<0,01
	TVG21-1-2		100,0	2,8	48,5	315700,0	551,0	3,7	64200,0	100,0			29,0	<0,01
	TVG21-1-3		100,0	3,6	55,5	351400,0	560,0	4,2	72400,0	100,0			23,2	<0,01
	TVG21-1-4		3900,0	8,4	112,0	259900,0	1176,7	5,5	28600,0	100,0			16,5	N/A
	TVG21-1-5		800,0	5,2	55,9	261100,0	1501,3	3,5	66300,0	200,0			9,5	N/A
	TVG21-1-6		800,0	5,2	55,9	259700,0	1458,6	3,3	66600,0	200,0			9,5	N/A
	TVG21-1-7		700,0	5,1	55,8	269100,0	1516,2	3,3	71100,0	200,0			9,5	N/A
	TVG21-2-1		300,0	7,3	1730,0	421400,0	328,0	12,7	1600,0	100,0			10,5	<0,01
	TVG21-2-2		600,0	13,0	1720,0	445900,0	392,9	30,6	4500,0	1100,0			34,7	<0,01
	TVG21-2-3		800,0	11,1	2030,7	376600,0	268,4	11,6	4100,0	100,0			10,4	N/A
	TVG21-2-4		1000,0	11,9	2084,7	377200,0	243,5	12,3	4000,0	100,0			11,4	N/A
	AVERAGE TVG21		800,0	6,0	431,7	325200,0	1098,3	8,0	49600,0	200,0			19,6	N/A
		S	**Ca**	**V**	**Mn**	**Fe**	**Co**	**Ni**	**Cu**	**Zn**	**Ga**	**Ge**	**As**	**Se**
MORB's mean composition	**MORB**	0,2	8,1	309,0	0,2	8,1	43,0	92,0	74,0	91,3	17,5	N/A	2,0	0,0
	E-MORB	0,2	8,2	295,0	0,2	7,9	42,5	90,0	74,0	88,1	17,0	N/A	2,1	0,0
	N-MORB	0,1	8,0	300,0	0,2	8,5	43,3	94,0	78,0	90,2	16,7	N/A	1,9	0,0
	D-MORB	0,2	8,3	310,0	0,2	7.7	43,8	91,0	71,0	94,2	17,2	N/A	2,3	0,0

Sr	Mo	Ag	Cd	In	Sn	Sb	Ba	Sr	Pb	Au	Hg	Tl	Pb	Bi	
665,0	29,0	188,0	391,0	10,0	138,0	34,0	2900,0	665,0	342,0	5,1	0,0	0,0	342,0	5,0	**Fouquet et al, (2010)**
3020,0	159,0	34,0	6,0	5,0	79,0	12,0	162000,0	3020,0	21,0	1,0	0,0	0,0	21,0	0,0	**Fouquet et al, (2010)**

Sr	Mo	Ag	Cd	In	Sn	Sb	Ba	Sr	Pb	Au	Hg	Tl	Pb	Bi	
293,0	51,0	35,0	51,0	8,0	225,0	21,0	600,0	293,0	209,0	8,4	N/A	N/A	209,0	12,0	**Fouquet et al, (2010)**
N/A	N/A	70,0	27,0	N/A	N/A	N/A	0,0	N/A	400,0	9,6	N/A	N/A	400,0	N/A	**Krasnov et al, [1995], Mozgova et al, [1999]**
N/A	N/A	N/A	N/A	N/A	N/A	N/A	1600,0	N/A	220,0	N/A	N/A	N/A	220,0	N/A	**Bogdanov et al, [1995]**
N/A	N/A	92,0	700,0	N/A	>50	N/A	100,0	N/A	700,0	23,8	N/A	N/A	700,0	27,0	**Bogdanov et al, [1995]**
154,0	49,0	79,0	356,0	10,0	1107,0	74,0	500,0	154,0	435,0	25,9	N/A	N/A	435,0	13,0	**Fouquet et al, (2010)**

Sr	Mo	Ag	Cd	In	Sn	Sb	Ba	Sr	Pb	Au	Hg	Tl	Pb	Bi	
1,6	37,4	0,7	0,1	2,0	3,5	<0,01	0,0	1,6	1,7			<0,01	1,7		**Cao et al, (2021)**
1,4	32,3	0,6	<0,01	1,7	2,5	<0,01	0,4	1,4	1,5			<0,01	1,5		**Cao et al, (2021)**
0,9	37,8	0,5	0,1	1,9	2,7	<0,01	0,8	0,9	1,2			1,2	1,2		**Cao et al, (2021)**
18,5	92,3	N/A	0,6	N/A	N/A	N/A	47,9	18,5	4,6			0,0	4,6		**Cao et al, (2021)**
0,9	61,2	N/A	1,1	N/A	N/A	N/A	4,0	0,9	3,9			N/A	3,9		**Cao et al, (2021)**
0,9	61,4	N/A	1,0	N/A	N/A	N/A	3,1	0,9	2,8			N/A	2,8		**Cao et al, (2021)**
1,0	59,0	N/A	1,0	N/A	N/A	N/A	2,7	1,0	4,1			N/A	4,1		**Cao et al, (2021)**
2,9	15,8	0,3	0,0	0,1	1,7	0,0	1,6	2,9	2,2			9,5	2,2		**Cao et al, (2021)**
21,6	22,5	0,8	0,6	0,3	2,5	1,1	8,2	21,6	18,1			0,2	18,1		**Cao et al, (2021)**
2,8	32,1	N/A	0,5	N/A	N/A	N/A	3,0	2,8	4,4			N/A	4,4		**Cao et al, (2021)**
2,3	34,3	N/A	0,6	N/A	N/A	N/A	3,3	2,3	4,7			N/A	4,7		**Cao et al, (2021)**
5,5	46,6	0,6	0,6	1,2	2,6	0,6	7,6	5,5	4,4			2,7	4,4		**Cao et al, (2021)**

Sr	Mo	Ag	Cd	In	Sn	Sb	Ba	Sr	Pb	Au	Hg	Tl	Pb	Bi	
129,0	0,5	0,0	0,1	0,3	0,9	0,5	29,2	129,0	0,6	N/A	N/A	0,0	0,6	N/A	**Gale et al, (2013)**
126,0	0,5	0,0	0,1	0,3	0,9	0,5	30,5	126,0	0,6	N/A	N/A	0,0	0,6	N/A	**Gale et al, (2013)**
130,0	0,4	0,0	0,1	0,3	0,9	0,5	28,1	130,0	0,6	N/A	N/A	0,0	0,6	N/A	**Gale et al, (2013)**
131,0	0,5	0,0	0,1	0,3	0,9	0,6	32,1	131,0	0,6	N/A	N/A	0,0	0,6	N/A	**Gale et al, (2013)**

Appendix IV.IV: Bulk geochemistry analyses: Element detection limit and analytical method.

Element	Detection limit (ppm)	Analysis Method
Cu	50000	FUS-ICP & Na2O2
Fe (total)	1000	FUS-ICP & TITR
Zn	1	MULT INAA / TD-ICP & FUS-Na2O2
S	500	SO4
Ba	1	FUS-ICP
Ca	100	FUS-ICP
Pb	5	TD-ICP
Cd	0,5	TD-ICP
Ag	0,5	MULT INAA / TD-ICP
As	1	INAA
Sb	0,1	INAA
Ni	1	TD-ICP
Co	0,1	INAA
Se	0,5	INAA
Mo	2	FUS-MS
In	0,1	FUS-MS
Sn	1	FUS-MS
Mn	10000	FUS-ICP
Sr	2	FUS-ICP
U	0,01	FUS-MS
Ge	0,5	FUS-MS
Bi	0,1	FUS-MS
Hg	1	INAA
Tl	0,05	FUS-ICP
Ga	1	FUS-MS
Au	0,001	INAA
V	5	FUS-ICP

Note:

INAA: Instrumental Neutron Activation Analysis

FUS-ICP: Fusion with Inductively Coupled Plasma

TD-ICP: Total Digestion with Inductively Coupled Plasma

FUS-MS: Fusion with Mass Spectrometry

FUS-ICP & Na_2O_2 - ICP using fusion with Sodium Peroxide

FUS-ICP & TITR: FUS-ICP using titration technique to determine the total iron content (Fe^{2+} and Fe^{3+})

MULT INAA / TD-ICP: Multiple Techniques - Instrumental Neutron Activation Analysis and Total Digestion with Inductively Coupled Plasma

MULT INAA / TD-ICP & FUS-Na2O2: combination of INAA and TD-ICP Analysis using FUS-Na_2O_2

SO4: Infrared Detection of Sulfur to determine the sulfate (SO_4^{2-})

Appendix IV.V.: Rare Earth Elements (REE) Composition of Rainbow sulfide samples (in this study), normalized to McDonough, W. F., & Sun, S. (1995).

Sample name	La	Ce	Pr	Nd	Sm	Eu	Gd	Tb	Dy	Ho	Er	Tm	Yb	Lu
Det. limit	*0,05*	*0,05*	*0,01*	*0,05*	*0,01*	*5*	*0,01*	*0,01*	*0,01*	*0,01*	*0,01*	*5*	*0,01*	*2*
SAL-03-03	0,22	0,08	0,01	< 0.05	0,01	34	0,02	< 0.01	0,02	< 0.01	0,01	< 0.005	< 0.01	< 0.002
SAL-03-04	0,19	0,11	< 0.01	< 0.05	0,01	< 0.005	0,01	< 0.01	0,01	< 0.01	< 0.01	< 0.005	< 0.01	< 0.002
SAL-03-06	0,9	0,89	0,07	0,15	0,01	122	0,02	< 0.01	0,03	< 0.01	0,01	< 0.005	< 0.01	< 0.002
SAL-03-08	0,13	0,11	0,01	0,05	0,01	14	< 0.01	< 0.01	0,01	< 0.01	< 0.01	< 0.005	< 0.01	< 0.002
SAL-04-02	1,57	1,39	0,09	0,25	0,02	0,16	0,04	0,01	0,03	0,01	0,01	< 0.005	< 0.01	< 0.002
SAL 05-01X	2,79	3,98	0,4	1,74	0,35	196	0,33	0,05	0,34	0,07	0,19	29	0,16	21
SAL-05-01(A4)	0,13	0,1	0,02	0,16	0,05	16	0,05	0,01	0,04	0,01	0,03	< 0.005	0,02	3
SAL-04-02X	0,42	0,59	0,05	0,12	0,03	135	0,03	< 0.01	0,03	0,01	0,01	< 0.005	0,01	2
SAL-05-03 (average)	0,275	0,345	0,035	0,14	0,04	75,5	0,04	< 0.01	0,035	0,01	0,02	< 0.005	0,015	2,5
SAL-05-05	4,39	3,91	0,28	0,8	0,11	322	0,1	0,01	0,07	0,01	0,03	< 0.005	0,02	3
Primitive Mantle [1]	0,237	0,613	0,093	0,457	0,148	0,056	0,199	0,036	0,246	0,055	0,160	0,025	0,161	0,025

[1] McDonough, W. F., & Sun, S. (1995). The composition of the Earth. Chemical Geology, 120(3-4), 223–253: https://doi.org/10.1016/0009-2541(94)00140-4

Appendix IV.VI.: Cu/Zn and Ba/Co ratios for each of the studied fields, color-coded to match Figure 10.2.

	Cu/Zn	Ba/Co
Rainbow (others)	0,8	0,6
Rainbow (others)	0,2	3857,1
Logatchev	9,9882	1,2000
Logatchev	12,5563	0,0000
Logatchev	2,9427	2,0566
Logatchev	0,5795	0,2000
Logatchev	0,8802	10,2041
SAL-Rainbow	0,0287	0,7416
SAL-Rainbow	0,0299	0,1794
SAL-Rainbow	59,6187	0,1288
SAL-Rainbow	9846,1538	0,2704
SAL-Rainbow	12,8964	0,0149
SAL-Rainbow	159,0909	2,9554
SAL-Rainbow	117,4359	0,0026
SAL-Rainbow	4,5607	0,0161
SAL-Rainbow	600,0000	0,0035
SAL-Rainbow	520,4403	0,0151
SAL-Rainbow	105,1195	0,4481
Tianzuo	710,0000	0,0000
Tianzuo	642,0000	0,0007
Tianzuo	724,0000	0,0015
Tianzuo	286,0000	0,0407
Tianzuo	331,5000	0,0027
Tianzuo	333,0000	0,0021
Tianzuo	355,5000	0,0018
Tianzuo	16,0000	0,0049
Tianzuo	4,0909	0,0209
Tianzuo	41,0000	0,0110
Tianzuo	40,0000	0,0134
Tianzuo	248,0000	0,0070
MORB's mean composition	0,8105	0,6791
MORB's mean composition	0,8400	0,7176
MORB's mean composition	0,8647	0,6490
MORB's mean composition	0,7537	0,7329

APPENDIX V: Correlation Coefficient matrixes.

APPENDIX V.I: Correlation Coefficient matrixes for the combined Cu-style samples, as well as each individual sample.

ALL Cu-STYLE SAMPLES

	Bi	Ga	Pb	Au	Ag	Ge	Cd	Mo	In	As	Sn	S	Ni	Se	Zn	Fe	Sb	Mn	Co	W	Te	Cu
Bi	1																					
Ga	-0,04142	1																				
Pb	-0,06402	-0,00699	1																			
Au	0,128924	-0,04033	-0,04689	1																		
Ag	0,069662	0,055347	0,049752	0,54669	1																	
Ge	0,040593	0,101551	0,015986	-0,03301	0,003141	1																
Cd	-0,0109	-0,0948	0,278752	0,082897	0,12976	-0,03625	1															
Mo	0,048962	0,016305	0,031719	-0,08595	-0,09321	-3,5E-05	0,09811	1														
In	0,074455	0,163512	0,029907	-0,03432	0,014713	-0,06263	0,039228	0,024027	1													
As	0,019072	-0,0994	-0,00411	-0,03312	-0,12385	0,040797	-0,06366	-0,02357	-0,05435	1												
Sn	0,026835	-0,05888	0,029534	0,478889	0,235508	0,004336	0,425713	0,042376	0,029294	-0,08164	1											
S	-0,24845	0,035167	-0,00378	-0,17834	-0,10499	0,028508	-0,00921	0,091735	-0,09643	0,100206	-0,1225	1										
Ni	-0,01792	-0,03844	0,070442	-0,00758	-0,04926	0,136319	-0,01751	0,098128	-0,03903	-0,03102	0,40823	0,014581	1									
Se	0,027638	0,078292	-0,02316	-0,0784	0,047821	-0,07032	-0,17459	0,147147	-0,09232	-0,0991	-0,10305	0,043424	-0,03639	1								
Zn	-0,03503	-0,09038	0,270688	-0,01356	0,061374	0,035834	0,921395	0,0834	0,014428	-0,04711	0,307311	0,027309	-0,01624	-0,18129	1							
Fe	-0,25972	0,101317	0,008361	-0,14256	-0,13706	-0,0251	-0,28652	0,019881	-0,1048	0,099022	-0,36175	0,585705	-0,13526	0,03415	-0,24377	1						
Sb	-0,039	-0,04563	0,154312	-0,03345	0,040581	0,04578	0,143261	-0,09335	0,064842	-0,10658	0,157592	-0,17406	-0,03128	-0,05112	0,108015	-0,25686	1					
Mn	0,01771	-0,03098	0,042961	-0,04814	-0,13954	-0,02739	0,035349	0,121932	-0,04085	-0,10991	0,081367	0,062242	0,245622	-0,06398	0,081041	-0,00583	0,01042	1				
Co	-0,1001	-0,00135	0,090803	-0,045	-0,08671	0,129281	0,031275	-0,02274	-0,05135	0,145194	0,266809	0,230762	0,757429	-0,22911	0,056396	0,23091	-0,06762	0,210859	1			
W	0,096728	-0,1476	0,009782	-0,04165	-0,12437	-0,04337	-0,10654	0,042533	0,104443	-0,04931	-0,12053	0,123138	-0,04263	0,06109	-0,09919	0,155404	0,011822	-0,10976	0,101755	1		
Te	-0,04297	0,16703	0,033751	0,202171	0,073531	0,15702	0,170079	0,117756	-0,05875	0,085607	0,268618	0,083533	-0,02056	-0,067	0,20299	-0,01661	-0,00143	0,089907	-0,03616	0,02642	1	
Cu	0,295555	-0,0233	-0,20323	0,032707	0,060448	-0,02515	-0,26965	-0,07141	0,106687	-0,0534	-0,02104	-0,55632	-0,14602	0,122648	-0,34731	-0,76058	0,19109	-0,09616	-0,47113	-0,08259	-0,12747	1

SAMPLE 03-06(1)

	Bi	Ga	Pb	Au	Ag	Ge	Cd	Mo	In	As	Sn	S	Ni	Se	Zn	Fe	Sb	Mn	Co	W	Te	Cu
Bi	1																					
Ga	#DIV/0!	1																				
Pb	#DIV/0!	0,278981	1																			
Au	#DIV/0!	0,15852	-0,05695	1																		
Ag	#DIV/0!	0,398628	-0,12761	-0,2078	1																	
Ge	#DIV/0!	0,380633	0,053714	-0,13628	0,813111	1																
Cd	#DIV/0!	#DIV/0!	#DIV/0!	#DIV/0!	#DIV/0!	#DIV/0!	1															
Mo	#DIV/0!	-0,27232	0,427182	-0,29764	0,260003	0,198907	#DIV/0!	1														
In	#DIV/0!	-0,04522	0,01545	0,011991	0,380706	0,255443	#DIV/0!	0,205242	1													
As	#DIV/0!	-0,19901	0,768954	-0,12094	-0,14648	0,052562	#DIV/0!	0,58792	0,177829	1												
Sn	#DIV/0!	#DIV/0!	#DIV/0!	#DIV/0!	#DIV/0!	#DIV/0!	#DIV/0!	#DIV/0!	#DIV/0!	#DIV/0!	1											
S	#DIV/0!	0,503872	0,370401	0,268983	0,186842	0,182935	#DIV/0!	0,271412	-0,33949	-0,0316	#DIV/0!	1										
Ni	#DIV/0!	0,159665	0,04745	-0,22507	0,26625	0,536834	#DIV/0!	0,03556	-0,02757	0,13009	#DIV/0!	0,169527	1									
Se	#DIV/0!	0,187052	0,101098	-0,18826	-0,21	-0,01657	#DIV/0!	-0,10604	-0,21671	-0,10548	#DIV/0!	0,157532	0,369591	1								
Zn	#DIV/0!	0,08761	-0,38876	-0,41266	0,410907	0,44238	#DIV/0!	-0,29629	0,24356	-0,14972	#DIV/0!	-0,56586	0,165192	-0,13844	1							
Fe	#DIV/0!	0,631085	0,33149	0,343146	0,262792	0,093062	#DIV/0!	0,202263	0,076018	-0,06228	#DIV/0!	0,751882	-0,10742	-0,19201	-0,38416	1						
Sb	#DIV/0!	-0,14206	-0,19449	-0,22619	0,010757	-0,11695	#DIV/0!	-0,25515	0,062531	-0,10852	#DIV/0!	-0,17332	0,411931	-0,18242	0,086588	-0,09287	1					
Mn	#DIV/0!	-0,20752	-0,2441	-0,04292	0,007738	-0,14021	#DIV/0!	-0,30589	0,16918	-0,1301	#DIV/0!	-0,1813	0,346239	-0,00182	0,019356	-0,22742	0,856938	1				
Co	#DIV/0!	0,388346	0,248899	0,288773	0,250434	0,073093	#DIV/0!	0,323204	0,313507	-0,06916	#DIV/0!	0,631438	-0,14348	-0,23965	-0,42805	0,907878	-0,07708	-0,2037	1			
W	#DIV/0!	-0,11447	-0,03583	0,124367	-0,16148	-0,14008	#DIV/0!	0,017683	-0,34453	-0,12998	#DIV/0!	0,273858	-0,0139	-0,1744	-0,32285	0,027704	-0,12514	-0,15003	0,098348	1		
Te	#DIV/0!	0,273772	0,010026	0,609078	0,133865	0,20588	#DIV/0!	-0,06015	-0,14131	0,119352	#DIV/0!	0,311364	0,259117	-0,06436	-0,10093	0,182151	-0,19194	-0,0105	-0,03188	0,24358	1	
Cu	#DIV/0!	-0,56969	-0,28099	-0,3018	-0,28446	-0,07818	#DIV/0!	-0,18525	-0,23614	0,104583	#DIV/0!	-0,61358	0,231169	0,290147	0,306931	-0,96856	0,09111	0,236013	-0,9466	-0,00398	-0,0249	1

SAMPLE 03-06(2)

	Bi	Ga	Pb	Au	Ag	Ge	Cd	Mo	In	As	Sn	S	Ni	Se	Zn	Fe	Sb	Mn	Co	W	Te	Cu
Bi	1																					
Ga	#DIV/0!	1																				
Pb	#DIV/0!	-0,1269	1																			
Au	#DIV/0!	-0,11873	0,496642	1																		
Ag	#DIV/0!	0,063323	0,480607	0,496553	1																	
Ge	#DIV/0!	-0,07533	0,030133	0,042194	-0,17111	1																
Cd	#DIV/0!	-0,17712	0,542611	0,196975	0,316065	-0,16811	1															
Mo	#DIV/0!	-0,20169	-0,02062	-0,23072	-0,27733	-0,31916	-0,08781	1														
In	#DIV/0!	-0,10444	0,314132	0,065886	0,45207	-0,2318	0,066705	-0,00039	1													
As	#DIV/0!	-0,13618	0,15447	0,122166	-0,07563	0,404098	-0,08404	-0,02213	-0,1959	1												
Sn	#DIV/0!	-0,13446	0,119407	-0,04767	0,008637	-0,17416	0,821622	-0,11741	-0,1119	-0,03631	1											
S	#DIV/0!	0,124725	-0,46976	-0,00945	-0,23614	0,217238	-0,84586	0,05121	-0,14068	0,161577	-0,62993	1										
Ni	#DIV/0!	0,439068	-0,25603	-0,36871	-0,13849	-0,03448	-0,40188	0,040109	0,047657	-0,07996	-0,3051	0,223961	1									
Se	#DIV/0!	0,212903	-0,28148	-0,2126	-0,12129	-0,16731	-0,43475	0,074244	0,12789	-0,25855	-0,33005	0,248336	0,319003	1								
Zn	#DIV/0!	-0,19263	0,497967	0,136564	0,294078	-0,05299	0,92438	-0,1752	0,045303	-0,06123	0,709056	-0,91397	-0,43131	-0,47299	1							
Fe	#DIV/0!	0,177796	-0,50163	-0,13374	-0,29418	0,059271	-0,92207	0,172083	-0,04587	0,065915	-0,70305	0,919124	0,420552	0,470161	-0,99968	1						
Sb	#DIV/0!	-0,17694	0,545005	0,303385	0,297094	0,368322	0,32803	-0,03069	0,215303	-0,16716	0,090218	-0,21945	-0,26525	-0,28508	0,287388	-0,28347	1					
Mn	#DIV/0!	0,039361	-0,13247	-0,01633	-0,29544	-0,04314	0,029366	0,194666	-0,14123	-0,21043	0,033378	-0,13738	-0,00734	0,295722	0,090234	-0,09237	-0,20743	1				
Co	#DIV/0!	0,37151	0,337615	-0,03504	0,185591	0,092388	0,506323	-0,34037	-0,00319	0,027117	0,393323	-0,5492	0,212648	-0,22058	0,561542	-0,57048	0,187957	0,077914	1			
W	#DIV/0!	-0,08605	-0,0036	-0,11392	-0,25221	0,042443	-0,26699	0,06541	0,265238	-0,17841	-0,20269	0,256903	-0,04679	0,063887	-0,28893	0,291853	0,152354	-0,09949	-0,25532	1		
Te	#DIV/0!	0,040376	0,026956	-0,36584	-0,19229	0,137338	0,161304	0,16826	-0,21404	0,123937	0,311175	-0,24011	0,108633	0,000519	0,252122	-0,25483	-0,07423	0,385301	0,211261	-0,13338	1	
Cu	#DIV/0!	0,185088	-0,4991	-0,13057	-0,29428	0,033683	-0,92044	0,182009	-0,05147	0,069737	-0,70519	0,921229	0,408222	0,470626	-0,99848	0,998378	-0,31616	-0,09203	-0,57794	0,294635	-0,25608	1

SAMPLE 03-08

	Bi	Ga	Pb	Au	Ag	Ge	Cd	Mo	In	As	Sn	S	Ni	Se	Zn	Fe	Sb	Mn	Co	W	Te	Cu
Bi	1																					
Ga	-0,0483	1																				
Pb	-0,11345	-0,02382	1																			
Au	0,110308	-0,07202	-0,08964	1																		
Ag	0,033366	-0,04428	-0,18261	0,740221	1																	
Ge	0,114049	0,288274	-0,0704	-0,04912	-0,08469	1																
Cd	0,108513	-0,1121	-0,13425	0,67025	0,585725	-0,12976	1															
Mo	0,09418	0,141142	0,09465	-0,17078	-0,14435	-0,01042	-0,0644	1														
In	0,205778	0,257369	-0,15773	-0,06753	-0,11084	0,07092	0,060989	0,003714	1													
As	0,132527	-0,15027	0,008928	-0,04743	-0,13769	-0,09727	-0,12575	0,082961	0,038346	1												
Sn	-0,01442	-0,04692	0,017736	0,532485	0,353738	0,06767	0,562119	-0,00393	0,140961	-0,1053	1											
S	-0,28115	-0,05627	0,233022	-0,21716	-0,19513	-0,08954	-0,2841	0,220587	-0,42526	0,098352	-0,03866	1										
Ni	-0,0484	-0,07293	0,174563	-0,02035	-0,08906	0,238781	-0,0524	0,151704	-0,06748	-0,04187	0,450802	0,089731	1									
Se	-0,18519	0,022134	0,263702	-0,27174	-0,21261	-0,15282	-0,36927	0,063233	-0,28718	0,129067	-0,36166	0,685044	-0,20653	1								
Zn	0,301345	0,010197	-0,01254	-0,12072	0,019228	0,076652	-0,01322	-0,07045	0,039385	-0,03173	0,096721	-0,2097	-0,12381	-0,11818	1							
Fe	-0,31129	0,129074	0,255765	-0,16738	-0,22276	-0,14446	-0,40598	0,13415	-0,3304	0,131863	-0,34396	0,700758	-0,15336	0,759515	-0,33339	1						
Sb	-0,09813	-0,0182	-0,14537	-0,0707	-0,04712	-0,01184	0,159943	-0,14497	0,327647	-0,08606	0,222948	-0,34472	-0,07223	-0,42414	0,157775	-0,41795	1					
Mn	0,114143	-0,20826	0,190335	-0,08796	-0,09942	0,057225	-0,11158	0,068432	-0,18155	-0,19809	0,193366	-0,02883	0,538775	-0,21064	-0,05475	-0,13537	-0,08906	1				
Co	-0,05219	-0,07343	0,17952	-0,02226	-0,09099	0,236725	-0,05641	0,160243	-0,07434	-0,03573	0,446766	0,098367	0,999723	-0,19997	-0,12862	-0,1439	-0,07544	0,535941	1			
W	0,179706	-0,17944	-0,02901	-0,06221	-0,11059	-0,1241	-0,16669	0,16789	0,139365	0,093884	-0,13747	0,113104	-0,06023	0,12006	0,025778	0,146218	-0,1197	-0,14509	-0,05589	1		
Te	-0,02022	0,202928	0,062662	0,413254	0,30017	-0,04051	0,335159	-0,11253	0,005051	-0,0371	0,4212	0,073323	-0,02171	0,034887	-0,02118	0,023726	0,021945	-0,17705	-0,02053	0,263983	1	
Cu	0,31961	-0,07828	-0,29537	-0,04294	0,10905	0,053473	0,251726	-0,16415	0,338539	-0,09183	-0,06507	-0,69469	-0,34999	-0,5572	0,431485	-0,83245	0,411735	-0,10548	-0,35813	-0,08455	-0,12443	1

SAMPLE 05-01(1)

	Bi	Ga	Pb	Au	Ag	Ge	Cd	Mo	In	As	Sn	S	Ni	Se	Zn	Fe	Sb	Mn	Co	W	Te	Cu
Bi	1																					
Ga	-0,08892	1																				
Pb	0,10485	0,027114	1																			
Au	0,326633	-0,20502	-0,24963	1																		
Ag	0,283971	-0,0557	-0,19354	-0,02304	1																	
Ge	-0,105	0,074165	-0,03679	-0,18627	0,707831	1																
Cd	#DIV/0!	#DIV/0!	#DIV/0!	#DIV/0!	#DIV/0!	#DIV/0!	1															
Mo	-0,21019	-0,19644	-0,06669	0,140938	-0,20196	0,044284	#DIV/0!	1														
In	-0,13163	-0,11811	-0,04797	0,369366	-0,3012	-0,13919	#DIV/0!	-0,07556	1													
As	-0,17292	-0,18432	0,419879	-0,08617	-0,12828	0,038981	#DIV/0!	0,194529	0,030662	1												
Sn	#DIV/0!	#DIV/0!	#DIV/0!	#DIV/0!	#DIV/0!	#DIV/0!	#DIV/0!	#DIV/0!	#DIV/0!	#DIV/0!	1											
S	-0,19127	0,103674	0,305777	0,01104	-0,31948	-0,00537	#DIV/0!	-0,0173	-0,04064	0,373227	#DIV/0!	1										
Ni	-0,1949	-0,11342	-0,21612	-0,24941	0,357242	0,443316	#DIV/0!	0,105542	0,126072	-0,22881	#DIV/0!	-0,43374	1									
Se	-0,1188	0,444071	-0,26764	-0,26517	0,272803	0,393431	#DIV/0!	-0,1201	-0,20246	-0,19905	#DIV/0!	-0,21016	0,149742	1								
Zn	0,11025	0,493978	0,270059	-0,10141	0,074569	0,431477	#DIV/0!	-0,13379	0,019977	-0,21356	#DIV/0!	0,331233	0,084811	0,191367	1							
Fe	-0,26996	0,207663	0,265108	-0,02767	-0,33218	-0,04513	#DIV/0!	-0,01399	-0,09628	0,422685	#DIV/0!	0,947351	-0,41166	-0,1734	0,281904	1						
Sb	-0,03861	-0,11534	0,152161	-0,19203	-0,23696	-0,13619	#DIV/0!	0,249723	-0,1491	-0,2127	#DIV/0!	-0,31336	0,161186	-0,15409	0,106556	-0,19937	1					
Mn	-0,17145	0,124861	-0,09875	0,212295	-0,25728	0,002221	#DIV/0!	0,257569	0,640176	-0,19882	#DIV/0!	-0,02674	0,316787	-0,20429	0,238742	-0,08516	0,053949	1				
Co	-0,23807	0,148438	0,398088	-0,13593	-0,38213	-0,1052	#DIV/0!	-0,08655	-0,13988	0,432929	#DIV/0!	0,858139	-0,39975	-0,24388	0,341363	0,90174	-0,05528	-0,12734	1			
W	0,131089	-0,1794	0,191716	0,301715	-0,33273	-0,27083	#DIV/0!	0,120677	0,016339	-0,19029	#DIV/0!	0,353391	-0,45532	-0,13867	0,288406	0,278499	0,339803	0,011587	0,344386	1		
Te	-0,14255	-0,02237	-0,15456	0,035333	0,44797	0,638615	#DIV/0!	0,37284	-0,08635	0,244234	#DIV/0!	0,188926	0,135313	0,212983	0,169155	0,216304	-0,18489	-0,14429	0,065636	0,024446	1	
Cu	0,205379	-0,21161	-0,27336	0,013724	0,400535	0,106587	#DIV/0!	0,027637	0,102523	-0,40048	#DIV/0!	-0,93164	0,446881	0,165929	-0,33078	-0,9797	0,130033	0,110417	-0,94289	-0,35162	-0,15165	1

SAMPLE 05-03

	Bi	Ga	Pb	Au	Ag	Ge	Cd	Mo	In	As	Sn	S	Ni	Se	Zn	Fe	Sb	Mn	Co	W	Te	Cu
Bi	1																					
Ga	#DIV/0!	1																				
Pb	#DIV/0!	-0,23224	1																			
Au	#DIV/0!	0,337089	-0,01114	1																		
Ag	#DIV/0!	-0,13954	-0,16845	-0,18086	1																	
Ge	#DIV/0!	#DIV/0!	#DIV/0!	#DIV/0!	#DIV/0!	1																
Cd	#DIV/0!	#DIV/0!	#DIV/0!	#DIV/0!	#DIV/0!	#DIV/0!	1															
Mo	#DIV/0!	-0,1553	-0,21854	0,442257	-0,01117	#DIV/0!	#DIV/0!	1														
In	#DIV/0!	0,686612	-0,08706	0,587015	0,120415	#DIV/0!	#DIV/0!	0,234981	1													
As	#DIV/0!	#DIV/0!	#DIV/0!	#DIV/0!	#DIV/0!	#DIV/0!	#DIV/0!	#DIV/0!	#DIV/0!	1												
Sn	#DIV/0!	-0,14702	0,073412	-0,02884	-0,19235	#DIV/0!	#DIV/0!	-0,27542	-0,14671	#DIV/0!	1											
S	#DIV/0!	0,26405	-0,25851	0,255044	0,203454	#DIV/0!	#DIV/0!	0,255295	0,272226	#DIV/0!	-0,48649	1										
Ni	#DIV/0!	-0,22275	-0,2306	-0,25407	0,40092	#DIV/0!	#DIV/0!	-0,16903	-0,09425	#DIV/0!	-0,18256	-0,26421	1									
Se	#DIV/0!	-0,02345	-0,04284	0,01653	0,421369	#DIV/0!	#DIV/0!	0,058	0,24443	#DIV/0!	-0,09685	0,234581	0,152423	1								
Zn	#DIV/0!	-0,19103	0,133158	-0,25924	-0,12002	#DIV/0!	#DIV/0!	-0,19258	-0,22917	#DIV/0!	-0,07233	-0,81401	0,481822	-0,17755	1							
Fe	#DIV/0!	0,192178	-0,1876	0,175833	-0,08771	#DIV/0!	#DIV/0!	0,388866	0,219289	#DIV/0!	-0,88629	0,590838	0,081024	0,164819	-0,08098	1						
Sb	#DIV/0!	-0,17635	0,661785	-0,30167	-0,25081	#DIV/0!	#DIV/0!	-0,34033	-0,18263	#DIV/0!	0,047776	0,091214	-0,23142	-0,11916	-0,16875	-0,01417	1					
Mn	#DIV/0!	-0,20597	0,43266	0,183277	-0,07774	#DIV/0!	#DIV/0!	0,203007	-0,16278	#DIV/0!	-0,16535	0,226123	-0,20529	-0,32395	-0,19484	0,143552	0,49387	1				
Co	#DIV/0!	0,311001	-0,21873	0,285894	-0,01116	#DIV/0!	#DIV/0!	0,349356	0,312315	#DIV/0!	-0,66258	0,911868	-0,22478	0,274404	-0,60159	0,831371	0,074397	0,142731	1			
W	#DIV/0!	-0,05647	0,094898	-0,15524	0,171362	#DIV/0!	#DIV/0!	0,02262	0,109874	#DIV/0!	-0,18286	0,336258	0,016017	0,749953	-0,25	0,324404	0,342774	-0,01571	0,408459	1		
Te	#DIV/0!	0,134167	0,058501	0,01416	-0,02407	#DIV/0!	#DIV/0!	-0,18514	0,168271	#DIV/0!	-0,16646	0,148881	0,548024	0,070577	-0,03678	0,249504	0,359056	0,060594	0,219396	0,287938	1	
Cu	#DIV/0!	-0,12688	0,018488	-0,09293	0,122593	#DIV/0!	#DIV/0!	-0,3586	-0,14001	#DIV/0!	0,898728	-0,28844	-0,16648	-0,11878	-0,2368	-0,92499	0,044173	-0,09208	-0,6053	-0,25993	-0,21328	1

SAMPLE 05-04(2)

	Bi	Ga	Pb	Au	Ag	Ge	Cd	Mo	In	As	Sn	S	Ni	Se	Zn	Fe	Sb	Mn	Co	W	Te	Cu
Bi	1																					
Ga	#DIV/0!	1																				
Pb	#DIV/0!	0,196062	1																			
Au	#DIV/0!	0,527959	0,468138	1																		
Ag	#DIV/0!	-0,31129	-0,20918	0,097323	1																	
Ge	#DIV/0!	0,461105	0,169006	0,534371	0,049271	1																
Cd	#DIV/0!	-0,12604	-0,25403	-0,16676	-0,0933	-0,15959	1															
Mo	#DIV/0!	0,207238	-0,00299	0,055537	-0,33219	-0,24438	-0,31784	1														
In	#DIV/0!	0,085665	-0,10808	0,043711	-0,26861	0,029156	0,937077	-0,30396	1													
As	#DIV/0!	-0,17174	0,083434	0,312319	-0,09894	-0,06818	-0,15279	0,178904	-0,14819	1												
Sn	#DIV/0!	#DIV/0!	#DIV/0!	#DIV/0!	#DIV/0!	#DIV/0!	#DIV/0!	#DIV/0!	#DIV/0!	#DIV/0!	1											
S	#DIV/0!	-0,4572	-0,518	-0,40837	0,085299	-0,33155	-0,21378	0,285048	-0,32636	0,300857	#DIV/0!	1										
Ni	#DIV/0!	-0,19032	-0,04132	0,279768	0,251833	-0,0994	-0,23048	-0,09494	-0,20993	0,152254	#DIV/0!	0,339968	1									
Se	#DIV/0!	0,07374	-0,04702	0,543089	0,031608	0,29636	-0,39562	0,287171	-0,31965	0,498566	#DIV/0!	0,226336	0,654674	1								
Zn	#DIV/0!	-0,24593	-0,41033	-0,32925	-0,43574	0,004758	0,363459	0,041848	0,364029	0,433521	#DIV/0!	0,401329	-0,37087	-0,06307	1							
Fe	#DIV/0!	-0,03341	-0,27245	0,000217	-0,05001	0,075904	-0,57357	0,485451	-0,55798	0,282925	#DIV/0!	0,787654	0,398157	0,575528	0,182664	1						
Sb	#DIV/0!	-0,2131	-0,35138	-0,26258	0,603762	-0,24775	0,121793	-0,33462	-0,04858	-0,18819	#DIV/0!	-0,21138	-0,28767	-0,42814	-0,1715	-0,49825	1					
Mn	#DIV/0!	-0,04406	0,14962	-0,25438	-0,2289	-0,24001	-0,18366	0,099736	-0,17813	-0,18231	#DIV/0!	0,120795	-0,2704	-0,38575	0,083279	0,183628	-0,06428	1				
Co	#DIV/0!	-0,15835	-0,29658	-0,15134	-0,16745	-0,10013	-0,46332	0,576704	-0,45424	0,038956	#DIV/0!	0,695822	0,401458	0,507047	0,121749	0,884476	-0,47642	0,275634	1			
W	#DIV/0!	0,052341	-0,03954	0,074972	0,06236	0,823729	0,124417	-0,3247	0,18082	-0,14232	#DIV/0!	-0,11468	-0,28401	0,037765	0,310362	0,030118	-0,19531	-0,2073	-0,08763	1		
Te	#DIV/0!	0,447634	-0,29979	-0,17181	-0,26906	-0,19395	0,059125	0,289115	0,063088	0,108548	#DIV/0!	0,351799	-0,20848	-0,22193	0,267473	0,24823	-0,10676	0,041958	0,018407	-0,21613	1	
Cu	#DIV/0!	0,032748	0,268035	-0,02301	0,054125	-0,10335	0,564902	-0,48501	0,539337	-0,27801	#DIV/0!	-0,77217	-0,38699	-0,5826	-0,19688	-0,99791	0,50313	-0,20233	-0,89305	-0,05381	-0,21455	1

SAMPLE 05-05(2)

	Bi	Ga	Pb	Au	Ag	Ge	Cd	Mo	In	As	Sn	S	Ni	Se	Zn	Fe	Sb	Mn	Co	W	Te	Cu
Bi	1																					
Ga	#DIV/0!	1																				
Pb	#DIV/0!	0,151769	1																			
Au	#DIV/0!	-0,22853	0,26286	1																		
Ag	#DIV/0!	0,490273	0,311267	0,215165	1																	
Ge	#DIV/0!	-0,06019	0,106853	0,231733	0,032385	1																
Cd	#DIV/0!	-0,07224	0,165968	0,661893	0,116702	-0,09468	1															
Mo	#DIV/0!	0,579366	0,266212	-0,15503	0,218135	0,068006	-0,10001	1														
In	#DIV/0!	-0,00511	0,040013	0,245646	-0,06492	-0,22841	0,529292	-0,08826	1													
As	#DIV/0!	0,078907	-0,44262	-0,23261	-0,24356	0,080124	-0,15072	-0,04091	0,029944	1												
Sn	#DIV/0!	#DIV/0!	#DIV/0!	#DIV/0!	#DIV/0!	#DIV/0!	#DIV/0!	#DIV/0!	#DIV/0!	#DIV/0!	1											
S	#DIV/0!	0,091402	0,089894	-0,17823	0,225277	0,226812	-0,32831	0,084943	-0,65988	-0,22535	#DIV/0!	1										
Ni	#DIV/0!	0,067015	-0,07493	0,051367	0,493529	0,333266	-0,1429	-0,18825	-0,37814	-0,2363	#DIV/0!	0,605855	1									
Se	#DIV/0!	0,015948	-0,15064	-0,07752	0,254901	-0,08374	-0,04132	-0,07872	-0,26231	-0,24412	#DIV/0!	0,519658	0,752311	1								
Zn	#DIV/0!	0,104983	-0,03188	0,026363	0,170567	-0,42299	0,140085	-0,35508	0,07847	-0,00956	#DIV/0!	-0,31693	-0,09922	-0,11712	1							
Fe	#DIV/0!	0,132453	0,100362	-0,17825	0,274387	0,226639	-0,3006	0,147997	-0,63601	-0,25742	#DIV/0!	0,984941	0,628845	0,588656	-0,33035	1						
Sb	#DIV/0!	0,25135	-0,24919	-0,19595	0,208269	-0,05569	-0,10426	-0,21881	-0,22365	-0,10527	#DIV/0!	0,110537	0,419555	0,373417	0,096793	0,108774	1					
Mn	#DIV/0!	0,284545	0,067541	-0,27962	-0,1432	-0,20441	-0,20911	0,289807	0,041933	0,060428	#DIV/0!	0,157573	-0,25747	-0,16223	-0,03536	0,124173	0,072653	1				
Co	#DIV/0!	-0,07127	-0,16157	-0,08465	-0,0651	0,223757	-0,16435	-0,18344	-0,37744	0,210908	#DIV/0!	0,625716	0,321594	0,112252	-0,20812	0,571297	-0,07391	0,003862	1			
W	#DIV/0!	-0,24985	-0,11979	0,297547	-0,22738	-0,07	0,534254	-0,13993	0,093669	-0,19413	#DIV/0!	0,028754	-0,04229	-0,00087	-0,13335	0,005196	-0,2573	-0,35744	0,311695	1		
Te	#DIV/0!	0,364857	0,094297	0,082162	-0,10795	0,294033	-0,08835	0,341104	-0,10506	0,275555	#DIV/0!	-0,17096	-0,20763	-0,28373	-0,15858	-0,20957	0,12942	0,077489	-0,24994	-0,18594	1	
Cu	#DIV/0!	-0,10782	-0,13733	0,097322	-0,29188	-0,23851	0,214443	-0,11136	0,626083	0,287877	#DIV/0!	-0,98259	-0,63486	-0,57711	0,318535	-0,99209	-0,10884	-0,07433	-0,59151	-0,07079	0,199907	1

APPENDIX V.II: Correlation Coefficient matrixes for the combined Sph-style samples, as well as each individual sample.

ALL SPH-STYLE SAMPLES

	Bi	Ga	Pb	Au	Ag	Ge	Cd	Mo	In	As	Sn	S	Ni	Se	Zn	Fe	Sb	Mn	Co	W	Te	Cu
Bi	1																					
Ga	-0,04419	1																				
Pb	-0,03236	-0,02932	1																			
Au	-0,07511	0,166779	-0,08085	1																		
Ag	-0,03334	-0,02866	-0,02278	-0,08001	1																	
Ge	-0,01806	-0,0696	0,261304	0,075378	-0,06648	1																
Cd	-0,09584	-0,21437	-0,16153	-0,05077	-0,15994	-0,06735	1															
Mo	0,005153	-0,10983	-0,15293	0,089512	-0,15421	-0,10002	0,030531	1														
In	0,195696	-0,08773	-0,06305	-0,20997	0,289834	0,033392	-0,14316	-0,07269	1													
As	0,018488	-0,06551	-0,07569	-0,08196	-0,05838	0,059588	0,118058	0,151604	0,114758	1												
Sn	-0,09109	0,25587	-0,09788	-0,11105	-0,09792	0,090323	0,123959	-0,07982	-0,09821	-0,09503	1											
S	-0,49631	0,1237	-0,45567	0,160903	-0,33163	-0,13891	0,064583	0,016071	-0,12504	0,023393	0,129441	1										
Ni	-0,08784	0,294599	-0,06355	0,222473	-0,02548	0,006032	0,030719	0,005439	-0,07173	-0,05517	0,103019	0,018229	1									
Se	-0,11716	-0,06055	-0,08212	0,076416	0,086898	-0,08012	0,018921	-0,00028	0,139623	0,006961	-0,0597	0,040823	-0,11547	1								
Zn	-0,18026	-0,32144	-0,15159	0,068123	-0,21835	-0,06054	0,616748	0,294778	-0,00079	0,170497	-0,23727	0,034318	-0,0793	0,02567	1							
Fe	-0,19697	0,354885	-0,13641	0,047675	-0,07387	-0,00986	-0,41444	-0,21294	-0,13332	-0,14942	0,367667	0,526754	0,124831	0,029079	-0,79303	1						
Sb	0,132154	-0,14381	-0,02237	0,055285	-0,10739	0,041819	0,381899	-0,11334	-0,02118	-0,05948	0,128342	-0,11158	-0,0849	-0,08831	0,281024	-0,28647	1					
Mn	-0,04738	-0,12498	-0,0983	0,081798	-0,0831	0,000328	0,246252	0,10925	-0,14982	0,008189	-0,01566	0,01047	0,079849	0,075228	0,307002	-0,21996	0,132193	1				
Co	-0,14902	0,209431	-0,10459	0,11296	-0,07983	-0,071	-0,37236	-0,18419	-0,08337	-0,13644	0,170275	0,579666	0,062075	0,075259	-0,65974	0,859368	-0,19765	-0,1896	1			
W	0,075734	0,114552	0,072918	0,011771	0,270089	-0,07591	-0,34548	-0,14197	-0,08716	-0,07515	-0,0253	-0,12216	0,055839	0,013208	-0,42537	0,252347	-0,14498	-0,05494	0,160963	1		
Te	-0,08281	-0,10024	0,090618	-0,08095	-0,07733	0,166998	0,036929	0,028415	-0,00421	0,094718	-0,08962	-0,00815	-0,22974	0,0263	0,084828	-0,05321	0,05183	0,088029	-0,10765	-0,16774	1	
Cu	-0,13783	0,380872	-0,09259	-0,01595	0,06421	0,045729	-0,46391	-0,15267	-0,10974	-0,13216	0,379588	0,146252	0,138276	-0,04037	-0,74401	0,785181	-0,24435	-0,22689	0,463868	0,372661	-0,02413	1

SAMPLE 03-03

	Bi	Ga	Pb	Au	Ag	Ge	Cd	Mo	In	As	Sn	S	Ni	Se	Zn	Fe	Sb	Mn	Co	W	Te	Cu
Bi	1																					
Ga	-0,04138	1																				
Pb	-0,05928	-0,0371	1																			
Au	0,002675	0,047625	-0,12249	1																		
Ag	-0,05842	-0,03907	-0,05605	-0,12119	1																	
Ge	-0,10359	-0,07246	0,472321	0,032607	-0,10428	1																
Cd	-0,11972	-0,16533	-0,23641	-0,13575	-0,23682	-0,33574	1															
Mo	-0,01107	0,014674	-0,24706	0,434504	-0,24592	-0,21558	0,027181	1														
In	0,356396	-0,07207	-0,10367	-0,17628	0,350588	-0,08087	-0,18751	-0,23271	1													
As	0,32247	-0,09568	-0,13667	-0,077	-0,10321	-0,12229	0,113969	-0,09801	0,185885	1												
Sn	0,014229	0,59797	-0,10642	-0,11197	-0,11142	0,073137	0,021034	-0,04151	-0,00395	0,048948	1											
S	-0,17606	0,094243	-0,69908	0,20708	-0,49099	-0,32725	0,299236	0,400073	-0,18357	0,086749	0,155727	1										
Ni	-0,03742	-0,09407	-0,10777	0,033232	-0,04856	-0,05143	0,007578	0,083986	-0,06051	0,062014	0,047529	0,037925	1									
Se	-0,17448	0,325785	-0,1637	0,109473	0,046694	-0,18725	0,146039	0,126013	0,155421	0,174593	0,209363	0,097364	-0,1718	1								
Zn	0,01328	-0,22643	-0,24064	0,033823	-0,34262	-0,4345	0,651305	0,252375	-0,10484	0,071541	-0,16839	0,30438	-0,15867	0,160951	1							
Fe	-0,18571	0,316119	-0,1764	0,099984	-0,07872	0,222518	-0,39323	0,036608	-0,07519	-0,02699	0,322885	0,384739	0,203748	-0,05395	-0,75153	1						
Sb	0,181854	-0,12327	-0,00186	0,116704	-0,17667	0,090104	0,541208	-0,22352	0,013263	0,229841	-0,01758	0,066764	-0,14933	-0,02307	0,274554	-0,21977	1					
Mn	0,081529	-0,0748	-0,17502	0,297376	-0,14834	-0,15536	0,215871	0,20062	-0,24287	-0,11456	-0,24356	0,105969	-0,00928	0,206083	0,365511	-0,27073	0,011129	1				
Co	-0,14012	0,345234	-0,15828	0,073553	-0,12014	0,166231	-0,41666	0,053412	-0,04771	0,006991	0,398328	0,371874	0,212821	0,021207	-0,72567	0,977861	-0,25609	-0,24668	1			
W	-0,10792	0,008981	0,114514	0,029655	0,437014	-0,03078	-0,31567	-0,04768	-0,10461	0,00741	-0,12793	-0,34063	0,256	0,078029	-0,42125	0,170584	-0,2409	0,001438	0,194648	1		
Te	-0,05633	-0,08895	0,093213	-0,11356	-0,12781	0,317834	-0,04049	-0,08594	0,000291	0,144042	-0,13687	0,040585	-0,22787	-0,12177	0,055774	-0,04026	0,187791	-0,10651	-0,09789	-0,21458	1	
Cu	-0,15572	0,165271	-0,1483	0,141236	0,103761	0,325428	-0,5307	-0,01733	-0,01734	-0,05022	0,14944	0,24738	0,149832	-0,17716	-0,82425	0,943025	-0,24984	-0,30915	0,887256	0,249801	0,027264	1

SAMPLE 04-02(2)

	Bi	Ga	Pb	Au	Ag	Ge	Cd	Mo	In	As	Sn	S	Ni	Se	Zn	Fe	Sb	Mn	Co	W	Te	Cu
Bi	1																					
Ga	#DIV/0!	1																				
Pb	0,126981	#DIV/0!	1																			
Au	-0,15896	#DIV/0!	-0,20614	1																		
Ag	-0,01243	#DIV/0!	0,143813	-0,04091	1																	
Ge	-0,09602	#DIV/0!	0,486492	0,095236	-0,0858	1																
Cd	0,096441	#DIV/0!	0,095865	-0,02904	-0,11448	0,337047	1															
Mo	-0,00888	#DIV/0!	0,093478	-0,13053	-0,01357	0,193053	-0,15192	1														
In	0,184768	#DIV/0!	0,388055	-0,35267	-0,19058	0,316095	0,4778	-0,09669	1													
As	-0,07799	#DIV/0!	-0,01585	-0,10956	-0,15609	0,191383	0,389598	-0,06043	0,742106	1												
Sn	-0,16776	#DIV/0!	0,273322	-0,26696	-0,0147	0,56559	0,148477	-0,1356	0,402233	0,114115	1											
S	-0,12261	#DIV/0!	-0,31076	0,150945	-0,42342	-0,15799	-0,20988	-0,35774	-0,2063	-0,22698	0,067303	1										
Ni	-0,15869	#DIV/0!	0,033885	0,171394	-0,12053	0,367308	0,291862	0,240481	0,31128	0,263767	0,179983	-0,05678	1									
Se	0,441294	#DIV/0!	-0,10994	-0,14522	-0,02132	-0,16628	0,076406	0,154061	0,095683	0,050642	-0,28257	-0,16162	0,129599	1								
Zn	0,043658	#DIV/0!	0,007322	0,283874	-0,07192	0,1041	0,424193	0,371672	0,077833	0,148753	-0,39972	-0,53239	0,278881	0,199448	1							
Fe	-0,015	#DIV/0!	-0,03812	-0,22201	0,000826	-0,0844	-0,35053	-0,41704	-0,06133	-0,15269	0,454071	0,58145	-0,25138	-0,2283	-0,9833	1						
Sb	0,322458	#DIV/0!	0,316186	-0,09749	0,279294	0,333781	0,113143	-0,23991	0,19028	-0,08036	0,283407	-0,13579	-0,16925	-0,01592	0,119576	-0,12062	1					
Mn	0,006535	#DIV/0!	0,037993	-0,27754	-0,28503	0,072667	0,184154	-0,04449	0,548859	0,538284	0,141531	-0,12341	0,107508	0,01509	0,205146	-0,19237	0,080772	1				
Co	0,00762	#DIV/0!	-0,16218	-0,1077	0,077609	-0,12007	-0,37128	-0,3608	-0,13287	-0,17956	0,443786	0,536016	-0,20039	-0,27231	-0,74572	0,811253	0,016784	-0,14562	1			
W	-0,07235	#DIV/0!	0,077634	0,045059	-0,09401	-0,04308	-0,48934	-0,21323	-0,1663	0,041656	-0,08272	0,158347	-0,246	-0,13902	-0,46929	0,384707	-0,14349	-0,07771	0,063169	1		
Te	0,183147	#DIV/0!	-0,19169	-0,02888	-0,20294	-0,26743	0,075105	0,223159	0,069242	0,020818	-0,17868	0,109286	-0,35015	-0,00344	0,114176	-0,09131	-0,20121	0,289918	-0,13834	-0,21389	1	
Cu	-0,0763	#DIV/0!	0,005142	-0,31075	0,163784	-0,1581	-0,50238	-0,32109	-0,13581	-0,12779	0,22531	0,488734	-0,31466	-0,14933	-0,95352	0,891046	-0,0938	-0,22265	0,613006	0,581266	-0,17761	1

SAMPLE 05-04(1)

	Bi	Ga	Pb	Au	Ag	Ge	Cd	Mo	In	As	Sn	S	Ni	Se	Zn	Fe	Sb	Mn	Co	W	Te	Cu
Bi	1																					
Ga	-0,08927	1																				
Pb	0,019655	-0,20025	1																			
Au	-0,12647	0,360101	0,064999	1																		
Ag	-0,18822	-0,18812	0,229316	-0,06977	1																	
Ge	-0,00788	-0,13972	0,175424	0,161297	-0,04814	1																
Cd	-0,02137	-0,30065	0,02699	-0,07767	0,590328	0,162859	1															
Mo	0,01597	-0,19911	0,326362	-0,18466	0,197705	-0,12126	0,170332	1														
In	0,06117	-0,17698	0,393961	-0,23003	-0,07503	0,096474	-0,16092	0,159529	1													
As	-0,1727	-0,14862	0,22725	-0,03286	0,34497	0,094474	0,258508	0,428738	-0,0842	1												
Sn	-0,16339	0,381704	-0,39667	-0,03528	-0,12907	-0,07121	0,092518	-0,11606	-0,34086	-0,25479	1											
S	-0,70471	0,106995	-0,22305	0,190288	-0,05523	-0,06853	-0,11767	-0,27856	-0,04492	-0,02281	0,038492	1										
Ni	-0,11697	0,548896	-0,03784	0,492485	-0,1623	-0,01418	-0,18613	-0,21734	-0,18123	-0,20602	0,133375	0,03781	1									
Se	-0,14625	-0,09718	-0,26785	0,164079	-0,27346	0,094773	-0,21321	-0,30719	0,023313	-0,27102	0,197444	0,202771	-0,19963	1								
Zn	-0,27671	-0,41915	0,512812	-0,04793	0,640252	0,273766	0,578838	0,359312	0,224571	0,397472	-0,40719	-0,13285	-0,18382	-0,26539	1							
Fe	-0,29087	0,432066	-0,57749	0,161837	-0,46296	-0,2295	-0,41326	-0,41599	-0,27672	-0,3421	0,481995	0,642082	0,234653	0,390492	-0,78962	1						
Sb	0,422001	-0,21976	0,175079	0,006057	0,232263	0,016295	0,143286	0,139785	0,018272	-0,0899	-0,34654	-0,50074	-0,08604	-0,17819	0,240763	-0,50386	1					
Mn	-0,12597	-0,17562	0,020383	0,047049	-0,10928	0,176343	0,238651	0,162274	-0,29404	-0,02875	-0,07023	-0,01955	0,133573	-0,18993	0,254189	-0,12969	0,218768	1				
Co	-0,17757	0,246862	-0,42044	0,245189	-0,37459	-0,22567	-0,39371	-0,35017	-0,1354	-0,24569	0,036136	0,734149	0,012667	0,309227	-0,63082	0,809808	-0,37763	-0,17623	1			
W	0,271379	0,242239	-0,14508	-0,05489	-0,40308	-0,14182	-0,36243	-0,1899	-0,05465	-0,21466	0,125052	0,011157	0,037521	-0,02776	-0,53786	0,361116	-0,09564	-0,1241	0,208245	1		
Te	-0,14242	-0,16455	0,129434	-0,04598	0,018628	0,114983	0,234979	0,118713	-0,07172	0,056348	0,0614	-0,00968	-0,20958	0,310137	0,162094	-0,05271	0,235229	0,323301	-0,11909	-0,10484	1	
Cu	-0,18475	0,552711	-0,38475	-0,01445	-0,36149	-0,14023	-0,34555	-0,20248	-0,2871	-0,25635	0,797158	0,077859	0,356534	0,231397	-0,61881	0,643363	-0,37343	-0,11159	0,134507	0,414953	-0,06123	1

APPENDIX V.III: Correlation Coefficient matrixes for the Po-style sample.

SAMPLE 03-04 (only Po-style sample)

	Bi	*Ga*	*Pb*	*Au*	*Ag*	*Ge*	*Cd*	*Mo*	*In*	*As*	*Sn*	*S*	*Ni*	*Se*	*Zn*	*Fe*	*Sb*	*Mn*	*Co*	*W*	*Te*	*Cu*
Bi	1																					
Ga	#DIV/0!	1																				
Pb	-0,21388	#DIV/0!	1																			
Au	-0,19421	#DIV/0!	0,015171	1																		
Ag	-0,23949	#DIV/0!	-0,43785	0,216083	1																	
Ge	-0,13215	#DIV/0!	-0,06384	-0,14566	0,099833	1																
Cd	0,46637	#DIV/0!	0,063567	-0,27877	-0,34376	-0,18968	1															
Mo	-0,16102	#DIV/0!	0,259896	-0,17337	0,02568	-0,34028	0,537033	1														
In	0,915929	#DIV/0!	-0,28994	0,1366	-0,11507	-0,17914	0,39166	-0,19105	1													
As	0,974264	#DIV/0!	-0,28315	-0,26017	-0,30045	-0,17703	0,424865	-0,15436	0,878971	1												
Sn	#DIV/0!	#DIV/0!	#DIV/0!	#DIV/0!	#DIV/0!	#DIV/0!	#DIV/0!	#DIV/0!	#DIV/0!	#DIV/0!	1											
S	-0,62113	#DIV/0!	0,332554	0,288021	0,031671	0,130121	-0,71994	-0,34604	-0,63741	-0,64442	#DIV/0!	1										
Ni	-0,11888	#DIV/0!	-0,33692	0,38012	0,199312	-0,13385	0,251745	0,199165	0,038819	-0,08463	#DIV/0!	-0,16223	1									
Se	-0,09889	#DIV/0!	-0,23267	0,827515	0,307467	-0,14375	-0,14195	-0,09149	0,307406	-0,13248	#DIV/0!	-0,08398	0,420817	1								
Zn	0,508055	#DIV/0!	0,041933	-0,28894	-0,33832	-0,19473	0,998587	0,519627	0,430765	0,468855	#DIV/0!	-0,7435	0,243824	-0,14406	1							
Fe	-0,41685	#DIV/0!	0,273371	0,301737	0,058211	0,10909	-0,81595	-0,50939	-0,42696	-0,44624	#DIV/0!	0,947885	-0,3189	-0,04833	-0,82646	1						
Sb	#DIV/0!	#DIV/0!	#DIV/0!	#DIV/0!	#DIV/0!	#DIV/0!	#DIV/0!	#DIV/0!	#DIV/0!	#DIV/0!	#DIV/0!	#DIV/0!	#DIV/0!	#DIV/0!	#DIV/0!	#DIV/0!	1					
Mn	-0,20779	#DIV/0!	0,170606	-0,28105	0,050014	-0,22092	0,529289	0,51507	-0,28168	-0,27836	#DIV/0!	-0,16539	-0,07283	-0,22604	0,506158	-0,34341	#DIV/0!	1				
Co	-0,35959	#DIV/0!	-0,22387	0,036631	0,116964	0,037838	-0,72256	-0,64599	-0,38895	-0,29867	#DIV/0!	0,653956	-0,22658	-0,11178	-0,7212	0,678525	#DIV/0!	-0,11646	1			
W	-0,14268	#DIV/0!	0,061141	-0,08532	-0,14829	0,81308	-0,2048	-0,16628	-0,19341	-0,16282	#DIV/0!	0,274617	-0,28867	-0,15521	-0,21243	0,241915	#DIV/0!	-0,18896	0,080147	1		
Te	-0,16088	#DIV/0!	0,122197	0,033101	0,011375	0,421263	-0,23093	-0,57046	-0,21808	-0,21552	#DIV/0!	0,237703	-0,2647	-0,17501	-0,23915	0,253737	#DIV/0!	0,036369	0,383931	0,079876	1	
Cu	-0,16648	#DIV/0!	-0,52557	-0,0478	0,49599	0,111475	-0,31323	0,026379	-0,03271	-0,04467	#DIV/0!	-0,33343	0,140838	0,290951	-0,29703	-0,28938	#DIV/0!	-0,25644	0,082862	-0,06681	-0,06933	1

APPENDIX VI: In-situ Sulfur (S) isotopic analysis.

APPENDIX VI.I: Table with δ ^{34}S values analyzed in sulfide phases - chalcopyrite (Cpy), isocubanite (Icb) and chalcocite (Ch).

Name	Type of deposit	Mineral	$\delta^{34}S$	2s	Observations
sal0303-sph-1	Sphalerite-style	Sph-I	-0,64	0,16	Prob, Sph-I considering the value
sal0303-sph-2	Sphalerite-style	Sph-I	-0,95	0,15	
sal0303-sph-3	Sphalerite-style	Sph-II	-1,15	0,16	Could be either I or II
sal0303-sph-4	Sphalerite-style	Sph-I	-1,11	0,15	
sal0303-sph-5	Sphalerite-style	Sph-I	-1,07	0,16	
sal0303-sph-6	Sphalerite-style	Sph-I	-1,19	0,16	Could be either I or II
sal0303-sph-7	Sphalerite-style	Sph-II	-2,27	0,15	
sal0303-sph-8	Sphalerite-style	Sph-I	-1,39	0,16	
sal0402-sph-1	Sphalerite-style	Sph-I	-0,93	0,18	
sal0402-sph-2	Sphalerite-style	Sph-I	-0,69	0,16	
sal0402-sph-3	Sphalerite-style	Sph-II	-1,55	0,15	
sal0402-sph-4	Sphalerite-style	Sph-I	-0,44	0,16	
sal0303-ccp-1	Sphalerite-style	Icb	-2,77	0,65	
sal0303-ccp-2	Sphalerite-style	Icb	-2,33	0,55	
sal0303-ccp-3	Sphalerite-style	Icb	-2,00	0,53	
sal0308-bon-1	Cu-Style	Ch	2,74	0,21	
sal0308-ccp-1	Cu-Style	Cpy	2,21	0,21	Likely has supergene influence
sal0308-ccp-2	Cu-Style	Cpy	2,61	0,19	
sal0308-ccp-3	Cu-Style	Cpy	2,99	0,19	
sal0308-ccp-4	Cu-Style	Cpy	2,62	0,20	
sal0308-ccp-5	Cu-Style	Cpy	2,54	0,21	
sal0308-bon-2	Cu-Style	Ch	3,18	0,20	
sal0308-bon3	Cu-Style	Ch	3,03	0,24	
sal0308-ccp-6	Cu-Style	Cpy	3,64	0,20	Likely has supergene influence
sal0308-ccp-7	Cu-Style	Cpy	3,15	0,19	Could have supergene influence
sal0308-ccp-8	Cu-Style	Cpy	2,93	0,21	Could have supergene influence
sal0308-ccp-9	Cu-Style	Cpy	2,33	0,19	
sal0308-ccp-10	Cu-Style	Cpy	2,44	0,20	
sal0308-ccp-11	Cu-Style	Cpy	2,93	0,19	near hole
sal0308-ccp-12	Cu-Style	Cpy	2,24	0,19	
sal0308-ccp-13	Cu-Style	Cpy	2,63	0,19	
sal0308-ccp-14	Cu-Style	Cpy	3,03	0,19	near hole + vent center
sal0402-ccp-1	Sphalerite-style	Icb	-1,91	0,58	
sal0402-ccp-2	Sphalerite-style	Icb	-1,80	0,58	
sal0501-ccp-1	Cu-Style	Likely Icb	2,68	0,22	Large grain
sal0501-ccp-2	Cu-Style	Likely Cpy	2,11	0,21	small cluster
sal0501-ccp-3	Cu-Style	Likely Icb	3,82	0,19	Large grain
sal0501-ccp-4	Cu-Style	Likely Cpy	2,30	0,19	small cluster
sal0501-ccp-5	Cu-Style	Likely Icb	2,17	0,22	Large grain
sal0501-ccp-6	Cu-Style	Likely Cpy	2,78	0,21	small cluster
sal0501-ccp-7	Cu-Style	Likely Icb	1,49	0,20	Large grain
sal0501-ccp-8	Cu-Style	Likely Cpy	2,28	0,22	small cluster

sal0505-ccp-1	Cu-Style	Cpy	2,21	0,19	Supergene enrichment influence
sal0505-ccp-2	Cu-Style	Cpy	3,02	0,20	late sulfide
sal0505-ccp-3	Cu-Style	Cpy	3,02	0,18	late sulfide
sal0505-ccp-4	Cu-Style	Cpy	3,04	0,19	late sulfide
sal0505-ccp-5	Cu-Style	Cpy	2,81	0,35	late sulfide
sal0505-ccp-6	Cu-Style	Cpy	2,15	0,39	late sulfide
sal0505-ccp-7	Cu-Style	Cpy	2,61	0,19	small clusters i,e, likely early sulfides
sal0505-ccp-8	Cu-Style	Cpy	2,19	0,31	small clusters i,e, likely early sulfides
sal0503-ccp-1	Cu-Style	Icb	1,99	0,21	
sal0503-ccp-2	Cu-Style	Icb	2,05	0,21	
sal0503-ccp-3	Cu-Style	Icb	1,91	0,21	
sal0503-ccp-4	Cu-Style	Icb	1,73	0,21	
sal0503-ccp-5	Cu-Style	Icb	2,33	0,19	
sal0503-ccp-6	Cu-Style	Icb	1,94	0,21	

APPENDIX VI.II: Images of the sample polished slices where S isotopes analyses were performed.

Sample	Slice	Detail of the analyses's location
SAL-03-03	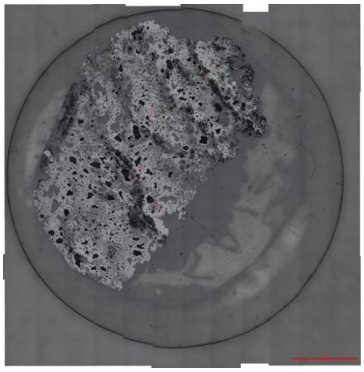	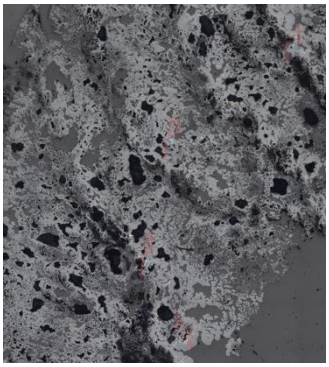
SAL-03-08	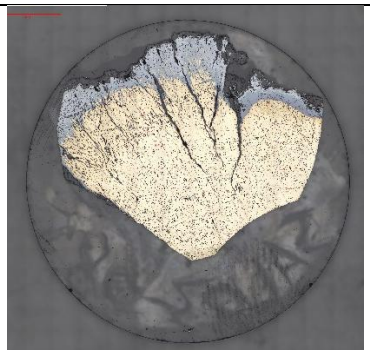	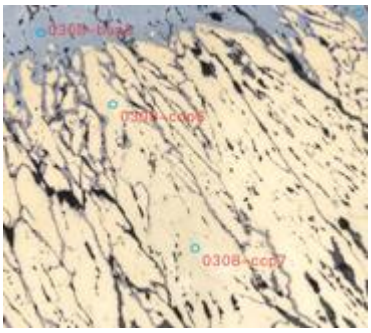
SAL-04-02	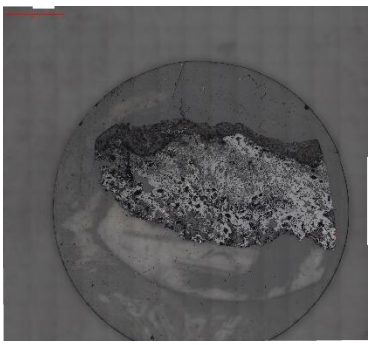	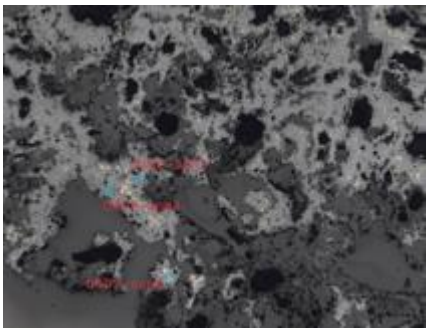
SAL-05-01	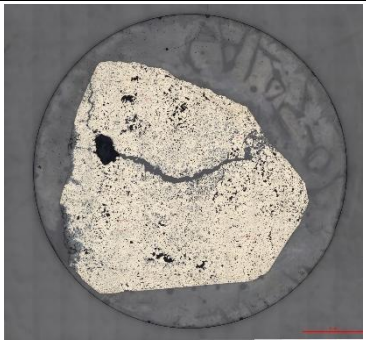	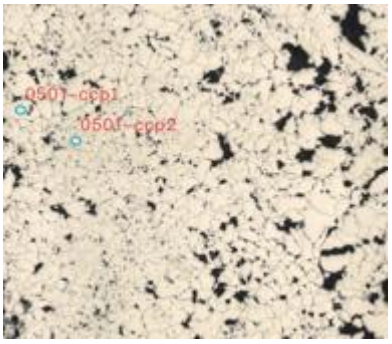

SAL-05-03	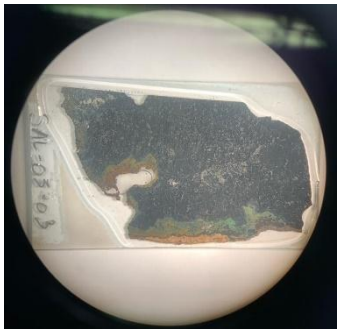	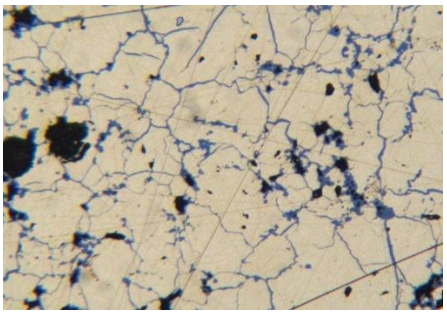
SAL-05-05	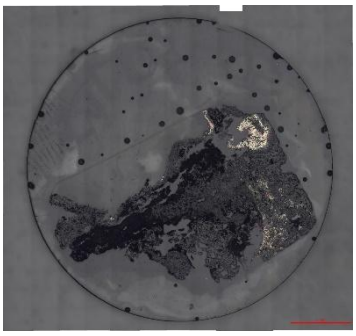	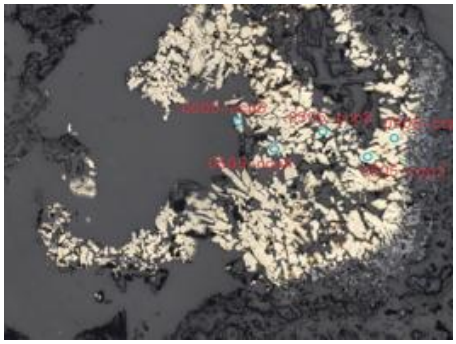

APPENDIX VII: Posters derived from the research conducted on this thesis.

APPENDIX VII.I: Ferreira, B., Dias, Á., & Marques, F. (2024). Hydrothermal Fields on the Portuguese Seafloor (Mid-Atlantic Ridge). In CIÊNCIAS Research & Innovation Day 2024.

INSTITUTO DOM LUIZ

CIÊNCIAS RESEARCH & INNOVATION

Ciências ULisboa

Geology

Institute Dom Luiz (IDL)
Coordinator: Filipe Rosas
Website: idl.ciencias.ulisboa.pt
Evaluation: Excellent

This work was funded by:
- *the Portuguese Fundação para a Ciência e a Tecnologia (FCT) I.P./MCTES through national funds: (PIDDAC) – UIDB/50019/2020 (https://doi.org/10.54499/UIDB/50019/2020), UIDP/50019/2020 (https://doi.org/10.54499/UIDP/50019/2020) and LA/P/0068/2020 (https://doi.org/10.54499/LA/P/0068/2020*
- *Macao Science and Technology Development Fund - SeaMin: FDCT-0041/2021/A1*
- *EU Research Projects - BLUE MINING :– 604500, 2014-2018*

Bernardo Ferreira, Ágata A. Dias e A. Filipa A. Marques

Hydrothermal Fields on the Portuguese Seafloor (Mid-Atlantic Ridge)

Portugal has one of the largest exclusive economic zones (EEZ) worldwide, spanning 1.7 million km^2, with sovereignty over the seabed within an extended 'continental shelf' of up to **2.4 million km^2**. This area features bathymetrically elevated segments of the Mid-Atlantic Ridge (MAR), influenced by the Azores mantle plume anomaly, particularly near the triple junction between the Eurasian, Nubian, and North American plates. The ridge is composed of a series of second-order, slow-spreading segments (19–25 mm/yr), separated by non-transform offsets (NTOs) that are characterized by tectonic activity, low magmatic supply, and low-angle detachment faulting. Here, we present the known hydrothermal fields (HFs) that have already been identified along the MAR within the present and extended area of the Portuguese 'continental shelf'. HFs have been shown to produce distinct hydrothermal regimes, fluid signatures, and mineralization processes that are specific to their host rock, depth and overall geological setting.

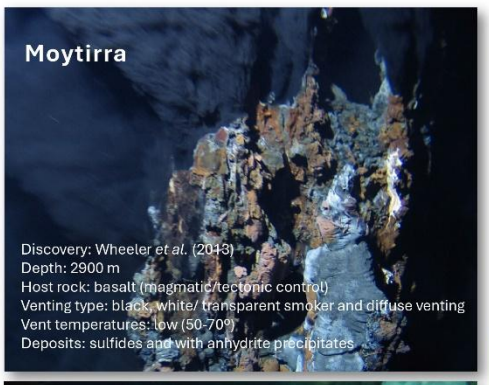

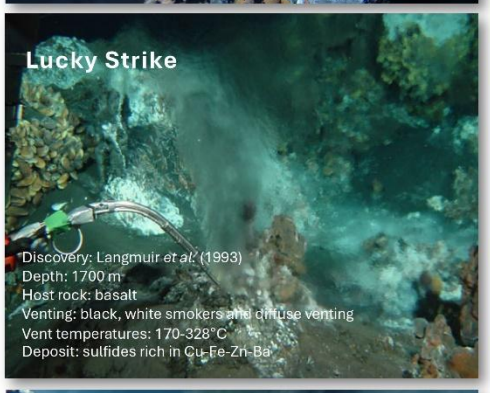

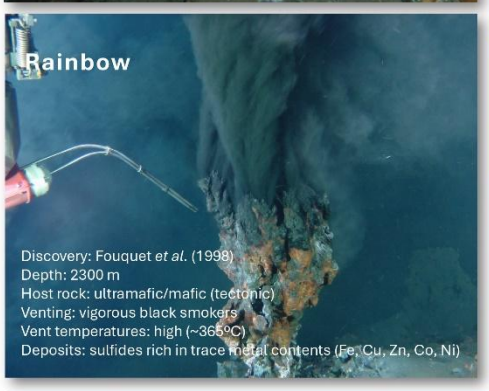

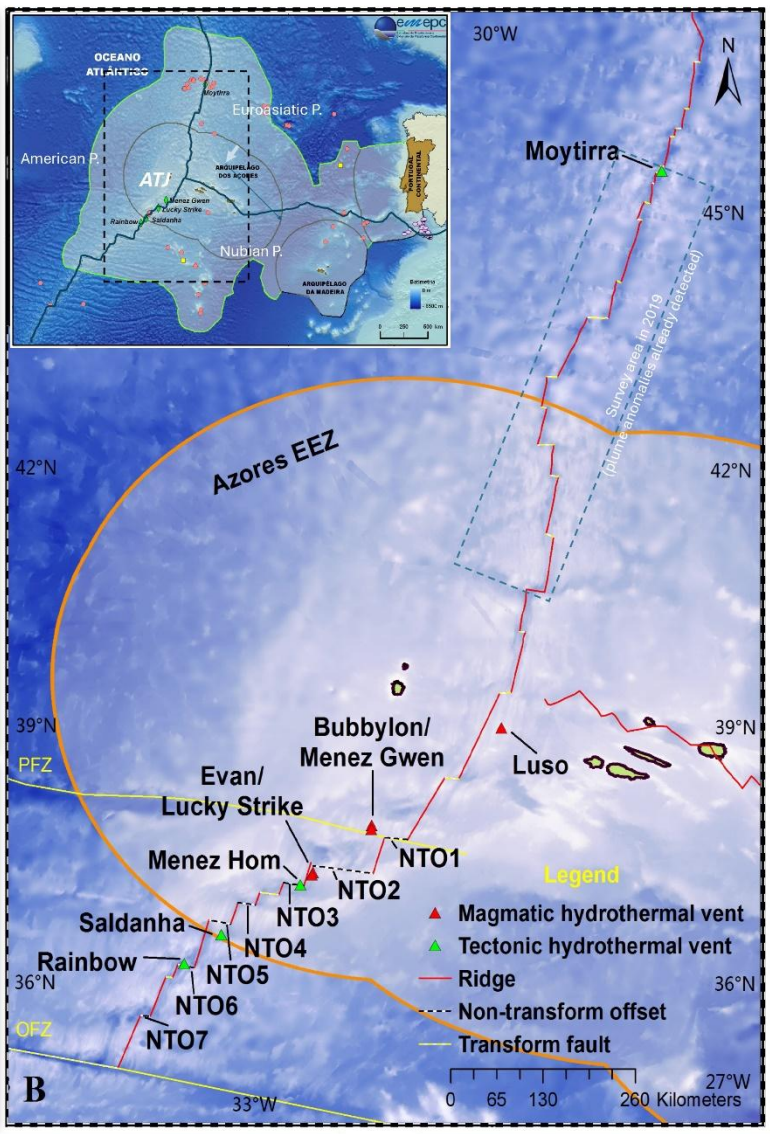

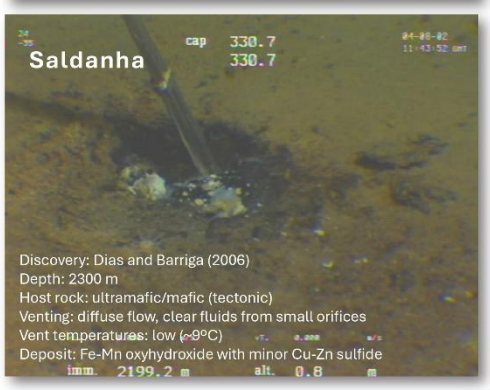

Geochemical Signatures of the Deposits Reflect Geological Settings

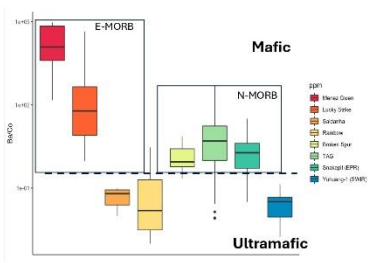

The Ba/Co ratio of the deposits is indicative of different geological settings.
Enrichment of Ni and Co is typical for ultramafic-hosted deposits

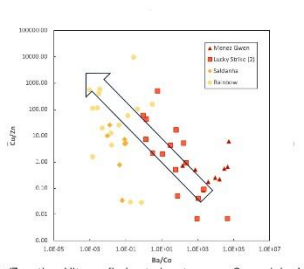

↑Cu/Zn ratios: Ultramafic-hosted systems are Cu-enriched
↑ [Cu] - sufide minerals assemblage of higher-T
↑ [Zn] - associated with precipitation at lower-T (<250°C)

Essential Equipment Used for Hydrothermal Field Exploration

Remotely Operated Vehicles (ROVs) | Deep-Sea Submersibles | Autonomous Underwater Vehicles (AUVs) | CTD (Conductivity, Temperature, Depth) | Multibeam Echosounder (Sonar)

Most of the HFs developed in close association with NTOs are linked to serpentinization fronts, primarily exhibiting low-temperature diffuse venting at the surface (e.g., Menez Hom and Saldanha). In contrast, the Rainbow HF is unique, featuring vigorous high-temperature venting of metal-rich fluids and producing significant sulfide mineralization. In diffuse systems, mineralization mainly occurs in the subsurface, with a precipitation sequence that starts with higher-temperature Cu-sulfides, followed by Cu-Zn and Fe sulfides, and culminating in oxyhydroxides near the surface (e.g., Saldanha and Menez Hom).

The heterogeneous geodynamic setting, including long-lived detachment faulting and the influence of Azores mantle anomalies, controls the nature of the host rocks (e.g., highly vesicular mafic volcanics or exposed serpentinized ultramafics), the hydrothermal regime, and the mineralization and deposition processes. Ultramafic-hosted HFs, such as Rainbow, have the potential to harbor large, high-grade seafloor massive sulfide (SMS) deposits.

The geochemical signatures of the water column and seafloor anomalies, together with the geotectonic context of the area, suggest the potential for discovering more HFs. This variability makes the Portuguese sector of the MAR an ideal natural laboratory for studying how different geological conditions generate distinct hydrothermal regimes and mineralization processes.

References

- Dias, Á A, *et al.* (2006) Mineralogy and geochemistry of hydrothermal sediments from the serpentinite-hosted Saldanha hydrothermal field (36˚34'N; 33˚26'W) at MAR. *Mar. Geol.*, 225, 157–175
- Dias Á A, *et al.* (2019) Geochemistry of Fe-Si-(Mn) Chimneys from Luso Vent Field, MAR. *Goldschmidt*, 10i, 445.
- Fouquet, Y., *et al.* (1998). FLORES diving cruise with Nautile near the Azores-First dives on the Rainbow field: hydrothermal seawater/mantle interaction. *InterRidge News*, 7(1), 24-28.
- Fouquet, Y., *et al.* (1994). A detailed study of the Lucky-Strike hydrothermal site and discovery of a new hydrothermal site:«Menez-Gwen». Preliminary results of DIVA 1 cruise. *Inter-Ridge News*, 3(2), 14-17.
- Wheeler, A. J., *et al.* (2013). Moytirra: Discovery of the first known deep-sea hydrothermal vent field on the slow-spreading Mid-Atlantic Ridge north of the Azores. *G3*, *14*(10), 4170-4184.
- Langmuir, C., *et al* (1993). Lucky strike-a newly discovered hydrothermal site on the Azores platform. *Ridge Events*, *4*(2), 3-5.

APPENDIX VII.II: Dias Á A, Marques A F A, Ferreira B, Pinto A, Costa P. (2025) Geochemical and Isotopic Constraints on Sulfide Deposition at the Rainbow Hydrothermal Field. Goldschmidt 2025, #31375. July 6-11, Prague.

Geochemical and Isotopic Constraints on Sulfide Deposition at the Rainbow Hydrothermal Field

Ágata. A. Dias[1,2,3], A. F. A. Marques[1], B. Ferreira[1], A. Pinto[2] & P. Costa[3]

1. DG-FCUL - Geology Department, Faculty of Sciences of the University of Lisbon and Instituto, Portugal
2. IDL - Instituto Dom Luiz, FCUL, Portugal
3. Institute of Science and Environment, University of Saint Joseph. Macau SAR.

GOLDSCHMIDT Prague 2025 6–11 JULY · Ciências ULisboa · INSTITUTO DOM LUIZ · #31375 · USJ Institute of Science and Environment

Summary

Fig 1. Rainbow black smoker

The Rainbow Hydrothermal Field (RHF; 36°14′N) is located at a non transform offset (NTO) of the slow-spreading Mid-Atlantic Ridge (MAR). Here, extensive faulting has uplifted deep-seated lithologies, forming a dome-shaped massif composed of ultramafic rocks with intrusions of mafic material like gabbros and basalts. The field hosts hydrothermal chimneys and mounds with venting activity ranging from high-T (up to ~360 °C), Cu-rich focused flow to lower-T Zn-rich diffuse flow.

Fluids are likely channeled to the seafloor along faults and fractures which have shifted their pathways over time, explaining the occurrence of inactive chimneys scattered around the area. This study investigates the metal distribution and sulfur isotopic composition in zoned sulfide chimneys to unravel fluid evolution, mixing regimes, and the depositional controls of mineralization at Rainbow HF.

Geological setting

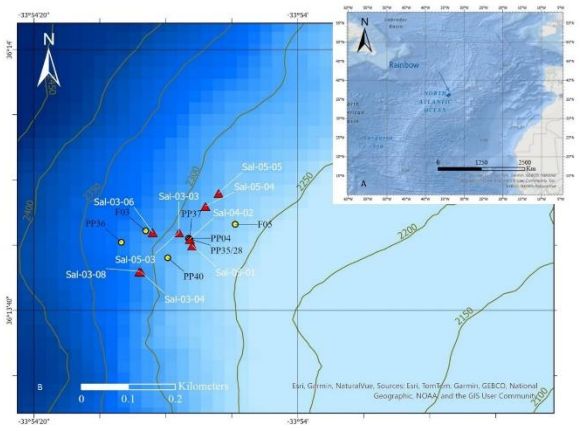

Fig 2. (A) Location of the Rainbow hydrothermal field along the Mid-Atlantic Ridge (MAR). (B) Detailed bathymetric map of the vent field showing sampling sites (red triangles). Yellow circles indicate reference markers left during oceanographic missions.

Samples: Nine sulfide chimney samples were collected during the 1998 Saldanha cruise using the submersible *Nautile* at depths of ~2,300 m. Several chimneys' edifices were observed, ranging from vent clusters to isolated edifices, as well as weakly active areas (mostly with diffuse venting and apparently inactive chimneys). Chimneys showing very active to less active venting, as well as apparently inactive structures in diffuse areas, were collected. Together, they represent different venting regimes, mineralization styles, and stages of hydrothermal evolution.

Methods: Polished sample sections were prepared from representative chimney fragments. Mineralogy and textures were examined by reflected light microscopy. Bulk geochemical compositions and *in-situ* sulfur isotope ratios ($\delta^{34}S$) were analyzed by INAA, ICP and LA-MC-ICP-MS respectively.

Main mineralogy, bulk geochemistry and S isotopic composition

Fig 3. Images of sulfide-rich samples and main mineral assemblages and selected metal concentrations (*Inner* – inner zones of the vent; *Outer* – Outer zones of the vent).

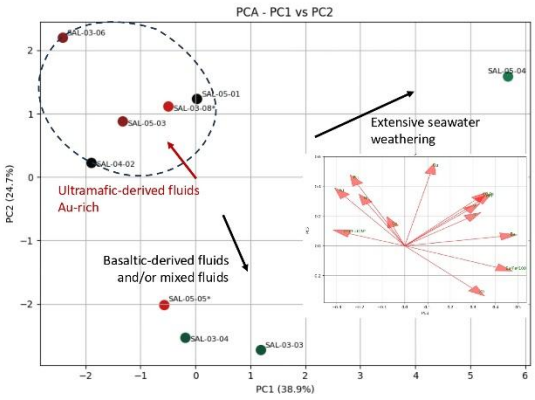

Fig. 5. Principal Component Analysis (PCA) based on the composition of selected metals in sulfide vent samples from the Rainbow hydrothermal field (HF), illustrating compositional variability and highlighting distinct geochemical signatures within the site.

Sulfur isotopic compositions ($\delta^{34}S$) of sulfide minerals from Rainbow vents range from –2.77‰ to +3.82‰, reflecting variable sulfur sources and mineralization conditions.
The most positive values (+2.11 to +3.64‰) are associated with Cu-rich phases, likely precipitated from high-T fluids with limited seawater-derived sulfate input. In contrast, sphalerite shows unusual negative $\delta^{34}S$ values (–2.27 to –0.44‰). Isocubanite exhibits the broadest isotopic range (–2.77 to +3.82‰) with heavier values associated with high-T mineralization. Compared to other ultramafic-hosted MAR systems, $\delta^{34}S$ signatures record lighter values, suggesting a stronger influence of basaltic-derived sulfur. However, microbial sulfate reduction may have contributed to late-stage $\delta^{34}S$ depletion in low-T zones, potentially affecting sphalerite and isocubanite formed during waning hydrothermal activity.

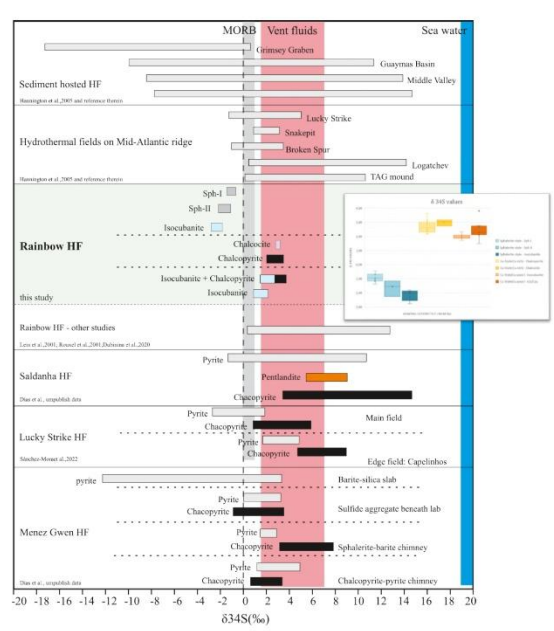

Fig 7. In-situ $\delta^{34}S$ values of sphalerite and Cu-sulfide minerals.

Rainbow mineralization

Sulfide mineralization at the Rainbow HF records multiple stages of fluid evolution, reflected in distinct mineral assemblages and metal distributions of its vents. Chimneys can be broadly classified as Cu-rich or Zn-rich, with variable Fe content. Cu-rich assemblages, dominated by chalcopyrite and isocubanite, are linked to focused high-T and metal-rich fluids that have interacted with ultramafic mantle rocks, showing also hydrothermal fluid-like REE patterns characterized by positive Eu anomalies. In contrast, Zn-rich assemblages (sphalerite ± sulfates) occur in lower-T or waning vent structures, suggesting late-stage remobilization, basaltic input, or microbial sulfate reduction.
Seawater alteration phases (bornite, digenite, covellite, and Fe-oxyhydroxides) are mainly found in inactive and diffuse-flow chimneys. This late seawater oxidative interaction was also responsible for the enrichment of seawater-derived elements (V and U) and Ce negative anomalies during oxidative weathering.
Sulfur isotope composition supports this evolution: Cu-rich phases exhibit heavier $\delta^{34}S$ values, reflecting high-T precipitation from fluids interacting with ultramafic and mafic rocks, with limited seawater sulfate input, while sphalerite shows negative $\delta^{34}S$ values, suggesting possible microbial interference.

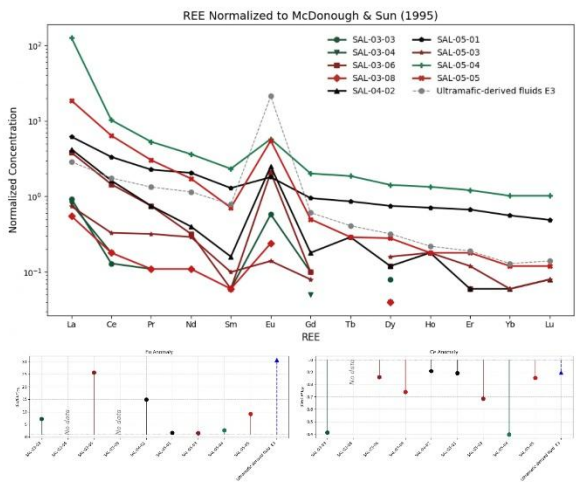

Fig 4. Chondrite-normalized REE patterns normalized and Eu/Eu* and Ce/Ce* anomalies.

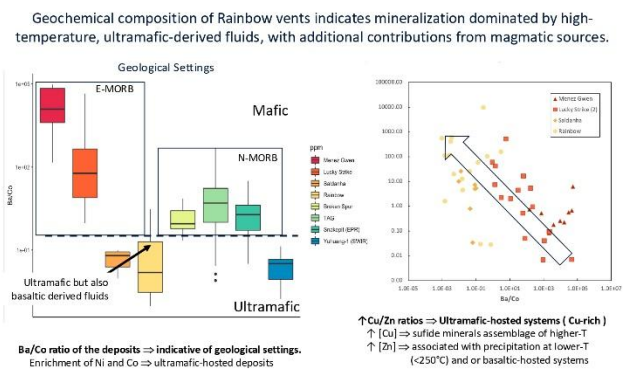

Fig 6. Ba/Co and Cu/Zn ratios as geochemical discriminators of MOR hydrothermal deposit settings.

This work was supported by the Macau FDCT (SeaMin project 0041/2021/A1) and by the Portuguese FCT, I.P./MCTES through national funds (PIDDAC): UID/50019/2025 and LA/P/0068/2020.